Optical Superlenses and Filters Based on Micro- and Nanoparticles

PRIFYSGOL
BANGOR
UNIVERSITY

Baidong Wu

Supervisor: Prof. Zengbo Wang

School of Computer Science and Engineering

Bangor University

A thesis submitted in partial fulfilment for the degree of

Doctor of Philosophy

2025

Declaration

I hereby declare that this thesis is the results of my own investigations, except where otherwise stated. All other sources are acknowledged by bibliographic references. This work has not previously been accepted in substance for any degree and is not being concurrently submitted in candidature for any degree unless, as agreed by the University, for approved dual awards.

Yr wyf drwy hyn yn datgan mai canlyniad fy ymchwil fy hun yw'r thesis hwn, ac eithrio lle nodir yn wahanol. Caiff ffynonellau eraill eu cydnabod gan droednodiadau yn rhoi cyfeiriadau eglur. Nid yw sylwedd y gwaith hwn wedi cael ei dderbyn o'r blaen ar gyfer unrhyw radd, ac nid yw'n cael ei gyflwyno ar yr un pryd mewn ymgeisiaeth am unrhyw radd oni bai ei fod, fel y cytunwyd gan y Brifysgol, am gymwysterau deuol cymeradwy.

Acknowledgements

I would like to thank my supervisor, Professor Zengbo Wang, for his guidance and support during my PhD. His clear academic thinking and patient advice helped me solve many problems, both large and small. Many key parts of this thesis came from discussions with him, and I am grateful for the time he devoted to explaining ideas and pointing me in the right direction, especially when the work became difficult.

I would also like to express my thanks to Dr. Liyang Yue for his guidance during my studies. I am also very grateful to Dr. Bing Yan and Dr. James N. Monks. Their suggestions on experiments and theory were always practical and to the point, and their help has had a direct impact on the results presented here.

My thanks also go to my colleagues, friends and especially to my family, whose constant encouragement and support have sustained me throughout these years, and I am especially grateful to my girlfriend, Ms. Keke Fang, whose unwavering companionship and thoughtful guidance supported me throughout the long and challenging process of writing this thesis.

Abstract

Advances in modern photonics increasingly rely on the ability to control light at scales far below its wavelength. Whether the goal is to resolve nanoscale structures in imaging or to maintain stable spectral behaviour in optical filtering, the central challenge is the same: how to manipulate light with high precision when traditional optical components approach their physical limits. Among the various strategies explored, micro- and nanoscale spherical structures have emerged as particularly powerful, as their symmetric geometry enables predictable and highly tunable interactions with light. This thesis builds on this unifying principle to explore how spherical particles can be engineered to enhance both super-resolution imaging and wide-angle optical filtering.

The study first examines TiO_2-based metamaterial solid immersion lenses (mSILs) fabricated using nano–solid–fluid assembly. Three geometrical variants, full-spherical, hemispherical and super-hemispherical were produced and evaluated under identical conditions. Systematic optical characterisation reveals that the super-hemispherical form offers the most favourable balance between imaging resolution and field-of-view. Complementary simulations and microscopy further show that bottom-surface nanoparticle penetration consistently correlates with improved image formation, providing new physical insight into the near-field coupling mechanisms governing mSIL performance.

To extend the investigation to biological superlenses, three distinct morphologies of yeast cells, including spherical, chemically fixed and naturally collapsed geometric variants, were analysed as lensing elements. By isolating geometry as a controlled variable, the study establishes that only collapsed or flattened cells generate stable sub-diffraction imaging in air, whereas spherical cells do not exhibit comparable behaviour under the tested conditions. This represents the first systematic demonstration that cell morphology is a primary determinant of biological superlensing capability, offering a physically grounded basis for future development of cell-derived optical lenses.

Building on the same light–sphere interaction principles, the thesis then develops a hybrid optimisation methodology for nanosphere-based metamaterial filters. The framework integrates single-particle resonance analysis, effective-index extraction and thin-film optimisation, enabling efficient and accurate design of multilayer nanosphere architectures without extensive three-dimensional parameter sweeps. Using this methodology, wide-angle

long-pass edge filters and SiNS@Au-based bandpass filters were realised with high optical density, minimal angular spectral shift (<10 nm) and stable transmission maintained up to 60° incidence. These devices surpass both conventional thin-film filters and previously reported metamaterial designs.

Together, the findings advance the fundamental understanding of light–sphere interactions across scales and provide practical design principles for next-generation super-resolution imaging systems and angle-tolerant optical filters.

Table of content

List of Figures

Figure 6.3 Design schematics for edge filters: (a) A SiNS that should be embedded in the host medium. (b) Single-layered unit cell. (c) Two-layered unit cell. (d) Three-layered unit cell. (e) Three-layered unit cell with ARC.

Figure 6.4 Transmission spectra contour plot for LP1 (a, b), LP2 (c, d), LP3 (e, f), and LP4 (g, h) designs and with TE (left column) and TM (right column) polarisations. The solid and dashed lines denote transmissions at 0° and 60° incident angles, respectively. Zones A, B, C, and D in (a, b) highlight targeted undesired peaks for elimination in subsequent designs.

Figure 6.5 The transmission spectra dependence of edge filter on (a) and (b), longitudinal distances, H_1 and H_2, between two adjacent SiNS's MFLs.

Figure 6.6 The interface of the ESM with LP3 converted and modelled accordingly. MgF_2 was selected as the top anti-reflection coating (ARC), while two additional SiN layers were inserted between the MgF_2–MFL and MFL–glass interfaces. The "Lock" panel was used to fix specific parameters in order to maintain consistency during the optimisation process.

Figure 6.7 (a, b) The average OD for stop band (350 nm–480 nm) and (c, d) average transmission for pass band (500 nm–1200 nm) of 4 edge filters under different AOIs (represented as Theta) and with both TE (left) and TM (right) polarised incidence.

Figure 6.8 The shift of edge wavelength of LP0–4 with TE- (a) and TM- (b) polarised AOI.

Figure 6.9 Tunability of edge wavelength range (highlighted by green arrows) in the three-metalayer configuration based on three stacked MFLs from LP1 by varying silicon nanoparticle size and applying (a) crystal and (b) amorphous silicon.

Figure 7.1 (a) Extinction coefficients and (b) approximated transmittance spectra as a function of incident wavelength for a single silicon nanosphere (SiNS, R_{SiNS} = 70 nm) with a gold shell (T_{shell} = 20 nm) under varying refractive indices of the host medium.

Figure 7.2 The thickness information of (a) optimised and (b) unoptimised conventional thin-film bandpass filters. (c, d) The transmittance comparison between two thin-film bandpass filters.

Figure 7.3 The schematic illustration of (b) single-MFL, (c) two-MFLs and (d) hybrid design with the fundamental gold coated SiNS as shown in (a).

Figure 7.4 Contour plots of transmission spectra for BP1 (a, b), BP2 (c, d), unoptimised BP3 (e, f) and optimised BP3 (g, h) designs under TE (left column) and TM (right column) polarisations. Solid and dashed lines represent transmission at 0° and 60° incidence angles, respectively. Zones A, B, and C in (a, b) indicate critical regions targeted for further optimisation.

Figure 7.5 Comparison of the transmission spectrums obtained via CST full-wavelength simulation and the K-K approximation. The inset shows the refractive index of the single-metalayer composing of the infinite unit cells.

Figure 7.6 The interface of the ESM with BP3 converted and modelled accordingly. The 1D PhC with $(0.5H\ L\ 0.5H)^3$ was placed on the top of BP2. The "Lock" panel was used to fix specific parameters in order to maintain consistency during the optimisation process.

Figure 7.7 (a, b) Average OD for the stop-band and (c, d) average transmission for the pass-band of three bandpass filters (BP1, BP2, BP3) under varying angles of incidence (AOI, represented as Theta) for both TE (left) and TM (right) polarised light. The BP1 design (Lotti et al., 2019) is reproduced from Ref. [7].

Figure 7.8 Comparison of pass-band central wavelength shift for BP0, BP1, BP2, and BP3 under TE (a) and TM (b) polarisation as a function of AOI.

Figure 7.9 Tunability of the transmission spectra for the two-MFLs (BP2) bandpass filter. (a) Effect of varying SiNS radius with a fixed gold shell thickness (T_{Shell} = 15 nm). (b) Effect of varying shell thickness with a fixed SiNS radius (R_{SiNS} = 70 nm).

List of Abbreviations

AOI ·	Angle of incidence
ARC	Anti-reflection coating
BF	Bright-field
CFD	Chemically fixed and dehydrated
CUT	Contrastive Unpaired Translation
ESM	Essential Macleod
FIT	Finite Integration Technique
FDTD	Finite-Difference Time-Domain
FOV	Field of view
FSS	Frequency Selective Surface
HMM	Hyperbolic Metamaterial
HS	Hydrated spherical
K–K	Kramers–Kronig
LSPR	Localised Surface Plasmon Resonance
MDM	Metal–Dielectric–Metal
MFL	Meta-film layer
mSIL	Metamaterial Solid Immersion Lens
NA	Numerical Aperture
NSFA	Nano–Solid–Fluid Assembly
NSOM	Near-field Scanning Optical Microscopy
OD	Optical Density
PhC	Photonic Crystal
PNJ	Photonic Nanojet
PO mode	Polarised mode
SEM	Scanning Electron Microscopy
SinCUT	Single-Image Contrastive Unpaired Translation
SiNS	Silicon Nanosphere
SIL	Solid Immersion Lens
SIM	Structured Illumination Microscopy
TE	Transverse Electric

TM	Transverse Magnetic
VSWF	Vector Spherical Wave Function

List of Publications

Journal Papers:

[1] **B. Wu**, J.N Monks, L. Yue, A. Hurst, Z. Wang, "Optimized Wide-Angle Metamaterial Edge Filters: Enhanced Performance with Multi-Layer Designs and Anti-Reflection Coatings," Photonics. 2024, 11, 446.

[2] **B. Wu**, L. Yue, Z. Wang, "Optimized wide-angle metamaterial bandpass filters with multi-layer design and 1D photonic crystal integration," Opt. Commun. 2025, 591, 132185.

[3] **B. Wu**, F. Khan, L. Yu, Z. Wang, "Shape-Dependent, Deep-Learning-Assisted Metamaterial Solid Immersion Lens (mSIL) Super-Resolution Imaging", arXiv preprint. 2026, 2603.24371.

[4] L. Yu, Z. Wang, L. Xu, L. Yue, B. Yan, I.V. Minin, O.V. Minin, **B. Wu,** Y. Chen, "Highly curved reflective W-shape and J-shape photonic hook induced by light interaction with partially coated microfluidic channels," arXiv preprint. 2022, 2209.03220.

[5] Y. Ivanova, M. R. M, J. Liu, L. Abtahi, **B. Wu**, A. S. Cooper, Z. Wang, D. W. Allan, A. Mudher, A. A. Comeault, L. Sivanatharajah, "Context-dependent toxicity of human Tau isoforms in a Drosophila tauopathy model," bioRxiv preprint. 2026, 10.64898/2026.03.20.713147

Conferences:

[1] **B. Wu**, Z. Wang, Y. Chen, L. Yue, B. Yan, "Design of Silicon Nanosphere-based Wide-angle Shin-free Metamaterial Edge Filter," in Frontiers in Optics + Laser Science, 2023, online, JM7A.35.

[2] **B. Wu**, Z. Wang, "Nano-Imaging with TiO_2 Superlenses: A Comparative Study of Design Variants," in Frontiers in Optics + Laser Science, 2023, online, JM7A.35.

[3] **B. Wu**, Z. Wang, L. Yue, "Optimized Wide-Angle Metamaterial Bandpass Filters: Enhanced Performance with Multi-Layer Designs and 1D Ternary Photonic Crystals," in The 1st International Online Conference on Photonics, 2024, online, 12.

[4] **B. Wu**, L. Yue, Z. Wang, "Yeast Cell as Biological Superlens for Super-resolution imaging," in Nanoparticles for Drug Delivery & Therapy on Ireland–Wales Research Alliance Workshop, 20th March 2026, Bangor, Wales.

[5] Y. Chen, Z. Wang, B. **Wu, B**. Yan, L. Yue, Y. Joya, "A New Method for Micro Fresnel Zone Plates Lens Design and Low-cost Fabrication by Laser Direct Writing," in Frontiers in Optics + Laser Science, 2022, online, JW5A.10.

[6] L, Yu, Z. Wang, L. Xu, L. Yue, B. Yan, **B. Wu,** Y. Chen, "Highly curved reflective W-shape and J-shape photonic hook induced by light interaction with partially coated microfluidic channels," in Frontiers in Optics + Laser Science, 2023, online, JW5A.36.

Chapter 1 Introduction

1.1 Introduction

The continuous miniaturisation of photonic and optoelectronic systems has placed enhanced demands on the precise control of light–matter interactions at subwavelength scales. This capability underpins a wide range of modern technologies, including high-resolution biomedical imaging, integrated circuit inspection, environmental sensing, laser protection and optical communication. Across these diverse applications, a shared scientific challenge emerges: how to reliably extract, manipulate and transmit optical information when structural features approach, or fall below, the wavelength of light.

Among the many structures explored for subwavelength light manipulation, micro- and nanoscale spherical particles represent a uniquely powerful and versatile platform. Their rotational symmetry produces analytically predictable scattering and near-field behaviour, providing a basis for controllable optical responses across multiple length scales. At the microscale, dielectric spheres generate photonic nanojets (PNJs), which is a tightly confined, high-intensity beams that is capable of illuminating nanoscale features and convert evanescent information into propagating light [1]. This behaviour offers a practical mechanism to surpass the classical diffraction limit, which typically restricts conventional imaging systems to resolutions no better than approximately $\lambda/2$ [2].

Recent advances in nano–solid–fluid assembly (NSFA) have enabled the fabrication of TiO_2-based metamaterial solid immersion lenses (mSILs) with geometric tunability across full-spherical, super-hemispherical and hemi-spherical and geometries [3]. Despite the promising imaging enhancements reported in the previous literature, key unresolved questions remain. In particular, the influence of mSIL geometry on resolution, field-of-view and near-field coupling has not been systematically established, and the physical origin and universality of the bottom-surface penetration effect remain poorly understood. Existing studies also lack controlled, like-for-like comparisons between different geometries, limiting our ability to identify true geometry-dependent behaviour. These gaps hinder the rational development and optimisation of next-generation mSIL technologies.

Biological cells have also been explored as natural superlenses because they are easy to obtain, biocompatible and simple to prepare [4]. Spherical yeast cells can improve imaging resolution under certain conditions, but their actual shapes often deviate from the ideal sphere.

Effects such as partial collapse, surface flattening or local deformation have not been examined in a controlled way. This lack of systematic morphological study leads to variations in reported imaging performance and makes it difficult to identify the optical mechanisms involved.

At the nanoscale, the same principles governing microscale superlensing extend to another important photonic application: nanosphere-based metamaterial filters [5, 6]. Classical thin-film interference filters experience significant spectral blue-shift and degraded blocking performance at oblique incidence. Although structure-based optimisation, photonic crystals and hyperbolic metamaterials offer partial solutions, they often impose fabrication complexity or strong polarisation dependence [7–11]. Periodic arrays of dielectric or core–shell nanospheres provide a more straightforward strategy for achieving wide-angle filtering, leveraging symmetry-induced angular robustness and well-defined resonant behaviour inherent to spherical particles.

Although this thesis covers two areas, super-resolution imaging and wide-angle optical filtering, both are based on the same fundamental idea: the interaction of light with spherical particles at micro- and nanoscale dimensions. The behaviour of these particles, including Mie resonances, near-field confinement, evanescent coupling and angle-dependent stability, provides the physical basis for improved resolution in mSILs and for better angular performance in metamaterial filters. This common framework supports the overall research approach used in this work.

1.2 Aim and objectives

This thesis aims to systematically investigate and optimise the optical behaviour of micro- and nanoscale spherical structures, with a unified focus on advancing super-resolution imaging and wide-angle optical filtering.

To accomplish this aim, the following research objectives are established:

1. To fabricate and characterise TiO_2-based metamaterial mSILs with full-spherical, super-hemispherical and sub-hemispherical geometries using NSFA, and to determine how geometry and near-field penetration behaviour govern imaging resolution, field-of-view and imaging contrast.

2. To re-evaluate the imaging performance of biological cells by examining yeast cell morphology under different preparation conditions (spherical, chemically fixed and partially collapsed) and to establish the relationship between cell geometry and imaging capability.

3. To develop a hybrid, computationally efficient design methodology for nanosphere-based metamaterial filters, combining full-wave numerical simulation, effective-index extraction and thin-film optimisation.

4. To design, optimise and validate wide-angle metamaterial optical filters, including a silicon-nanosphere long-wave-pass edge filter and a SiNS@Au-based bandpass filter, and to benchmark their optical density, angular tolerance and transmission performance against both classical thin-film designs and the original designs.

1.3 Contributions

The original research conducted in this thesis has produced the following contributions:

1. New physical insight into geometry-dependent behaviour of TiO_2 mSILs: This work demonstrates that super-hemispherical mSILs uniquely achieve the optimal balance between resolution and field-of-view, and provide direct experimental and numerical evidence that bottom-surface nanoparticle penetration is a decisive indicator of imaging quality across multiple geometries.

2. First systematic investigation of geometry-dependent behaviour in biological cell-based superlenses: This thesis provides the first controlled study on how yeast-cell geometry influences superlensing performance. Three typical shapes were examined: spherical cells, chemically fixed cells and naturally collapsed cells. The results show that only collapsed or flattened cells can produce stable sub-diffraction imaging in air, while spherical cells do not show this effect under the same conditions. These findings establish a direct link between cell morphology and achievable resolution, and offer a clearer physical basis for the future development of cell-based optical lenses.

3. A unified, hybrid optimisation framework for nanosphere-based metamaterial filters: A combined methodology integrating single-particle resonance modelling, effective-index extraction and thin-film optimisation is developed, providing a general, efficient design

strategy that significantly reduces reliance on computationally intensive 3D parameter sweeps.

4. Realisation of wide-angle metamaterial edge and bandpass filters with state-of-the-art performance: Using the above framework, this thesis demonstrates long-pass edge filter with minimal spectral shift (<10 nm) compared to conventional filters and considerably high optical density (OD_{edge}> 2.55). The SiNS@Au-based bandpass filter also achieves an optical density ($OD_{bandpass}$ > 2.31) and spectral shift (< 20 nm). Performance is most stable under TE illumination and across all angles of incidence, both filters maintain stable transmission at incidence angles up to 60°. Their performance exceeds that of conventional thin-film designs and previously reported metamaterial filters.

1.4 Thesis Outlines

Chapter 2 reviews the theoretical foundations and existing literature relevant to the thesis, including the diffraction limit, Mie scattering, PNJ formation, microsphere-assisted imaging, solid immersion lenses, biological superlenses and thin-film filter design. Emphasis is placed on their limitations and the motivations for the current research.

Chapter 3 presents the analytical, numerical and experimental methods used throughout the study. This includes Mie-theory-based calculations, CST STUDIO (CST) full-wave simulations, effective-index extraction, thin-film optimisation using Essential Macleod (ESM), and fabrication and characterisation techniques for both mSILs and biological lenses.

Chapters 4 and 5 provide detailed investigations into TiO_2 mSIL geometries and biological cell-based superlenses, respectively, analysing their imaging performance and underlying optical mechanisms.

Chapters 6 and 7 describe the design, optimisation and evaluation of nanosphere-based long-pass edge filters and bandpass filters, demonstrating the advantages of the proposed hybrid design methodology.

Chapter 8 concludes the thesis with a summary of findings, broader implications, identified limitations and recommendations for future research directions.

1.5 References

[1] Z. Wang, W. Guo, L. Li, B. Lukyanchuk, A. Khan, Z. Liu, Z. Chen, M. Hong, “Optical

virtual imaging at 50 nm lateral resolution with a white-light nanoscope," Nat. Commun. 2011, 2, 218.

[2] Abbe, E. "Beiträge zur Theorie des Mikroskops und der mikroskopischen Wahrnehmung," Archiv. Mikrosk. Anat. 1873, 9, 413–418.

[3] W. Fan, B. Yan, Z. Wang, L. Wu, "Three-dimensional all-dielectric metamaterial solid immersion lens for subwavelength imaging at visible frequencie," Sci. Adv. 2016, 2, e1600901.

[4] Y. Li, X. Liu, B. Li, "Single-cell biomagnifier for optical nanoscopes and nanotweezers," Light Sci Appl. 2019, 8, 61.

[5] J. N. Monks, L. Yue, B. Yan, B. Aldred, A. Hurst, Z. Wang, "A wide-angle shift-free metamaterial filter design for anti-laser striking application," Opt. Commun. 2018, 429, 53–59.

[6] F. Lotti, A. Mirzaei, P. Wang, A.E. Miroshnichenko, A.V. Zayats, "Nanoparticle-based metasurfaces for angular-independent spectral filtering applications," J. Appl. Phys. 2019, 126, 213101.

[7] H. Shin, M. F. Yanik, Shanhui Fan, R Zia, M. L. Brongersma, "Omnidirectional resonance in a metal–dielectric–metal geometry," Appl. Phys. Lett. 2004, 84, 22, 4421–4423.

[8] C. Chen, K. Tetz, W. Nakagawa, Y. Fainman, "Wide-field-of-view GaAsAlxOy one-dimensional photonic crystal filter," Appl. Opt. 2005, 44, 8, 1503–1511.

[9] Y. Kanamori, T. Ozaki, K. Hane, "Reflection color filters of the three primary colors with wide viewing angles using common-thickness silicon subwavelength gratings," Opt. Express. 2014, 22, 21, 25663–25672.

[10] H. Choi, S. Choi, Y. Yoo, E. Jeon, Y. Yi, S. Park, D. Choi, H Kim, "Transmission-type photonic crystal structures for color filters," Opt. Express. 2013, 21, 18317–18324.

[11] F. Wu, G. Lu, C. Xue, H. Jiang, Z. Guo, M. Zheng, C. Chen, G. Du, H. Chen, "Experimental demonstration of angle-independent gaps in one-dimensional photonic crystals containing layered hyperbolic metamaterials and dielectrics at visible wavelengths," Appl. Phys. Lett. 2018, 112, 4, 041902.

Chapter 2 Literature Review

2.1 Fundamentals of Optical Resolution

2.1.1 Diffraction Limits

In macroscopic optics, the behaviour of light is typically described by geometric optics in which light propagates as a straight ray. However, due to the intrinsic wave nature of light, this straight-line behaviour breaks down when light encounters apertures or structures comparable in size to its wavelength. In such scenario, the diffraction occurs and refers to a phenomenon where wavefronts bend, spread, and interfere after passing through an opening or around an obstacle. This fundamental consequence of the wave equation governing electromagnetic fields leads to a finite spatial resolution in any imaging system, regardless of the quality of lenses or detectors, and it this limit is known as the optical diffraction limit.

The resolution limit of the microscope was first proposed by Ernst Abbe in 1873 to describe the minimum resolvable distance, d, of a microscope, which is fundamentally constrained by the wavelength, λ, of the illuminating light and the numerical aperture ($N.A.$) of the optical system [1]. This relation is expressed as:

$$d = \frac{\lambda}{2\,N.A.} \tag{2.1.1}$$

where $N.A. = n(\sin\alpha)$, n and α are the refractive index of the medium and the half-angle of the maximum cone of light that can be collected by the lens. This formula indicates that achieving higher resolution requires either shorter wavelengths or higher numerical apertures.

A related but more practical definition of resolution is given by the Rayleigh criterion, which considers the smallest distance at which two point-sources can be distinguished based on the overlap of their diffraction patterns [2]. It can be expressed as:

$$\mathrm{d}_{Rayleigh} = 0.61\frac{\lambda}{N.A.} \tag{2.1.2}$$

By applying Heisenberg's uncertainty principle to optical diffraction limit case, the position (Δx) and momentum (Δp_x) uncertainties associated with the x-direction of a photon satisfy the following relation:

$$\Delta x \Delta p_x \geq \frac{h}{4\pi} \tag{2.1.3}$$

where h is Planck's constant; And the momentum can be expressed by wavevector as: p_x =

$k_x(h/2\pi)$. Consequently, Eq. (2.1.3) can be re-written as follows in wave optics:

$$\Delta x \Delta k_x \geq \frac{1}{2} \tag{2.1.4}$$

Eq. (2.1.4) indicates that there is a fundamental trade-off between how tightly light can be confined in space and the range of spatial frequencies it can contain. In simple terms, resolving smaller features requires higher spatial frequencies. This inverse relation can be approximately expressed as $\Delta x \propto 1/k_x$, meaning that larger transverse wavevectors represent finer spatial features. Since the transverse wavevector directly represents the spatial frequency of the object, only a limited portion of these frequency components can propagate through an optical system, while those beyond a certain limit become non-propagating, or evanescent, and thus cannot be captured in conventional imaging.

The limitation of accessible spatial frequencies, as indicated by Eq. (2.1.4), can be further understood by examining the decomposition of the optical wavevector and distinguishing between propagating and evanescent components, which is discussed in the next section.

2.1.2 Evanescent and Propagating Waves

The diffraction limit arises because only a limited range of spatial information carried by light can propagate through space. When light interacts with nanostructures smaller than its wavelength, the scattered field contains both low-frequency components that travel freely and high-frequency components that describe the fine details of the object. However, these high-frequency components decay rapidly near the surface and cannot reach the far-field region, which ultimately restricts the achievable resolution in conventional optical imaging.

To describe this behaviour quantitatively, in a surrounding medium with refractive index of n_i in which light with wavelength, λ_i, and total wavevector, k_i, propagating must satisfy following relations [3]:

$$k_i^2 = k_x^2 + k_y^2 + k_z^2 \tag{2.1.5}$$

where k_x, k_y and k_z are wavevector components in x-, y- and z-direction, respectively. The magnitude of wavevector k_i can also be expressed as follows:

$$|k_i| = \frac{2\pi}{\lambda_i} = n_i k_0 \tag{2.1.6}$$

where k_0 is wavenumber in free space. For a given transverse wavevector component, $k_{\parallel} = \sqrt{k_x^2 + k_y^2}$, the longitudinal component k_z is given by:

$$k_z = \sqrt{k_i^2 - k_{\parallel}^2} \tag{2.1.7}$$

There are two possible types of solutions for k_z. When k_z is real, the wave propagates freely through the medium and carries optical energy into the far field. These are known as propagating waves. Conversely, when k_z is imaginary ($k_z = i\sqrt{k_{\parallel}^2 - k_i^2}$), the field amplitude decays exponentially along the propagating direction, indicating an evanescent wave:

$$E(z) = E_0 \mathrm{e}^{-\sqrt{k_{\parallel}^2 - k_i^2} Z} = E_0 \mathrm{e}^{-K_z Z} \tag{2.1.8}$$

where E_0 represents the electric-field amplitude at the sample surface ($z = 0$), K_z is the decay constant of the evanescent field along the z-direction, and Z denotes the physical distance from the surface.

Such exponentially decaying fields are so called evanescent waves. They are unable to transport energy into the far field but remain confined within a subwavelength distance—typically less than one wavelength—from the surface.

As discussed earlier in Eq. (2.1.4), achieving higher resolution (a smaller Δx) requires larger transverse wavevectors (k_x). However, when k_x exceeds the maximum propagating value allowed by the medium, the longitudinal component k_z becomes imaginary, and the field turns into an evanescent wave. This explains why the attempt to resolve finer features inevitably leads to non-propagating, exponentially decaying fields near the surface. This intrinsic limitation links the diffraction limit directly to the physical boundary between propagating and evanescent fields.

2.1.3 Existing Super-Resolution Imaging

The previous sections have established that the diffraction limit in optical imaging from the loss of evanescent components carrying high-spatial-frequency information. Once these components decay near the surface, only the propagating part of the optical field can be collected by a conventional objective, resulting in a fundamental resolution barrier.

To overcome this limitation, extensive research has been devoted to developing optical strategies that can either recover, amplify, or convert evanescent waves into propagating forms. Over the past decades, several categories of existing super-resolution imaging approaches have been proposed, including near-field detection, far-field optical modulation, and other engineered optical schemes. A brief overview of their working principles and

representative examples is presented below, providing references for the discussion of microsphere-assisted super-resolution imaging in the next section.

1. Near-field scanning optical microscopy (NSOM)

The concept of near-field optical imaging was first proposed by Synge in 1928, and became experimentally achievable in the 1980s through the pioneering work of Pohl and Betzig [4]. The technique breaks the diffraction limit by directly detecting the evanescent field using a nanoscale probe positioned only a few nanometres above the sample surface.

Pohl et al. first demonstrated sub-diffraction imaging with a resolution of approximately λ/20, while Betzig et al. later improved it to λ/43 using an aperture-based probe. Subsequent apertureless configurations further enhanced the resolution to below 10 nm, benefiting from higher optical throughput and reduced signal loss [5].

Despite providing genuine optical super-resolution and wide applicability in biological and material studies, NSOM suffers from several drawbacks, including slow point-by-point scanning speed, shallow penetration depth, and mechanical fragility of the probe tip. These limitations confine its use primarily to surface and near-surface characterisation.

2. Near-field Metal-based Metamaterial Superlenses (M-MSL)

Metamaterials are artificially engineered media composed of periodic subwavelength structures that can manipulate electromagnetic waves in ways unattainable by natural materials. By amplifying evanescent components, they enable optical imaging beyond the diffraction limit.

The first experimental realisation of a metal-based superlens was achieved using a nanometre-thick silver film, resolving 40 nm features (≈ λ/6) under UV illumination. This verified Pendry's theoretical prediction of evanescent wave amplification and marked a milestone in plasmonic superlensing [6]. Later designs incorporated subwavelength surface gratings to couple near-field information into propagating modes, allowing far-field detection of sub-diffraction features [7]. Further progress led to hyperbolic metamaterial lenses (hyperlenses), formed by curved metal–dielectric multilayers supporting hyperbolic dispersion, which achieved far-field resolutions around 130 nm [8].

Despite these advances, metallic superlenses remain constrained by strong absorption losses, short working distances, and fabrication difficulties associated with nanoscale curved multilayers. These limitations restrict their efficiency and large-scale applicability.

3. Far-field Super-resolution Imaging Techniques

While near-field imaging achieves sub-diffraction resolution by directly collecting evanescent waves, far-field super-resolution techniques rely on optical field modulation and computational reconstruction, allowing sub-diffraction imaging under conventional microscope configurations.

Structured Illumination Microscopy (SIM) improves spatial resolution by illuminating the sample with periodic light patterns of varying orientations and phases. The resulting Moiré interference shifts high-spatial-frequency information into the detectable range, and computational reconstruction yields up to a twofold enhancement in lateral resolution (typically ~100 nm). Owing to its fast imaging speed, low phototoxicity, and compatibility with live-cell studies, SIM has become one of the most practical far-field super-resolution methods, though its resolution gain remains modest.

Fluorescence-based super-resolution microscopy achieves nanometre-scale imaging by controlling the activation or emission of fluorescent molecules so that only a sparse subset emits at any time. The positions of these emitters are localised with nanometre precision and reconstructed into a high-resolution image, achieving resolutions down to tens of nanometres. Despite its capability for visualising dynamic processes in living cells, the method requires complex optical modulation, photo-switchable fluorophores, and lengthy data acquisition, which limit its accessibility for general applications.

2.2 Light Interactions with Spherical Particles

While various super-resolution techniques reviewed in previous session have demonstrated sub-diffraction imaging capabilities, however, they often require complex instrumentation, fluorescent labelling, or near-field scanning. In contrast, microsphere-assisted super-resolution imaging offers a simple, label-free, and far-field approach to super-resolution. It is capable of achieving subwavelength resolution by exploiting the photonic nanojet effect generated by dielectric microspheres. This unique combination of simplicity, compatibility with white light, and real-time imaging makes it a compelling alternative for label-free super-resolution microscopy [9].

To understand the physics behind of this phenomenon, it is necessary to determine how light interacts with micro- and nano-scale spherical particles. In the visible wavelength range, particles with diameters between approximately 100 nm and 10 μm are generally referred to

as mesoscopic and nanoscopic structures, respectively. This research focuses on both scale ranges: mesoscopic microspheres serving as dielectric superlenses, and nanospheres forming the fundamental unit-cell of metamaterial based optical filters. The optical response of these spherical particles cannot be adequately described by geometric optics, since their dimensions are comparable to or smaller than the wavelength of light. Instead, light must be treated as an electromagnetic wave governed by Maxwell's equations.

Within this framework, Mie theory provides the analytical foundation for describing how spherical particles scatter and absorb light of arbitrary size and refractive index [10]. It reveals that the interaction between incident electromagnetic waves and a particle leads to complex distributions of internal and scattered fields, which can exhibit strong resonances and near-field enhancement. These resonant effects form the theoretical basis for understanding photonic nanojet (PNJ) formation and the unique focusing characteristics of microspheres discussed in the following sections.

2.2.1 Mie Theory

Mie theory is proposed in 1908 to calculate the exact solution for Maxwell's equations under a spherical coordinate [10]. It can be used to describe the optical response of a spherical particles with any size and refractive index to an incident plane electromagnetic wave. It expands the incident, scattered, and internal electromagnetic fields into an infinite series of vector spherical harmonics (VSWF), from which key optical parameters such as scattering efficiency, absorption efficiency, extinction cross section, and angular scattering intensity distribution can be derived. The optical responses are primarily determined by following parameters: the particle size (a), refractive index (n_p), incident light wavelength (λ) and refractive index of medium (n_m). The full derivation and intermediate steps are presented in *Appendix A*, while the key analytical results are summarised below.

By solving the boundary conditions, two sets of Mie scattering coefficients, a_ℓ and b_ℓ, are obtained. These coefficients determine the relative contribution of electric and magnetic multipole modes to the total optical response. The most commonly used measurable quantities derived from Mie theory are the scattering (Q_s), extinction (Q_e), and absorption efficiencies (Q_a), which are expressed as [3]:

$$Q_s = \frac{2}{k^2 a^2} \sum_{\ell=1}^{\infty} (2\ell + 1) \left(\left| a_\ell^2 \right| + \left| b_\ell^2 \right| \right) \tag{2.2.1}$$

$$Q_e = \frac{2}{k^2 a^2} \sum_{\ell=1}^{\infty} (2\ell + 1) Re\,(a_\ell + b_\ell) \tag{2.2.2}$$

$$Q_e = Q_s + Q_a \tag{2.2.3}$$

The terms in the summation, denoted by ℓ, represent successive multipole orders, with $\ell = 1$ corresponding to the dipole, $\ell = 2$ to the quadrupole, and higher ℓ values describing higher-order contributions.

2.2.2 Photonic Nanojets (PNJ) and Near-field Focusing

Although Mie theory has long described light scattering by spheres, its focus historically lay on far-field characteristics such as extinction efficiency. The discovery of the PNJ in the early 2000s revealed a new near-field focusing phenomenon, where a highly localised, non-evanescent light beam forms just beyond the shadow-side of a dielectric microsphere illuminated by a plane wave. Such PNJs typically arise in non-absorbing spheres of moderate to high refractive index, with diameters comparable to the illumination wavelength. The effect was first observed in 2000, and later modelled by FDTD simulations in 2004 [11, 12].

Systematic studies have shown that the lateral resolution of a PNJ can reach approximately $\lambda/2n$, and the phenomenon occurs non-resonantly across a wide size range (~2λ– 40λ) when the refractive index contrast is below about 2:1. Compared with microcylinders, spherical particles generate stronger and more confined 3D nanojets.

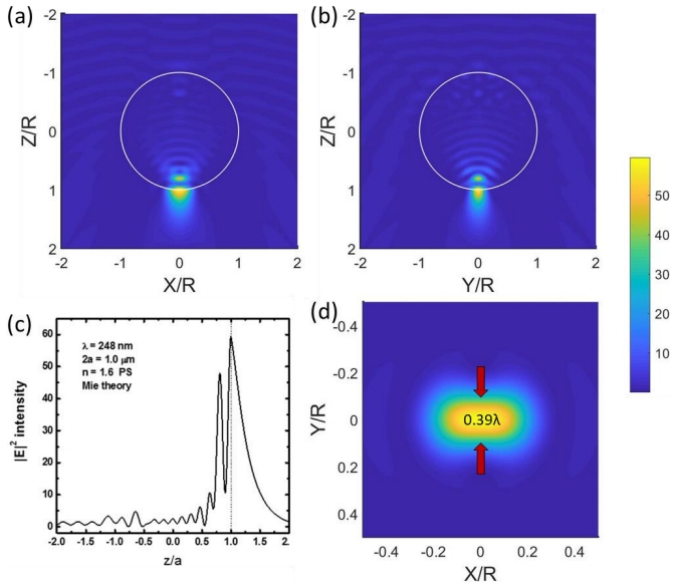

Figure 2.1 Photonic nanojet (PNJ) effect generated by illuminating a polystyrene microsphere (D =1um, n =1.6) with a plane wave (λ = 248 nm) propagating along the z-axis. The electric field distributions in the (a) XZ-, (b) YZ-, and (d) XY-planes show strong field enhancement beneath the microsphere. The cutting plane in (d) corresponds to the location of maximum enhancement. (c) shows the one-dimensional intensity profile plotted along the z-axis, corresponding to the propagation direction [15].

For instance, as seen in Fig. 2.1, simulations of a polystyrene sphere (D = 1 μm, n = 1.6) under 248 nm illumination reveal a maximum field enhancement of ~60 at the particle boundary and a beam waist of ~0.39λ, outperforming classical Rayleigh (0.61λ) and Sparrow (0.5λ) limits. The cross-sectional field distribution shows elliptical confinement aligned with the incident polarisation [15].

PNJs bridge the near-field and far-field regimes: they originate in the near field but propagate several wavelengths beyond the particle surface while maintaining sub-diffraction confinement. When a microsphere is placed on a nanostructured surface, evanescent waves carrying high spatial frequencies can couple into the sphere and be transformed into propagating modes, which are then collected by a conventional objective. This evanescent-to-propagating conversion underpins the far-field super-resolution capability of microsphere-assisted imaging [16].

The next section (Section 2.3) will further extend this understanding by reviewing representative super-resolution imaging techniques, with emphasis on microsphere-assisted and solid-immersion lens systems.

2.3 Micro-superlenses-assisted Imaging

2.3.1 Microsphere-assisted Imaging

1. Microsphere-assisted Wide-field Microscopy

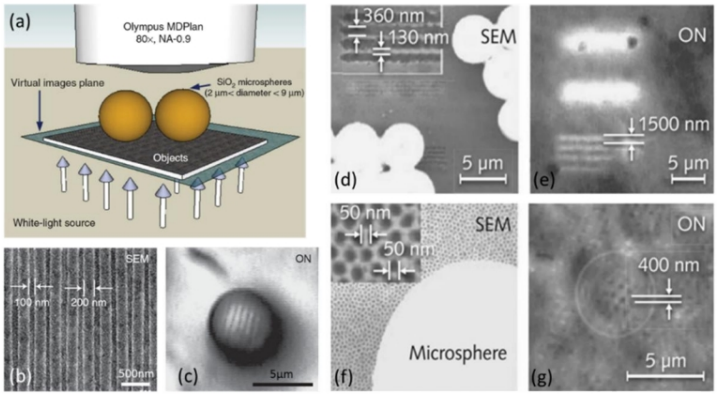

Figure 2.2 (a) Experimental setup of the microsphere-assisted super-resolution imaging system combing with microspheres and conventional optical microscope. (b) Scanning electron microscopy (SEM) image of a Blu-ray disc surface with 200 nm-wide tracks and 100 nm-wide grooves. (c) Optical reflection-mode image of the Blu-ray captured through the microsphere superlens system. (d) SEM image of a nanoscale diffraction grating composed of 300 nm-wide lines separated by 130 nm. (e) Corresponding transmission-mode optical image captured using the microsphere, clearly resolving the grating lines with an apparent magnification of 4.17×. (f) SEM image of a gold-coated fishnet membrane structure with 50 nm pores spaced 50 nm apart. (g) Transmission-mode optical image of the fishnet sample obtained via the microsphere superlens, demonstrating an optical magnification of approximately 8× [9].

This microsphere-assisted super-resolution imaging system under white-light illumination employing SiO_2 microspheres with diameter among 2-9 μm was firstly reported by Wang et al [9]. in 2011, as seen in Fig. 2.2. The SiO_2 microspheres were placed on the sample surface with subwavelength features. Those microspheres convert high-spatial-frequency near-field information into magnified virtual images that can subsequently be captured in the far field by a conventional microscope.

As shown in Fig. 2.2 (b–g), the system can resolve the subwavelength features under both transmission and reflection illumination modes. In Fig. 2.2 (b, c) a Blu-ray disc disc with 200 nm-wide lines and 100 nm-wide grooves is resolved using a 4.7 μm SiO_2 microsphere in reflection mode. Another sample which consists of 360 nm-wide lines separated by 130 nm distance were imaged in transmission mode, as seen in Fig. 2.2 (d. e). These patterns appear as two unresolved bright spots without the assistance of microspheres, demonstrating the resolution limit of conventional optical microscopy. Lastly, Fig. 2.2 (f, g) demonstrate the microsphere's ability to resolve 50 nm pores in a gold-coated fishnet membrane, achieving a resolution between λ/8 and λ/14 within the visible range, and providing a magnification factor of approximately 8x.

This work served as a critical milestone, initiating a new direction in label-free super-resolution imaging using dielectric microspheres. Following this early demonstration, researchers have explored a wide range of parameters to optimise resolution and contrast in microsphere-assisted imaging. Typical parameters include particle size and refractive indices of microsphere and host medium.

For example, polystyrene microspheres with diameters of 30–100 μm (n = 1.59) have achieved super-resolution imaging in air, resolving Blu-ray disc features with ~120 nm resolution [16]. Subsequently, high-index $BaTiO_3$ microspheres (n = 1.90) immersed in isopropyl alcohol revealed that resolution strongly depends on particle refractive index and size [17]. Small 4.2 μm $BaTiO_3$ spheres resolved ~75 nm features (~ λ/7), whereas larger ones (50–220 μm) were limited to ~λ/4. Li et al. further demonstrated that 100 μm $BaTiO_3$ microspheres in water could image adenoviruses with ~75 nm resolution [18]. Additionally, partial embedding of SiO_2 microspheres in ethanol or SU-8 layers was shown to enhance imaging contrast due to improved coupling with evanescent fields [19, 20]. Overall, these studies confirm that refractive index, particle size, and embedding medium critically determine the resolution in microsphere-assisted optical microscopy.

2. Microsphere assisted confocal microscopy

To further improve the imaging resolution, researchers have combined microsphere with laser confocal microscopy to improve contrast and resolution [21]. Laser confocal microscopy provides higher resolution and contrast than white-light wide-field microscopy due to its point-by-point laser scanning working strategy, the use of a pinholes and the typically shorter wavelength of laser light compared to broadband white light, as highlighted in Fig. 2.3 (a). It illuminates single point on the sample surface at a time using a focused laser beam. At each scanning position, the reflected signal is collected to form the final image. In addition, the pinholes efficiently reject out-of-focus light further improving spatial resolution and contrast. As a result, the resolution limit of a confocal microscope is approximate $0.4\lambda/N.A$.

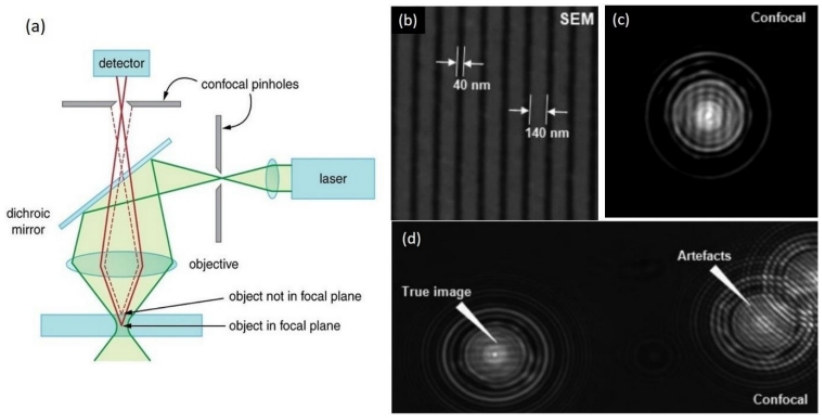

Figure 2.3 (a) Schematic illustration of scanning laser confocal microscope with focused laser beam and pinholes highlighted. (b) SEM image and (c) laser-confocal microscope captured image of sub-wavelength feature sample with 40-nm-wide lines and 140 nm spacing. (d) Artefacts due to neighbouring microsphere interference versus true pattern under single microsphere [21].

Fig. 2.3 (b, c) show the SEM image and the corresponding laser confocal image obtained by coupling a laser confocal microscope with SiO_2 microspheres of approximately 3 μm in diameter, successfully resolving features with 40 nm-wide lines and 140 nm spacing [21]. Compared with wide-filed microscopy, several concentric rings are observed potentially because of near-field interactions of particle. Furthermore, interference effects arising from coherent illumination between adjacent microspheres can introduce grating-like artifacts that do not correspond to actual sample features, as demonstrated in the right panel of Fig. 2.3 (d). In contrast, when a single microsphere is used in isolation, it is still capable of resolving the underlying sub-diffraction-limited structures. Since then, serval variants of this microscopy strategy have been developed. For example, Yan et al. achieved 25 nm lateral resolution by combining fused silica with a conventional scanning laser confocal microscope [22]. Yang et al. reported that a 50 μm silica microsphere combing with a commercial confocal microscope can achieve an axial resolution up to 100 nm and enhanced contrast up to 4.56 times [23].

3. Scanning Microsphere Superlenses

Combining microspheres with wide-field or confocal microscopy has demonstrated superior label-free super-resolution performance. However, their limited field of view and immobility restrict large-area or targeted imaging. To overcome this, several techniques introduced mechanical manipulation to precisely control microsphere positioning. Krivitsky et al. first attached a SiO_2 microsphere to a glass micropipette connected to a translation stage, enabling three-dimensional movement [24]. Building on this, the scanning superlens microscopy (SSUM) technique employed an AFM cantilever for accurate and high-throughput imaging [25]. More recently, Luo et al. developed the self-sensing scanning superlens microscopy (3SUM) system, which integrates real-time force feedback for stable imaging on complex surfaces [26]. These developments extend the original mechanical-control route, enhancing imaging adaptability though at the expense of increased assembly complexity and calibration demands.

4. Self-propelled Scanning Microsphere Superlenses

Construct self-propelled microsphere robots, known as swimming microrobots, is another strategy to control the movement of microspheres with using mechanical arm. For example, Li et al. partially coated thin layers of platinum (Pt) and nickel (Ni) onto high-refractive-index dielectric spheres [27]. When immersed in hydrogen peroxide (H_2O_2) solution, the platinum catalyses the decomposition of H_2O_2 into oxygen and water, generating a local chemical gradient that induces autonomous propulsion. Meanwhile, the Ni layer provides magnetic responsiveness, allowing precise steering of the microrobot via an external magnetic field. This enables active scanning of the microsphere across the sample surface for large-area, label-free super-resolution imaging without mechanical contact.

5. Engineered Microsphere superlenses

Apart from the aforementioned techniques leveraging mechanical arms and autonomous propulsion to improve the reusability and mechanical reliability of microsphere-based imaging, another solution is encapsulating high refractive index microspheres within a transparent host material, such as PMMA or PDMS, to form a coverslip-like device [28]. This design allows the microsphere to be embedded in a solid thin film and contact with the sample surface directly. As a result, repeated used and operating the setup by hand is allowed.

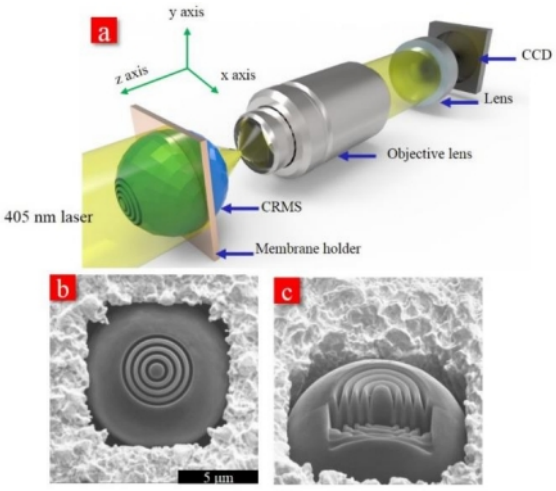

Figure 2.4 (a) Schematic illustration of an enhanced photonic PNJ formed on the opposite side of the lens due to engineered concentric rings structures. Top view (b) and cross-section (c) of concentric rings [29].

Recent studies have shown that manipulating the surface of microspheres can effectively tailor the characteristics of photonic nanojets. As seen in Fig. 2.4, Wu et al. introduced concentric ring structures on the illumination side of the microsphere enables significant narrowing of the PNJ beam width, with both simulated and experimental results showing reductions of approximately 29% in FWHM [29]. In summary, these strategies that manipulate the geometry of microsphere offer new possibilities for enhancing resolution in optical imaging, sensing, and nanoscale fabrication.

2.3.2 Early Solid Immersion Superlenses (SILs)

This concept of solid immersion superlenses (SILs) was originally developed from a prototype in 1990, Mansfield et al. replaced liquid immersion with a high-refractive-index SIL (n = 2.00), they achieved real-time super-resolution imaging, successfully resolving 100 nm line structures under 436 nm illumination. Notably, the geometry is not a hemi- or hyper-hemi-spherical structure but a modified conical structure with the tip cut off to form a flat bottom surface measuring 100 μm across [30].

2.3.2.1. Concept and Geometrical Classification

Following this early demonstration, SILs evolved into more standardised geometries that are easier to model and fabricate. Among these, the sub-hemispherical and super-hemispherical types have become widely studied. Sub-hemispherical and super-hemispherical SILs are usually described by their height-to-width ratio $F = H/W$, where structures with $F \geq 0.5$ are classified as super-hemispherical SIL, and those with $F < 0.5$ as sub-hemispherical SIL. These SIL geometries can produce super-resolution imaging through two main processes. The first

is the formation of a highly confined photonic nanojet-like focus near the lens surface [31]. The second is the coupling of high spatial-frequency information, which carries the fine structural details of the sample, into propagating components that can reach the far field. Together, these effects enable SILs to resolve features beyond the diffraction limit, similar to full spherical superlenses [32].

2.3.2.2. Theoretical Analyses

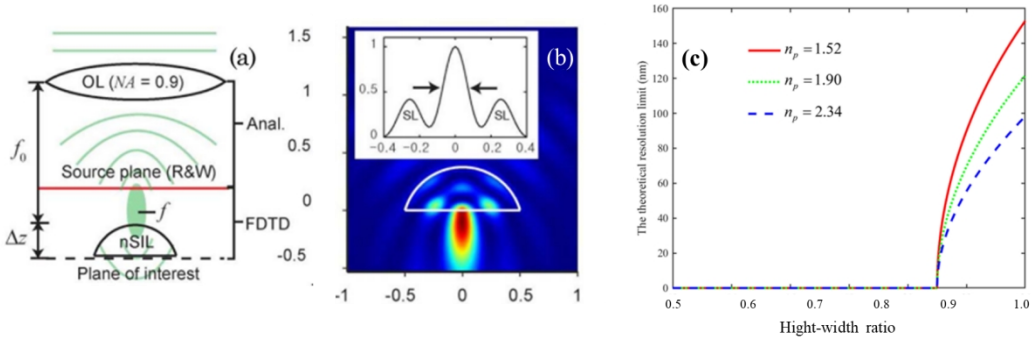

Figure 2.5 (a) Illustration of a SIL combined with an object lens. (b) Electric field intensity distribution ($|E|^2$) of a SIL illuminated by plane wave. Inset shows the electric field intensity along y = 0, indicating the FWHM (arrows) and SL intensity [31]. (c) The dependence of theoretical resolution limit of a 24 μm on superlens material index and hight-width ratio ranging from 0.875 to 1.0 [32].

First, in 2010, the early theoretical work of SIL conducted by Mason and through FDTD method summarised the subwavelength phenomena inside or in the neighbourhood of a dielectric superlens [31]. Their simulated electric field intensity ($|E|^2$) image of a plano-convex superlens (also known as SILs) illuminated by a plane wave clearly show that a tightly confined photonic "nanojet" similar to that of full-spherical superlens' at the lower interface can be generated, leading to sub-diffraction focusing and illumination, as seen in Fig. 2.5 (b). Moreover, they suggest that, when combined with high-*N.A.* objectives, the potential resolution of micro-sized SILs can be significantly boosted compared to conventional macroscopic SIL, as it achieves focal spots up to 15% narrower than theoretical limits.

Second, Wang et al. proposed that the flat surfaces of sub-hemi- and super-hemispherical SILs enable a complete process in which evanescent waves carrying high spatial frequency components are converted into propagating waves, transmitted into the interior of the SIL, successfully escape from within the lens, and ultimately propagate to the far field [32]. Their theoretical estimation of the resolution limit as a function of the height-to-width ratio indicates that the resolution is positively correlated with the refractive index of the SIL material. As a result, there has been increasing interest in employing materials with higher

refractive indices. In addition, the resolution limit is shown to be inversely related to the height-to-width ratio, as illustrated in Fig. 2.5 (c). Although their analysis only covers a narrow range of height-width ratio from 0.875 to 1.0, the results still suggest that the theoretical resolution of a full-spherical superlens is inferior to that of a SIL with a higher height-to-width ratio.

These findings indicate that both the geometrical configuration and the refractive index of the SIL material might influence its imaging performance, which could encourage further exploration of geometry optimisation and high-index designs.

2.3.2.3. Experimental Demonstrations

The original experimental demonstration of the hemi-spherical geometry used for super-resolution imaging was reported by Lee in 2009 [33]. They successfully fabricated nanoscale lenses (size ranging from 0.05 – 3 μm) with plano-spherical convex' (PSC) structures (as known as sub-hemispherical geometry) through the self-assembly of calix hydroquinone. The upper curved surface maintains a near-spherical profile with less than 3% deviation from ideal sphericity and a roughness below 1 nm. By observing the lens through a conventional objective (*N.A.* = 0.9, λ = 472 nm, 100x), the sub-wavelength metallic stripes with 250 nm spacing, was resolved by both face-up and face-down lens, as seen in Fig. 2.6 (a, c). However, face-down lens offers slightly higher magnification. Their results prove that such incomplete spherical structures can be applied in super-resolution imaging, but their imaging quality is limited by the refractive index of material (n = 1.50) and low height-width ratio.

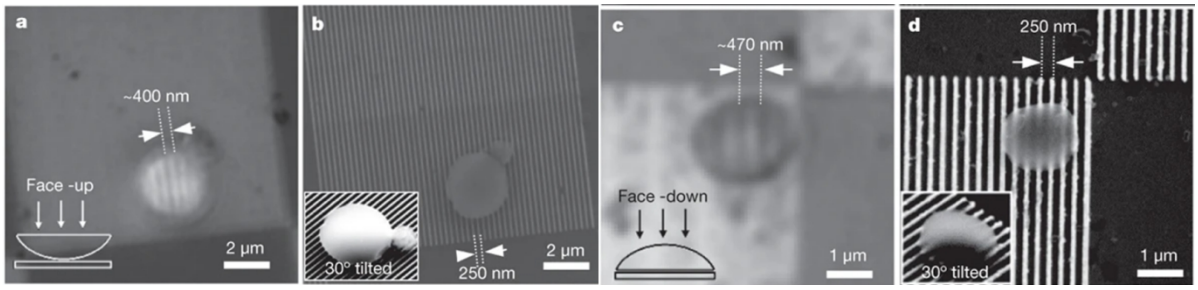

Figure 2.6 Optical images (a,c) and SEM images (b, d) of face-up and face-down SILs on a substrate with features having period of 250 nm [33].

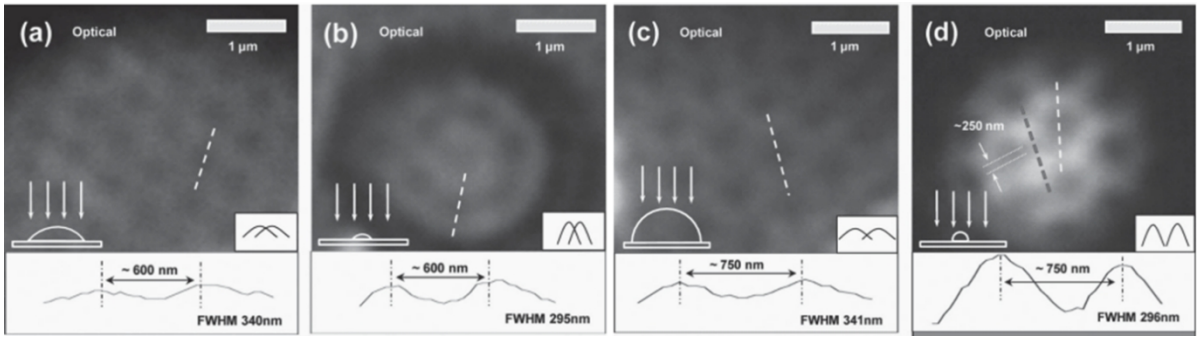

Figure 2.7 Optical images of SILs with lower (a-b) and higher (c-d) height-width ratio in different size [34].

To investigate the influence of height-width ratio to image quality, in 2012, Kang et al. performed an early investigation into the super-resolution imaging performance of SIL with high- and low- height-width ratio and varying size [34]. Their results indicate that smaller SIL with high-height-width ratio provides higher resolution. Specifically, Fig. 2.7 (a, b) shows neither the 3 μm nor 10 μm flat SIL is able resolve 130 nm gap. However, Fig. 2.7 (c, d) indicates that despite the 130 nm gap is still not resolved by the SILs with higher heigh-width-ratio, the smaller high ratio SIL (Fig. 2.7 d) is able to visualise the honeycomb pattern. These results indicate that the imaging resolution is highly dependent on SIL height-width ratio size.

In the same year, Vlad et al. [35] carried out a more comprehensive comparison of the super-resolution performance of full-spherical superlenses and SILs with different geometries. Their fabricated SILs achieved super-resolution imaging for features down to 180 nm. They also provided a clear summary of how the height-to-width ratio influences imaging performance. A reduced height-to-width ratio, as shown in Fig. 2.8 row (a), increases the field of view but lowers both magnification and focal depth. This trade-off affects the practical quality of the image, as illustrated in Fig. 2.8 row (c).

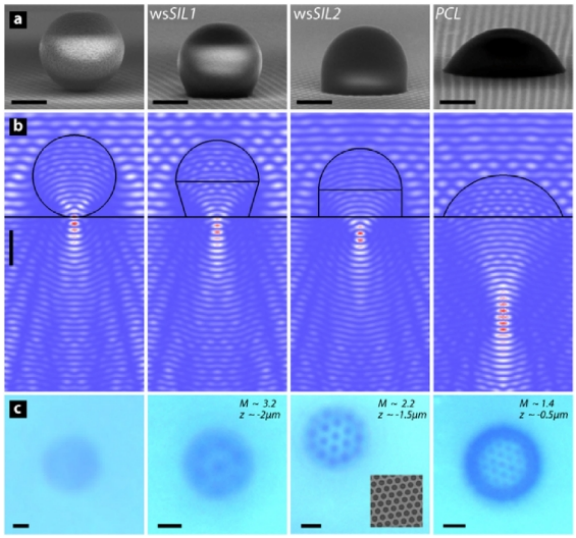

Figure 2.8 row (a) Various of superlenses with decreasing height-width ratio, their simulated focal point, row (b), and optical images (*N.A.* =0.9) with these superlenses [35].

As a result, they suggested that the 'half-melted' (wsSIL2 in Fig. 2.8 row (a), third column) configuration is the optimal lens which is able to resolve 180 nm gratings at visible wavelengths with reasonable magnification (2.2x). However, full-spherical superlens with sizes comparable to the 'half-melted' configuration (below 4 μm in diameter) are incapable of achieving super-resolution imaging, as their focal points remain confined within the microsphere volume, preventing the formation of observable virtual images. Super-resolution imaging becomes attainable only when the focal point extends beyond the sphere boundary, enabling the resolution of magnified virtual features. This condition typically requires a full-spherical superlens with a diameter of at least 4 μm [35].

The remarkable super-resolution imaging performance of SIL was also proved by Hou et al. in 2015 [36]. Since above two study only tested SIL with size below 10 μm, the FOV of them is not satisfactory. In 2016, Gu et al. successfully fabricated the larger SILs (diameter around 20 μm) and investigated the influence of height-width ratio onto the FOV and magnification [37]. That is, the height-width ratio increases leads to increased magnification but decreased FOV.

2.3.2.4. Summary

The sections 2.3.2.2 and 2.3.2.3 have shown that geometrical configuration parameters play key roles in determining the imaging performance of SILs. From a geometrical perspective, the transition from hemi-spherical, super-hemispherical and full-spherical configurations reveals that the height-to-width ratio governs the focal position and virtual-image magnification. Theoretical and field-distribution analyses indicate that the planar interface of

a SIL not only supports a subwavelength photonic nanojet-like focus, but also enables the conversion of evanescent waves into propagating modes, thereby extending imaging resolution beyond the diffraction limit. Experimental results demonstrate a trade-off among field of view (FOV), magnification, and focal depth.

Early studies mainly examined geometrical factors, with particular attention to the height-to-width ratio, while the role of refractive index received little consideration. More recent work has broadened this view by looking at both geometry and refractive index together, with the aim of improving resolution and achieving more stable imaging performance.

Building upon these insights, recent research has focused on:

1. Adopting materials with higher refractive indices to elevate the theoretical resolution limit and extend the focal point beyond the interface,
2. Introducing nanostructured or metamaterial architectures capable of modulating and amplifying near-field interactions, in order to further enhance super-resolution imaging performance.

2.3.3 Advanced Superlenses

2.3.3.1 Sub- and Super-hemispherical mSILs

1. Bottom-Up Self-Assembled TiO_2 mSILs

More recently, various bottom-up self-assembled metamaterial solid immersion superlenses (mSILs) fabrication techniques have been developed by using solvent evaporation, capillary-driven colloidal clustering or gravity-induced deformation of high refractive indices nanomaterial and monomer.

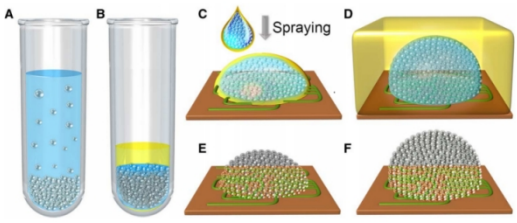

Figure 2.9 The precipitant (B) of centrifuged aqueous suspension of (A) TiO_2 nanoparticles with organic solvent mixture added. The NSFA processes of mSIL on an IC chip (C-F) [38].

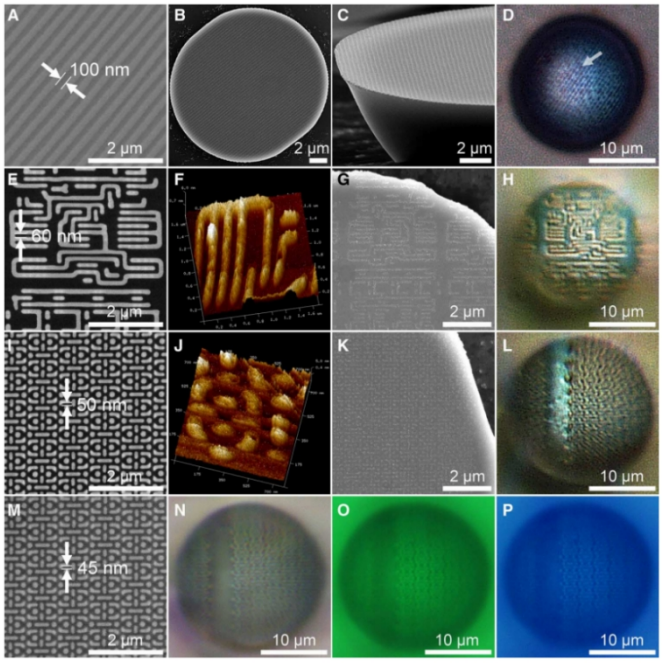

Figure 2.10 SEM images were captured for a Blu-ray disc featuring 100 nm-wide grooves (A) and wafer patterns with pitches of 60 nm (E), 50 nm (I), lastly, gold-coated thin-film coated pattern with 45 nm gap (M). The corresponding bottom surfaces of the TiO_2-based mSILs, which were removed from these respective substrates, are shown in (B), (C), (G), and (K). AFM characterization performed on the 60 nm (F) and 50 nm (J) pitch wafer patterns. Optical microscopy images obtained through mSILs focused on the Blu-ray disc (D) and on the various nanopatterned wafers (H, L, N–P) demonstrate magnifications of approximately 1.8×, 3.1×, 3.0×, and 3.1×, respectively. The sample in was imaged under white light (H, L, N), green light (~540 nm) (O), and blue light (~470 nm) (P) [38].

In particular, Fan et al. introduced a novel three-dimensional all-dielectric mSIL consisting of densely packed 15 nm TiO_2 nanoparticles with high-refractive index (n =2.55) via a nano-self-solid-fluid assembly method, as illustrated in Fig. 2.9 [38].

They successfully fabricated sub- and super-hemispherical mSILs directly on both Blu-ray discs and silicon chip surface. Super-hemispherical mSILs demonstrate remarkable super-resolution capabilities that achieving feature recognition a wide range of samples from 100 nm down to 45 nm under white-light illumination while enabling a high contrast and large FOV, as seen in Fig. 2.10 (D, H, L, N).

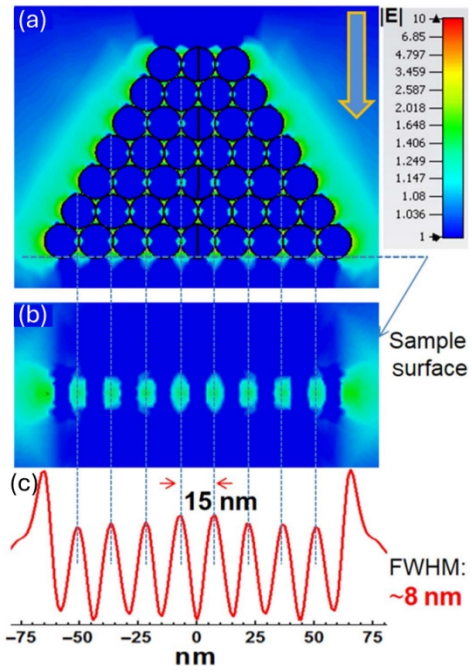

Figure 2.11 (a) The electric field distribution of closely packed TiO_2 nanoparticles illuminated by a plane wave with cross-sectional image depicting an (b) enhanced array of evanescent waves at sample surface. (c) The one-dimensional electric field density plot of the array of evanescent waves [38].

However, the best theoretical resolution of a homogeneous SIL with comparable size and under white light illumination (λ = 550 nm) is $\lambda/2n$ = 108 nm. This is because unlike conventional homogeneous SILs, this TiO_2 mSIL benefits from strong near-field coupling between adjacent nanoparticles.

To illustrate this strong coupling effect, a simplified 3D model consisting of closely stacked nanoparticles was built up in CST STUDIO, as shown in Fig. 2.11. When mSIL is illuminated by a plane wave (λ = 550 nm), there are strong electric field confinement can be observed in the small air gap between adjacent air nanoparticles, particularly, the sub-wavelength on sample surface can be illuminated by this array of evanescent wave (Fig. 2.11 b). Fig. 2.11 (c) shows the centre to centre spacing between these illumination spots match the size of nanoparticles having an FWHM resolution of approximately 8 nm. The conventional homogenous high refractive index SIL lacking this ability to enhance the focused evanescent wave illumination strength is one crucial factor that unable to offer a such high resolution.

In addition, transferring high–spatial frequency information carried by evanescent wave back into far-field propagating wave is also crucial for achieving super-resolution imaging. This mechanism was further investigated by simulating two incoherent point sources which contain all evanescent wave components. Two point-sources were placed beneath a

homogeneous TiO_2 slab and a metamaterial slab consisting of closely stacked TiO_2 nanoparticles, respectively. Fig. 2.12 (a, b) illustrates the simulation setup, where the two point-sources were separated by 45 nm and operated at a wavelength of λ= 550 nm to match experimental conditions.

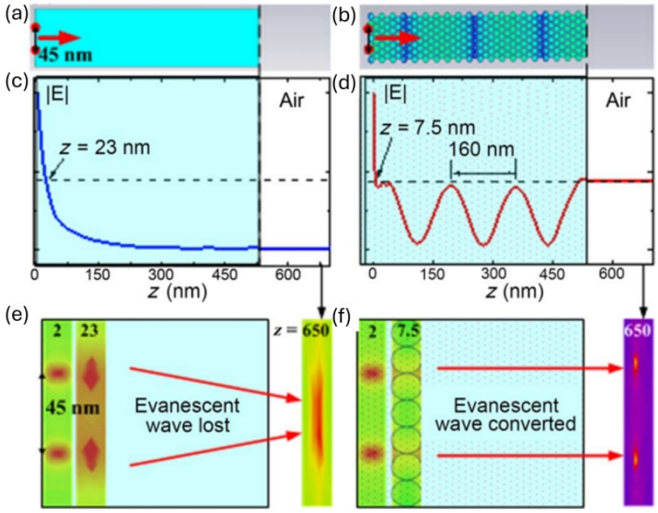

Figure 2.12 Two incoherent and TE polarised point sources placed beneath a homogeneous (a) and closely packed TiO_2 metamaterials (b). Mean electric field amplitude in two materials in the direction of propagating (c, d). Two point-sources separately imaged by two materials in far-field (e, f) [38].

The mean electric field amplitude of point-source in two materials along z-direction are plotted in Fig. 2.12 (c, d). As expected, the amplitude in both materials exhibit significantly decay due to the evanescent nature. However, in the case of the homogeneous TiO_2 slab, this exponential attenuation continues without recovery, resulting in the two point-sources remaining unresolved in the far field, as shown in Fig. 2.12 (e). In contrast, at z = 7.5 nm, the metamaterial slab enables a periodic and undamped modulation of the evanescent waves. After calculation, despite the long propagation distance from z = 7.5 nm to z = 550 nm, the electric field energy at z = 550 nm remains comparable to that at z = 7.5 nm. This efficient preservation and conversion of evanescent components into propagating waves leads to the two point-sources to be resolved in far filed, as shown in Fig. 2.12 (f).

In summary, with the help of simulation, Fan et al. demonstrated that mSILs enable a complete optical pathway—from the conversion of far-field propagating waves into evanescent waves at the sample interface, followed by their interaction and modulation within the metamaterial structure, and finally reconversion of evanescent waves carrying high-spatial-frequency into a far-field propagating waves that can be effectively collected by an objective lens.

More importantly, they also admitted that the penetration effect is critical to achieving high resolution. The characterisation of the bottom surface of these mSILs reveals a unique penetration behaviour which have not been reported in other literatures to our knowledge. That is, the nanoparticle-based fluid partially imprinted subwavelength structures during NSFA process (Fig. 2.10 C, G, K). In other words, the sub-diffraction features were effectively "projected" onto the bottom surface of these mSIL. This effect leads to multiple scattering and localized field enhancement within the densely packed nanoparticle network and thus allowing the lens to illuminate and resolve sub-wavelength features that are typically inaccessible to conventional single-particle lenses. Unfortunately, despite the effect was observed, no further simulation conduced to further verify this phenomenon.

2. Bottom-Up Self-Assembled ZrO_2 mSILs

More research was conducted building upon the fundamental principles of this nano-metamaterial self-assembly method. For instance, Zhu et al. developed hybrid mSIL consisting of high-refractive-index dielectric nanoparticles (ZrO_2) embedded deformable polymer matrix [39]. This strategy preserves the super-hemispherical geometry while enhancing mechanical adaptability of this mSIL, particular for imaging aqueous sample including live organisms and biomolecule.

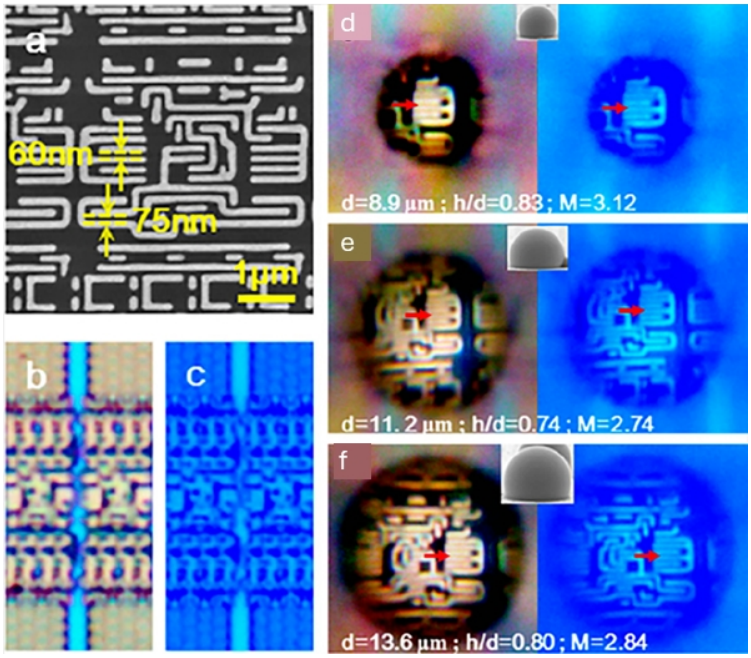

Figure 2.13 (a) SEM image of IC chip with 60 nm and 75 nm gap that cannot be resolved by while-light (b) and blue-light illumination (c). The feature imaged by mSILs with varying size and illuminated by white-light (left) and blue-light (right), respectively. Insets are SEM images of each mSIL.

However, in this study, the the maximum relative contents of ZrO_2 is 47.5 wt%, giving the highest effective refractive index of only n = 1.71. This significantly lower refractive index leads to weaker imaging performance than that of TiO_2 nanoparticles based mSIL (n = 1.92). A sub-wavelength feature (Fig. 2.13 a) was imaged using three ZrO_2 hybrid mSILs of different diameters, as show in Fig. 2.13 (d–f), and with the highest achievable refractive index in this study. Without the aid of blue-illumination, the 60 nm gap that is clearly resolved by TiO_2 mSIL becomes barely distinguishable with ZrO_2 hybrid mSIL, despite both types of mSILs demonstrating the penetration effect.

It is worth noting that their work focuses on material adjustment rather than a fundamental change in fabrication, and the structures are directly formed on the specimen surface. As a result, they naturally exhibit a penetration effect, comparable to that of self-assembled TiO_2 mSILs. However, due to relatively low effective refractive index, despite the penetration effect, their super-resolution performance remains weaker than that of TiO_2-based mSILs, highlighting the importance of a high refractive index.

3. Bottom-Up Self-Assembled and dehydrated TiO_2 mSILs

Besides the super-hemispherical mSILs exhibiting penetration effect, it is worth contrasting this with studies where such penetration is not present. For example, Wang et al. developed a scalable, bottom-up method to fabricate TiO_2 SILs through a two-step dehydration process, yielding sub-millimetre-sized mSIL. To fabricate mSIL, 15 nm TiO_2 nanoparticles in aqueous suspension were directly deposited onto a hydrophobic polycarbonate thin film immersed in silicone oil [40]. A super-hemispherical shape with very high height-width ratio (over 0.8) could be generated under the combined action of silicone oil/water interfacial tension and gravity. Then, controlled dehydration solidified the droplet into a transparent mSIL with flexible size ranging from 375 μm to 675 μm but slightly lower heigh-width ratio up to 0.69.

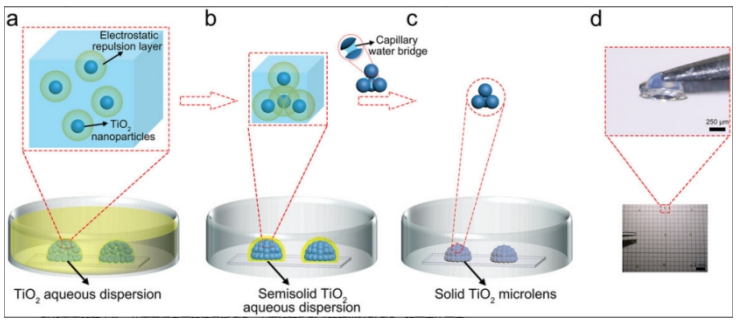

Figure 2.14 Schematic illustration of fabrication processes of sub-millimetre-sized mSILs. The aqueous suspension of TiO_2 nanoparticles (a) is directly deposited in hot silicon oil for initial dehydration followed by completely evaporating residual water (b) to from a closely packed millimetre-sized mSIL (c, d).

This fabrication process shown in Fig 2.14 is easy to operate while does not require costly equipment. The mSILs fabricated by this technique exhibiting satisfied mechanical strength and easy-to-handle size and capable of imaging various sample including nanospheres array (size ranging from 300 nm – 400 nm), pearlite microstructure and live cell.

Although the effective refractive index of the TiO_2 mSIL fabricated via the silicone oil-assisted NSFA process was raised to n = 2.00, along with the strong local field confinement resulting from densely packed 15 nm nanoparticles, the overall imaging resolution was not significantly improved. In fact, it was noticeably poorer than that achieved by earlier TiO_2 mSILs as reported in literature [38]. One critical reason is the absence of penetration effect, as the mSIL was transferred onto the sample surface only after solidification, and thus could not imprint the underlying subwavelength features. Additionally, the relatively low height-width ratio (< 0.69) likely reduced their effective curvature and spatial confinement, further limiting their resolution compared to mSILs with higher ratio.

4. Top-Down Precision-Fabricated mSIL

The refractive index of mSIL was further improved to n = 2.34 in the same year [41]. Wu et al. developed a super-hemispherical SIL through top-down focused ion beam (FIB) milling of the high-index BTG microspheres enabling precise curvature control and achieving sub-50 nm resolution under a 10× objective (Fig. 2.15).

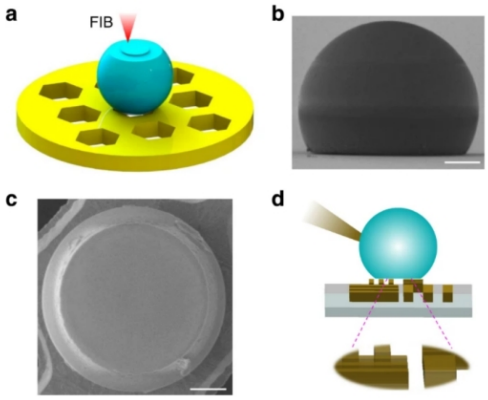

Figure 2.15 (a) Schematic illustration of fabrication method of a SIL (b) with flat bottom surface (c). (d) Virtual imaging mode of SIL [41].

However, despite its high refractive index, the FIB-fabricated mSIL exhibited poor image contrast when imaging more complicated 60 nm-wide grating-like chip features. This is inferior to the high-contrast results achieved using the NSFA TiO_2 nanoparticle-based mSILs, under similar conditions. This reduced performance is attributed not only to the absence of penetration effect, but also to the lack of nano-metamaterial which is capable of near-field

modulation or multiple scattering. As a result, despite the use of ultra-high refractive index materials, the actual resolution enhancement of FIB-based SILs remains modest and not commensurate with their optical index.

Furthermore, the FIB fabrication process requires expensive and time-consuming processes. Only one SIL can be processed at a time, and the resulting lens must be manually positioned and aligned, limiting its practicality for large-area or high-throughput imaging applications. In contrast, bottom-up self-assembled mSILs offer a more scalable, parallel approach with easier integration into practical microscopy platforms.

2.3.3.2 Full-spherical mSILs

By applying the NSFA technique based on TiO_2 nanoparticles to fabricate full-spherical structure, the microsphere-assisted super-resolution imaging has taken a further step forward.

In 2021, our group successfully fabricated full-spherical lens via NSFA of TiO_2 nanoparticles [42]. Fig. 2.16 (a, b) illustrate the configurations of a BTG microsphere and a TiO_2 nanoparticles-based microsphere, respectively. The imaging performance including FOV, contrast and of two types of microspheres of sub-wavelength features was compared in this study. The TiO_2-based microsphere demonstrates superior imaging performance across all aspects. Notably, it successfully resolves a 90 nm feature that the BTG microsphere fails to resolve.

However, when comparing the effective refractive indices of the two types of microspheres, the difference becomes negligible. As reported in previous literature, the composite TiO_2 lens exhibits an effective refractive index of 1.92–1.95 (depending on nanoparticle index), which closely matches the homogeneous BTG microsphere with a nominal refractive index of 1.92 [42]. To further investigate the underlying mechanism, the analyse focus was shifted towards to nanoscale, therefore, full-wave FEM simulations were conducted using CST Studio, enabling detailed comparison of electric field distributions and far-field resolution capabilities.

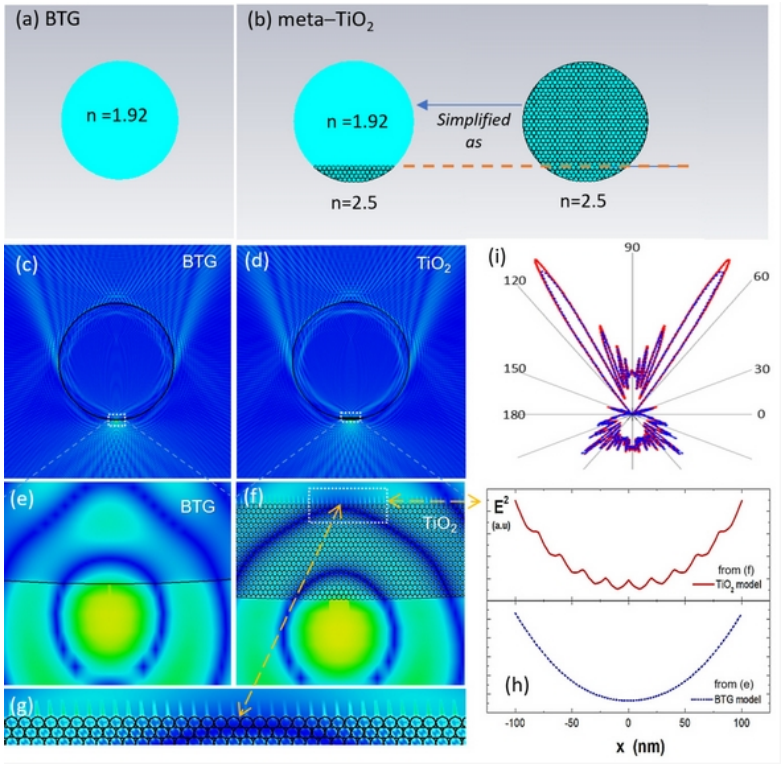

Figure 2.16 Modelling of a BTG (a) and TiO_2 (b) microspheres and the electric fields distribution (c, d) while illuminated by a dipole point source placed at the bottom of the microspheres, respectively, and with magnified view of near-field distribution of two microspheres (e, f). (h) 1D plots of near-field intensity along indicated location in (f). (i) Far-filed scattering comparison of two microspheres.

To save the computational resources, the TiO_2 lens is simplified as a 2D cylinder consisting of two parts, as illustrated in Fig. 2.16 (b), the upper part is set as homogeneous material with fixed refractive index of 1.92 while the lower part consists of TiO_2 20 nm nanoparticles with refractive index of 2.50. An electric dipole source with polarisation perpendicular to the plane is placed at the bottom of two microspheres in other to analyse the collection of radiation energy in the far-field, particularly the evanescent and propagating wave components. The far-field pattern of two types of microspheres, as shown in Fig. 2.16 (i), indicate that more energy can be scattered by the TiO_2 lens, evidenced by its longer main lobe (red solid line). This observation is further supported by the electric field distribution diagrams (Fig. 2.16 e–g), which show a clear array of photonic nanojets generated by the densely packed TiO_2 nanoparticles, as highlighted in Fig. 2.16 (f). Notably, the size of each nanojets closely matched to the physical dimensional of the individual TiO_2 nanoparticles, suggesting that the substructure plays a direct role in near-field energy transferring. In other words, this high-frequency modulation allows more evanescent wave components be transferred to propagating wave components into the far-field, as depicted in (h). As a result, this TiO_2 microsphere offers strong near-field coupling and scalable fabrication, showing great potential for practical, low-cost super-resolution imaging applications.

2.3.3.3 Summary

In summary, this progression from perfect microspheres and SILs to engineered high-refractive index microspheres and SIL reflects a continuous refinement of both material design and optical function. Each structural evolution not only expands the versatility of microlens-assisted imaging but also deepens our understanding of light confinement, focusing behaviour, and near-field interaction at the subwavelength scale.

Among the reported advanced superlenses, the self-assembled TiO_2-based mSILs have exhibited the highest imaging resolution and contrast under white-light illumination. However, the physical origin of their superior performance remains incompletely understood. Previous studies briefly attributed this enhancement to the high packing density of nanoparticles, and suggesting that densely packed nanostructures could generate finer photonic nanojet arrays. The effect of penetration, which results from the partial imprinting of subwavelength surface features during NSFA, has not been examined in detail. Therefore, a more comprehensive comparison that evaluates the imaging performance of TiO_2 lenses across different geometries while explicitly incorporating the contribution of the penetration effect is needed.

2.3.4 Biological Superlenses

2.3.4.1 Cylindrical Bio-superlens

In addition to isotropy microspheres and artificially engineered microspheres, recent studies have explored biologically based label-free super-resolution imaging. As the “biosuperlenses” offer distinct advantages in terms of biocompatibility, structural simplicity, and cost-friendly. Monks et al. firstly demonstrated that spider silk is a compelling candidate for super-resolution imaging due to its cylindrical geometry, transparency, and reasonably high refractive index (n = 1.55) to manipulate light at the subwavelength nanoscale [43]. The silk being placed on sample surface shown in Fig. 2.17, as a cylindrical superlens, with a diameter of approximately 6.8 μm and under white-light illumination is capable of resolving 100 nm features and offering a magnification of 2.1x. This subwavelength imaging capability was achieved by collecting near-field evanescent waves and projecting magnified virtual images into the far field.

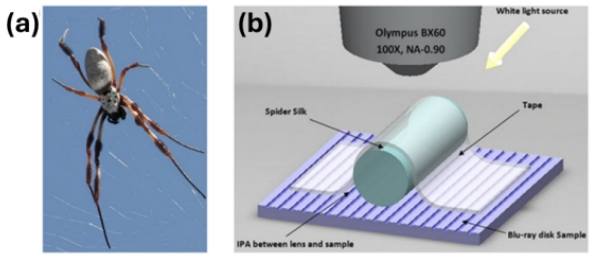

Figure 2.17 Schematic drawing of (a) Nephila edulis's spider (b) silk-based super-resolution imaging experimental setup [43].

2.3.4.2 Full-spherical Bio-superlenses

1. Scanning cells microscopy

Li et al. developed a bio-super-resolution imaging setup, which leveraging the trapping effect at the apex of a tiny fibre at which a spherical micro-scale cell can be trapped [44]. The trapping effect was achieved by a near-infrared laser beam (980 nm) into a strong optical gradient field at its apex. This configuration achieved label-free imaging laid the foundation for future precise optical control in a biocompatible and non-invasive manner.

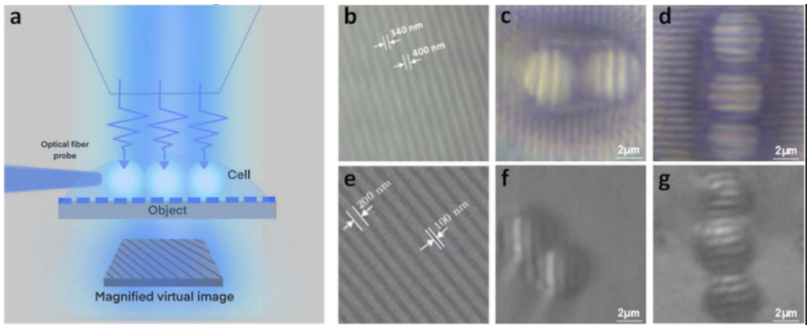

Figure 2.18 (a) Schematic of the experimental setup used to capture optical images of multiple yeast cells. SEM images and optical images captured by (b–d) double- and (e–g) triple-cells of DVD and blu-ray discs, respectively. This setup demonstrates extended FOV compared to single-cell trapping imaging system that single-cell setup [45].

Despite precise control of a single bio-cell being promising, this technique suffers from limited FOV as only one bio-cell can be used for capturing imaging, as illustrated in Fig. 2.18 (a). To address this, Jiang et al. proposed that chained-cell configuration by optically trapping multiple yeast cells using a tapered fibre is feasible [45]. Fig. 2.18 (c, d, f, g) show that each cell acts as an individual microsphere superlens, enabling parallel imaging of nanostructures to both DVD and Blu-ray disc features under white-light illumination. The chain structure significantly enhances imaging throughput, since each cell can simultaneously perform independent super-resolution imaging enabling a larger FOV compared to aforementioned single cell imaging.

2. Bio-superlenses array

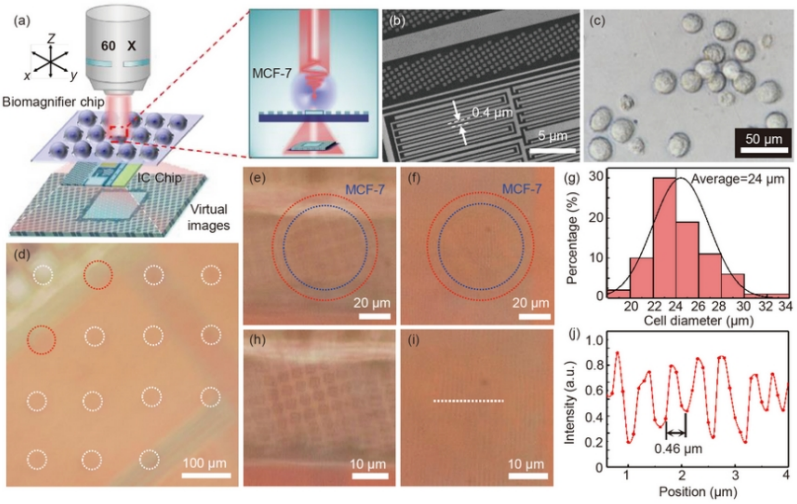

Figure 2.19 (a) Schematic illustration of the cellular lens array imaging setup. (b) SEM image of the IC chip structure. (c) Optical image obtained through a cellular lens. (d) Placement of the cellular lens array on the IC chip, with (e) and (f) showing cells located at different regions of the chip. (g) Particle size distribution of MCF-7 cells. (h, i) Magnified views of the IC chip areas highlighted in (e) and (f), respectively. (j) Intensity profile along the dashed line across the chip structure shown in (i) [46].

In 2023, Liao et al. developed a novel biological superlens array by combining maskless lithography with natural sedimentation-driven self-assembly, as shown in Fig. 2.19 (a) [46]. The precise controlling of the geometrical parameters of the photopolymerised hydrogel templates enables MCF-7 cells to be embedded into predefined micropores and finally form a highly ordered and functional microlens array (Fig. 2.19 d). In their study, the average size of MCF-7 cells is approximately 24 μm (Fig. 2.19 g) resulting in fabricating hydrogel modules with micropores of 25 μm in diameter to closely match the cell size and ensure optimal accommodation. Fig. 2.19 (e, f, h, i) indicate that the sub-wavelength features of an IC chip could not be resolved without the present of biological superlenses array setup. This setup enables a magnification of 1.15, as evidenced by the measured and real period of 0.46 μm and 0.4 μm, respectively.

Experimental results demonstrate that this modular design supports wide-field, parallel imaging. The strategy offers a scalable platform allowing a wide range selection in cells size and demonstrating strong potential for applications in biological super-resolution imaging.

2.1 Self-propelled bio-superlens

Another more primitive strategy is utilising the innate phototaxis of cyanobacteria, Schuergers et al. experimentally and theoretically analysed the underlying mechanisms of the characteristic [47]. Their displacement was measured and analysed by an experimental setup

(Fig. 2.20 a) which allows observing the movement of live cells in real-time while illuminated by LED light source from different directions. Fig. 2.20 (b–e) shows that the cells' movement is strongly influenced by the direction of the illumination. Notably, when exposed to two orthogonal light sources of equal intensity, most cells moved toward the central region between the two light directions. Fig. 2.20 (f) indicate that cells start to move one minute after the illumination, moreover, while being illuminated by a single LED, their absolute clustering level in agreement. However, while being illuminated by two orthogonal light sources of equal intensity, the clustering level of those cells was slightly lower than single illumination.

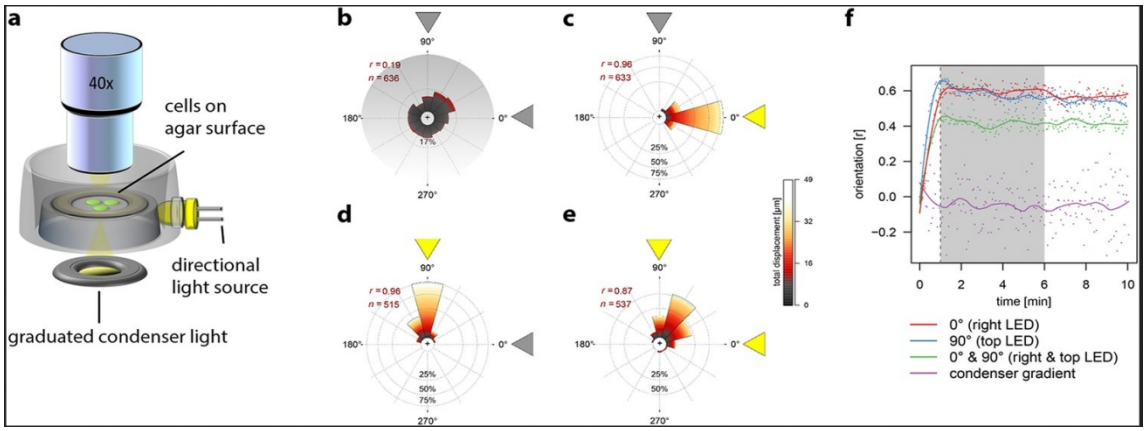

Figure 2.20 (a) Schematic illustration of experimental setup including two LED light source, objective lens and graduated condenser light. (b-e) The dependence of cells' movement on the direction of LED illumination. (f) The absolute clustering level of cells as a function of time after applying the different illumination conditions [47].

Fig. 2.20 indicate that each cell functions analogously to a microscopic eyeball, as it can respond to a photonic nanojet that forms on the side opposite to the incident illumination. This nanojet is generated due to the cell's spherical geometry and semi-transparent body, moreover, the nanojet can be detected by the membrane-embedded photoreceptors such as PixJ1. Through a series of biological signalling events, the cyanobacterial cell finally moves toward the light source. In conclusion, despite no super-resolution imaging experiments is performed in this study, their results not only reveal the mechanism of cyanobacteria innate phototaxis, but also offer valuable insights for the design of next generation and light-directed super-resolution imaging strategies that leverage the active, directional movement of living cells.

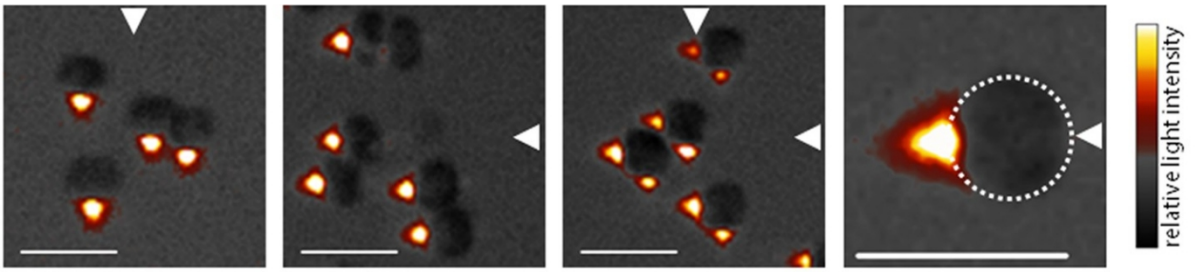

Figure 2.21 The nanojet generated forms on the side opposite to the incident illumination. Notably, while illuminated by two LED from two directions, two separate nanojets can be generated.

2.3.4.3 Summary

In summary, biological superlenses are essentially based on two geometries: cylindrical and spherical. Spider silk illustrates the cylindrical case, while various bio-cells exploit the spherical form to generate photonic nanojets for super-resolution imaging. Geometrically, the sphere represents the highest degree of rotational symmetry, and the cylinder can be regarded as its reduced-symmetry form, which explains their related light-focusing behaviours. These two morphologies thus provide the structural foundation for biocompatible, label-free super-resolution imaging.

2.4 Deep Learning for Image-to-Image Translation

Deep learning has become an important tool for establishing relationships between different imaging modalities. Image-to-image translation methods aim to convert an image from one domain into the style of another domain while preserving its underlying structural information [48]. This capability is relevant to micro-superlens-assisted imaging in both prefabricated microsphere systems and nanoparticle-based mSILs. In conventional microsphere-assisted imaging, prefabricated full spheres can in principle be repositioned or scanned across the sample surface by using a mechanical tip together with a high precision translation stage. However, such procedures increase experimental complexity and are not well suited to routine large-area mapping. For mSILs formed from NSFA, the situation is more restrictive, because at its formation position and cannot be moved to probe other regions without risking damage to the lens–sample interface. If a reliable mapping from SEM morphology to optical appearance can be learned, optical responses at unmeasured locations could be predicted computationally.

If a reliable mapping from SEM morphology to optical appearance can be learned, optical responses at unmeasured locations could be predicted computationally. Recent advances in

unpaired translation methods provide opportunities to achieve this goal without requiring strictly matched training datasets. The following subsections summarise the main developments in unpaired translation and form the basis for the method adopted later in this thesis.

2.4.1 CycleGAN Model

CycleGAN, proposed in 2017, introduced an effective way to perform image-to-image translation without requiring paired datasets [49]. The method learns two mappings between two image domains together with a constraint that attempts to recover the original image after a forward and backward translation. This cycle consistency condition allows the framework to maintain the structural content of the input image even when no direct correspondence is available. CycleGAN uses two generator networks to perform the translation and two discriminator networks to evaluate the realism of the generated images.

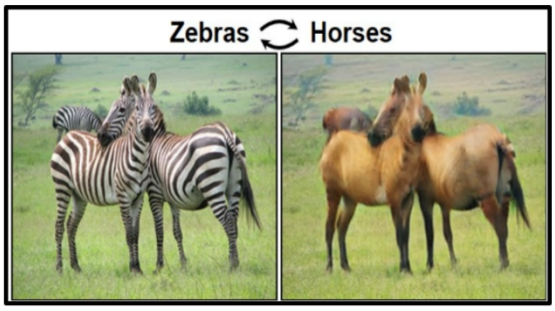

Figure 2.22 Example application of CycleGAN translating zebra and horse images [49].

A well-known illustration of this concept is shown in Fig. 2.22, demonstrating how CycleGAN successfully translates between horse and zebra images. The model has been widely used in situations where paired data are difficult or impossible to obtain, including style conversion, image enhancement and preliminary cross-modality translations. Its main limitation is that the cycle-consistency constraint may restrict how well local fine features can be preserved, especially in applications that require accurate retention of small-scale structural information.

2.4.2 CUT Model

As illustrated in Fig. 2.23, the CUT framework introduces a patchwise contrastive learning strategy to enforce consistency between spatial regions of the input and output. Contrastive Unpaired Translation (CUT) offers an alternative approach to unpaired translation by

replacing the cycle consistency requirement with a contrastive learning objective [50]. Instead of relying on a forward–backward reconstruction, CUT focuses on maintaining correspondence between local features in the source and target domains. It does this by maximising agreement between features extracted from matching spatial regions of the input and output while separating them from non-matching regions. This patch-based learning strategy encourages the translated image to retain the essential structural information from the input. Compared with earlier adversarial methods, CUT typically requires fewer training objectives and lower computational complexity, while often producing sharper and more structurally consistent results. The method is well suited to cross-modality imaging tasks where structural integrity of the input image is important and where collecting paired data is difficult.

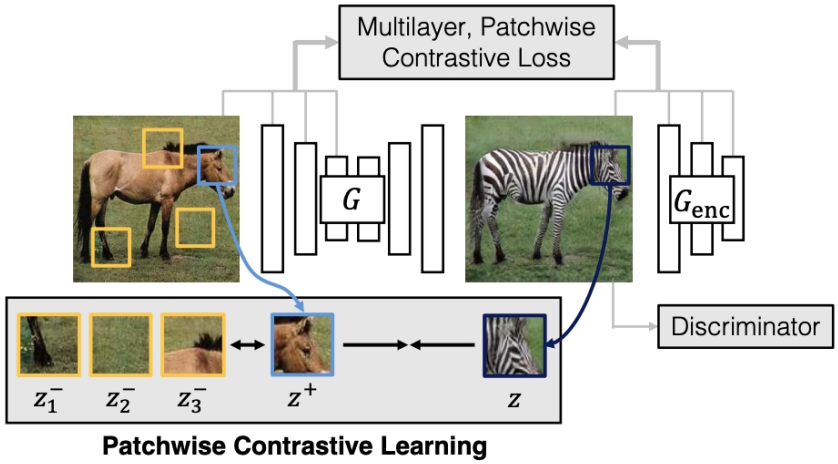

Figure 2.23 Patchwise Contrastive Learning for one-sided translation in CUT model [50].

2.4.3 SinCUT Model for Cross-Modality Conversion

Single-Image Contrastive Unpaired Translation (SinCUT) extends the CUT framework to situations where only a single pair of images from two domains is available [51, 52]. While CUT requires multiple samples from each domain, SinCUT modifies the contrastive learning objective so that the model can be trained from a single approximately aligned example. The key idea is to exploit spatial redundancy within the image so that the encoder can still learn consistent local feature correspondences across the two domains. This makes SinCUT suitable for imaging scenarios where only limited cross-modality data can be collected.

In microscopy research, SinCUT has been applied to problems in which structural information is readily available but optical data are sparse. This matches the conditions of micro-superlens imaging, where SEM can provide large-area morphological maps of the

sample but optical images through the mSIL are restricted to a single location due to the fixed lens position. Under such asymmetric data conditions, SinCUT enables the model to learn a relationship between SEM morphology and optical appearance without requiring multiple paired datasets. Once trained, the model can generate predicted optical responses from SEM images acquired at other positions, which provides a data-driven means of extending the effective imaging range.

2.5 Blue-shift in Thin-film Filters

Thin-film filters play a crucial role in a wide range of modern applications, including optical communication, laser systems, spectroscopy and remote sensing [53–56]. Meanwhile, since these applications usually experience complex illumination conditions, the demand for thin-film optical filter with high spectral stability under various of illumination has becoming increasingly critical. However, the angular dependence of spectral response, as evidenced by the reduced robustness demonstrated by thin-film filters at oblique AOI, limits the application of thin-film filters under such scenarios [57]. For instance, wide field-of-view (FOV) imaging and display systems, such as augmented reality (AR) and virtual reality (VR), require optical components that maintain stable performance under large incident angles [58].

To understand and mitigate this issue, it is essential to review the working principles of thin-film interference, mathematical description, and performance impact of the blue-shift phenomenon. The following sections begin by outlining the foundational mechanisms of thin-film filters before progressing to the theoretical and practical implications of blue-shift under varying incidence angles.

2.5.1 Working Principles of Thin-film Filters

An optical thin-film filter operates by selectively reflecting, transmitting, or absorbing electromagnetic waves over specific wavelength ranges through controlled interference. Since the early development of metal-coated glass in the 1930s and the subsequent quarter-wave multilayer design, thin-film filters have become essential in optical communication, laser systems, lithography, and aerospace technologies. Their operation relies on constructive and destructive interference between reflected and transmitted beams, determined by phase shifts at interfaces with differing refractive indices [59]. A 180° phase shift occurs upon reflection at a boundary of lower refractive index, while none occurs at higher-index interfaces. Consequently, alternating high- and low-index quarter-wave layers are stacked to produce the desired spectral response (Fig. 2.24).

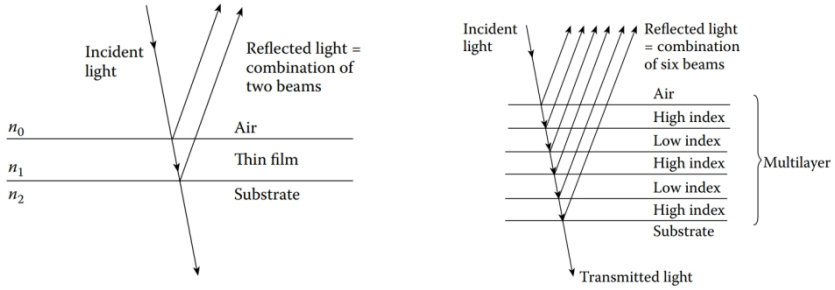

Figure 2.24 A simplified single layer thin-film filter (left) a multilayer consisting of alternate high and low index quarter-waves layers (right) [59].

2.5.2 Theoretical Origin and Description of Blue-shift

When light incidence a thin-film filter at an oblique angle, the change in optical path length and effective refractive index modifies the interference condition, causing the transmission or reflection bands to shift toward shorter wavelengths. This is known as the blue-shift effect [60].

According to Snell's law, the relationship between the incidence and refraction angles (θ_0 and θ_1) is given by:

$$n_0 sin\theta_0 = n_1 sin\theta_1 \tag{2.5.1}$$

Where n_0 and n_1 are the refractive indices incidence and refraction medium, respectively.

The central wavelength (λ_θ) of transmitting or a reflection band at oblique AOI is defined by:

$$m\lambda_\theta = 2n_1 dcos\theta_1 \tag{2.5.2}$$

Where m and d are interference order and physical thickness of thin-film, respectively.

As the θ_0 increases, $cos\theta_1$ decreases, resulting a shorter λ_θ that satisfies the interference condition. For multilayer systems, the relation can be approximated using an effective refractive index (n_{eff}), the magnitude of the blue-shift is inversely related to n_{eff} and positively to the AOI of the thin-film stack Eq. (2.5.3). The formular is visualised in Fig. 2.25.

$$\lambda_\theta = \lambda_0 \sqrt{1 - \frac{\sin^2 \theta}{n_{eff}^2}} \tag{2.5.3}$$

where λ_0 is central wavelength at normal incidence.

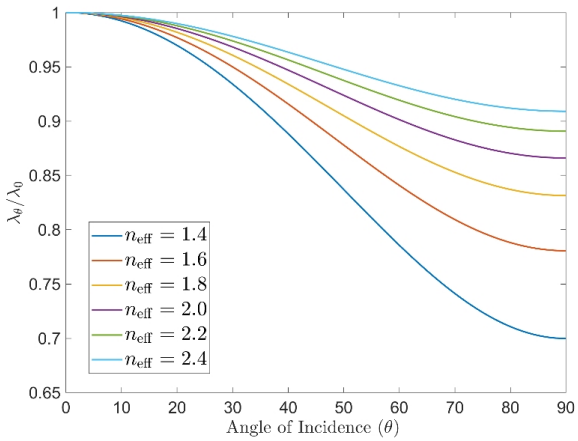

Figure 2.25 The dependence of central wavelength on AOI and effective refractive index.

2.5.3 Early Mitigation Attempts

As discussed above, the central wavelength of thin-film filters shifts toward shorter wavelengths with increasing AOI, causing spectral instability. To mitigate this, two straightforward approaches have been explored. The first is to broaden the transmission or blocking bands, which maintains acceptable performance at high AOI but leads to spectral distortion and reduced mechanical stability due to the increased number of coating layers [60]. The second uses absorption-based colour filters made from organic dyes, whose responses are angle-independent since they rely on molecular absorption rather than interference. Examples include anthraquinone and azo derivatives for red, and phthalocyanine derivatives for green filters [61]. However, their poor thermal and UV stability limits practical use [62]. These two methods, while conceptually simple, are therefore not discussed this work.

2.5.4 Summary

In summary, the blue-shift in thin-film filters originates from the change in optical path length and effective refractive index under oblique incidence, which changes the interference condition. Although several conceptually simple mitigation strategies have been proposed, achieving angle-independent interference filters with high spectral precision remains a significant challenge in optical engineering.

2.6 Mitigation of Blue-shift: Existing Wide-angle Strategies

Researchers have extensively explored improvements in optical structure design, material selection, and underlying response mechanisms. In recent years, a variety of engineering strategies have been proposed to enhance the spectral stability and practical applicability of thin-film filters under complex illumination conditions. The following sections systematically

review representative blue-shift mitigation techniques and their physical principles, focusing on three major directions: structural design optimisation, incorporation of functional layers, and the development of metamaterial-based architectures.

2.6.1 Structure-based Filters

2.6.1.1 Metal–dielectric–metal (MDM) Filters

Structural optimisation strategies have been developed to enhance angular spectral stability. This structural mitigation approach employs metallic layers to manipulate the optical interference conditions. A representative example is the symmetric multi-cavity configuration, specifically, the metal–dielectric–metal (MDM) structure, which achieves optical path compensation through symmetric metallic mirrors enclosing a dielectric layer.

Shin et al. made an early contribution by proposing an MDM microcavity structure exhibiting angle-insensitive, or omnidirectional, resonance, where the resonance wavelength remains nearly constant regardless of the incidence angle [63]. They demonstrated that the reflection phase and propagation phase within the cavity can nearly cancel each other over a wide angular range, ensuring that the total round-trip phase shift remains approximately 2π at all AOIs, as illustrated in Fig. 2.26 (a). This condition is satisfied when the dielectric layer has a thickness close to one-quarter of the surface plasmon wavelength, and its dielectric constant is nearly equal in magnitude but opposite in sign to that of the metal. In their study, SiO_2 and Ag were used as the dielectric and metallic layers, respectively, as shown in the inset of Fig. 2.26 (b).

Fig. 2.26 (b) presents the total electromagnetic energy distribution within the dielectric region as a function of wavelength and incident angle, obtained via transfer matrix analysis. The design exhibits strong AOI insensitivity from 0° to 80°. Although energy attenuation increases at larger AOIs, the result provides direct evidence of omnidirectional resonance and establishes a foundational principle for the design of AOI-insensitive optical filters in subsequent research.

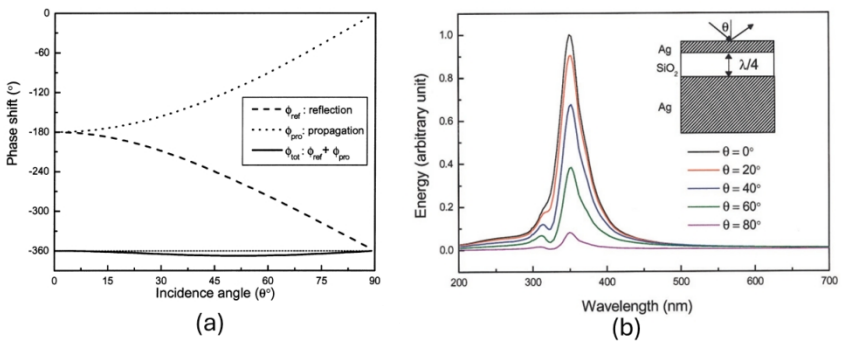

Figure 2.26 (a) The round-trip phase shift of an MDM structure in which the dielectric constant of the two materials is approximately equal in magnitude but opposite in sign, and the dielectric layer thickness is close to one-quarter of the surface plasmon wavelength. The aggregate reflection phase, propagation phase shift and total round-shit are plotted by dashed line, dot line and solid line, respectively. (b) total electromagnetic energy stored within the dielectric spacer layer as a function of wavelength and incidence angle [63].

Building upon the MDM structure, many AOI insensitive filter have been developed. For instance, in 2014, Lee et al. adopted similar MDM configuration while introducing amorphous-silicon (α-Si) as dielectric layer [64]. The introduction of α-Si was crucial because its high refractive index (ranging from 3.5–4.0) in visible wavelength regime enables strong optical confinement and allows the design to remain ultrathin while still achieving resonant enhancement. Despite minor absorption existing in the short-wavelength, the trade-off was acceptable, particularly for red and green colour filters.

As a result, their configuration (Ag–α-Si–Ag) demonstrated vivid and consistent colours (red, green and blue shown in Fig. 2.27) at all AOI up to 70°.

Figure 2.27 (a) Image of fabricated colour filters showing (a) red, (b) blue and (c) green with transmission peak at 622 nm, 530 nm and 485 nm, respectively [64].

Another representative MDM design also employed Ag as metallic layer while replaced SiO_2 to SiO_x as dielectric spacer [65]. This strategy allows precise controlling of the refractive index of the dielectric layer, allowing it to fulfill the dispersion-flattening condition and to adjust the central wavelength, as revealed in Fig. 2.28. This modulation of refractive index was achieved by adjusting the oxygen content during reactive magnetron sputtering. Both simulated and measured spectral responses of Ag–SiO_x–Ag configuration indicate that the use of SiO_x enabled high flexibility in choosing the central wavelength across nearly whole visible spectrum while maintaining the AOI insensitive, as evidenced by Fig. 2.28.

In summary, although various MDM configurations have been proposed [66–70], most aim to maintain colour consistency at high AOI by stabilising reflection spectra or acting as absorbers, rather than achieving high transmission across wide angles. In addition, due to the

high reflectivity and intrinsic Ohmic losses of metals, typical MDM structures show limited transmission (usually below 50%) and broad pass-bands [71, 72]. These shortcomings restrict their use in applications demanding both angular tolerance and high transmission. To address this, extended and modified MDM designs have been developed to improve transmission efficiency and spectral selectivity while retaining angular stability.

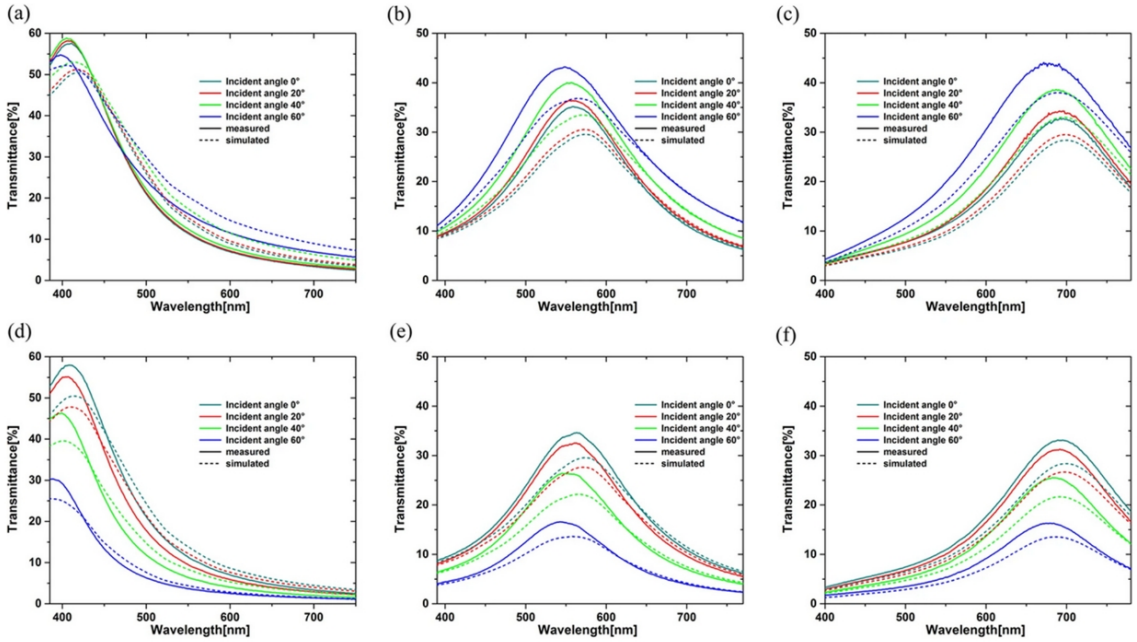

Figure 2.28 Transmission spectra of filters under TM-polarised incidence, cantered at (a) 399.1 nm, (b) 506.9 nm, and (c) 614.9 nm, respectively. The corresponding transmission spectra of each filter under TE-polarised incidence (d-f) [65].

2.6.1.2 Extended and modified MDM Filters

All aforementioned designs are variants strictly building upon triple-layer configurations inherently showing limited flexibility in tuning both spectral shape and angular robustness due to the constrained degrees of freedom in thickness optimisation. Therefore, introducing more layers can instantly provide better design flexibility. This approach enables more accurate control of optical phase and resonance conditions.

For example, Jen et al. proposed a five-layers configuration—MDMDM (Ag–α-Si– Ag–α-Si–Ag—based on widely used triple-layer MDM configuration, as seen in Fig. 2.29 (a). Although this design demonstrates narrower pass-band and consistent angular tolerant performance up to 70° at TM polarisation, as evidenced by Fig. 2.29 (c), compared to conventional MDM design, the transmission (<16%) was not significantly enhanced due to high optical loss of metallic layers [73].

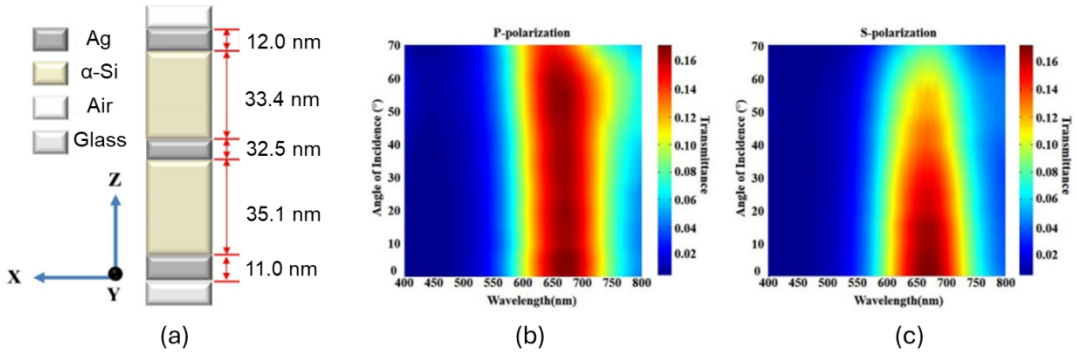

Figure 2.29 (a) Schematic of 5-layers MDMDM filter. Transmission spectra under varying AOI for (b) TM and (c) TE polarisations, respectively [73].

Complementing above work, as seen in Fig. 2.30 (a), they introduced a simpler, four-layer Ag/α -Si bandpass filter targeting the near-infrared at 950 nm while offering high transmission above 70% at normal incidence [74]. Remarkably, Fig. 2.30 (b, c) show that the fabricated structure exhibited only a minor peak shift (<10 nm) at AOI up to 60°. The peak transmittance decreased by approximately 10%, indicating excellent angular stability. However, the blocking performance was insufficient. Transmission in the stop-band exceeded 10% across all AOIs, which compromises spectral selectivity in applications requiring strong out-of-band rejection.

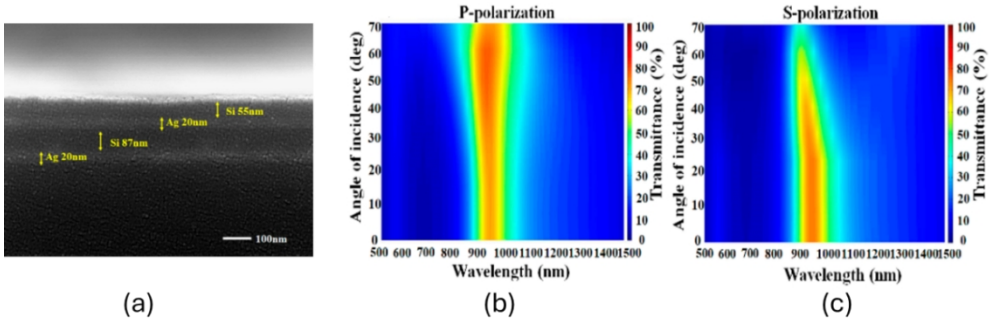

Figure 2.30 (a) Cross-sectional SEM image of a modified MDM filter. Transmission spectra under varying AOI for (b) TM and (c) TE polarisations, respectively [74].

The low transmission issues can also be mitigated by introducing dielectric AR layers on both side of the MDM configuration. Zhang et al. added AR layers on two side of MDM based filter to enhance the transmitting performance [75]. Fig. 2.31 compares the transmission of an MDM configuration without and with AR layers under varying AOI. The introduction of AR significantly enhanced the transmission at normal incidence from only 20% to over 40%. Moreover, the undesirable side peak observed in the ultraviolet (UV) region was effectively suppressed due to the improved impedance matching introduced by the AR coating. However,

the introduction of AR also leaded to a marked reduction in transmission at high AOI, down to 15% at 75° incidence, despite showing angular insensitivity in terms of the central resonance wavelength. This could potentially because the predesigned phase-matching condition deviates from the optimal design point as the optimisation of AR coating is usually for normal incidence.

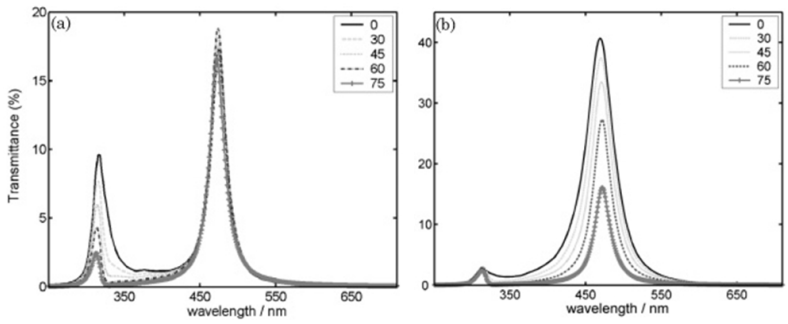

Figure 2.31 The transmission spectra of an MDM based bandpass filter under varying AOI: (a) without and (b) with AR layers, respectively [75].

Besides incorporating multi-layers in design, another novel MDM configuration (Ag-TiO_2-Ag) introducing tapered etalon was proposed to further improve the angular tolerant and transmission performance (up to 60% at normal incidence) at high AOI [76]. This design used TiO_2 dielectric cavity with a linearly tapered thickness along the device length, as showin in Fig. 2.32 (a). This gradient in cavity thickness leads to a spatially tuneable resonance wavelength, enabling position-dependent spectral selection.

Notably, this design functions as a linear variable colour filter, unlike conventional uniform filters exhibiting uniform optical responses, its resonance wavelength varies continuously along the lateral direction of the device. In other words, the transmission spectrum in Fig. 2.32 (b, c, d) are position-dependent and suitable for applications in miniaturised spectrometers or hyperspectral imaging. Nevertheless, this inherently limits the design's applicability in scenarios requiring spatially uniform filtering behaviours.

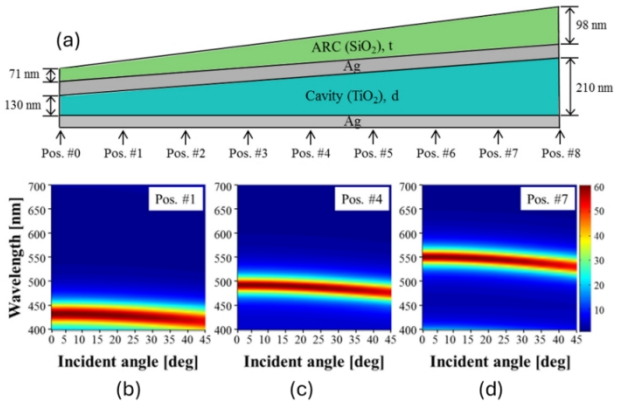

Figure 2.32 (a) The schematic representation of linear variable colour filter based on a tapered etalon. The transmission spectra with varying AOI at position (b) 1, (c) 4, and (d) 7, respectively, as highlighted in (a) [76].

2.6.1.3 Summary

In summary, MDM-based filters and their structural variants more or less offer angular tolerance by carefully designing the thickness of each layer in order to match dispersion-flattening condition. However, they suffer from limited transmission efficiency and inconsistent optical response at high AOI, making them less suitable for applications requiring both high transmittance, high blocking and wide-angle performance [77].

2.6.2 Photonic Crystal-based Filters

Photonic crystals (PhCs) consisting of periodic stacks of dielectric layers have emerged as a promising method to mitigate blue-shift issue. Their ability to engineer photonic bandgaps and defect states enables precise control to transmission characteristics, including bandwidth, angular tolerance, and spectral shape. The PhCs can be categorised into one-dimensional (1D), two-dimensional (2D), and three-dimensional (3D) configurations, according to the spatial dimensionality of their refractive index periodicity, as shown in Fig. 2.33 [78]. Each category offers distinct optical responses in terms of angular tolerance and spectral control. In this section, representative works within each category are introduced to illustrate the underlying mechanisms and their effectiveness in mitigating angular spectral shifts.

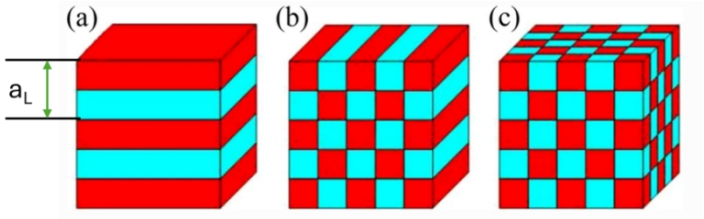

Figure 2.33 Schematic illustration of (a) 1D, (b) 2D and (c) 3D PhCs consisting of two materials with different refractive index and with spatial period of material represented by a_L [78].

1. One-dimensional Photonic Crystal (1D PhC) Filters

The typical architecture of a 1D PhC is referred as a Bragg stack because it consists of alternating high- and low-refractive-index dielectric layers arranged periodically along a single spatial axis, typically z-axis. Such periodic arrangement can generate a photonic bandgap (PBG) in which the propagation of light with certain wavelength is forbidden due to Bragg reflection. Unlike conventional thin-film filters that rely on interference without requiring strict periodicity, 1D PhCs require regular and periodic modulation of optical impedance to establish well-designed PBG. This concept was originally demonstrated in the microwave regime by John in the 1980s [79]. Since then, 1D PhC have been extended to the visible and infrared regions, owing to advances in nanofabrication and their advantages in achieving high reflectivity, tuneable spectra, and even angular tolerance.

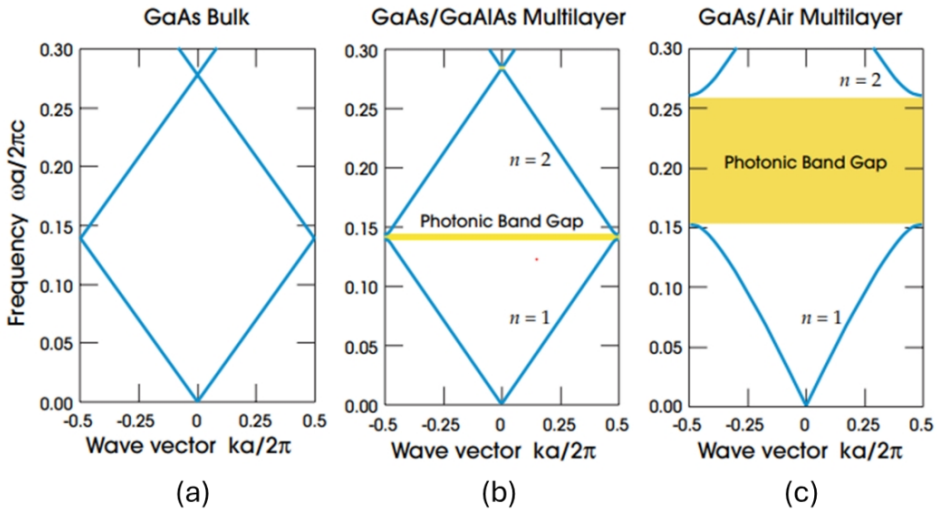

Figure 2.34 Photonic band structures of three one-dimensional photonic crystal configurations: (a) homogeneous GaAs with no dielectric contrast, (b) GaAs/GaAlAs multilayer with low dielectric contrast, and (c) GaAs/Air multilayer with high dielectric contrast [80].

To illustrate the concept of PBG, Fig. 2.34 compares three crystal configurations without, with narrow and with wide PBG, respectively [80]. Starting from Fig. 2.34 (a), a homogeneous material gallium arsenide (GaAs), with a dielectric constant ~ 13, is used. The periodic thickness (a_L), the combined thickness of one high- and one low-index layer, can be arbitrarily assigned, and resulting a continuous linear dispersion with no photonic band gap. This is because the linear dispersion extends smoothly beyond the first Brillouin zone edge, located at the normalised Bloch wavevector ($ka_L/2\pi$) equals 0.5 ($k = \pi/a_L$), and then folds back smoothly again.

In Fig. 2.34 (b), both GaAs and aluminium gallium arsenide (GaAlAs, dielectric constant ~

12) are used. Owing to the small dielectric contrast (13 vs 12), light experiences minor reflection at each interface. This results in limited interference and a narrow photonic band gap, separating band 1 and band 2. In contrast, Fig. 2.34 (c) shows a GaAs/air multilayer with a much higher dielectric contrast, resulting strong reflection at the interfaces. This enhances Bragg scattering and leads to stronger destructive interference and therefore a much wider band gap. Generally, higher dielectric contrast causes greater mode localization across layers and larger frequency splitting at the band edge.

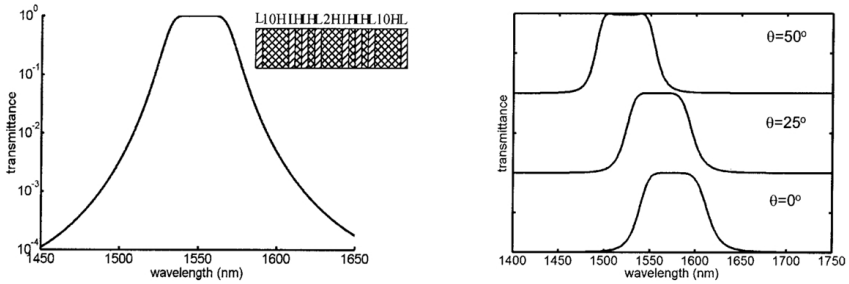

Figure 2.35 (a) Transmission (in logarithmic scale) of a flat-topped bandpass filter incorporating three resonant cavities under normal incidence. (b) The angular dependence of transmission spectra with TE polarised incidence [81].

Some early examples demonstrate that such bandgap concept is promising for angle-tolerant optical filter designing. In 2005, Chen et al. proposed a multilayer GaAs–Al_xOy filter incorporating multiple resonant cavities to achieve a flat-topped pass-band with wide angular tolerance, as shown in Fig. 2.35 (a) [81]. This design was built upon 1D PhC while using high refractive index to generate stop-band through Bragg reflection can be regarded as a photonic bandgap. Although Fig. 2.35 (b) shows that the blue-shift was mitigated, their design is only functional for one polarisation. All simulations and measurements were limited to the TE case, leaving the TM angular performance unverified. Moreover, the use of high-index-contrast materials in this case enhances the polarisation sensitivity of the multilayer structure, as shown in Fig. 2.25. Particularly, Brewster angle effect occurring at TM-polarised incidence can lead to significant drop of reflection near a specific angle and finally a narrowing or even disappearance of the photonic bandgap.

In 2009, Xu et al, reported a metal-dielectric ternary 1D PhC using ZnS/Ag/MgF_2 layers. This filter demonstrates a visible-region bandpass filter with angle tolerance up to 70° for both TE and TM polarisations [82]. The structure benefits from the strong resonance tunnelling effects introduced by the metal–dielectric combination, which improves angular tolerance. However, the transmission spectrum in Fig. 2.36 exhibits significant fluctuations in the pass-band,

particularly at high AOI, which lacks spectral flatness and robustness across the angular range. These irregularities are likely attributed to the intrinsic absorption and dispersion of the metallic Ag layers.

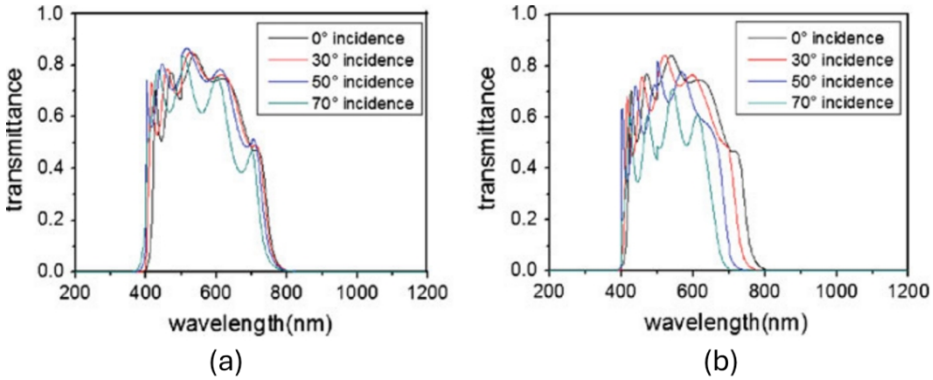

Figure 2.36 The angular dependence of transmission spectra with (a) TM and (b) TE polarised incidence [82].

Another representative design in Fig. 2.37 (a) and based on 1D PhC was reported by Lee et al. that incorporating α-Si and dielectric silicon nitride (Si_3N_4) [83]. By deploying the high refractive index contrast between the two materials, the design achieves a sharp, high purity of red reflection with minimal spectral distortion across a wide angular range (up to ±70°) for both TE and TM polarisations, as evidenced by Fig. 2.37 (c, d). Moreover, AR layer was considered in their study to ensure the purity of reflected colour, as revealed by Fig. 2.37 (b). Lastly, the dependence of reflection band edge slope was discussed in their study that a greater number of layer pairs enables sharper edge slope. This compact and lithography-free multilayer design offered a robust, scalable alternative to conventional metal-based structural colour technologies.

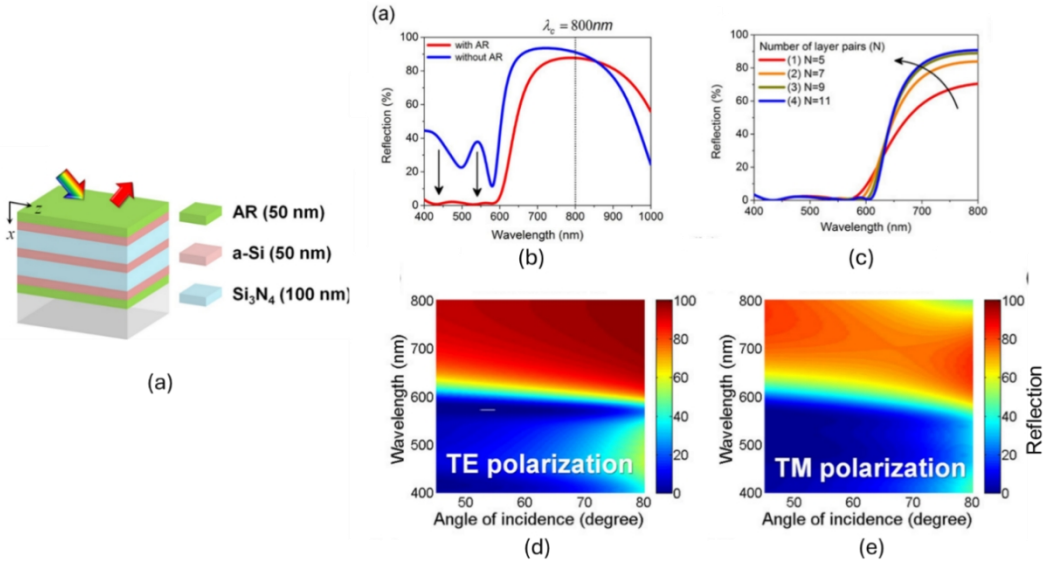

Figure 2.37 (a) Schematic sketch of an AOI tolerant 1D PhC based reflection mode colour filter

consisting of α-Si and Si_3N_4. (b) Comparison of spectral reflectance with and without an AR layer. (c) Simulated reflectance spectra for different numbers of α-Si/Si_3N_4 layer pairs, showing that increased stack number sharpens the band edge slope, resulting in improved spectral selectivity and higher reflectivity in the stop-band region. (d, e) Transmission spectra dependence on AOI at TE and TM polarisation [83].

Leveraging the same material system and design principles, they transformed the reflective structural colour concept into a transmissive longwave-pass edge filter with enhanced blocking performance [84]. The structure (Fig. 2.38 a) employs a 7-layer ternary 1D PhC configuration (H/2 L H/2, where H and L denote quarter-wavelength thickness) that effectively blocks visible light due to high absorption of α-Si showing in Fig. 2.38 (b), while maintaining high transmission in the near-infrared (NIR) range. This work demonstrates outstanding angular insensitivity (up to ± 60°) at both TM and TE polarisations, as evidenced by Fig. 2.38 (c, d).

Although this design achieves excellent angular stability, visible-light blocking, and near-infrared transmission, enabling cyan, magenta, and yellow (CMY) decorative effects, its colour-tuning capability remains limited. The CMY variation mainly depends on phase modulation within the dielectric layers, adjusting short-wavelength reflectance, while the spectral edge of the near-infrared band stays nearly fixed. Thus, despite partial tunability of decorative colours, the transmission edge lacks flexibility due to the structural constraints of the one-dimensional design, limiting adaptation to specific spectral requirements in practical use.

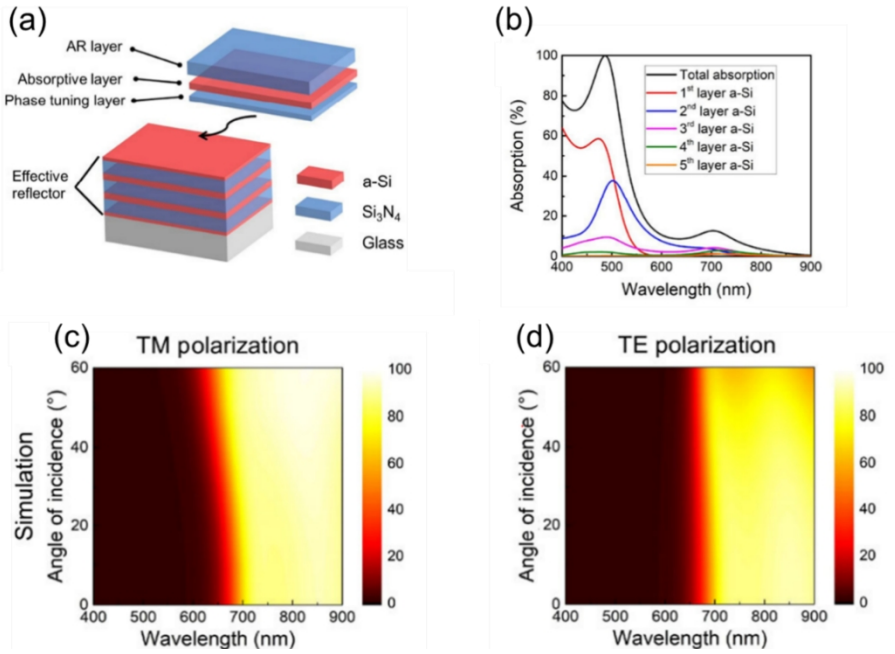

Figure 2.38 (a) Schematic sketch of an AOI tolerant 1D PhC based colour filter consisting of α-Si and Si_3N_4. for decoration purpose [84].

Overall, 1D PhCs present a mature and structurally simple route to blue-shift mitigation, combining high reflectivity with design flexibility. However, challenges remain in achieving polarisation-independent performance, broad spectral tunability, and low-loss operation—factors that motivate the exploration of 2D/3D PhCs and metamaterial-based architectures.

2. Two-dimensional (2D) and three-dimensional (3D) Photonic Crystal Filters

The multi-directional periodicity of 2D and 3D PhCs offer increased symmetry and more flexible control over the propagation of light, especially angle-invariant behaviours. However, their fabrication often involves complex and costly fabrication techniques. As a result, much recent attention has shifted toward metamaterials, which can achieve angle-independent responses via localised resonances such as electric/magnetic dipoles or localised surface plasmonic resonances (LSPRs). These subwavelength modes are inherently less sensitive to incident angle. As a result, this section highlights only a few representative 2D and 3D photonic crystal designs that have demonstrated angular insensitive performance.

In 2024, Kanamori et al. designed reflection colour filters by using Si pillar-shaped 2D PhCs gratings on the quartz substrate with varying grating periods, respectively [85]. Although the authors claimed AOI tolerant performance, they emphasised that the perceived hue remains unchanged primarily because the spectral shift remains within the same colour range as observed by the human eye rather than achieving minor blue-shift of spectra.

A transmission-type colour filter based on 3D PhC was proposed by Choi. The core concept is employing a woodpile like configuration, which inherently exhibits an omnidirectional photonic bandgap capable of maintaining stable band-rejection and bandpass characteristics across wide AOI and at both TE and TM polarisation [86].

By implementing index modulation and period modulation, selective transmission of red/green/blue wavelength bands can be achieved. However, complex fluctuations in the transmission spectra are observed in their results, which can be attributed to the combined effects of the intrinsic structural transmission behaviours of the woodpile photonic crystal and coherent Fabry–Perot interference between the stacked layers.

In summary, 1D PhCs remain simple and effective but still face limitations such as polarisation dependence and restricted spectral tunability. In contrast, 2D and 3D PhCs can

offer better angular control, yet their practical application is limited mainly by the high fabrication complexity. These drawbacks together motivate the shift toward metamaterial-based designs for achieving robust angle-insensitive filtering.

2.6.3 Metamaterial-based Filters

In recent years, metamaterials have emerged as a powerful platform for manipulating electromagnetic waves in unprecedented ways. Metamaterials are referred to artificial man-made materials with subwavelength periodicity that do not exist in nature [87]. Unlike conventional materials whose optical properties are determined by intrinsic composition, the characteristics of metamaterials are derived from precisely engineered subwavelength scale geometry, enabling extraordinary phenomena such as negative refractive index, anisotropy, and epsilon-near-zero (ENZ) behaviours.

In the context of mitigating the blue-shift issue commonly observed in conventional optical filters, one of the key advantages of metamaterials lies in their exceptional tunability in terms of geometry and dimensional parameters. By precisely designing the shape, size, orientation, and arrangement of subwavelength units, it becomes possible to control light–matter interactions in a highly customized manner. This symmetric structure adaptability allows for the engineering of angular-insensitive or angle-tolerant spectral responses, offering a promising route to suppress undesired spectral shifts under oblique incidence.

2.6.3.1 Hyperbolic metamaterial (HMM) filters

Hyperbolic metamaterials (HMMs) have been developed in past decade as its characteristics are strongly dependent on anisotropic artificial media that enabling the opposite signs of their principal permittivity components. As seen in Fig. 2.39, in other words, the effective permittivity perpendicular ($\varepsilon_{\perp}$) and parallel ($\varepsilon_{/\!/}$) to the optical axis, respectively, must meet the relation that $\varepsilon_{\perp} \cdot \varepsilon_{/\!/} < 0$. This relationship leads to an open hyperboloid isofrequency surface rather than a closed ellipsoid. This unusual dispersion behaviours allows new ways of controlling light propagation, which can be utilised for PBG design [88].

As a result, HMMs have attracted considerable interest due to their potential in PBG engineering, spontaneous emission control, perfect absorption, and laser applications [89, 90]. Particularly, their application in mitigating the blue-shift issue as they support angle-insensitive PBG under TM polarisation, whose band edges remain nearly fixed with increasing incident angle—unlike the blue-shift issue observed in conventional and not optimised all-dielectric 1D PhCs. HMMs can be realised through multilayer metal–dielectric

stacks or nanowire arrays, providing broad tunability and compatibility with planar fabrication.

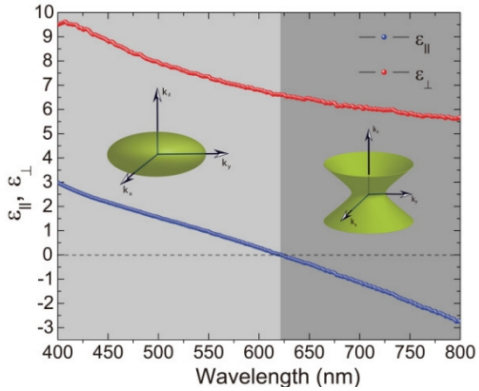

Figure 2.39 Illustration of a multilayered structure's effective perpendicular ($\varepsilon_{\perp}$) and parallel ($\varepsilon_{\parallel}$) permittivity transferring from a closed ellipsoid to an open hyperboloid [90].

Wu et al. designed an HMM based AOI insensitive filter using a classic periodic configuration $[(CD)^{S}B]^{N}$, with a periodicity of S = 3 for the HMM layers and N = 3 for the main structure [91], as shown in Fig. 2.40 (a). Their design demonstrates AOI insensitive reflectance and a resulting blocking band approximately from 375 nm to 425 nm with AOI up to 75°. However, the transmission in other wavelength regions remains very low, with a maximum of only 0.24, and progressively drops to 0.05 as the AOI increases.

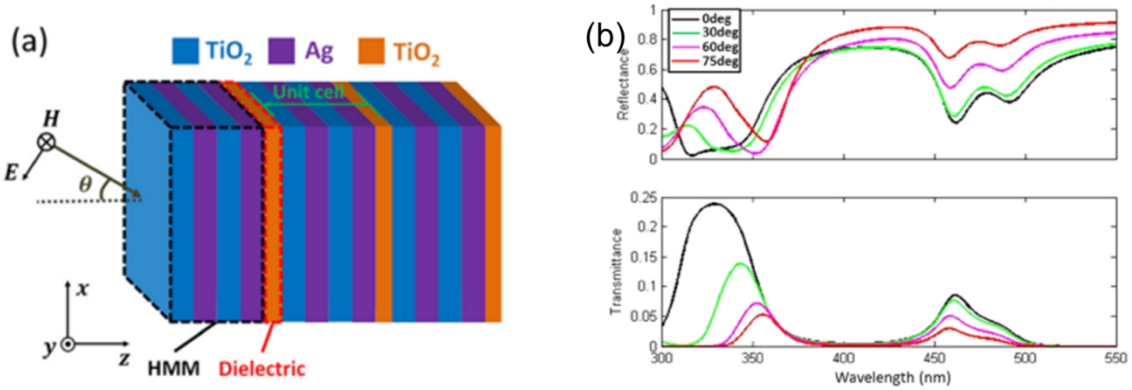

Figure 2.40 Illustration of a multilayered HMM design in $[(CD)^{S}B]^{N}$ configuration [91].

Another representative example showing an AOI dependent narrow pass-band was designed by Xue [92]. Fig. 2.41 (a) confirms the narrow AOI independent pass-band up to 85° and with high efficiency blocking band out of designed pass-band. Nevertheless, the transmission of pass-band is only approximately 0.25, as seen in Fig. 2.41 (b).

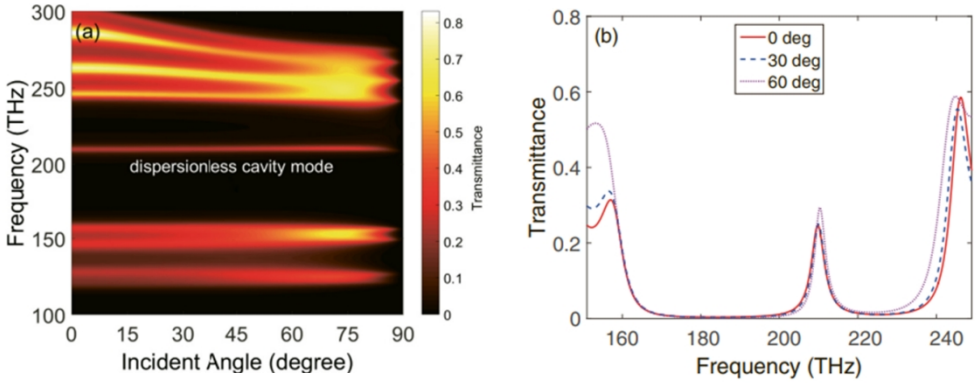

Figure 2.41 Illustration of a multilayered HMM design in $[(CD)^{S}B]^{N}$ configuration [92].

Wells et al. [93] designed a plasmonic nanorod-based HMM filter (Fig. 2.42) that exhibits minimal blue-shift up to 60° incidence, effectively suppressing the angular dependence typical of conventional interference filters. The structure consists of vertically aligned gold nanorods embedded in an alumina matrix, forming a uniaxial composite with tunable anisotropic permittivity controlled by nanorod length and spacing. Although the design maintains a stable resonance wavelength, its transmission decreases with angle (to ~0.2 at 40°) due to coupling inefficiency and metallic losses.

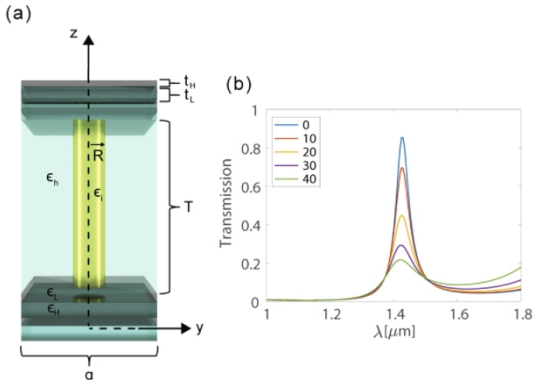

Figure 2.42 (a) Illustration of a nanorod-based HMM design and (b) transmission spectrum at varying AOI [93].

In summary, despite HMM based designs demonstrating AOI independent performance, such structures are typically effective only under TM-polarised incidence. This is because, at TM incidence, both k_x and k_z components are involved, allowing the wave to experience the anisotropic permittivity tensor of the HMM, which is essential for realising the desired filtering effect. Moreover, the intrinsic losses associated with metal or doped-semiconductor layers in HMM structures result in relatively low overall transmission in reported bandpass filters, typically ranging from 10% to 40% when AOI exceeds 20°.

2.6.3.2 Frequency selective surfaces (FSS) filters

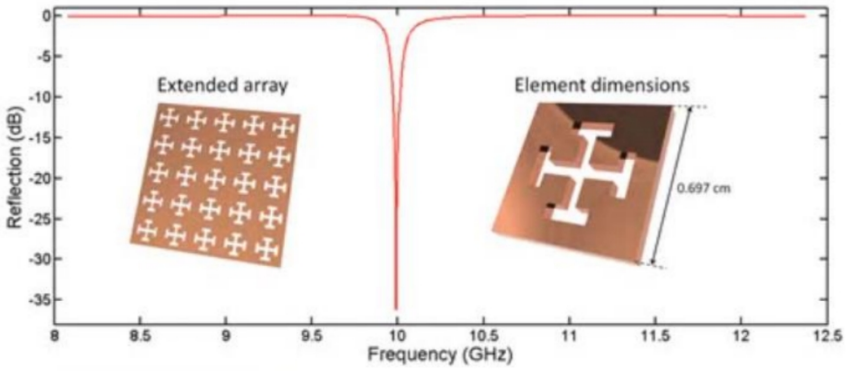

Figure 2.43 Schematic illustration of frequency selective surfaces (FSS) [96].

Most filters discussed previously are based on stacked homogeneous thin films, where spectral control is achieved through interference governed by layer thickness and refractive index. This vertical layering approach contrasts with frequency selective surfaces (FSS), which rely on geometric modulation in the transverse plane. Instead of multiple layers, FSS employ periodic nanoscale patterns such as crosses, slots, or rings on a single conductive film (Fig. 2.43), offering greater flexibility in tailoring electromagnetic responses [94, 95].

A common example is the Jerusalem-cross aperture, which produces a bandpass response. The geometry of an FSS unit cell, however, can be adjusted to meet different spectral requirements. According to Babinet's principle, converting a slot array into its complementary metallic dipole array reverses the spectral behaviour, turning a bandpass into a bandstop response or vice versa, as illustrated in Fig. 2.44 [96].

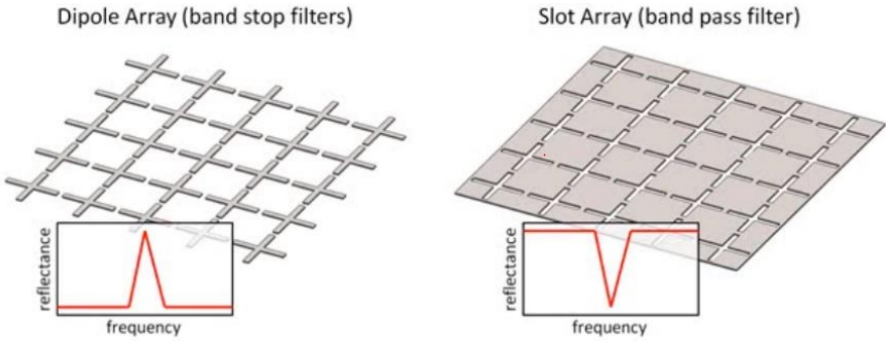

Figure 2.44 Schematic illustration of a dipole array (left) and slot array (right) and their corresponding optical responses demonstrating complementary frequency response [96].

To mitigate the blue-shift issue, Labeke et al. designed a structure consisting of a square array of coaxial annular apertures perforated into a metallic film (e.g., silver), forming a subwavelength periodic pattern, as illustrated in Fig, 2.45 (a) [94]. Unlike other metamaterial

optical filters, this design does not rely on surface plasmon resonances, but instead operates based on a Fabry–Pérot-like cavity resonance supported within the coaxial apertures. As shown in Fig. 2.45, numerical simulations demonstrate that the transmission peak can exceed 80% efficiency, and most importantly, the resonance wavelength remains stable across a wide range of incidence angles.

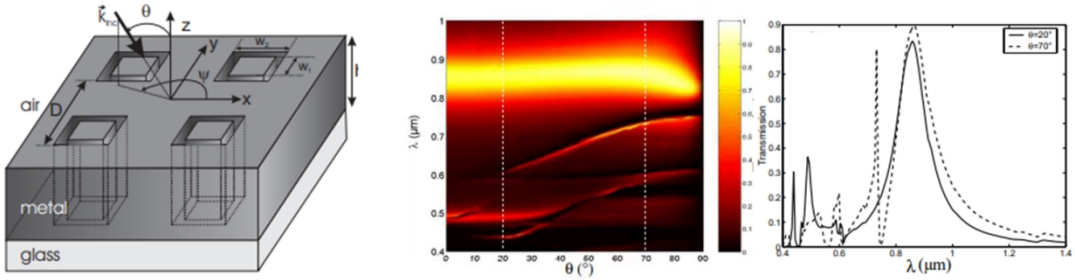

Figure 2.45 (a) Schematic illustration of FSS with square array of coaxial annular apertures. (b) Transmission spectra with varying AOI and (c) line figure at 20^{o} and 70^{o}.

However, the design exhibits certain limitations. The pass-band features a relatively broad full width at half maximum (FWHM), typically greater than 150 nm, and the blocking performance in the stop-band, especially in visible wavelength regime, is insufficient, as illustrated in Fig. 2.45 (c). This can potentially be further improved by introducing conventional edge filters and AR layer.

2.6.3.3 Nanostructure-based filters

In addition, three-dimensional (3D) nanostructure-based optical filters have emerged as a promising method to mitigate the blue-shift issue while achieve special control in visible wavelength and NIR regimes. Unlike planar multilayer stacks or patterned 2D FSS, these designs rely on three-dimensional nanoscale unit cell, including nanospheres, nanodisk, nanocubes, or core-shell particles, to manipulate light via angle-independent localised resonances, Mie scattering, or dipole absorption [1–4]. Owing to their inherent subwavelength confinement and polarisation diversity, such nanostructures can exhibit optical responses that are less sensitive to the AOI, especially when arranged in dense or disordered ensembles. This section reviews representative nanostructured systems that demonstrate wide-angle filtering capabilities, highlighting their underlying mechanisms, fabrication approaches, and trade-offs in spectral selectivity and transmission performance.

1. Metallic nanostructures

Metallic nanoparticles have been widely used to design optical filters due to their distinctive

absorption performance in specific wavelength regimes, enabled by localised surface plasmonic resonance (LSPR) [101]. LSPR refers to the collective oscillation of conduction electrons at the surface of a metallic nanoparticle when it is excited by incident light, as shown in Fig. 2.46 (a). Therefore, the plasmonic behaviour in a nanoparticle can be analogised to a damped harmonic oscillator, as illustrated in 2.46 (b), where the collective oscillation of the electron cloud is driven by the incident resonant electromagnetic wave. In this model, the electron cloud oscillates as an electric dipole aligned with the polarisation direction of the incoming electric field. This resonance condition occurs at a specific frequency that is strongly dependent on the particle's size, shape, material, and the surrounding dielectric environment. When resonance is achieved, a strong enhancement of the local electromagnetic field is observed near the nanoparticle surface, resulting in strong optical absorption and scattering features. These unique optical responses make LSPR an effective mechanism for selectively attenuating or enhancing transmission in tailored spectral regions, thereby offering a tuneable platform for compact, high-performance optical filters.

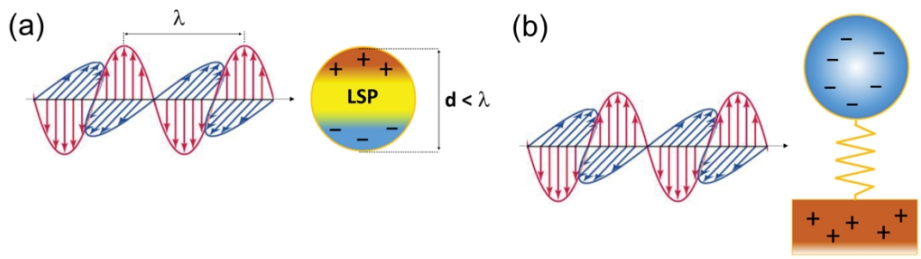

Figure 2.46 Schematic illustration of (a) localised surface plasmonic resonance (LSPR) and (b) its simplified mode acting as a damped harmonic oscillator [101].

Despite LSPR can occurs in most of metallic nanoparticles, only Au, Ag and Al are commonly selected to design LSPR based optical filters [102–104]. This because only a few elemental metals possess the necessary optical properties to support strong LSPR in the visible and near-infrared regions. Among them, Au, Ag and Al are the most effective due to their combination of high free electron density and relatively low optical losses. These metals exhibit a negative real part of the dielectric function (Re[ε]) and a small imaginary part (Im[ε]) over a broad spectral range, which are essential for achieving sharp and intense plasmonic resonances.

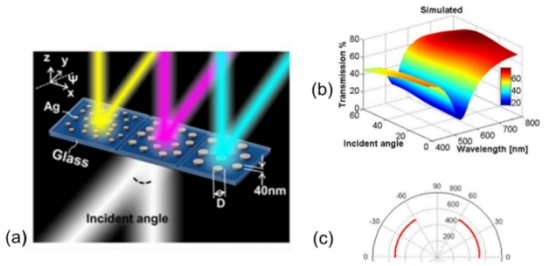

Figure 2.47 (a) Schematic illustration of the AOI independent colour filter consisting of randomly distributed silver nanodisks with tuneable transmitted colour performance. (b) AOI independent transmission spectrum of nanodisks based colour filter. (c) Polar plots of resonant wavelength as a function of incident angle [98].

Fig. 2.47 (a) shows an AOI and polarisation independent metamaterial colour filter consisting of non-periodic and randomly distributed Ag nanodisks [98]. This design leverages LSPR excited individually on each spatially isolated nanodisks, without additional interparticle coupling, to ensure a clear pass-band and angular independence. The absence of structural periodicity allows each nanodisk to behave as an isolated resonator and removes the requirement for in-plane wavevector matching. As seen in Fig. 2.47 (b, c), this filter enables a robust and broadband angle-insensitive response up to 60°.

Another representative example showing in Fig. 2.48 (a) was proposed by Monks et al., who designed a wide-angle, shift-free optical filter based on a three-dimensional periodic arrangement of silver nanoparticles [105]. The structure utilises small-sized Ag nanoparticles (~9 nm in diameter) as the functional core to support enhanced LSPR, which leads to a higher extinction factor (Q_{ext}). This enables strong blocking performance without relying on a high nanoparticle fill fraction. Such a strategy not only achieves effective suppression at the target wavelength but also preserves high transmission in the pass-band. Moreover, the resonance wavelength remains stable over a wide range of incident angles (0° to 85°), demonstrating excellent angular tolerance, as evidenced by nearly no shift blocking notch in Fig. 2.68 (b). This design is promising for high-efficiency spectral filtering in laser protection and related applications

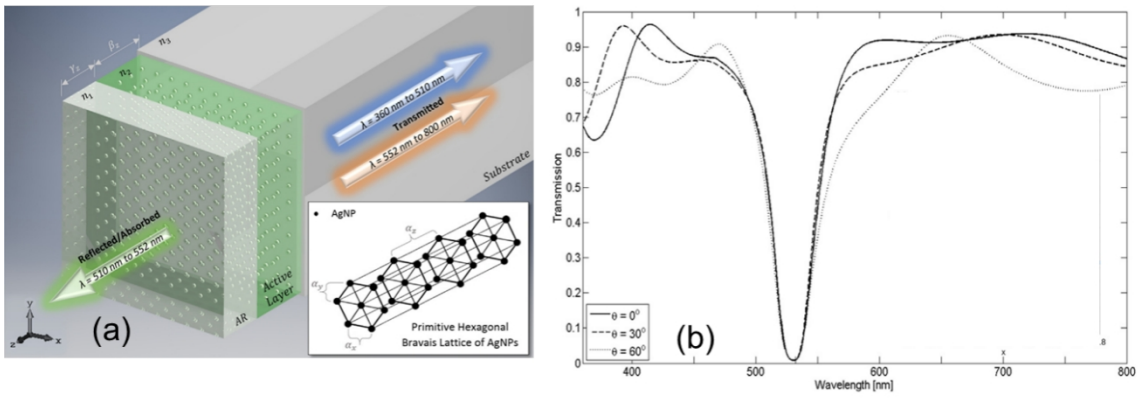

Figure 2.48 (a) Schematic illustration of the AOI independent filter consisting of 3-layers of periodically distributed silver nanospheres and its (b) transmission spectrum at varying AOI [105].

2. Dielectric nanostructures

In addition to metallic nanoparticles, dielectric nanostructures, especially silicon-based filter, have gained increasing attention for angle-tolerant and spectrally selective optical filtering. Owing to their high refractive index, low loss, and Mie resonances (electric and magnetic dipoles), silicon nanospheres offer a promising alternative to conventional thin films, enabling strong absorption and precise spectral control. Their self-assembled dense arrays further enhance directional scattering, ensuring spectral stability over a wide range of incidence angles [106].

One early study by Shokeen et al. [107] employed silicon nanospheres in the top and bottom buffer layers of a thin-film photovoltaic structure, enhancing light trapping via directional Mie scattering. Although spectral responses at oblique incidence were not explicitly analysed, the results showed that Mie resonances can be effectively excited without normal incidence, owing to guided scattering that maintains efficient coupling and suppresses destructive interference, indicating strong potential for angle-tolerant optical performance.

A solar cell design employing randomly distributed silicon nanospheres (SiNS), as shown in Fig. 2.49 (a–c), demonstrates high angular tolerance, maintaining strong absorption even at large incidence angles compared with conventional thin-film structures [108]. This robustness arises from broadband Mie resonances, which are intrinsically less sensitive to illumination direction. In random arrangements, enhanced near-field coupling between adjacent spheres further strengthens local field confinement, leading to improved absorption under both TE and TM polarisations. These results provide preliminary evidence that spherical silicon nanoparticles exhibit intrinsically high absorptivity and hold strong potential for maintaining efficient light filtering under at wide AOI.

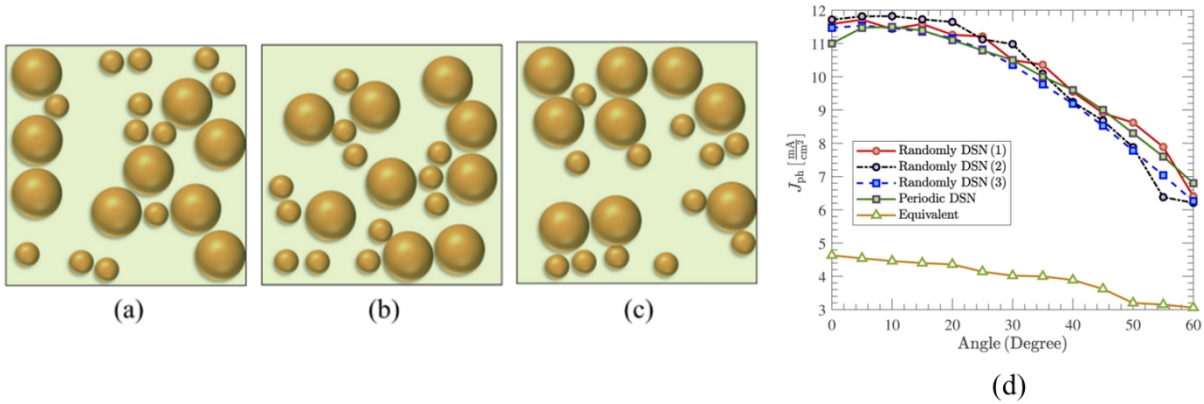

Figure 2.49 (a, b, c) Three examples of random distribution of SiNS and along with (d) a comparison of the current generation rates of various designs as a function of AOI [108].

2.6.3.4 Summary

In summary, metamaterials offer a much wider design space than photonic crystals because their optical behaviour is mainly determined by local subwavelength resonances rather than long-range periodic structures. Simple forms such as HMM multilayers and FSS patterns usually have limited tunability and work only within a narrow spectral range. For instance, HMM filters generally show good angular stability only for TM polarisation. In contrast, both metallic and dielectric nanoparticles have shown stable resonance responses over a wide range of incident angles, which indicates strong potential for use in wide-angle and spectrally selective optical filters.

2.7 Research Fundamentals

The Mie theory describes the exact and complete optical responses of a single spherical particle in nanoscopic or mesoscopic scales, however, it is insufficient to fully describe the optical response of multi-layers of periodically or randomly arranged nanospheres in complex external dielectric environment. However, the numerical method does not require to rigorous mathematical simplifications or idealized assumptions, which are often required in analytical approaches. It enables to build the model and resolve the solution according to the practical structure of and boundary conditions of a 3D complex mode. Due to the convenience, high flexibility and efficiency of numerical solutions, it is widely used in dealing with aforementioned complex scenarios.

2.7.1 Finite Difference in Time Domain (FDTD)

The finite-difference time-domain (FDTD) method is one of the most widely used numerical techniques for solving Maxwell's equations in the time domain [109]. It discretises both

space and time into a uniform grid and updates the electric and magnetic field components in an explicit time-stepping manner. By directly tracking the temporal evolution of the electromagnetic fields, FDTD enables broadband spectral information to be obtained from a single simulation. The method is conceptually straightforward and well suited for analysing light–matter interactions at the nanoscale, including near-field enhancement, scattering, and transmission processes in dielectric or plasmonic structures. Owing to its generality and numerical stability, FDTD has been extensively applied to nanophotonics, metamaterials, and subwavelength imaging studies, providing an important foundation for more advanced numerical frameworks such as the finite integration technique (FIT).

2.7.2 Finite Integration Technique (FIT)

The finite integration technique (FIT), proposed by Weiland in the 1970s [110], is a numerical method for solving Maxwell's equations in both time and frequency domains. It discretises the electromagnetic fields onto a grid while preserving key physical laws such as charge conservation and field continuity, ensuring numerical accuracy and physical consistency when modelling complex geometries and materials.

In the frequency domain, FIT reformulates Maxwell's equations into a system of linear equations that describe the steady-state response of the structure at a specific frequency. Compared with time-domain methods like FDTD, the frequency domain solver directly calculates field distributions without the need for temporal propagation, making it particularly efficient for resonant, periodic, and steady-state problems.

CST Studio Suite implements the FIT-based frequency domain solver as one of its core electromagnetic solvers. It has been widely validated and used for analysing nanophotonic components, plasmonic metamaterials, and dielectric resonators, where accurate modelling of field enhancement, scattering, and spectral characteristics is essential [111]. The solver also supports dispersive materials, periodic boundary conditions, and open boundaries through perfectly matched layers (PMLs), making it well suited for studying optical filters and microsphere-assisted imaging systems.

2.7.3 Transfer-Matrix Method for Multilayer Optical Systems

The computational core of ESM is based on the Transfer-Matrix Method (TMM), a well-established analytical approach for calculating the propagation of electromagnetic waves through stratified media [112]. In this method, each layer in the optical system is represented by a 2×2 matrix that relates the electric and magnetic field components at the entrance and

exit interfaces. By multiplying the matrices of all layers in sequence, the global response of the multilayer stack—including reflectance, transmittance, and optical admittance—can be precisely calculated for any given wavelength and angle of incidence.

To illustrate the principle of the TMM, consider the simplest case of a single thin-film of refractive index n_1 and thickness d_1 on a semi-infinite substrate with refractive index n_s, under illumination from air ($n_0 = 1$). When a plane wave is incident upon this structure, multiple reflections occur at the air–film (indicated by index "α") and film–substrate interfaces (indicated by index "β"). To describe the wave propagation through the film, the electric and magnetic fields at boundaries α (E_α and H_α) and β (E_β and H_β) have following relationships:

$$\begin{bmatrix} E_\alpha \\ H_\alpha \end{bmatrix} = \begin{bmatrix} cos\delta & (isin\delta)/\eta_1 \\ i\eta_1 cos\delta & cos\delta \end{bmatrix} \begin{bmatrix} E_\beta \\ H_\beta \end{bmatrix} \tag{2.7.1}$$

where δ denotes phase thickness given by $\delta = 2\pi n_1 d_1 / \lambda$. η_1 is admittance of thin-film defined in Eq. (2.7.2).

$$\eta_1 = Y * n_1 \tag{2.7.2}$$

where $Y = 2.6544 * 10^{-3}$ S is admittance in free space.

Eq. (2.7.3), which contains characteristic matrix $\begin{bmatrix} B \\ C \end{bmatrix}$, can thus be derived by dividing E_α and normalising the Eq. (2.7.1).

$$\begin{bmatrix} E_\alpha/E_\beta \\ H_\alpha/E_\beta \end{bmatrix} = \begin{bmatrix} B \\ C \end{bmatrix} = \begin{bmatrix} cos\delta & (isin\delta)/\eta_1 \\ i\eta_1 cos\delta & cos\delta \end{bmatrix} \begin{bmatrix} 1 \\ \eta_s \end{bmatrix} \tag{2.7.3}$$

where B and C are normalised electric field and magnetic field are represented, respectively. $\eta_s = Y * n_s$ is admittance of substrate.

The admittance of this single layer thin-film group defined by $Y = H_\alpha / E_\alpha$ can be rewritten according to Eq. (2.7.3).

$$Y = \frac{H_\alpha}{E_\alpha} = \frac{C}{B} = \frac{\eta_s cos\delta + i\eta_1 sin\delta}{cos\delta + i(\eta_s/\eta_1) sin\delta} \tag{2.7.4}$$

This formulation can be readily generalised to a multilayer system consisting of q individual layers, where the overall characteristic matrix under oblique incidence (θ_0) is obtained by taking the ordered matrix product of each layer's characteristic matrix, as given in Eq. (2.7.5):

$$\begin{bmatrix} B \\ C \end{bmatrix} = \left\{ \prod_{r=1}^{q} \begin{bmatrix} cos\delta_r & (isin\delta_r)/\eta_r \\ i\eta_r cos\delta_r & cos\delta_r \end{bmatrix} \right\} \begin{bmatrix} 1 \\ \eta_s \end{bmatrix} \tag{2.7.5}$$

where

$$\delta_r = 2\pi n_r \quad d_r \quad cos\theta_r / \lambda$$

$$\eta_r = Yn_r cos\theta_r \text{ (TE polarisation)}$$

$$\eta_r = Yn_r / cos\theta_r \text{ (TM polarisation)}$$

The θ_r can be determined by Snell's law in Eq. (2.5.1):

$$n_0 sin\theta_0 = n_r sin\theta_r = n_s sin\theta_s \tag{2.7.6}$$

As a result, the total admittance for a thin-film group consisting of q layers, each layer of r has a transfer M_q.

$$M_{total} = M_1 \cdot M_2 \cdot \ldots \cdot M_q \tag{2.7.7}$$

The total characteristic matrix captures the cumulative optical response of the multilayer structure. This method enables the calculation of reflectance, transmittance, and absorptance by applying boundary conditions at the input and output media.

In summary, the transfer-matrix method provides a rigorous analytical basis for modelling thin-film interference effects in multilayer optical systems. It allows precise evaluation of reflectance, transmittance, and phase characteristics for both TE and TM polarisations over a wide range of angles and wavelengths. This theoretical framework forms the foundation for the multilayer optimisation work carried out using ESM in Chapter 3.

2.8 References

[1] Abbe, E. "Beiträge zur Theorie des Mikroskops und der mikroskopischen Wahrnehmung," Archiv. Mikrosk. Anat. 1873, 9, 413–418.

[2] S. Zhou, L. Jiang, "Modern description of Rayleigh's criterion," Phys. Rev. A 2019, 99, 1, 013808–013828.

[3] Z. Wang, "Optical Resonance and Near Field Effects: Small Particles Under Laser Irradiation," Ph.D. Thesis, Doctor of Philosophy, National University of Singapore, 2005.

[4] E. H. Synge, "A suggested method for extending the microscopic resolution into the ultramicroscopic region," Phil. Mag. 1928, 6, 35 356–362.

[5] D. W. Pohl, W. Denk, and M. Lanz, "Optical stethoscopy: Image recording with resolution λ/20," Appl. Phys. Lett. 1984, 44, 7, 651–653.

[6] N. Fang, Z. Liu, T.-J. Yen, X. Zhang, "Regenerating evanescent waves from a silver superlens," Opt. Express. 2003, 11, 7, 682–687.

[7] S. Durant, Z. Liu, J. M. Steele, X. Zhang, "Theory of the transmission properties of an optical far-field superlens for imaging beyond the diffraction limit," J. Opt. Soc. Am. B 2006, 23, 11, 2383–2392.

[8] Z. Liu, H. Lee, Y. Xiong, C. Sun, X. Zhang, “Far-Field Optical Hyperlens Magnifying Sub-Diffraction-Limited Objects,” Science. 2007, 315, 5189, 1686–1686.

[9] Z. Wang, W. Guo, L. Li, B. Lukyanchuk, A. Khan, Z. Liu, Z. Chen, M. Hong, “Optical virtual imaging at 50 nm lateral resolution with a white-light nanoscope,” Nat. Commun. 2011, 2, 218.

[10] R. B. Penndorf, “An Approximation Method to the Mie Theory for Colloidal Spheres,” J. Phys. Chem. 1958, 62, 12, 1537–1542.

[11] Y. F. Lu, L. Zhang, W. D. Song, Y. W. Zheng, B. S. Luk’yanchuk, “Laser writing of a subwavelength structure on silicon (100) surfaces with particle-enhanced optical irradiation,” J. Exp. Theor. Phys. Lett. 2000, 72, 9, 457–459.

[12] Z. Chen, A. Taflove, and V. Backman, “Photonic nanojet enhancement of backscattering of light by nanoparticles: a potential novel visible-light ultramicroscopy technique,” Opt. Express. 2004, 12, 7, 1214–1220.

[13] J. Bewersdorf, A. Egner, and S. W. Hell, “4Pi-Confocal Microscopy Is coming of Age,” Imaging Microsc. 2004, 24–25.

[14] M. C. Lang, T. Staudt, J. Engelhardt, S. W. Hell, “4Pi microscopy with negligible sidelobes,” New J. Phys. 2008, 10, 043041.

[15] B. Yan, “All-Dielectric Superlens and Applications,” Ph.D. Thesis, Doctor of Philosophy, Bangor University, 2018.

[16] S. Lee, L. Li, Z. Wang, “Optical resonances in microsphere photonic nanojets,” J. Opt. 2014, 16, 015704.

[17] A. Darafsheh, G. F. Walsh, L. D. Negro, V. N. Astratov, “Optical super-resolution by high-index liquid-immersed microspheres Available to Purchase,” Appl. Phys. Lett. 2012, 101, 14, 141128.

[18] L. Li, W. Guo, Y. Yan, S. Lee, T. Wang, “Label-free super-resolution imaging of adenoviruses by submerged microsphere optical nanoscopy,” Light Sci. Appl. 2013, 2, e104.

[19] X. Hao, C. Kuang, X. Liu, H. Zhang, Y. Li, “Microsphere based microscope with optical super-resolution capability,” Appl. Phys. Lett. 2011, 99, 20, 203102.

[20] R. Ye et al., “Experimental imaging properties of immersion microscale spherical lenses,”

Sci. Rep. 2014, 4, 3769.

[21] Z. Wang, “Microsphere super-resolution imaging,” Nanoscience, The Royal Society of Chemistry, United Kingdom, 2016, 3, 193–210.

[22] Y. Yan, L. Li, C. Feng, W. Guo, S. Lee, M. Hong, “Microsphere-coupled scanning laser confocal nanoscope for sub-diffraction-limited imaging at 25 nm lateral resolution in the visible spectrum,” ACS Nano. 2014, 8, 2, 1809–1816.

[23] X. Yang, M Hong, “Enhancement of axial resolution and image contrast of a confocal microscope by a microsphere working in noncontact mode,” Appl. Opt. 2021, 60, 17, 5271–5277.

[24] L.A. Krivitsky, J. J. Wang, Z. Wang, “Luk’Yanchuk, B. Locomotion of microspheres for super-resolution imaging,” Sci. Rep. 2013, 3, 3501.

[25] S. Wang, D. Zhang, H. Zhang, X. Han, R. Xu, “Super-resolution optical microscopy based on scannable cantilever-combined microsphere,” Microsc. Res. Tech. 2015, 78, 12, 1128–1132.

[26] H. Luo, X. Wang, Y. Wen, S. Li, T. Zhang, C. Jiang, F. Wang, L. Liu, H. Yu, “Self-Sensing Scanning Superlens for Three-Dimensional Noninvasive Visible-Light Nanoscale Imaging on Complex Surfaces,” Nano Lett. 2023, 23, 10, 4311–4317.

[27] J. Li, W. Liu, T. Li, I. Rozen, J. Zhao, B. Bahari, B. Kante, J. Wang, “Swimming Microrobot Optical Nanoscopy,” Nano Lett. 2016, 16, 10, 6604–6609.

[28] K. W. Allen, N. Farahi, Y. Li, N. I. Limberopoulos, D. E. Walker, A. M. Urbas, “Super-resolution imaging by arrays of high-index spheres embedded in transparent matrices,” in NAECON 2014 - IEEE National Aerospace and Electronics Conference, Dayton, USA, 2014, 50–52.

[29] M. X. Wu, B. J. Huang, R. Chen, Y. Yang, J. F. Wu, R. Ji, X. D. Chen, M. H. Hong, “Modulation of photonic nanojets generated by microspheres decorated with concentric rings,” Opt. Express, 2015, 23, 15, 20096–20103.

[30] S. M. Mansfield, G. S. Kino, “Solid immersion microscope,” Appl. Phys. Lett. 1990, 57, 24, 2615–2616.

[31] D. R. Mason, M. V. Jouravlev, K. S. Kim, “Enhanced resolution beyond the Abbe diffraction limit with wavelength-scale solid immersion lenses,” Opt. Lett. 2010, 35, 12, 2007–2009.

[32] H. Wang, W.Shi, J. Wang, X. Zhou, P. Li, “Converting evanescent waves into propagating waves by hyper-hemi-microsphere,” Opt. Express, 2024, 32, 14, 25451–25462.

[33] J. Y. Lee, B. H. Hong, W. Y. Kim, S. K. Min, Y. Kim, M. V. Jouravlev, R. Bose, K. S. Kim, I. Hwang, L. J. Kaufman, C. W. Wong, P. Kim, K. S. Kim, “Near-field focusing and magnification through self-assembled nanoscale spherical lenses,” Nature. 2009, 460, 498–501.

[34] D. Kang, C. Pang, S. M. Kim, H. S. Cho, H. S. Um, Y. W. Choi, K. Y. Suh, “Shape-Controllable Microlens Arrays via Direct Transfer of Photocurable Polymer Droplets,” Adv. Mater. 2012, 24, 13, 1709–1715.

[35] A. Vlad, I. Huynen, S. Melinte, “Wavelength-scale lens microscopy via thermal reshaping of colloidal particles,” Nanotechnology. 2012, 23, 285708.

[36] J. Hou, L. Yao, J. Ren, M. Guo, Y. H. Ye, “Magnification and resolution of microlenses with different shapes,” Micro & Nano Lett. 2015, 10, 7, 351–354.

[37] G. Gu, R. Zhou, H. Xu, G. Cai, Z. Cai, “Subsurface nano-imaging with self-assembled spherical cap optical nanoscopy,” 2016, 24, 5, 4937–4948.

[38] W. Fan, B. Yan, Z. Wang, L. Wu, “Three-dimensional all-dielectric metamaterial solid immersion lens for subwavelength imaging at visible frequencie,” Sci. Adv. 2016, 2, e1600901.

[39] H. Zhu, M. Chen, S. Zhou, L. Wu, “Synthesis of High Refractive Index and Shape Controllable Colloidal Polymer Microspheres for Super-Resolution Imaging,” Macromolecules. 2017, 50, 2, 660–665.

[40] W. Wang, B. Yan, H. Wang, Y. Chen, X. Nie, C. Yi, Z. Wang, Z. Xu, J. Zeng, W. Fan, “Wide-Field and Real-Time Super-Resolution Optical Imaging By Titanium Dioxide Nanoparticle-Assembled Solid Immersion Lens,” Small. 2023, 19, 2207596.

[41] G. Wu, Y. Zhou, M. Hong, “Sub-50 nm optical imaging in ambient air with 10× objective lens enabled by hyper-hemi-microsphere,” Light Sci Appl. 2023, 12, 49.

[42] R. Dhama, B. Yan, C. Palego, Z. Wang, “Super-Resolution Imaging by Dielectric Superlenses: TiO2 Metamaterial Superlens versus BaTiO3 Superlens,” Phtonics. 2021, 8, 6, 222.

[43] J. N. Monks, B. Yan, N. Hawkins, F. Vollrath, Z. Wang, “Spider Silk: Mother Nature’s Bio-Superlens,” Nano Lett. 2016, 16, 9, 5842–5845.

[44] Y. Li, X. Liu, B. Li, “Single-cell biomagnifier for optical nanoscopes and nanotweezers,” Light Sci Appl. 2019, 8, 61.

[45] C. Jiang, Y. Yue, B. Yan, T. Dong, X. Cui, P. Chen, Z. Wang, “Label-free non-invasive subwavelength-resolution imaging using yeast cells as biological lenses,” Biomed. Opt. Express. 2021, 12, 11, 7113–7121.

[46] X. Liao, H. Yu, Z. Ge, T. Zhang, Y. Zhong, B. Liu, L. Liu, “Assembly method of biological lens array based on maskless lithography,” Sci Sin Tech. 2023, 53, 4, 536–546.

[47] N. Schuergers, T. Lenn, R. Kampmann, M. V. Meissner, T. Esteves, M. Temerinac-Ott, J. G. Korvink, A. R. Lowe, C. W. Mullineaux, A. Wilde, “Cyanobacteria use micro-optics to sense light direction,” eLife. 2016, 5, e12620.

[48] P. Isola, J. Y. Zhu, T. Zhou, A. A. Efros, “Image-to-Image Translation with Conditional Adversarial Networks,” in IEEE Conference on Computer Vision and Pattern Recognition (CVPR), Honolulu, United States, 2017, 5967–5976. GitHub: https://github.com/phillipi/pix2pix

[49] J. Y. Zhu, T. Park, P. Isola, A. A. Efros, “Unpaired Image-to-Image Translation Using Cycle-Consistent Adversarial Networks,” in IEEE International Conference on Computer Vision (ICCV), Venice, Italy, 2017, 2242–2251.

[50] T. Park, A. A. Efros, R. Zhang, J. Zhu, “Contrastive Learning for Unpaired Image-to-Image Translation,” in European conference on computer vision, Glasgow, United Kingdom, 2020, 319–345.

[51] J. Song, C. Meng, S. Ermon, “Denoising Diffusion Implicit Models,” in The International Conference on Learning Representations (ICLR), online, 2021.

[52] T. Park, “CUT: Contrastive Unpaired Translation,” GitHub: https://github.com/taesungp-/contrastive-unpaired-translation (accessed on 26 Nov 2025).

[53] H, Pan, X. Chen, X, Xia, “A review on the evolvement of optical-frequency filtering in photonic devices in 2016–2021,” Renew. Sustain. Energy Rev. 2022, 161, 112361.

[54] M. F. Silva, T. C. Granado, R. H. Gonnella, J. P. C. Costa, Y. A. O. Assagra, J. H. Correia, “Optical filters for narrow-band imaging on medical devices,” in SBMO/IEEE MTT-S International Microwave and Optoelectronics Conference (IMOC), Aguas de Lindoia, Brazil, 2017.

[55] E. Kallos, G. Palikaras, “Volume manufacturing and industrial applications of metamaterials: Rolling lithography, holography, laser filtering and photovoltaics,” in 11th International Congress on Engineered Materials Platforms for Novel Wave Phenomena (Metamaterials), Marseille, France, 2017.

[56] P. Chang, H. Shi, Z. Wang, J. Miao, T. Shi, H. Guo, “Cesium Faraday Optical Filter for Wireless Optical Communication System,” in 13th International Conference on Wireless Communications and Signal Processing (WCSP), Changsha, China, 2021.

[57] L. Frey, L. Masarotto, M. Armand, M. L. Charles, O. Lartigue, “Multispectral interference filter arrays with compensation of angular dependence or extended spectral range,” Opt. Express. 2015, 23, 9, 11799–11812.

[58] X. Luo, F. Zhang, M. Pu, Y. Guo, X. Li, X. Ma, “Recent advances of wide-angle metalenses: principle, design, and applications,” Nanophotonics. 2022, 11, 1, 1–20.

[59] H. Macleod, “Thin-Film Optical Filters (fourth ed.),” CRC Press, 2010, Boca Raton, United States, 299–401.

[60] J. N. Monks, J. Williams, A. Hurst, Z. Wang, “Shift-free fixed-line laser protection filter technology,” in Technologies for Optical Countermeasures XVII; and High-Power Lasers: Technology and Systems, Platforms, Effects IV, Online, 2020, 1153908

[61] J. Park, Y. Park, J. Park, “Synthesis and Physical Property Measurement of New Red Pigment based on Anthraquinone Derivatives for Color Filter Pigments,” Mol. Cryst. Liq. Cryst. 2011, 551, 1, 116–122.

[62] C. Sakong, Y. D. Kim, J. H. Choi, C. Yoon, J. P. Kim, “The synthesis of thermally-stable red dyes for LCD color filters and analysis of their aggregation and spectral properties,” Dyes Pigm. 2011, 88, 2, 166–173.

[63] H. Shin, M. F. Yanik, Shanhui Fan, R Zia, M. L. Brongersma, “Omnidirectional resonance in a metal–dielectric–metal geometry,” Appl. Phys. Lett. 2004, 84, 22, 4421–4423.

[64] K. T. Lee S. Seo, J. Y. Lee, L. J. Guo, “Ultrathin metal-semiconductor-metal resonator for angle invariant visible band transmission filters,” Appl. Phys. Lett. 2014, 104, 23, 231112.

[65] K. Mao, W. Shen, C. Yang, X. Fang, W. Yuan, Y. Zhang, X. Liu, “Angle Insensitive Color Filters in Transmission Covering the Visible Region,” Sci Rep. 2016, 6, 19289.

[66] K. T. Lee, S. Seo, L. J. Guo, “High-Color-Purity Subtractive Color Filters with a Wide Viewing Angle Based on Plasmonic Perfect Absorbers,” Adv. Opt. Mater. 2015, 3, 3, 347–352.

[67] D. Kim, H. Kim, I. Jung, T. Y. Kim, H. Kwak, J. H. Jung, C. K. Hwangbo, H. J. Park, K. T. Lee, “Manipulation of resonance orders and absorbing materials for structural colors in transmission with improved color purity,” Opt. Express. 2022 30, 7, 11740–11753.

[68] O. A. M. Abdelraouf, X. C. Wang, C. H. G. Ken, C. B. L. Nelson, S. K. Ng, W. D. Wang, X. R. Wang, Q. J. Wang, H. Liu, “All-Optical Switching of Structural Color with a Fabry–Pérot Cavity,” Adv. Photonics Res. 2023, 4, 11, 2300209.

[69] Z. Li, S. Butun, and K. Aydin, “Large-area, Lithography-free super absorbers and color filters at visible frequencies using ultrathin metallic films,” ACS Photonics. 2015, 2, 2, 183–18.

[70] M. A. Kats, S. J. Byrnes, R. Blanchard, M. Kolle, P. Genevet, J. Aizenberg, F. Capasso, “Enhancement of absorption and color contrast in ultra-thin highly absorbing optical Coatings,” Appl. Phys. Lett. 2013, 103, 10, 101104.

[71] S. Cao, N. Chen, Y. Jiang, “Angle insensitive filters based on Fabry–Pérot resonance structures,” J. Appl. Phys. 2024, 136, 19, 193102.

[72] J. X. Liu, L. H. Meng, K. D. Gu, L. Xia, W. C. Tang, H. W. Yang, “Design and Numerical Simulation of a Bandpass Filter Nano-film,” Chin. J. Phys. 2021, 69, 230–239.

[73] Y. J. Jen, C. C. Lee, K. H. Lu, C. Y. Jheng, Y. J. Chen, “Fabry-Perot based metal-dielectric multilayered filters and metamaterials,” Opt. Express. 2015, 23, 26, 33008–33017.

[74] Y. J. Jen, M. J. Lin, “Design and Fabrication of a Narrow Bandpass Filter with Low Dependence on Angle of Incidence,” Coatings. 2018, 8, 7, 231.

[75] J. L. Zhang, W. D. Shen, P. Gu, Y. G. Zhang, H. T. Jiang, X. Liu, “Omnidirectional narrow bandpass filter based on metal-dielectric thin films,” Appl. Opt. 2008, 47, 33, 6285–6290.

[76] P. Ji, C. S. Park, S. Gao, S. S. Lee, D. Y. Choi, “Angle-tolerant linear variable color filter based on a tapered etalon,” Opt. Express. 2017, 25, 23, 2153–2161.

[77] C. Song, Y. Feng, Z. Bao, G. Liu, J. Wang, “Angle-Insensitive Color Filters Based on Multilayer Ultrathin-Film Structures,” Plasmonic. 2020, 15, 255–261.

[78] X. Lv, B. Zhong, Y. Huang, Z. Xing, H. Wang, W. Guo, X. Chang, Z. Zhang, “Research Progress in Preparation and Application of Photonic Crystals,” Chin. J. Mech. Eng. 2023, 36, 39.

[79] S. John, “Strong localization of photons in certain disordered dielectric superlattices,” Phys. Rev. Lett. 1987, 58, 2486.

[80] J. D. Joannopoulos, R. D. Meade, S. G. Johnson, J. N. Winn, “Photonic Crystals: Molding the Flow of Light (second ed.),” Princeton University Press, 2011, United States, 46.

[81] C. H. Chen, K. Tetz, W. Nakagawa, Y. Fainman, “Wide-field-of-view GaAs/AlxOy one-dimensional photonic crystal filter,” Appl. Opt. 2005, 44, 8, 1503–1511.

[82] X. F. Xu, J. Y. Ding, “A wide band-pass filter of broad angle incidence based on one-dimensional metallo-dielectric ternary photonic crystal,” Opt. Quant. Electron. 2009, 41, 1027–1032.

[83] K. T. Lee, C. Ji, D. Banerjee, L. J. Guo, “Angular- and polarization-independent structural colors based on 1D photonic crystals,” Laser & Photonics. Rev. 2015, 9, 3, 354–362.

[84] C. Ji, C. Yang, W. Shen, K. Lee, Y. Zhang, X. Liu, L. J. Guo, “Decorative near-infrared transmission filters featuring high-efficiency and angular-insensitivity employing 1D photonic crystals. Nano Res. 2019, 12, 543–548.

[85] Yoshiaki Kanamori, Toshikazu Ozaki, and Kazuhiro Hane, "Reflection color filters of the three primary colors with wide viewing angles using common-thickness silicon subwavelength gratings,” Opt. Express. 2014, 22, 21, 25663–25672.

[86] H. J. Choi, S. Choi, Y. E. Yoo, E. Jeon, Y. Yi, S. Park, D. S. Choi, H. Kim, “Transmission-type photonic crystal structures for color filters,” Opt. Express. 2013, 21, 15, 18317–18324.

[87] Y. Liu, X. Zhang, “Metamaterials: a new frontier of science and technology”, Chem. Soc. Rev. 2011, 40, 5, 2494.

[88] A. Poddubny, I. Iorsh, P. Belov, and Y. Kivshar, Nat. Photonics. 2013, 7, 948.

[89] Q. Wei, D. Bi, X. Qi, M. Ren, F. Wu, “Angle-independent topological interface states in one-dimensional photonic crystal heterostructures containing hyperbolic metamaterials,” Opt. Lett. 2025, 50, 2, 451–454.

[90] Z. Guo, H. Jiang, H. Chen, “Hyperbolic metamaterials: From dispersion manipulation to applications,” J. Appl. Phys. 2020, 127, 7, 071101.

[91] F. Wu, G. Lu, C. Xue, H. Jiang, Z. Guo, M. Zheng, C. Chen, G. Du, H. Chen, “Experimental demonstration of angle-independent gaps in one-dimensional photonic crystals containing layered hyperbolic metamaterials and dielectrics at visible wavelengths,” Appl. Phys. Lett. 2018, 112, 4, 041902.

[92] C. Xue, Y. Ding, H. Jiang, Y. Li, Z. Wang, Y. Zhang, H. Chen, “Dispersionless gaps and cavity modes in photonic crystals containing hyperbolic metamaterials,” Phys. Rev. B 2016, 93, 125310.

[93] B. M. Wells, F. Lotti, M. E. Nasir, A. V. Zayats, V. A. Podolskiy, “Angle-insensitive plasmonic nanorod metamaterial-based band-pass optical filters,” Opt. Express. 2021, 29, 8, 11562–11569.

[94] D. V. Labeke, D. Gérard, B. Guizal, F. I. Baida, L. Li, “An angle-independent Frequency Selective Surface in the optical range,” Opt. Express. 2006, 14, 25, 11945–11951.

[95] Z. Tan, K. McDonald, “Babinet’s principle for electromagnetic fields,” Joseph Henry Laboratories, 2012, Princeton University, Princeton, NJ.

[96] R. Rumpf, “21st Century Electromagnetics. Lecture 7a - FSS and Metasurfaces,” 2019, Texas, United States.

[97] F. Lotti, A. Mirzaei, P. Wang, A.E. Miroshnichenko, A.V. Zayats, “Nanoparticle-based metasurfaces for angular-independent spectral filtering applications,” J. Appl. Phys. 2019, 126, 213101.

[98] M. Ye, L. Sun, X. Hu, B. Shi, B. Zeng, L. Wang, J. Zhao, S. Yang, R. Tai, H. J. Fecht, Jian. Jiang, D. Zhang, “Angle-insensitive plasmonic color filters with randomly distributed silver nanodisks,” Opt. Lett. 2015, 40, 21, 4979–4982.

[99] O. Nicoletti, F. D. L. Peña, R. K. Leary, D. J. Holland, C. Ducati, P. A. Midgley, "Three-dimensional imaging of localized surface plasmon resonances of metal nanoparticles," Nature. 2013, 502, 80–84.

[100] P. K. Jain, M. A. El-Sayed, "Universal scaling of plasmon coupling in metal nanostructures: extension from particle pairs to nanoshells," Nano Lett. 2007, 7, 9, 2854–2858.

[101] V. Amendola, R. Pilot, M. Frasconi, O. M. Maragò, M. A. Iatì, "Surface plasmon resonance in gold nanoparticles: a review," J. Phys.: Condens. Matter. 2017, 29, 203002.

[102] M. G. Blaber, M. D. Arnold, M. J. Ford, "A review of the optical properties of alloys and intermetallics for plasmonics," J. Phys.: Condens. Matter, 2010, 22, 143201.

[103] M. D. Arnold, M. G. Blaber, "Optical performance and metallic absorption in nanoplasmonic systems," Opt. Express. 2009, 17, 5, 3835–3847.

[104] V. Amendola, S. Scaramuzza, A. Agnoli, S. Polizzi, M. Meneghetti, "Strong dependence of surface plasmon resonance and surface enhanced Raman scattering on the composition of Au–Fe nanoalloys," Nanoscale. 2014, 6, 3, 1423–1433.

[105] J. N. Monks, L. Yue, B. Yan, B. Aldred, A. Hurst, Z. Wang, "A wide-angle shift-free metamaterial filter design for anti-laser striking application," Opt. Commun. 2018, 429, 53–59.

[106] M. J. Mendes, A. Araújo, A. Vicente, H. Águas, I. Ferreira, E. Fortunato, R. Martins, "Design of optimized wave-optical spheroidal nanostructures for photonic-enhanced solar cells," Nano Energy. 2016, 26, 286–296.

[107] P. Shokeen, A. Jain, A. Kapoor, "Silicon nanospheres for directional scattering in thin-film solar cells," J. Nanophotonics. 2016, 10, 3, 036013.

[108] M. A. Shameli, S. R. Mirnaziry, L. Yousefi, "Distributed silicon nanoparticles: an efficient light trapping platform toward ultrathin-film photovoltaics," Opt. Express. 2021, 29, 8, 28037–28053.

[109] A. Taflove, S. C. Hagness, "Computational electrodynamics: the finite-difference time domain method (Third ed.)," Artech House, 2005, Boston, United Kingdom.

[110] T. Weiland, "A discretization method for the solution of Maxwell's equations for six-component fields," AEÜ – Int. J. Electron. Commun. 1977, 31, 3, 116–120.

[111] CST Studio Suite 2024, Dassault Systèmes, Germany. Available: https://www.3ds.com/products-services/simulia/products/cst-studio-suite/ (accessed on 26 Nov 2025)

[112] H. Macleod, "Thin-Film Optical Filters (fourth ed.)," CRC Press, 2010, Boca Raton, United States, 44–49.

Chapter 3 Methodology

3.1 Introduction

This chapter outlines the theoretical, numerical, and experimental methodologies employed to investigate the optical response of micro- and nanostructured spherical systems.
The work integrates three complementary computational tools and corresponding experimental procedures:

1. xMie, an analytical solver based on Mie theory, to model electromagnetic field distributions of individual spheres.
2. CST Studio Suite, a numerical simulator employing the finite-integration technique (FIT), for analysing complex particle assemblies and metamaterial structures.
Together, these two tools provide complementary analytical and numerical approaches, enabling cross-validation of simulation results and ensuring the reliability of the modelling framework.
3. Essential Macleod (ESM), a thin-film design software based on the transfer-matrix method (TMM), for optimising multilayer and anti-reflection coatings.

The theoretical and numerical sections are followed by descriptions of the experimental fabrication of TiO_2-based microsphere superlenses (mSILs) and the preparation of biological samples used for imaging validation.

Together, these methods establish a rigorous framework for correlating analytical predictions, numerical simulations, and experimental verification presented in later chapters.

3.2 Theoretical and Numerical Simulation Framework

3.3.1 Analytical modelling: xMie

xMie is a simulation software developed by Prof Zengbo Wang and Prof Boris Luk'yanchuk based on the analytical solution of Mie theory. It is designed to model the electromagnetic field distribution both inside and outside a single microsphere situated in a homogeneous medium and illuminated by a uniform light source. By analytically solving Maxwell's equations for spherical particles, xMie enables accurate simulations of scattering and near-field enhancement, particularly the PNJ effect. The software features a MATLAB-based graphical user interface, allowing users to define the diameter and refractive index of the particle, and wavelength of incident wave, to visualise electric field intensity distributions.

With its high computational efficiency and visual output capabilities, xMie serves as a fundamental tool for verifying the optical response of spherical structures and lays the theoretical foundation for more advanced numerical simulations introduced later in this chapter.

3.2.2 Numerical Modelling: CST Studio Suite

CST Studio Suite (Frequency-Domain Solver) is a commercial electromagnetic modelling package based on the Finite Integration Technique (FIT). It numerically solves Maxwell's equations in the frequency domain, enabling precise computation of near-field and far-field optical responses of complex 3D geometries. In this project, CST was employed to:

- simulate scattering and field enhancement of TiO_2 microspheres formed by self-assembly; and
- evaluate transmission spectra of periodic silicon-nanosphere (SiNS) arrays used in wide-angle metamaterial filters.

The frequency-domain solver provides high spectral resolution suitable for studying resonant and angular-dependent phenomena. Triangular or tetrahedral meshes were refined near curved interfaces, and *unit-cell* boundary conditions were applied to minimise artefacts and ensure numerical accuracy.

3.2.3 Validation of Simulation Methods (xMie vs CST)

Before applying CST to complex non-analytical systems, its accuracy was verified against the analytical xMie model using a benchmark SiNS in vacuum.

1. Near-field Validation

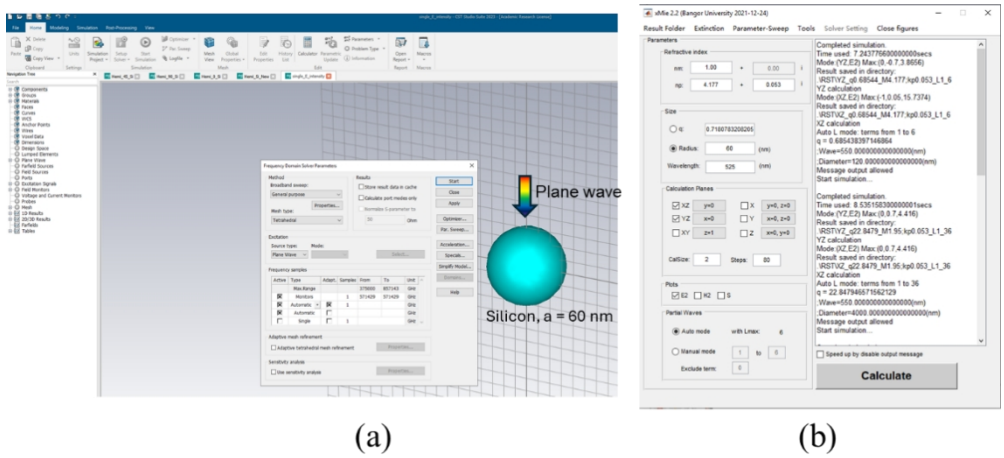

Figure 3.1 (a) Schematic illustration of a SiNS built in CST STUDIO and with frequency domain solver and (b) setting interface of xMie.

To validate the near-field results obtained from two different simulation tools, a SiNS with a radius of r = 60 nm was independently modelled in two software and illuminated by a plane wave with a wavelength of 525 nm. As illustrated in Fig. 3.1 (a), the SiNS was placed in vacuum and enclosed with an open boundary to perform a perfectly matched layer (PML). The local mesh size within the SiNS was refined to r/5 to ensure numerical accuracy. For the analytical solution obtained from xMie, all physical and optical parameters were manually configured, as shown in Fig. 3.1 (b).

The contour plots of the electric field intensity, computed as the squared magnitude of the electric field $|E|^2$, are presented in Fig. 3.2 (a) and (b). These plots exhibit a high degree of visual similarity, indicating strong qualitative agreement. To provide a more quantitative comparison, a one-dimensional field intensity profile along the x-axis passing through the centre of the sphere is shown in Fig. 3.2 (c). This line plot demonstrates that the analytical and numerical results are in close agreement, as further confirmed by a normalised mean squared error (NMSE) of 0.0021.

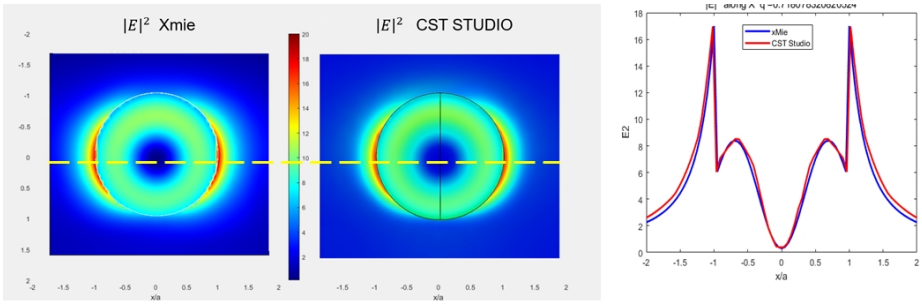

Figure 3.2 Electric field intensity of a SiNS with a = 60 nm and illuminated by a plane wave with 525 nm wavelength obtained from (a) xMie and (b) CST STUDIO, respectively. (c) 1D line plot across SiNS centre highlighted in yellow dash line.

2. Far-field validation

The far-field patterns obtained through two simulation methods were also quantitatively compared in Fig. 3.3, the normalised extinction factor (Q_{ext}), absorption factor (Q_{abs}) and scattering (Q_{sca}) of single SiNS illuminated by plane wave with wavelength ranging from 400 nm to 800 nm were calculated and plotted in Fig. 3.3. This consistency is further supported by the NMSE of 0.0068, 0.0185 and 0.0053 for Q_{ext}, Q_{abs} and Q_{sca} comparisons, respectively, indicating a high level of accuracy and reliability between the analytical and numerical methods.

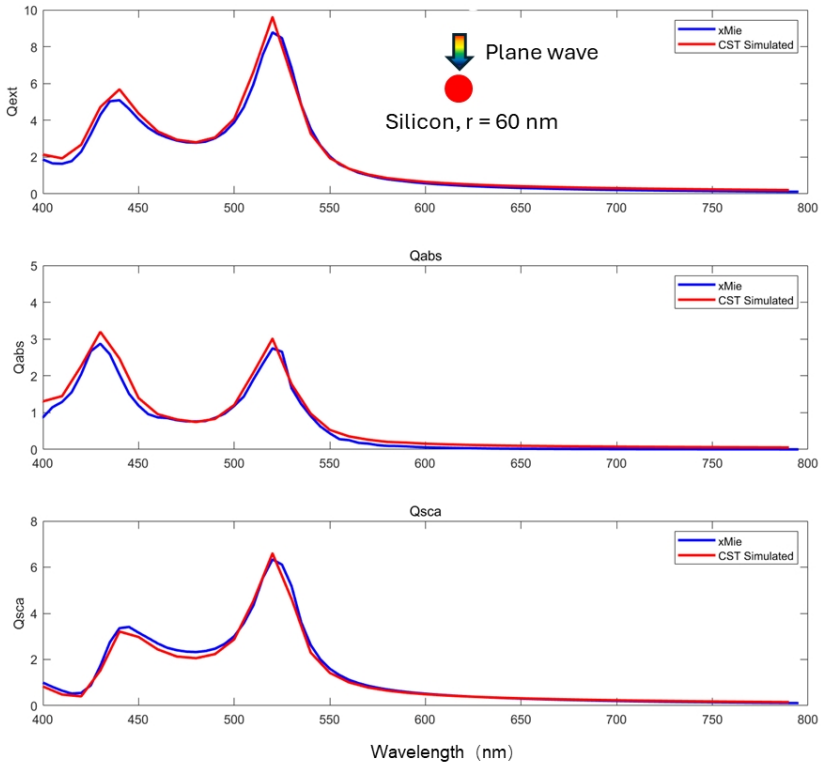

Figure 3.3 The comparison of Q_{ext}, Q_{abs}, and Q_{sca} of a single SiNS under plane wave illumination (400–800 nm), calculated by xMie and CST STUDIO. Top, middle, and bottom panels show Q_{ext}, Q_{abs}, and Q_{sca}, respectively, with NMSE values of 0.0068, 0.0185, and 0.0053.

In summary, both near-field and far-field simulations show excellent agreement, establishing CST Studio Suite as a reliable numerical framework for modelling subwavelength spherical structures. The following sections employ CST to investigate more complex assemblies—nanoparticle-based superlenses and wide-angle metamaterial filters—that lie beyond the scope of analytical models.

3.3 Modelling of Complex Optical Structures

3.3.1 TiO_2 Nanoparticle-Based Superlenses (mSILs)

Three-dimensional dielectric microsphere superlenses (mSILs) made from TiO_2 nanoparticles were modelled in CST Studio to interpret their experimentally observed super-resolution imaging.

The simulation included full-spherical, super-hemispherical, and hemispherical geometries (Fig. 3.4). Due to the complexity of these nanoparticle-based superlenses, each consisting of millions of 20 nm nanoparticles, it is practically infeasible to model such structures exactly by drawing every nanoparticle. Therefore, a simplified two-region model was implemented in CST:

- **Upper region:** treated as a homogeneous medium (n = 1.92), representing an effective medium with approximately 61.3 % nanoparticle filling (TiO_2, n = 2.55) [6].
- **Lower region:** composed of 20 layers of hexagonally close-packed TiO_2 nanoparticles to preserve realistic penetration effects on patterned substrates (IC chip with 60 nm features). Both penetration and non-penetration cases were analysed.

To further reduce computational demand, the 3D spherical structure was simplified into a two-dimensional cylindrical model. In this model, a z-polarised electric dipole source, oriented perpendicular to the simulation plane, was placed near the bottom of the nanoparticle lens to analyse how the mSILs — with or without the penetration effect (as shown in the right and left columns of Fig. 3.4) — collects dipole radiation, including both propagating and evanescent wave components, and directs them into the far field. The model was discretised using tetrahedral meshes with a density of λ/4, where λ is the wavelength of the incident light. This meshing strategy ensures sufficient resolution to capture fine-scale near-field interactions within the nanoparticle composite.

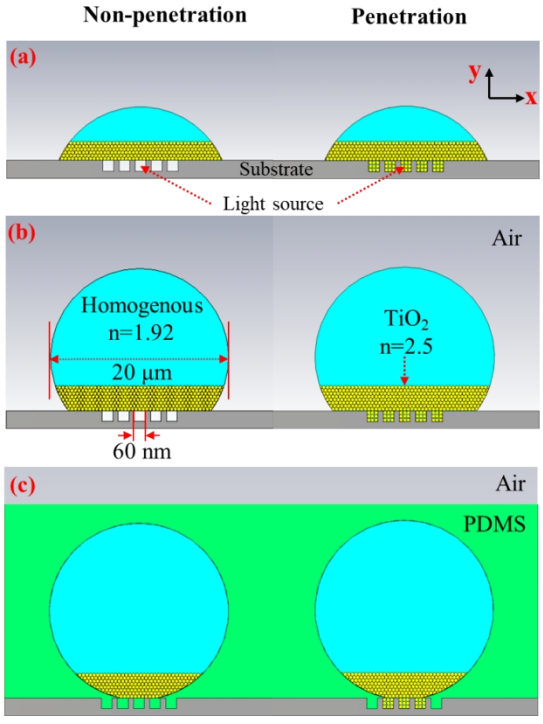

Figure 3.4 Schematic representation of the simulation configurations for (a) hemi-spherical, (b) super-hemispherical, and (c) full-spherical mSILs, with and without the nanoparticle penetration effect. Each structure consists of an upper homogeneous region and a lower region composed of 20 layers of hexagonally close-packed TiO_2 nanoparticles.

As illustrated in Fig. 3.4 (a–c), three variants of mSILs with height-to-width ratios of 0.3, 0.8, and 1.0 were constructed with a diameter of 20 μm, incorporating both non-penetration (left) and penetration (right) scenarios. The PDMS (n = 1.4) used as the host medium for full-spherical mSIL is represented in green and fills the nanoscale gaps when the penetration effect is not considered. To simulate the experimentally observed partial penetration in full-spherical mSILs, only three nanoscale gaps were filled with TiO_2 nanoparticles, while the remaining gaps were filled with PDMS. For super-hemi and sub-hemi mSIL geometries, all nanoscale gaps were either filled with air or TiO_2 nanoparticles, while all other parameters remained unchanged.

This configuration allows analysis of how evanescent waves generated in the near field are converted into propagating waves in the far field. The differences in optical responses between the two penetration scenarios, as well as among the three mSIL variants, are crucial for explaining their distinct imaging capabilities.

3.3.2 Wide-Angle Metamaterial Filters

To exploit the strong extinction and high symmetry of SiNS arrays, CST Studio Suite was employed to design and optimise wide-incidence-angle optical metamaterial filters. Both randomly distributed and periodically arranged SiNS arrays exhibit pronounced extinction and wavelength-selective scattering, making them ideal for developing wide-angle optical filters. In this study, periodic arrays were chosen to achieve angle-insensitive transmission performance suitable for practical filtering applications.

A unit-cell model with periodic boundary conditions was constructed to represent an infinite two-dimensional cubic lattice array. Each unit cell consisted of a single SiNS of radius R embedded in a silicon-nitride (SiN) host medium, placed on a semi-infinite glass substrate. The bottom of the SiN layer was directly connected to an output port to minimise internal reflections and ensure accurate evaluation of the transmission spectrum. The array was illuminated by a linearly polarised plane wave within the wavelength range of 350 –1200 nm, under both normal and oblique incidence for TE and TM polarisations. Mesh densities of $\lambda/10$ in the host medium and $R/5$ within the SiNS ensured numerical accuracy and stability. The frequency-domain solver of CST provided high spectral resolution for analysing steady-state resonances and angular-dependent behaviour.

Two representative configurations were investigated:

- Edge filter: it composed of a SiNS array with radius R = 60 nm and periodicity $P = 2R$ + 25 nm
- Band-pass filter: it based on a core–shell SiNS–Au array with silicon-core radius R = 70 nm, gold-shell thickness T = 20 nm, and periodicity $P = 2\ (R + T) + 40$ nm. These parameter sets were chosen to maintain a consistent spacing between adjacent nanospheres, ensuring controlled optical coupling and spectral selectivity. For the core–shell configuration, the inclusion of the metallic (Au) shell introduces localised surface plasmon resonances (LSPRs) that shape the spectral band-pass response, while the dielectric SiNS lattice contributes angular robustness through Mie-type scattering.

Simulations were conducted to evaluate transmission, reflection, and absorption spectra as a function of wavelength and angle of incidence. The far-field results provided insights into the spectral position of the pass and stop bands, as well as the angular tolerance of each filter design. These findings formed the computational foundation for the subsequent thin-film optimisation using ESM, where multilayer thicknesses and admittance matching were further refined to enhance wide-angle transmission performance.

3.3.3 SEM-to-Optical Image Translation Based on Contrastive Learning

In this study, a SinCUT model based on contrastive learning was used to translate SEM images into optical images. This approach allows us to estimate how the mSIL would image different areas of chip surface even though the lens cannot be physically moved after fabrication. The model learns a cross-modal relationship from a single pair of SEM and optical images obtained from the same location on the sample.

(a) SEM Image Pre-processing

To enable meaningful SEM-to-optical translation using the SinCUT model, the SEM image was pre-processed so that its appearance more closely matches the statistical properties of optical mSIL images while preserving nanoscale geometry. Before filtering, both the SEM and optical images were resized to 256 × 256 pixels and coarsely aligned. Coarse alignment is sufficient because precise pixel-level matching is extremely difficult to achieve manually due to differences in magnification, distortion, and illumination. SinCUT operates on local patch statistics rather than fixed spatial correspondences, making coarse alignment adequate.

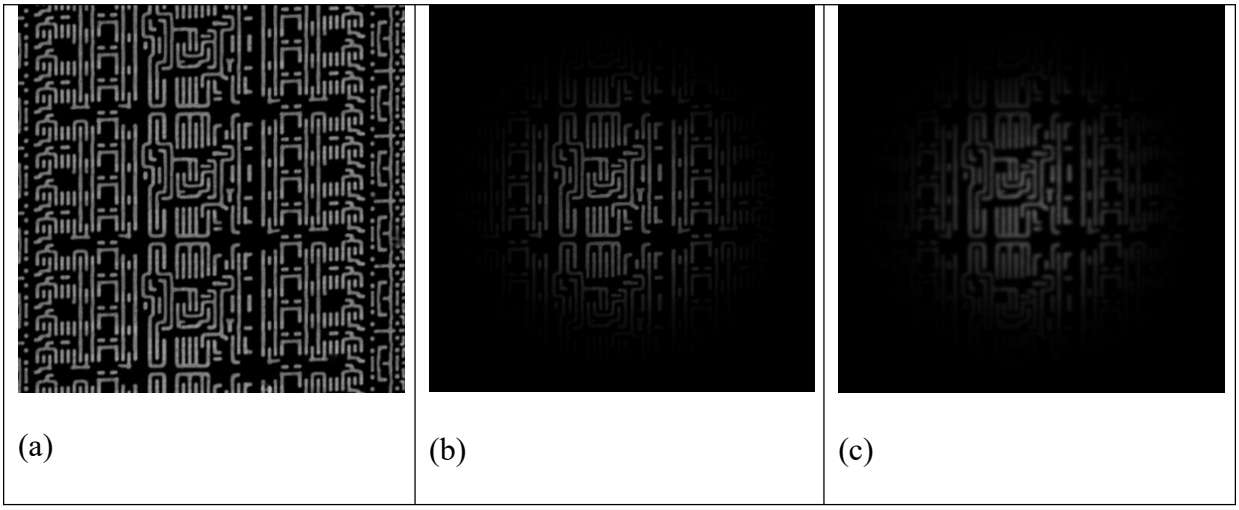

Figure 3.5. SEM pre-processing steps for SinCUT training: (a) Original SEM image, (b) SEM image after applying the vignetting mask, (c) Final SEM image after vignetting and Gaussian blurring, used as the SinCUT input.

To emulate the bright-centre and dim-edge illumination pattern typical of mSIL optical images, a radial vignetting mask was applied. For each pixel at (x, y) relative to the image centre (x_c, y_c), the Euclidean distance:

$$d(x, y) = \sqrt{(x - x_C)^2 + (y - y_C)^2} \tag{3.3.1}$$

was computed and normalised using:

$$r(x, y) = d(x, y)/d_{max} \tag{3.3.2}$$

where d_{max} is maximum radial distance.

A linear attenuation profile was then applied,

$$M_{vig}(x, y) = 1 - \alpha r(x, y) \tag{3.3.3}$$

where α controls the strength of the vignetting.

Optical mSIL images also contain reduced high-frequency detail compared with SEM images. To mimic this behaviour, the vignetted SEM image was smoothed using a Gaussian kernel

$$G(x, y) = \frac{1}{2\pi\sigma^2} exp[-\frac{x^2+y^2}{2\sigma^2}] \tag{3.3.4}$$

and convolved to produce blurred image (I_{blur}) from vignetted image (I_{Vig}):

$$I_{blur} = I_{vig} * G \tag{3.3.5}$$

This filtering preserves the sample geometry while producing an optical-like texture. The resulting pre-processed SEM image was used as the SEM-domain input for SinCUT training. Fig. 3.5 illustrates the full transformation pipeline.

(b) Model Training

Training was performed on a single SEM–optical pair resized to 256 × 256 pixels. To manage GPU memory and enhance robustness, the SinCUT model was trained using randomly sampled 128 × 128 crops extracted from the aligned pair during each iteration. This cropping procedure acts as natural data augmentation and ensures that the learned translation does not depend on a fixed spatial offset or magnification. Random scaling was also applied to increase the diversity of training samples.

All training parameters follow the default SinCUT configuration. The model was trained for 16 epochs with a batch size of one and a learning rate of 0.002. All experiments were conducted on an NVIDIA RTX A4000 GPU with 16 GB of memory. This setup yielded stable convergence and produced the cross-modal translation results presented.

3.4 Thin-Film Design and Optimisation

3.4.1 Optimisation via Essential Macleod

Following CST simulations, multilayer performance was refined using ESM, a thin-film design tool based on the Transfer-Matrix Method (TMM)**.** The optimisation aimed to improve angular performance, transmission efficiency, and reflection suppression by adjusting layer thicknesses and adding anti-reflection coatings (ARCs) or dielectric multilayers.

For the edge filter, which consists of three SiNS-based metamaterial layers, the simulated results already showed a well-defined and angle-independent blocking band. However, a reduction in transmission was observed at large angles of incidence for both TE and TM polarisations in the near-infrared region. This reduction was mainly attributed to admittance mismatch between the multilayer structure and air. To overcome this issue, an ARC layer with an intermediate refractive index was introduced. By fine-tuning the ARC thickness in ESM, the overall optical admittance was better matched to air, resulting in higher transmission at oblique angles while maintaining strong rejection in the stop band.

For the band-pass filter, the optimisation process incorporated a one-dimensional photonic-crystal (1D PhC) stack beneath the metamaterial layer. The 1D PhC acted as an angularly robust edge filter that complemented the localised surface plasmon resonance (LSPR) effect from the Au shell in the core–shell SiNS array. This configuration effectively suppressed side

lobes near the pass-band edge and enhanced both spectral selectivity and angular tolerance. To achieve this, the combined optical admittance of the meta-layer and 1D-PhC stack was tuned to match that of air as closely as possible.

The theoretical background of the TMM used in ESM is described in Chapter 2. In this study, the method was implemented to calculate reflection and transmission spectra for multilayer systems over a broad wavelength and angular range. Built-in optimisation algorithms, such as gradient and needle methods, were employed to refine layer thicknesses and refractive indices until the desired spectral performance was achieved.

In summary, ESM provided an efficient and accurate approach for refining multilayer parameters derived from CST simulations. The optimised designs exhibited improved transmission, enhanced angular robustness, and reduced reflection losses, bridging the numerical modelling and practical implementation of metamaterial-based optical filters.

3.4.2 Extraction of Effective Refractive Index of Meta-Layers

Although ESM is highly suitable for thin-film optimisation, it assumes that all layers in the multilayer stack are homogeneous and isotropic. When the design incorporates meta-layers composed of subwavelength periodic structures, such as SiNS arrays, this assumption no longer holds. The optical response of such structures arises from complex near-field coupling and collective scattering effects, and therefore an equivalent or effective refractive index must first be extracted before meaningful modelling can be performed in ESM.

Two approaches were examined in this study to determine the effective refractive index of meta-layers: the Bruggeman Effective Medium Approximation (BEMA) and the Kramers–Kronig (K–K) dispersion relation.

BEMA: The Bruggeman effective medium model is one of the most widely used analytical approximations for estimating the dielectric properties of a mixture composed of two or more phases. It treats the system as a random isotropic mixture and averages the permittivity of different components according to their volume fractions. For a two-component composite, the effective permittivity ε_{eff} is defined by.

$$f\frac{\varepsilon_1 - \varepsilon_{eff}}{\varepsilon_1 + 2\varepsilon_{eff}} + (1-f)\frac{\varepsilon_2 - \varepsilon_{eff}}{\varepsilon_2 + 2\varepsilon_{eff}} = 0 \qquad (3.4.1)$$

where ε_1 and ε_2 denote permittivity of two materials, respectively. f is filling factor of material.

The BEMA model provides reasonable estimates for mixtures of randomly distributed, isotropic inclusions such as spherical nanoparticles embedded in a host medium. However,

for meta-layers exhibiting periodicity, strong electromagnetic coupling, or anisotropic arrangements, this model often fails to capture key near-field effects and directional propagation characteristics. Consequently, BEMA tends to oversimplify the optical behaviour and may significantly underestimate the real part of the refractive index.

To obtain a more accurate description of the optical response for such engineered metamaterials, the Kramers–Kronig (K–K) dispersion relation was employed. The K–K method provides a rigorous mathematical relationship between the real and imaginary parts of a complex refractive index. By knowing the absorption spectrum (the imaginary component k(ω)) across a sufficiently broad frequency range, the real part n(ω′) can be determined by

$$n(\omega') = n_{host} + \frac{2}{\pi} P \int_0^{\infty} \frac{\omega k(\omega)}{\omega^2 - \omega'^2} d\omega \tag{3.4.2}$$

Here, n_{host} is the refractive index of the host medium. The integral in Equation (3.4.2) is evaluated using the Hilbert transform method, where P indicates the Cauchy principal value, ensuring the integral remains well-defined by symmetrically excluding the singularity at $\omega=\omega'$.

The imaginary part (k) can be determined from simulated transmission (T) and reflection (R) data as detailed in [3, 4].

$$\frac{1-R}{T} = exp\,(4\pi kd/\lambda) \tag{3.4.3}$$

where d is the meta-layer thickness.

Fig. 3.6 presents the transmission spectra calculated by CST, the Bruggeman approximation, and the K–K model, respectively. The curve derived from the Bruggeman approximation demonstrates a mismatch of the $\lambda_{Cut\text{-}on}$ (defined as the wavelength where T equals 0.5Tpeak) when compared to the results from the CST and those indirectly obtained from the K–K model. The Bruggeman approximation, as described in Equation (3.4.1), is thus not suitable for this study, due to its failure to account for the strong near-field interplay between adjacent particles.

In contrast, the transmission spectrum derived using the refractive index obtained from the K–K method shows good agreement with the CST results, particularly in the short-

wavelength bands and at the edge wavelength. The mean-square error (MSE) between the K–K model and the CST simulation was found to be 0.00053, approximately one order of magnitude smaller than that of the Bruggeman approximation (0.00692). Although minor discrepancies are still observed at longer wavelengths, the K–K approach successfully reproduces the key physical characteristics of the system, especially around the resonance region.

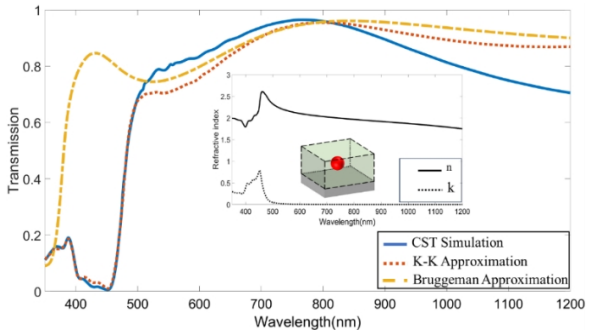

Figure 3.6 Comparison of transmission spectra of metafilm consisting of periodic arranged SiNS calculated by CST, the Bruggeman model, and the K–K model, respectively. The inset shows a unit cell of the meta-layer.

This analysis confirms that while the Bruggeman model provides a simple first-order estimate, it is insufficient for accurately modelling the optical properties of periodic metamaterial layers where inter-particle interactions dominate. The Kramers–Kronig method, being data-driven and physically rigorous, offers a much more reliable extraction of the effective refractive index for such nanostructured systems.

3.5 Experimental Methodology

3.5.1 Fabrication of TiO_2-Based mSILs

A low-cost, scalable bottom-up nano–solid–fluid assembly (NSFA) technique was employed in this work. This method relies on the combined effects of gravity and oil–water interfacial tension to drive the spontaneous formation of dielectric microsphere structures.

Fig. 3.7 illustrates the fabrication process. In this work, anatase-phase TiO_2 nanoparticles with an average diameter of 20 nm and a refractive index of 2.5 (XuanChengJingRui New Material Co., Ltd., China) were used. Building on our previously reported method, we introduced a three-step centrifugation process to further remove oversized and irregular particles. Specifically, aqueous suspensions were centrifuged (Avanti J-E centrifuge, Beckman Coulter) sequentially at 17,500 RPM, 20,000 RPM, and 21,000 RPM for 20

minutes, 20 minutes, and 90 minutes at 10 °C, respectively. The precipitates collected after the first and second centrifugation steps, however, the supernatant, which contained uneven nanoparticles and impurities, were discarded. Following the third centrifugation, the supernatant was carefully removed to avoid diluting the tightly packed nanoparticle precipitate at the bottom of the tube.

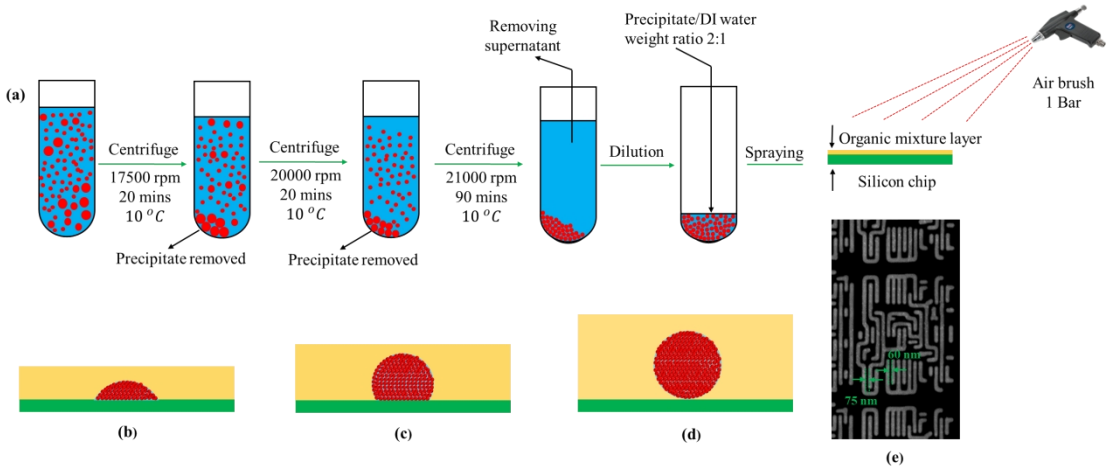

Figure 3.7 Schematic illustration of the fabrication procedure for TiO_2 nanoparticle-based mSILs (a), and the dependence of mSIL geometry on the thickness of the organic mixture layer, from thin to thick, corresponding to (b) sub-hemi mSIL, (c) super-hemi mSIL and (d) full-spherical mSIL, respectively. (e) Silicon chip with nanoscale surface patterns, onto which the mSILs are sprayed during the fabrication process.

Subsequently, deionized water—at a mass equal to half that of the nanoparticle precipitate—was added to the tube for dilution, and the mixture was left undisturbed for 3 hours to allow the formation of a TiO_2 gel. The TiO_2 gel was then loaded into an air-brush (AB932, SEALEY, United Kingdom) and sprayed at 45° onto the surface of a of silicon chip coated with a thin layer of an organic mixture consisting of hexane and tetrachloroethylene with a volume ratio of 1:2. The organic mixture thin layer is indispensable, as the formation of mSIL relies on a phase transition driven by the combined effects of gravity and oil/water interfacial tension [5, 6]. This transition occurs when the dispersed droplets of the nano–solid-fluid are sprayed onto the surface of a silicon chip with precoated organic mixture layer. Therefore, precisely controlling the duration of this transition is crucial for shaping the mSIL: a longer transition time tends to produce lenses with a higher height-to-width ratio, eventually approaching a full-spherical geometry. Organic mixture layers with thicknesses of approximately 300 µm, 600 µm, and 900 µm were used, corresponding to evaporation times of 3, 6, and 9 minutes, respectively, to form sub-hemispherical, super-hemisphere, and full-spherical mSILs. In addition, the low surface tension of hexane facilitates nanoscale

penetration of the mSILs. In this work, an air gun pressure of 1.0 bar was used, which has been shown to produce a moderate number of mSILs with an average diameter of approximately 20 μm [5].

The fabricated mSILs were initially characterised by SEM and the stage was tilted to 80° to determine the geometry (Zeiss EVO 10, with accelerating working voltage of 20 kV). Afterwards, fabricated mSILs were examined through Olympus DSX-1000 wide-field microscope (40x, *N.A.*=0.8 at 455 nm white-light peak wavelength) and Olympus OLS-5000 laser confocal microscope (100x, *N.A.*=0.95 at 405 nm). For full-mSILs lenses, they were embedded in polydimethylsiloxane (PDMS) layer with thickness of approximately 300 μm to reduce strong reflection caused by the refractive index mismatch between the TiO_2 full-mSILs and air. This embedding enhances near-field optical coupling and ultimately enables super-resolution imaging [6]. The SEM characterisation of the bottom surface of the mSILs was performed by detaching the lenses from the silicon chip using double-sided adhesive tape, followed by coating them with a 10 nm thick gold layer. In this work, the samples were sputter-coated with a thin gold layer using a thermal evaporator (Edward E306A, Sweden). The system was pumped down to a base pressure of approximately 8×10^{-6} mbar before deposition. Gold was thermally evaporated at a controlled deposition rate of ~1 Å/s, monitored in real time by a quartz crystal thickness sensor, until a final film thickness of 10 nm was achieved. This conductive layer effectively suppressed charging artefacts and enabled stable, high-contrast SEM imaging.

3.5.2 Fixation and Preparation of Yeast Cells

To investigate the imaging characteristics of biological microspheres, yeast cells were employed as natural dielectric lenses due to their near-spherical geometry and optical transparency. However, in their native aqueous state, biological cells are highly deformable and sensitive to drying, which can lead to collapse or shape distortion. Therefore, proper fixation and dehydration are essential to preserve structural integrity prior to microscopy or imaging experiments.

Table 3.1 The complete fixation processes of yeast cells.

Step Category	Step Description	Conditions/Notes
Preparation	Centrifuge yeast suspension (in PBS) Remove supernatant, retain precipitate	3000 rpm, 10 min
Fixation	Add 2.5% glutaraldehyde and pipette to mix Incubate at 4 °C for 4 hours	Ensure even dispersion for fixing
1st washing	Centrifuge to remove glutaraldehyde Add PBS and resuspend precipitate	3000 rpm, 10 min Ensure gentle mixing
2nd washing	Repeat above processes	Same as above
Dehydration	Add 30% ethanol incubate 10 min Centrifuge to remove ethanol	Pipette gently to disperse 3000 rpm, 10 min
	Repeat with 50%, 70%, 80%, 90%, 95% ethanol Centrifuge to remove ethanol	Same as above
Final dehydration	Add 100% ethanol (1st time), incubate 10 min Centrifuge and discard 100% ethanol	Same as above
	Repeat above processes	
Final Step	Add 100% ethanol again, resuspend, no centrifugation	Final storage step before drying

In the case of yeast cells, which possess both a plasma membrane and a rigid polysaccharide-based cell wall, effective fixation must stabilise internal structures while also accounting for the limited permeability of the cell wall. To achieve this, fixation was performed using 2.5% glutaraldehyde solution (diluted from 50% glutaraldehyde, Glentham LIFE SCIENCES Co. Ltd., United Kingdom) at 4 °C. Glutaraldehyde is a well-established cross-linking fixative that reacts with amino groups in proteins to form covalent bonds, thereby preserving the cellular architecture and preventing enzymatic degradation. The solution was prepared using phosphate-buffered saline (PBS) to maintain osmotic balance during fixation. Samples were immersed in the fixative for sufficient duration to ensure thorough penetration through the cell wall and uniform cross-linking of intracellular components.

Following fixation, the samples underwent graded ethanol dehydration to remove water gradually while minimising osmotic shock. The dehydration process was performed in

successive ethanol concentrations (30%, 50%, 70%, 90%, and 100%), with each step lasting approximately 10 minutes. This stepwise replacement of water with ethanol reduced surface tension effects and prevented structural collapse during subsequent air drying.

After dehydration, the samples were gently air-dried at room temperature prior to imaging under a scanning electron microscope (SEM). Because SEM operates under high vacuum, any residual moisture would otherwise vaporise and cause structural damage. The gradual dehydration protocol therefore ensured that the cells retained their overall morphology while becoming sufficiently rigid for high-vacuum imaging.

When the cells were characterised by SEM on a Blu-ray Disc substrate, an additional conductive coating step was required because the polymer disc surface is non-conductive and would otherwise lead to severe charging under the electron beam. The samples were thus sputter-coated with a thin gold layer (10 nm).

3.5.3 Key Equipment

Several imaging and characterisation instruments were employed to examine the morphology and optical performance of the fabricated samples.

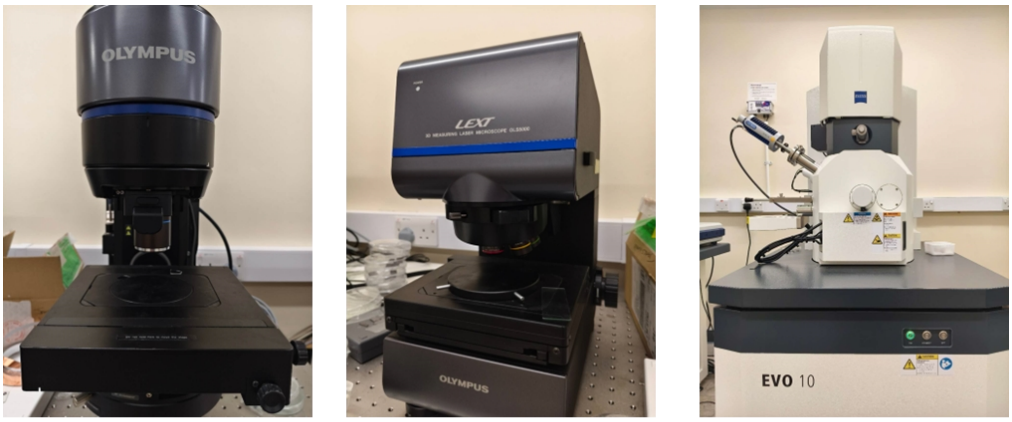

Figure 3.8 The main characterisation equipment used in this work: (a) DSX-1000 digital wide-field digital microscope; (b) LEXT OLS-5000; (C) Zessi EVO10.

DSX-1000 digital microscope (~405 nm, Olympus, Japen), as shown in Fig. 3.8 (a), was used for bright-field (BF) and polarised optical (PO) imaging, providing rapid, non-destructive inspection of subwavelength surface features through dielectric superlenses and biological cells acting as microlenses. In PO mode, linearly polarised illumination enables analysis of polarisation-dependent reflection and scattering, which is essential for examining

polarisation-sensitive samples such as Blu-ray discs. This system allowed preliminary optical characterisation of chip patterns (~60 nm features) and Blu-ray disc structures prior to high-resolution electron microscopy analysis.

OLS-5000 laser confocal microscope (Olympus, Japen), as shown in Fig. 3.8 (b), was employed to perform high-resolution optical imaging of the same samples. Owing to its shorter illumination wavelength (~405 nm), the system provided improved lateral resolution compared with the DSX-1000, enabling clearer visualisation of nanoscale surface features on the chip patterns and Blu-ray discs.

For nanoscale morphological characterisation, a **Zeiss EVO10 scanning electron microscope**, as shown in Fig. 3.8 (c), was used to image both TiO_2 mSILs and biological microspheres under high-vacuum conditions. The SEM provided detailed structural information on surface texture, packing density, and fabrication quality, with acceleration voltages typically in the range of 10–20 kV depending on the sample type.

Together, these instruments provided complementary imaging capabilities across micro- to nanoscale resolution, ensuring accurate characterisation of the structures used in subsequent optical experiments.

3.6 Summary

This chapter presented the complete theoretical, numerical, and experimental framework used to study the optical behaviour of micro- and nanostructured spherical systems. Analytical, numerical, and experimental methods were integrated to provide a coherent link between simulation and practical validation.

The analytical tool xMie, based on Mie theory, was employed to model light–particle interactions and served as a benchmark for validating numerical simulations performed in CST Studio Suite. Excellent agreement between xMie and CST in both near- and far-field regions confirmed the accuracy of the numerical method. CST was then applied to analyse two key structures: TiO_2-based mSILs and wide-angle SiNS metamaterial filters. The mSIL models revealed how near-field evanescent waves are transformed into propagating components, while the SiNS array models provided insights into angularly tolerant filtering effects.

Multilayer optimisation was subsequently performed using ESM, which implements the TMM. This optimisation refined CST-derived designs by adjusting layer thicknesses, optical

admittance, and anti-reflection coatings to improve transmission and angular stability. To enable accurate thin-film modelling of metamaterial layers, two approaches were assessed for effective refractive-index extraction: the Bruggeman Effective Medium Approximation (BEMA) and the Kramers–Kronig (K–K) method. The K–K approach achieved one-order-of-magnitude higher agreement with CST spectra and was therefore adopted for all subsequent analyses.

Experimentally, TiO_2-based mSILs were fabricated using a gravity- and interfacial-tension-driven self-assembly method, allowing precise control of curvature by varying solvent-layer thickness and evaporation time. Yeast cells were prepared as biological microspheres through glutaraldehyde fixation and graded ethanol dehydration to preserve structural integrity for imaging. Their morphologies were characterised using DSX-1000 microscopy**,** laser confocal microscopy**,** and Zeiss EVO10 scanning electron microscope, providing complementary information from micro- to nanoscale resolution.

Together, these analytical, numerical, and experimental methodologies form a unified framework for studying microsphere- and metamaterial-based optical systems. The validated models and fabricated structures described here provide the foundation for the results and discussion presented in following chapters.

3.7 References

[1] Z. Wang, “Optical Resonance and Near Field Effects: Small Particles Under Laser Irradiation,” National University of Singapore, 2005.

[2] CST Studio Suite 2024, Dassault Systèmes, Germany. Available: https://www.3ds.com/products-services/simulia/products/cst-studio-suite/ (accessed on 26 Nov 2025)

[3] J. E. Bertie, S. L. Zhang, “Infrared intensities of liquids. ix. the Kramers–Kronig transform, and its approximation by the finite Hilbert transform via Fast Fourier transforms,” Can. J. Chem. 1992, 70, 520–531.

[4] W. Q. Hong, “Extraction of extinction coefficient of weak absorbing thin films from special absorption,” J. Phys. D Appl. Phys. 1989, 22, 384–1385.

[5] W. Fan, B. Yan, Z. Wang, L. Wu, “Three-dimensional all-dielectric metamaterial solid immersion lens for subwavelength imaging at visible frequencie,” Sci. Adv. 2016, 2, e1600901.

[6] R. Dhama, B. Yan, C. Palego, Z. Wang, “Super-Resolution Imaging by Dielectric Superlenses: TiO2 Metamaterial Superlens versus BaTiO3 Superlens,” Phtonics. 2021, 8, 6, 222.

Chapter 4 Shape-Dependent TiO_2 mSIL Super-Resolution Imaging

4.1 Introduction

According to Abbe's diffraction limit, a conventional lens-based microscopy system cannot resolve two objects separated by a distance smaller than approximately half the wavelength of the light source in air [1]. Fluorescence-based super-resolution imaging techniques were developed to overcome this limitation [2]. Although these technologies offer imaging resolutions down to 1 nm, their application is restricted to samples that can be labelled with fluorophores. In addition, fluorescent dyes may be harmful to live samples and can alter the intrinsic properties of biological specimens [3].

To address these challenges, label-free super-resolution imaging techniques such as near-field–enhanced dielectric microsphere-assisted microscopy (MSM) and hyperlens-assisted microscopy have been widely studied [4,5]. However, hyperlens-based microscopy, which relies on complex metal–dielectric composite structures, suffers from significant optical losses and requires sophisticated and costly nanofabrication, making it less practical than MSM [6]. MSM and its related variants, in contrast, offer high-resolution imaging under broadband illumination by optimising material selection, immersion media, and microsphere geometry at relatively low cost. For example, transparent high-index microspheres such as polystyrene (PS) in air, fused silica (SiO_2) in water, and barium titanate ($BaTiO_3$) in water have achieved resolutions of 120 nm, 50 nm, and 40 nm, respectively [7, 8].

Beyond the use of prefabricated microspheres, transfer-printing techniques have been explored to fabricate hemispherical and super-hemispherical lenses with controllable placement and potential scalability [9,10]. However, the resolution of such lenses is constrained by the relatively low refractive index of typical printing materials. Focused ion beam (FIB) milling offers an alternative route by precisely shaping high–refractive-index materials, but the method is experimentally demanding and unsuitable for large-scale fabrication [11].

A practical and low-cost alternative uses high–refractive-index titanium dioxide (TiO_2)

nanoparticles to form sub-hemispherical (sub-mSIL) and super-hemispherical (super-mSIL) lenses through nano–solid–fluid assembly (NSFA) [12]. Under white-light illumination, TiO_2 nanoparticle-based super-mSILs have demonstrated resolutions down to ~45 nm with high contrast and a wide virtual field of view. Two mechanisms were proposed to explain this behaviour. First, the flat bottom of the super-mSIL enhances evanescent-wave reception and suppresses lateral movement of the microlens, preventing air gaps that would otherwise exceed the evanescent penetration depth [13]. However, when illuminated with a monochromatic source, the theoretical lateral resolution of an ideal homogeneous super-hemisphere should be significantly worse than the experimentally observed performance of TiO_2-based super-mSILs, despite their similar geometry. SEM characterisation of the mSIL bottom surface revealed that TiO_2 nanoparticles penetrate deeply into the underlying nanostructures, filling nanoscale gaps and locally enhancing near-field coupling. Full-wave three-dimensional simulations have shown that such nanoparticle penetration can illuminate nanostructures more effectively and strengthen focused evanescent fields, although earlier simulations did not explicitly incorporate the penetration process.

Building on the TiO_2-based NSFA method, our group recently developed a simpler and more repeatable fabrication protocol for micro-full-spherical (full-mSIL) lenses [14]. These lenses exhibit higher imaging contrast, a wider field of view, and better resolution than prefabricated $BaTiO_3$ microspheres. However, the penetration behaviour of TiO_2-based full-mSILs has not yet been investigated, and no comparative study has evaluated the imaging performance of sub-, super-, and full-mSILs fabricated under identical conditions.

In this work, we systematically compare the imaging performance of these three geometries using wide-field and laser-confocal microscopy, supported by SEM characterisation of their bottom surfaces. Wide-field imaging reveals that the super-mSIL provides the best resolution (down to ~60 nm), the highest contrast, and a moderate field of view and magnification. Full-wave simulations further show that nanoparticle penetration enhances the collection of propagating-wave energy in the far field, with the super-mSIL benefiting most from this effect.

In addition to the experimental and numerical investigations, we introduce a deep-learning framework motivated by a practical limitation of mSIL imaging. Because each mSIL becomes immobilised at the location where it forms, it cannot be repositioned to image multiple spatial regions, making large-area mapping challenging. Recent advances in deep-

learning-based microscopy and cross-modality image translation [15-17] offer opportunities to overcome this constraint. Here, we employ a contrastive unpaired image-translation model to learn a mapping from SEM morphology to optical response, enabling virtual prediction of mSIL imaging at previously unmeasured positions and establishing the basis of an mSIL digital-twin concept.

Together, these contributions provide both mechanistic insight into how lens geometry affects super-resolution performance and a complementary computational route for extending the effective imaging capability of TiO_2 mSILs.

4.2 Characterisation of TiO_2 mSILs

In this section, the TiO_2 mSILs are systematically characterised in terms of their morphology, nanoparticle penetration behaviour, and corresponding optical imaging performance. First, three representative lens geometries, including full-spherical, sub-hemispherical, super-hemispherical mSIL, were fabricated by controlling the phase-transition duration via the thickness of the organic mixture layer as described in Section 3.5.1. The overall geometric distribution of the fabricated lenses was examined through tilting-view SEM imaging and statistical analysis of their aspect ratios, thereby confirming the feasibility of controlling lens geometry via the phase-transition duration. Subsequently, individual lenses from each group were selected for detailed SEM inspection of their bottom surfaces and penetration quality, followed by wide-field and laser-confocal imaging of sub-wavelength features on the silicon chip, enabling a direct link between geometry, penetration behaviour and super-resolution imaging performance.

4.2.1 SEM geometry and penetration analysis

Low-magnification SEM imaging was first conducted on the three fabricated samples to observe their overall morphological features. Tilting-view SEM images (Fig 4.1 a–c) primarily confirm the success of the fabrication of full-spherical, super-hemispherical and sub-hemispherical mSILs.

To further verify the reliability of the fabrication method, 200 mSILs were randomly selected from each sample for hight-width-ratio analysis. Ratios of three samples were grouped into uniform bins ranging from 0.65–1.0, 0.65–1.0 and 0.25–0.65, respectively, with ±0.2 tolerance in the measured values.

The statistical results show that the full-spherical geometry is the most successfully produced,

with 100% of the lenses exhibiting an aspect ratio above 0.95. This high consistency arises from the longest phase-transition duration, during which the nano–solid-fluid undergoes more complete gravitational collapse, stronger deformation driven by the oil/water interface and finally forming a densely packed and highly symmetric spherical structure. For the super- and sub-hemispherical mSILs, the distributions are centred around aspect ratios of approximately 0.85 and 0.40, respectively. With nearly 70% of the lenses falling within the ranges 0.80–0.90 and 0.35–0.45, this indicates that varying the phase-transition duration through the organic-layer thickness provides an effective and controllable route for tailoring the mSIL aspect ratio.

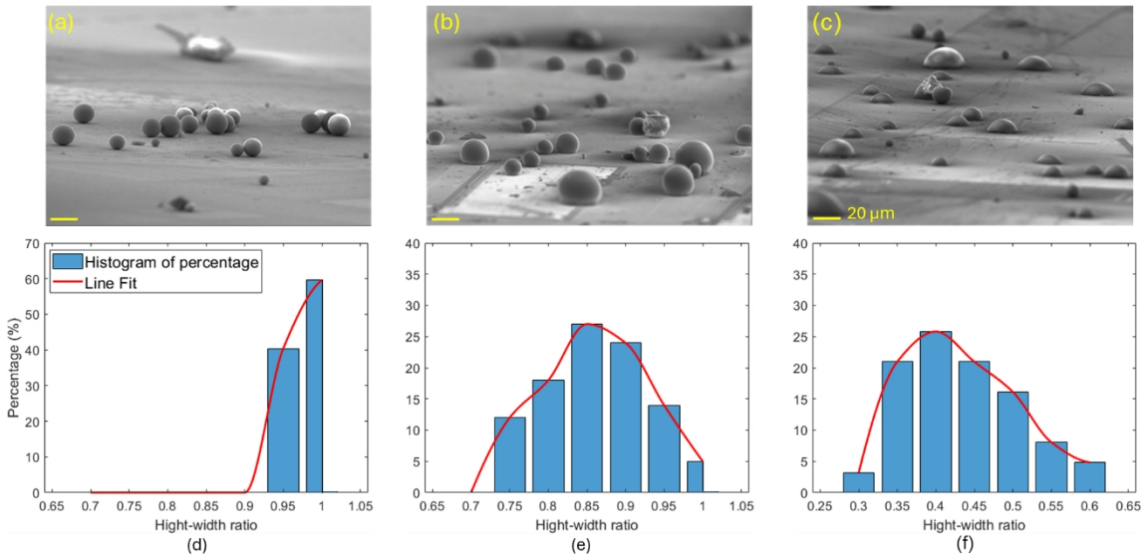

Figure 4.1 (a–c) Tilting-view SEM images of the TiO_2 mSILs fabricated under three phase-transition durations, corresponding to full-spherical, super-hemispherical and sub-hemispherical mSIL, respectively. (d–f) Statistical distribution of hight-width distribution of the corresponding samples.

Alongside the controllable tuning of aspect ratio, the nanoparticle penetration at the lens–substrate interface is second key structural characteristic that was examined next. Fig 4.2 presents the systematic characterisation of the three TiO_2 mSIL variants. For each variant, the corresponding tilting-view SEM image is shown in Fig. 4.2 (a, e, i), representing the sub-hemispherical, super-hemispherical and full-spherical mSILs, respectively.

The bottom-surface structure of each mSIL variant was examined to assess the quality of nanoparticle penetration. As shown in Fig. 4.2 (f), the super-hemispherical mSIL exhibits clear and uniform penetration, with TiO_2 nanoparticles fully filling the nanoscale grooves and reproducing the underlying surface texture. This behaviour is consistent with previous reports. A similar penetration trend is observed in the sub-hemispherical mSIL (Fig 4.2 b); however, numerous defects appear across its bottom surface, likely resulting from the much shorter phase-transition duration, which negatively affects its subsequent imaging performance.

For the full-spherical mSIL (Fig. 4.2 j), to the best of our knowledge, no prior studies have reported bottom-surface characterisation of full-spherical NSFA-assembled mSILs. In our earlier work, TiO_2-based full-spherical mSILs demonstrated superior imaging resolution compared with pre-fabricated BTG microspheres, despite both exhibiting similar effective refractive indices. That conclusion was drawn from near- and far-field full-wave simulations, which did not include bottom-surface structure or nanoparticle penetration in the model. In this work, Fig. 4.2 (j) reveals a small but distinct penetration region, where the underlying silicon texture is imprinted onto the lens bottom. This structural evidence provides an additional and important explanation for the enhanced imaging performance of TiO_2-based full-spherical mSILs. The detailed mechanism by which penetration contributes to improved resolution will be further addressed in later section.

4.2.2 Optical imaging performance (wide-field and confocal)

The silicon chip was imaged through the three mSILs using a wide-field microscope in bright-field mode, as shown in Fig 4.2 c, g, and k, and followed by laser confocal-microscopy in sub-figure d, h, and l. The sub-mSIL lens enables the broadest field of view, approximately 11.07 μm^2, and followed by super-mSIL and full-mSIL lenses with measured areas of 7.16 μm^2 and 4.75 μm^2, respectively.

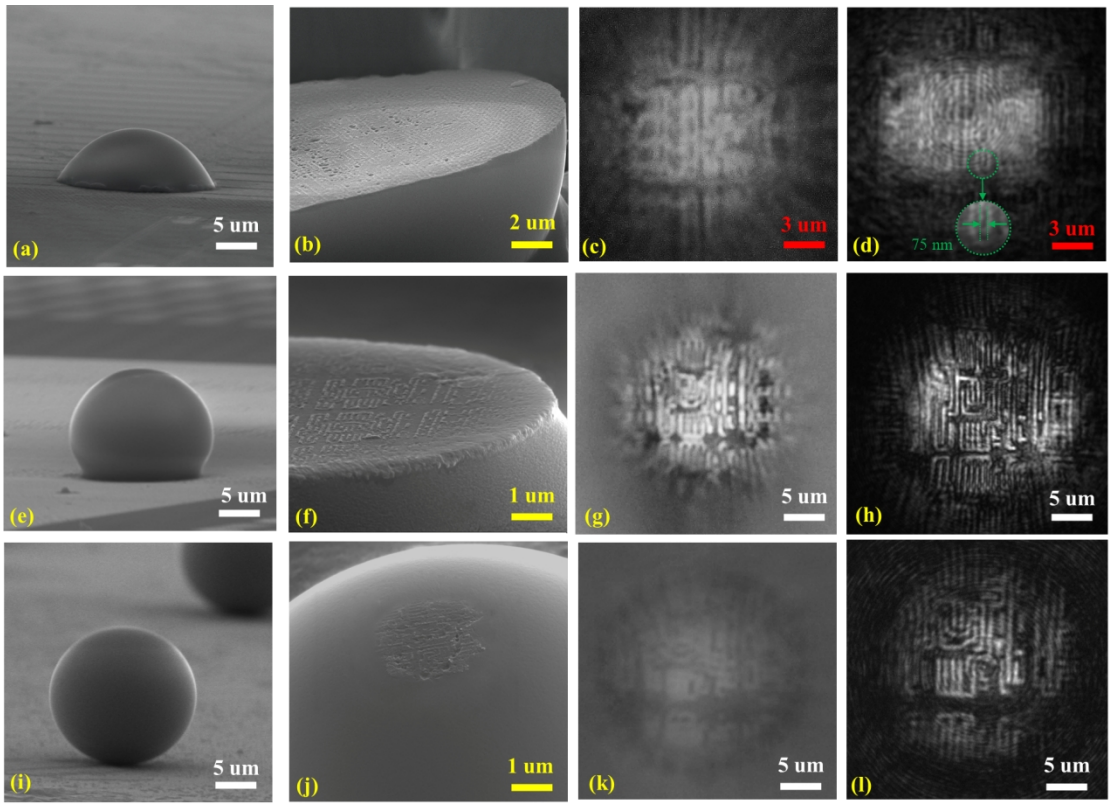

Figure 4.2 The SEM images of (a) sub-hemispherical, (e) super-hemispherical and (i) full-spherical mSIL and their bottom surface characterisation (b), (f) and (j), respectively. Wide-field microscopy images, (c), (g) and (k), and laser-confocal microscopy images, (d), (h) and (l) focused on pattern of silicon chip.

In terms of magnification, the full-mSIL lens provided the highest magnification (5.1x), and decreased to 4.6x and 2.6x for the super-mSIL and sub-mSIL lenses, respectively. The observed decrease in magnification with a reduced height-to-width ratio is consistent with previous research.

Despite not having the highest magnification factor, the super-hemispherical mSIL lens exhibited the highest imaging resolution and contrast under wide-field microscopy, clearly resolving a 60 nm-wide gap on the silicon chip that was not observable with the full-hemispherical or sub-hemispherical mSIL. Under laser confocal microscopy, this 60 nm gap was subsequently resolved by both super-hemispherical and full- hemispherical mSIL as the single-wavelength laser illumination offers a shorter wavelength and tighter focus, which further improves the system's lateral resolution compared to wide-field microscopy.

The sub- hemispherical mSIL, however, was unable to resolve the 60 nm gap using either of the two microscopy techniques. Under wide-field microscopy, it revealed a clear outline of the chip pattern with reasonable contrast but lacked super-resolution capability. In contrast, under confocal microscopy, it demonstrated modest degree of super-resolution and was able to faintly resolve nanostructures as small as 75 nm, as highlighted in Fig 4.2 d. These results indicate that the sub- hemispherical mSIL has some potential for improved super-resolution performance under confocal microscopy; however, this capability is strongly limited by the insufficient nanoparticle penetration at its bottom surface.

Building on the above imaging results, further analysis of the white-light data reveals clear wavelength-dependent behaviour, as shown in Fig. 4.3. The RGB image (a) and combined red-green (RG) channel (b) reveal clear nanoscale structural features within the dashed region, showing strong agreement with the SEM reference image (c). The image was further decomposed into individual grayscale red, green, and blue channels (d–f), corresponding to typical wavelength bands of approximately 620–750 nm (red), 495–570 nm (green), and 450–495 nm (blue). Among them, the red channel (d) provides the highest contrast and clarity, while the blue channel (f) contributes the least. This enhanced performance in the red channel can be attributed to the lower scattering of longer wavelengths, consistent with Rayleigh's law ($\propto 1/\lambda^4$), which enables deeper penetration and less image degradation from surface

nanostructures. These findings highlight the broadband imaging capability of the super-hemispherical mSIL and the importance of wavelength-dependent analysis for optimising image contrast.

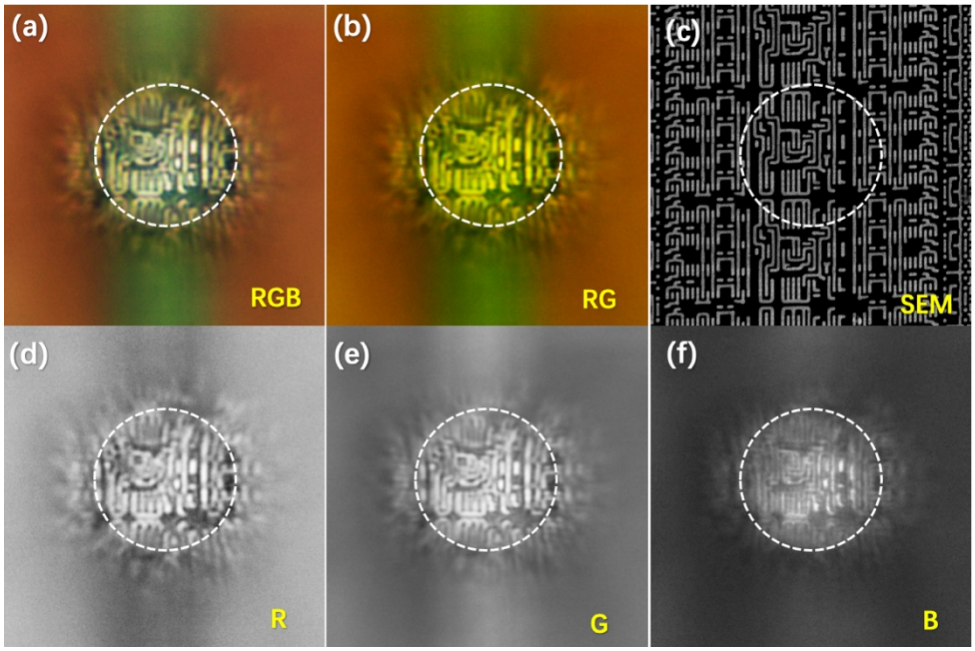

Figure 4.3 Wide-field imaging of a semiconductor chip using a TiO_2-based super-hemispherical mSIL under white light: (a) RGB image; (b) combined red-green channels; (c) SEM reference; (d–f) individual red, green, and blue channels. Dashed circles indicate regions used for resolution comparison.

4.3 Deep Learning–Enabled SEM–Optical Translation

4.3.1 Motivation

A practical limitation of nanoparticle-based mSIL imaging is that each lens is immobilised at the position where it forms during the NSFA process. Unlike prefabricated microspheres, the mSIL cannot be conveniently repositioned to probe different regions of the sample without specialised micromanipulation. Although mechanical or microrobotic actuation could theoretically move the lens, such procedures introduce experimental complexity, risk damaging the nanoparticle penetration interface, and are unsuitable for routine or large-area imaging. In contrast, SEM provides rapid and high-resolution morphological information over the entire chip surface. If a reliable mapping can be established between the SEM morphology (domain A) and the corresponding optical appearance through the mSIL (domain B), then optical responses at arbitrary, unmeasured locations could be reconstructed computationally. In effect, the trained model serves as a digital twin of the physical mSIL, providing a virtual counterpart that predicts how the same lens would image different regions

of the substrate without any physical movement. This motivates the use of deep learning–based image translation to generate virtual optical images directly from SEM input, effectively enabling large-area imaging without physically moving the lens.

4.3.2 SinCUT model and training

To achieve this, we employed a Single-Image Contrastive Unpaired Translation (SinCUT) model [18] to learn a cross-modal mapping between SEM and wide-field optical images. SEM and optical images of the same region were first scaled and manually aligned so that the structural features within the viewing-window area were approximately matched. These nearly paired examples were used to train the SinCUT model, which maximises patch-wise mutual information between input and output, ensuring that nanoscale structural details from the SEM are preserved while their appearance is transformed into the corresponding optical domain.

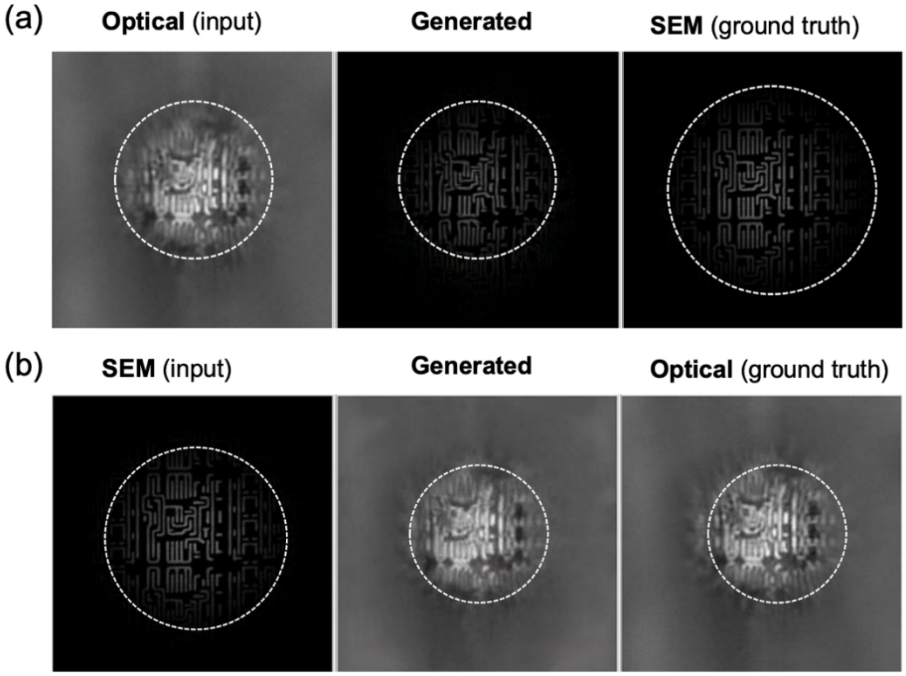

Figure 4.4 SinCUT bidirectional image translation. (a) Optical input generated SEM-like output, and SEM ground truth. (b) SEM input generated optical output, and optical ground truth.

Fig 4.4 demonstrates the performance of the SinCUT model in translating between the SEM and optical imaging domains. In Fig 4.4 (a), an optical image is used as input and the model generates an SEM-like output, which closely reproduces the structural geometry and intensity patterns of the true SEM target. Conversely, Fig 4.4 (b) shows the reverse translation, where SEM morphology is used to predict the corresponding optical appearance through the mSIL. The generated optical image accurately captures the overall contrast distribution, central-zone

intensity enhancement, and characteristic distortion features observed in the real optical measurement. Across both translation directions, the model preserves fine nanoscale structures within the dashed region and maintains the geometry-dependent contrast signatures associated with each mSIL type. These results confirm that SinCUT successfully learns a bidirectional mapping between SEM morphology and optical imaging response, enabling faithful cross-modal prediction and supporting the digital-twin interpretation of the mSIL imaging system.

The viewing-window behaviour in Fig 4.4 shows an interesting asymmetry: in the Optical→SEM direction (Fig 4.4 a), the generated SEM-like output largely preserves the view-window size of the optical input, whereas in the SEM→Optical direction (Fig. 4b), the generated optical-like image does not follow the larger SEM window but instead converges toward the characteristic optical window observed in the ground truth. This behaviour reflects a well-known property of contrastive unpaired translation models such as SinCUT. Because patch-wise contrastive learning constrains local structural similarity rather than enforcing global geometric consistency, the model tends to preserve input geometry only when translating into a domain whose global appearance is more weakly structured (as in the SEM domain). In contrast, when translating into the optical domain, the model adapts the output geometry toward the dominant statistical features of that domain—here, the stable and well-defined bright viewing-window typical of mSIL optical images. Despite these geometric adjustments, the generated images in both directions closely reproduce the nanoscale patterns, contrast relationships and structural organisation within the dashed region, demonstrating that the model accurately captures the cross-modal mapping relevant for interpreting mSIL imaging behaviour.

4.3.3 Generalisation to unseen regions and the digital-twin concept

Fig 4.5 evaluates how the SinCUT model performs when the sample is shifted to neighbouring positions around the central training region A. Panel (a) illustrates the spatial relationship of the five locations: A is the only region used for training, while B, C, D and E are unseen test regions. Panels (b) and (c) show the SEM inputs and the corresponding predicted optical outputs at these locations. When the sample is moved vertically to regions D and E, the reconstructed optical images closely match the expected structure and contrast. This strong generalisation arises because most nanoscale patterns in D and E also appear within region A, allowing the model to reproduce them reliably. For the horizontal positions B and C, the model likewise produces optical predictions that are globally consistent with the

expected appearance: the overall brightness distribution, viewing-window shape and major structural motifs are well captured. However, both B and C show a similar local issue: a small portion of the pattern is reconstructed less faithfully (highlighted by the dashed box). This occurs because these specific structural features do not appear in the training region A; with only a single SEM–optical pair used for training, the SinCUT model has no prior exposure to these unseen geometries. Consequently, the model performs well on structures that fall within the statistical distribution of A but struggles with features outside it. Importantly, this limitation does not undermine the value of the approach: the results demonstrate that accurate cross-modal translation is achievable even with minimal training data, establish the feasibility of an mSIL digital-twin framework, and identify pattern diversity—not model capability—as the key factor governing generalisation. Future work will therefore focus on incorporating multiple training regions or applying structural-augmentation strategies to broaden pattern coverage and achieve more complete reconstruction across all unseen locations.

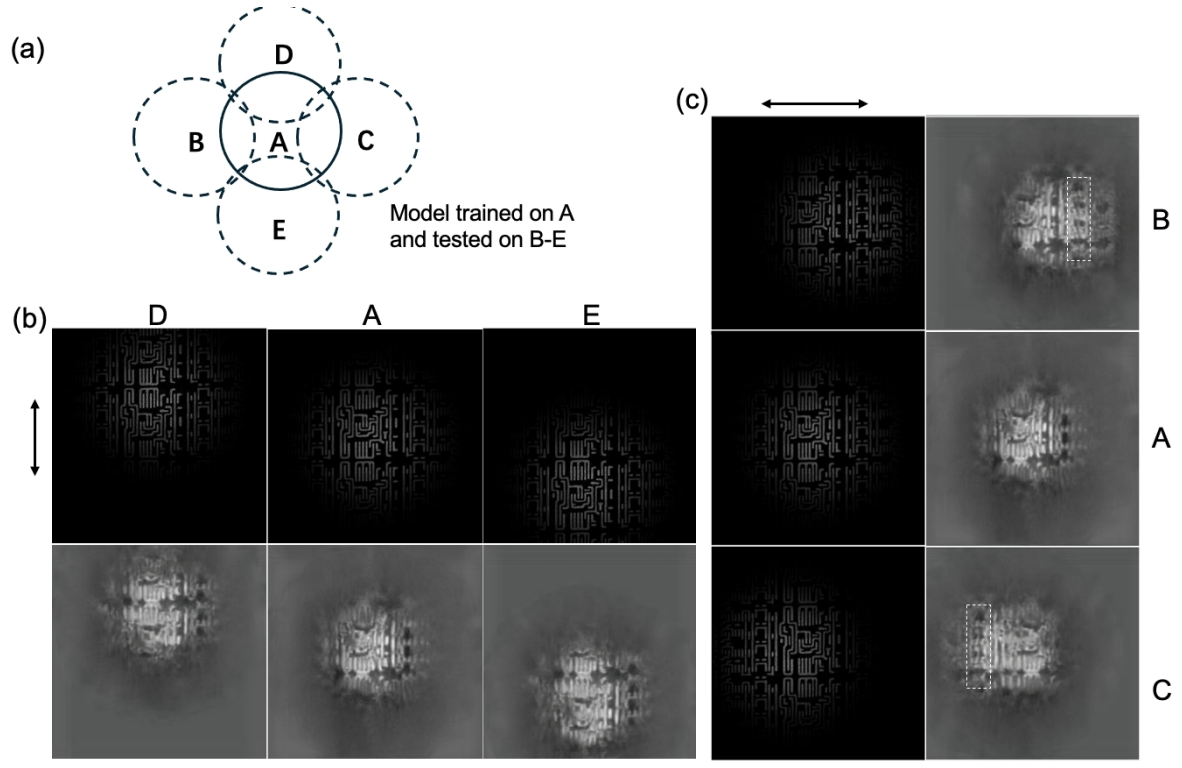

Figure 4.5 Generalisation of the SinCUT model to unseen locations. (a) Schematic showing the training region (A) and neighbouring test regions (B–E). (b) Predicted optical images for SEM inputs at D–A–E (vertical direction). (c) Predicted optical images for SEM inputs at B–A–C (horizontal direction).

4.4 Mechanism of Shape-Dependent Imaging

4.4.1 CST modelling framework

To investigate the imaging mechanism of these mSILs, a full-wave 3D simulation (CST STUDIO, version 2023) was conducted to demonstrate the near- and far-field optical responses. Our previous research suggested that the effective refractive index of the TiO_2 nanoparticles close-packed is 1.92 and with a filling factor of 61.2% [14]. Each mSIL is composed of millions of TiO_2 nanoparticles. To ensure the computational load remained manageable, the majority of the model was simplified as a homogenous material (n =1.92), while the region contacting with nano-pattern was modelled as a TiO_2 nanoparticles closely-packed region. In addition, the geometries of those 3D mSILs were simplified by 2D cylinders. As illustrated in Fig 4.6 (a, d, g) three variants of mSILs with height-width ratio of 0.3, 0.8 and 1.0 were constructed in CST STUDIO with a diameter of 20 μm, incorporating both non-penetration (left) and penetration (right) scenarios. The PDMS used as host medium for full-mSIL is represented in green, and it fills up those empty nanoscale gaps when the penetration effect is not considered. To simulate the experimentally observed partial penetration in full-mSILs, only 3 nanoscale gaps are filled with TiO_2 nanoparticles, while remaining gaps were filled with PDMS. For super-mSIL and sub-mSIL geometries, all nano-scale gaps were either filled with air or TiO_2 nanoparticles while all other parameters were kept unchanged. The light source was simplified to an electric dipole with central wavelength of 455 nm that is perpendicular to the plane and positioned at the centre of the middle gap. This configuration enables us to analyse how evanescent waves generated in the near-field are finally converted to propagating wave in the far-field. The differences in the optical responses between two penetration scenarios, as well as among three variants of mSILs are crucial for explaining their distinct imaging capabilities.

4.4.2 Penetration-driven near-field and far-field behaviour

The far-field patterns shown in Fig 4.6 (b, e, h) suggest that the main characters of far-field, such as main lobe direction and main lobe width, are not significantly affected by penetration effect. However, an enhancement in the main lobe magnitude indicating increased energy collection is observed across all three variants after the penetration effect is considered. The highest enhancement (8.8%), indicating improved energy collection, is observed in the super-mSIL and followed by 3.8% and 3.5% for full-mSIL and sub-mSIL, respectively. This trend aligns with experimental super-imaging observations, where the super-mSIL lens exhibited the best super-imaging resolution. Despite the simulated enhancement levels of the full-mSIL and sub-mSIL are similar, in experiments, the poor penetration quality, as shown in Fig 4.2

(b), occurring at the bottom of sub-mSIL during experiments likely diminishes this enhancement. Notably, the far-field pattern of full-mSIL, when the PDMS is introduced as host medium, exhibits multiple sharp peaks rather than single broad main lobe, as observed from super-mSILs and sub-mSILs. This distribution disperses the energy collection of propagating wave in far-field, and may result in lower imaging contrast compared to super-mSILs and sub-mSILs.

When the electric field polarisation lies in the x–y plane and the magnetic field is oriented perpendicular to the x–y plane, the far-field scattering plot demonstrates a trend consistent with the previous results (Fig. B2).

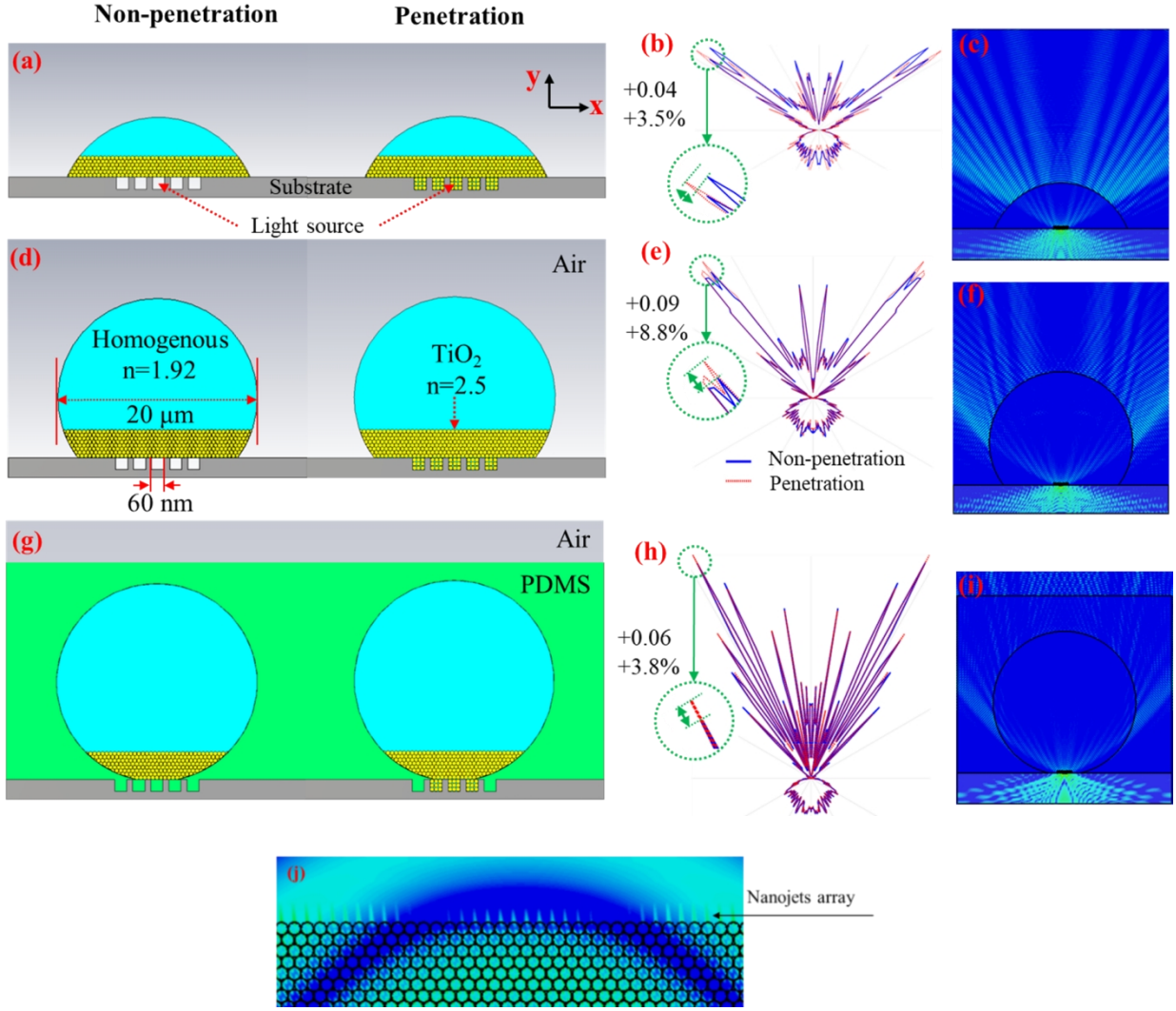

Figure 4.6 The schematic illustrations of the simplified models of (a) sub-mSIL, (d) super-mSIL and (g) full-mSIL lenses, respectively, with 20 μm diameters, each incorporating non-penetration (left) and penetration (right) scenarios and their corresponding far-field scattering patterns in (b), (e) and (h). The electric field distributions of three lenses in (c), (f), and (i). (j) Nanojets array of super-mSIL in enlarged view of the region highlighted by the red dashed box in (f).

Electric field (E-field) distributions of the three mSIL variants schematically illustrate how radiation energy is coupled into far-field, as shown in Fig 4.6 (c, f, i) respectively. The magnified image of E-field locating around the penetration area is shown in Fig 4.6 (j). It clearly shows a photonic nanojets array, which enhances the conversion of the evanescent wave in near-field into the propagating wave in far-field while no significant difference is observed across three mSILs in this aspect.

Overall, we can conclude that the super-resolution imaging capability of TiO_2 nanoparticle-based mSILs depends on both their geometries and the penetration quality of the nanoparticles, providing valuable guidance for fabricating and optimizing the performance of other similar mSILs.

4.5 Discussion

The combined experimental, computational, and deep learning results provide a unified understanding of how mSIL geometry and nanoparticle penetration jointly determine super-resolution performance. The SEM characterization confirms that super-mSILs consistently achieve the deepest and most uniform penetration into the nanoscale grooves of the substrate, which directly enhances near-field coupling and explains their superior resolution in both wide-field and confocal modalities. The full-wave simulations further show that this penetration effect increases far-field energy collection, particularly for the super-mSIL geometry, in agreement with experimental observations.

The deep learning framework offers an additional perspective on mSIL behaviour. By training a SinCUT model on a single SEM–optical pair, we demonstrate that the SEM→optical mapping can be learned with high fidelity for most nanoscale patterns within the training distribution. The model generalises effectively to neighbouring regions whose structural motifs are also present in the training area, supporting the concept of an mSIL digital twin. At the same time, the reduced reconstruction accuracy for local features that do not appear in the training region highlights the role of pattern diversity, rather than model capacity, as the primary limitation of the current approach. This insight suggests that expanding the training set to multiple spatial locations or enhancing pattern variability through augmentation would yield a more complete virtual imaging framework across larger chip areas.

Taken together, these findings demonstrate that mSIL performance emerges from the interplay between lens shape, penetration quality, and local sample geometry, while also establishing a promising computational direction for digitally extending the lens's effective field of view.

4.6 Conclusion

This work provides the first systematic comparison of TiO_2-based sub-mSIL, super-mSIL, and full-mSIL lenses fabricated under identical conditions, revealing clear correlations between lens geometry, nanoparticle penetration, and super-resolution imaging performance. The super-mSIL lens achieves the best experimental resolution and contrast, which is attributed to its large and high-quality penetration area. SEM characterization and full-wave simulations consistently show that the penetration of TiO_2 nanoparticles enhances the conversion of evanescent waves into propagating waves, thereby improving far-field energy collection and enabling superior imaging.

In addition to these physical insights, we demonstrate a deep learning–based SEM–to–optical translation framework that acts as a digital twin of the mSIL imaging process. The SinCUT model reconstructs optical responses with high fidelity across most unseen locations, validating the feasibility of computational virtual imaging. The observed limitations at regions containing previously unseen nanoscale geometries highlight the need for expanded training data or structural augmentation, providing a clear path for future improvement.

Overall, this study offers both mechanistic understanding and computational tools for advancing TiO_2 mSIL technology, laying the groundwork for scalable, high-contrast, label-free super-resolution imaging systems.

4.7 References

[1] Abbe, E. "Beiträge zur Theorie des Mikroskops und der mikroskopischen Wahrnehmung," Archiv. Mikrosk. Anat. 1873, 9, 413–418.

[2] M. Weber, M. Leutenegger, S. Stoldt, S. Jakobs, T. S. Mihaila, A. N. Butkevich, S. W. Hell, "MINSTED fluorescence localization and nanoscopy" Nat Photon. 2021, 15, 5, 361-366.

[3] G. Wu, M. Hong. "Optical Microsphere Nano-Imaging: Progress and Challenges," Engineering-Prc. 2024, 102–123.

[4] Z. Wang, W. Guo, L. Li, B. Lukyanchuk, A. Khan, Z. Liu, Z. Chen, M. Hong, "Optical virtual imaging at 50 nm lateral resolution with a white-light nanoscope," Nat. Commun. 2011, 2, 218.

[5] E. T. F. Rogers, J Lindberg, T. Roy, S. Savo, J. E. Chad, M. R. Dennis, N. I. Zheludev, “A super-oscillatory lens optical microscope for subwavelength imaging,” Nat. Mater. 2012, 2, 432–435.

[6] H. Wang, C. Hao, H. Lin, Y. Wang, T Lan, C. Qiu, B. Jia, “Generation of super-resolved optical needle and multifocal array using graphene oxide metalenses,” Opto-Electron Adv. 2021, 4, 20032.

[7] S. Lee, L. Li, Y. Ben-Aryeh, Z. Wang, W. Guo, “Overcoming the diffraction limit induced by microsphere optical nanoscopy,” J. Opt. 2013, 15 125710.

[8] P. Li, G. Li, H. Yu, F. Wang, L. Liu, W. Li, “Advances in Dielectric Microspherical Lens Nanoscopy: Label-Free Superresolution Imaging,” IEEE Nanotechnol. Mag. 2021, 15, 38.

[9] D. Kang, C. Pang, S.M. Kim, H.S. Cho, H.S. Um, Y.W. Choi, K.Y. Suh, “Shape-Controllable Microlens Arrays via Direct Transfer of Photocurable Polymer Droplets,” Adv. Mater. 2012, 24, 1709–1715.

[10] P. Li, H. Yu, Y. Wen, W. Zhao, L. Liu, W. Li, “Direct Transfer Printing of Dielectric Nanoparticle Assembled Superlens Array for Super-resolution Imaging” in IEEE 19th International Conference on Nanotechnology (IEEE-NANO), Macao, China, 2019, 405–409.

[11] G. Wu, Y. Zhou, M. Hong, “Sub-50 nm optical imaging in ambient air with 10× objective lens enabled by hyper-hemi-microsphere,” Light Sci Appl. 2023, 12, 49.

[12] W. Fan, B. Yan, Z. Wang, L. Wu, “Three-dimensional all-dielectric metamaterial solid immersion lens for subwavelength imaging at visible frequencie,” Sci. Adv. 2016, 2, e1600901.

[13] H. Wang, W. Shi, J. Wang, X. Zhou, P. Li, “Converting evanescent waves into propagating waves by hyper-hemi-microsphere,” Opt. Express. 2024, 32, 14, 25451–25462.

[14] R. Dhama, B. Yan, C. Palego, Z. Wang, “Super-Resolution Imaging by Dielectric Superlenses: TiO2 Metamaterial Superlens versus BaTiO3 Superlens,” Phtonics. 2021, 8, 6, 222.

[15] Y. Rivenson, Z. Göröcs, H. Günaydin, Y. Zhang, H. Wang, A. Ozcan, “Deep learning microscopy,” Optica. 2017, 4, 11, 1437–1443.

[16] H. Wang, Y. Rivenson, Y. Jin, Z. Wei, R. Gao, H. Günaydın, L.A. Bentolila, C. Kural, A. Ozcan, “Deep learning enables cross-modality super-resolution in fluorescence microscopy,” Nat methods. 2019, 16, 1, 103–110.

[17] T. Park, A. A. Efros, R. Zhang, J. Zhu, “Contrastive Learning for Unpaired Image-to-Image Translation,” in European conference on computer vision, Glasgow, United Kingdom, 2020, 319–345.

[18] T. Park, “CUT: Contrastive Unpaired Translation,” GitHub: https://github.com/taesungp-/contrastive-unpaired-translation (accessed on 26 Nov 2025).

Chapter 5 Yeast Cell Biological Superlenses

5.1 Introduction

Over the past decade, biological superlenses have emerged as a promising alternative to artificial dielectric microspheres for achieving label-free optical super-resolution. Their intrinsic advantages, including natural availability, low fabrication cost, and biocompatibility make them attractive for live-cell applications where traditional solid superlenses are unsuitable. Various developed biological materials were reviewed in section 2.3.4, including spider silk, yeast cells, epithelial cells and algal cells [1–5]. Each of them demonstrates distinctive optical behaviours derived from their geometry, refractive index, and microstructure.

The first bio-superlens was made of cylindrical spider silk, which act as dielectric cylindrical lenses with sub-diffraction focusing ability. The single silk superlens (~6.8 μm in diameter, $n \approx 1.55$) successfully resolved 100 nm-wide surface features under white-light illumination, producing a magnification of approximately 2x [1]. Despite their robustness and reusability, the inherently anisotropic cylindrical bio-lenses cause anisotropic magnification, leading to a twisted image angle relative to the original line pattern.

In contrast, more explorations of bio-superlenses were developed based on isotropic spherical biological cells including yeast, algal, and mammalian cells. Their refractive indices (typically 1.38–1.45) are comparable to that of silica, allowing them to act as transparent micro-lenses when illuminated in aqueous or other host mediums.

Li et al. demonstrated that a single yeast cell, when trapped at the apex of an optical fibre using near-infrared laser tweezers, could resolve sub-wavelength Blu-ray disc features [2]. Jiang's subsequently extended this approach to chains of optically trapped yeast cells, enabling parallel imaging and an enlarged FOV [3]. However, these optical-tweezer configurations require precise three-dimensional control and introduce mechanical constraints that limit throughput and reproducibility.

To overcome these limitations, recent studies have explored bio-superlens arrays and self-assembled configurations. Liao et al. organised MCF-7 cells into hydrogel-templated microlens arrays achieving wide-field imaging with moderate magnification (~1.1–1.2x), though still limited by fabrication complexity and low refractive-index contrast [4]. Other

work investigated the phototactic behaviour of cyanobacteria, where light-induced photonic nanojets inspired concepts for active or self-steering bio-superlenses, yet without direct imaging demonstrations [5].

Despite this diversity of bio-superlenses, most studies remain proof-of-concept or application-driven demonstrations, whereas the optical behaviour of hemispherical and cell-shaped lenses has been largely unexplored. In addition, studies on artificial solid-immersion lenses (SILs) and TiO_2-based metamaterial lenses indicate that super-hemispherical configurations play a crucial role in determining near-field coupling and virtual-image formation. Such a perspective opens a new research avenue, linking biological morphology with near-field optical performance.

Yeast cells are optically transparent, easy to culture, and possess a mechanically stable wall that can maintain shape through various hydration states, making them ideal for systematic study. This chapter therefore examines three representative configurations:

(a) Hydrated Spherical Cells (HS) – naturally hydrated cells freely suspended in liquid;

(b) Chemically Fixed and Dehydrated Spherical Cells (CFD) – chemically treated cells retaining near-spherical form; and

(c) Air-Dried Super-Hemispherical Cells (ADSH) – naturally collapsed cells on solid substrates forming near-super-hemispherical geometries.

By comparing their structural characteristics and imaging performance under identical optical conditions, this study investigates how cell morphology—from fully spherical (HS and CFD) to super-hemispherical (ADSH)—influences near-field coupling and imaging resolution.

To the best of our knowledge, this is the first systematic comparison of yeast cells used as superlenses across different geometries. The following sections present the structural characterisation, imaging behaviour, and supporting simulations for each configuration, establishing how variations in cell shape translate into differences in optical performance.

5.2 Morphology of Yeast Cell Superlenses

The morphologies of three representative structural variants of yeast cells (HS, CFD and ADSH) introduced in the previous section were examined. These groups are defined by their preparation methods and represent distinct structural regimes characterised by different height-to-width ratios, surface textures, and shape integrity. For scanning electron

microscopy (SEM) characterisation, all samples were deposited on silicon substrates and imaged at an 80° tilting angle to characterise their three-dimensional morphology and accurately measure their height-to-width ratios. The following subsections describe and compare these morphological features in detail, supported by SEM observations and statistical analysis.

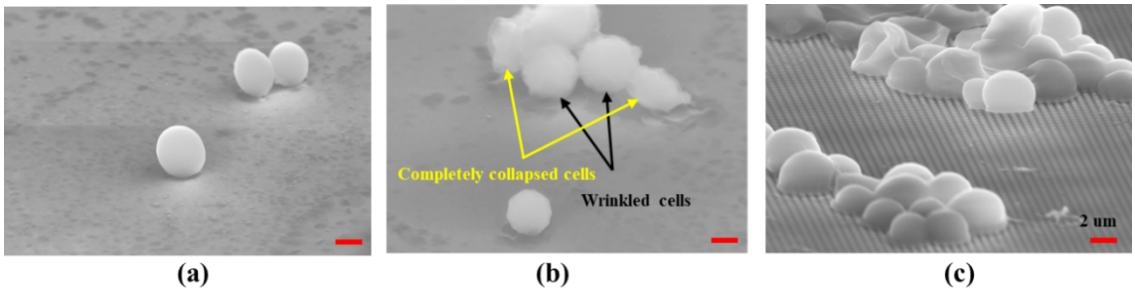

Figure 5.1 SEM images of yeast cell morphologies: (a) CFD with smooth cell wall, (b) cell wall wrinkled and completely collapsed CFD (respectively highlighted by black and yellow arrows), and (c) ADSH cells.

5.2.1 Hydrated Spherical Cells (HS)

This variant refers to naturally hydrated yeast cells that maintain a spherical shape only when suspended in liquid. Due to softness of cell wall, unlike fixed or dried samples, they do not retain this geometry on solid substrates. Therefore, HS cells serve as a baseline model for studying the morphological influence on imaging performance, representing the most straightforward form that can be optically manipulated without any additional chemical fixation treatment. These cells exist only in liquid environments, and upon drying in air they collapse into ADSH cells with super-hemispherical geometries. Their imaging performance under fibre-trapped equipment has been reported in earlier studies and were summarised in Section 2.3.4 [2, 3]. In the present work, only a brief characterisation of their imaging performance is provided in the following section, while the main focus is placed on the latter two variants, for which no prior studies have been reported in the literature.

5.2.2 Chemically Fixed and Dehydrated Spherical Cells (CFD)

CFD cells refer to those yeast cells chemically fixed and dehydrated by glutaraldehyde. Glutaraldehyde served as the primary fixative to crosslink cell wall proteins to form a rigid structural network. This process renders the CFD cells mechanically robust, allowing them to maintain a nearly spherical shape after dehydration.

The CFD cells displayed relatively uniform sizes and high height-to-width ratios (typically

0.90–1.00), indicating that most of them retained a near-spherical morphology after dehydration (Fig. 5.1 a). A small fraction of cells were completely collapsed and unable to preserve their full-spherical geometry due to excessive contraction of the cell wall during drying (as highlighted by yellow arrows in Fig. 5.1 b). Among the cells that remain approximately spherical, mild surface shrinkage and wrinkling are frequently observed, as highlighted by black arrows in Fig. 5.1 (b). This effect is likely caused by the multi-step ethanol dehydration process, during which rapid solvent exchange and surface tension gradients lead to uneven stress on the cell wall, resulting in local folding or crumpling. Even with careful handling during dehydration, such surface wrinkling is difficult to avoid. While the overall morphology is preserved, these fine surface irregularities can scatter light and disturb near-field symmetry, significantly reducing imaging resolution and reproducibility.

5.2.3 Air-Dried Super-Hemispherical Cells (ADSH)

When yeast suspensions were left to dry naturally on a solid substrate without any chemical treatment, the evaporation of water gradually removed buoyant forces and caused the lower hemisphere of each cell to collapse. The resulting geometry formed a distinct super-hemispherical profile, with height-to-width ratios around 0.65–0.85 (Fig. 5.1 c). ADSH cells usually maintain smooth, continuous outer surfaces, since slow and uniform dehydration minimises stress. The increased base contact area enhances mechanical stability and provides stronger optical coupling with the substrate, enabling more efficient interaction with evanescent fields.

5.2.4 Statistical Analysis of Morphological Variation

To ensure that the morphological observations are representative and statistically reliable, quantitative analysis was performed based on a broader set of SEM images. These include extended views of ADSH and CFD cells across large substrate areas to evaluate their surface quality, geometric variations and height-width ratio distribution. This section presents the statistical results derived from these datasets, providing a quantitative basis for the subsequent discussion on their optical performance.

ADSH cells (Fig. 5.2 a, b) and CFD cells (Fig. 5.2 d, e) within randomly selected regions measuring 50 × 50 μm² were examined for height-to-width ratio analysis. As shown in Fig. 5.2 (a, b), the majority of ADSH cells preserved their super-hemispherical configuration while maintaining a smooth outer wall. Such structural integrity and surface uniformity are beneficial for achieving high-quality super-resolution imaging, as they minimise light

scattering and enhance the stability of near-field coupling. This aspect will be discussed in a later section.

In contrast, Fig. 5.2 (d, e) shows that majority of CFD cells exhibit wrinkled outer walls. During SEM imaging, the thicker and smoother regions of the cell generate stable secondary electron signals, appearing uniformly bright, whereas the thin wrinkled areas allow part of the electron beam to penetrate or scatter away from the surface. This reduces the local secondary electron yield and creates an intensity variation, making the wrinkled areas appear semi-transparent in the images. Consequently, although CFD cells may seem relatively smooth at low magnification, their surfaces actually contain fine folds and irregularities that can disrupt optical symmetry and degrade imaging resolution.

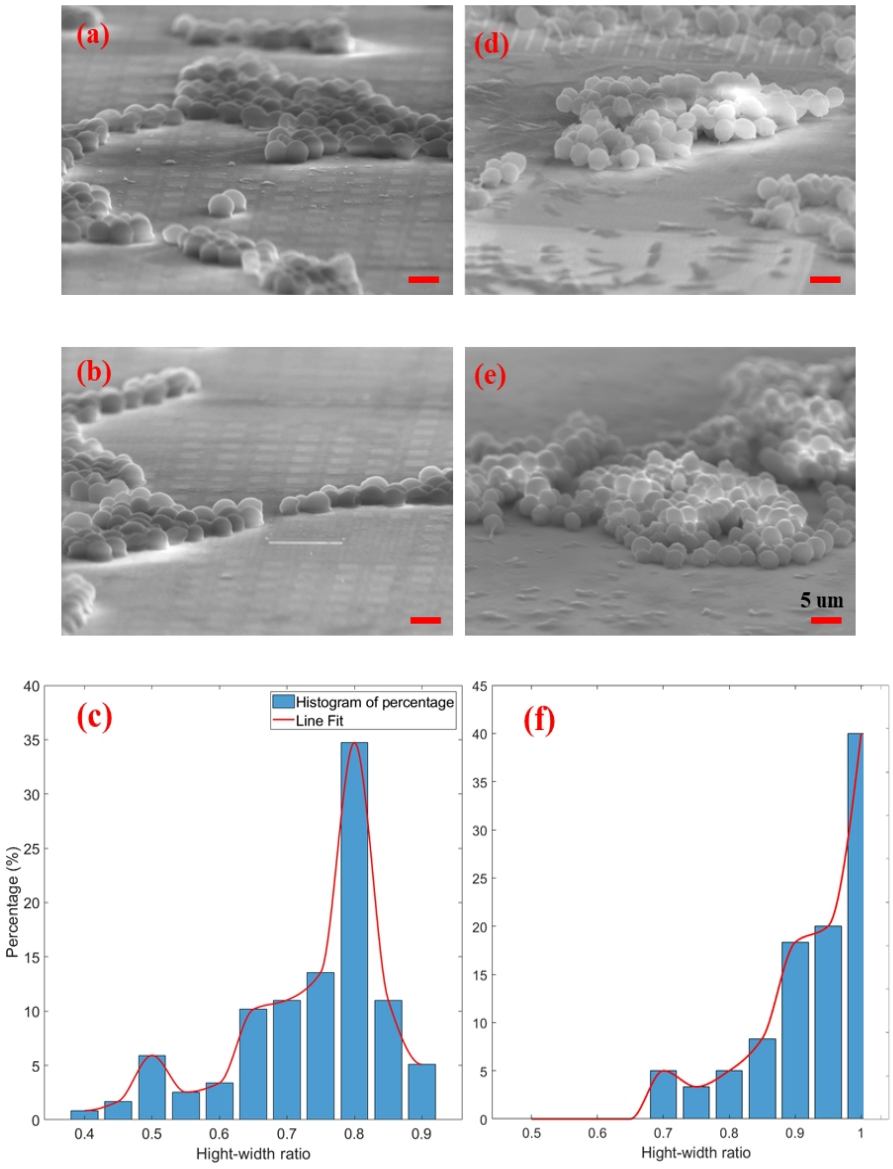

Figure 5.2 Representative SEM images of randomly selected regions (~50 × 50 μm²) containing (a, b) ADSH cells and (d, e) CFD cells, along with their corresponding height-width ratio distributions in (c)

and (f), respectively.

The statistical distribution of height-to-width ratios of are performed in Fig. 5.2 (c, f). Ratios of ADSH and CFD are grouped into uniform bins ranging from 0.4 to 0.9 and 0.5 to 1.0, respectively, with ±0.2 tolerance in the measured values. The resulting histogram was normalised to express the frequency of each bar as a percentage of the total cell count. To better visualise the overall trend, a smooth curve was plotted by connecting the tops of the histogram bars through piecewise interpolation, reflecting the shape of the frequency distribution while preserving the original data values.

The ratio distribution of ADSH cells, shown in Fig. 5.2 (c), exhibits a dominant peak at 0.80, representing 34.7% of all measurements, with secondary peaks at 0.75 (13.6%) and 0.85 (11.0%). By accounting for other ratio regimes, overall, approximately 80% of the cells fall within the high-ratio super-hemispherical range (0.65–0.85), while fewer than 20% lie outside this interval.

In contrast, the ratio distribution of CFD cells, presented in Fig. 5.2 (f), indicates that the majority (41.1%) have a ratio of 1.00, with additional groups around 0.95 (20.2%) and 0.90 (19.5%). Overall, more than 80% of CFD cells exhibit ratios above 0.90, whereas only about 19.2% remain within the super-hemispherical regime (<0.9). These statistical results are consistent with the morphological observations, which show that most CFD cells retain a nearly spherical shape, confirming that the fixation and dehydration processes effectively preserved their structural integrity.

These results clearly show that the two differently prepared cell types present entirely distinct height-to-width ratio distributions. The following section investigates how these morphological variations influence their optical behaviour and super-resolution imaging performance.

5.3 Super-resolution Imaging Performance

The optical imaging performance of the three yeast-cell configurations including HS, CFD, and ADSH was systematically evaluated under wide-field and confocal microscopy to investigate how morphology influences near-field coupling and imaging resolution. In the wide-field configuration, two imaging modes were employed: Bright-field (BF) and Polarised light observation (PO), allowing assessment of both intensity-based and polarisation-sensitive contrast.

Testing both HS and CFD cells in water revealed no consistent measurable super-resolution under either wide-field or confocal imaging. However, when CFD and ADSH cells were examined in air, distinct imaging performance differences emerged. CFD cells behaved as dielectric microspheres, producing sub-diffraction resolution comparable to engineered glass spheres and demonstrating potential as a biocompatible solid-state superlens. ADSH cells, naturally formed through evaporation, exhibited the most consistent and high-contrast imaging, functioning as stable near-field lenses without further processing.

These results highlight the strong dependence of imaging performance on morphology and environmental state. Further details are presented in the following sections for each case.

5.3.1 Full-spherical Yeast Cells

5.3.1.1 Imaging in water

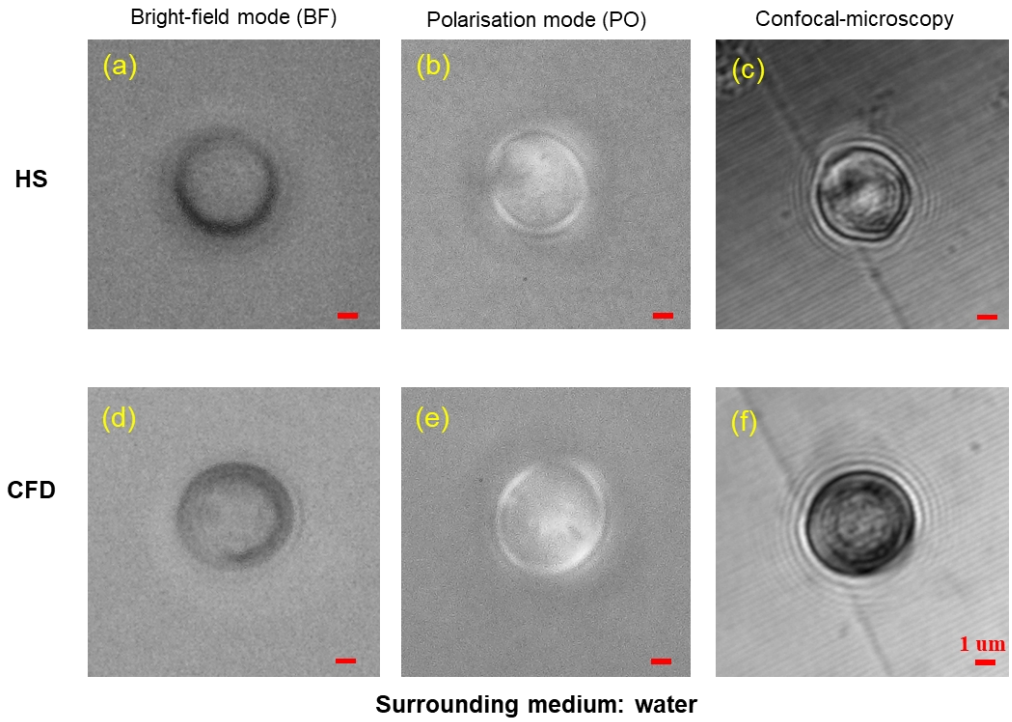

Figure 5.3 Comparative imaging of spherical yeast cells in water. Top row (a–c): HS cells; bottom row (d–f): CFD cells. Imaging modes: BF, PO, and confocal. Scale bar: 1 µm.

Figure 5.3 compares the imaging performance of HS and CFD cells in water, using wide-field (BF and PO) and confocal microscopy. In our case, the fibre trap was not used, in other words, cells were allowed to float freely in water above the Blu-ray disc surface, and images were acquired once the freely floating cells had come to visually remained stable in position.

The comparison results shown in Fig. 5.3 indicate that neither HS (a–c) nor CFD cells (d–f)

were able to resolve the Blu-ray disc pattern under any of the applied microscopy techniques or imaging modes. While confocal microscopy appeared to reveal very limited strip-like patterns within the cell profile, these were insufficient to resolve individual groove structures. The lack of an optical fibre trapping setup and a stable water-film condition are likely responsible for the absence of clear sub-diffraction features in our observations. In previous optical-fibre-trapping studies [2,3], the trapping fibre maintained the cells in close proximity to the sample within a flat aqueous layer, ensuring reproducible near-field coupling. By contrast, our droplet-based environment introduced a curved meniscus and evaporation-driven fluctuations, leading to uncontrolled cell–sample spacing. As a result, yeast cells only occasionally approached the surface closely enough to interact with the evanescent field, but such events were transient and irreproducible. To enable a more rigorous comparison, future studies could employ a microfluidic chamber with tuneable liquid thickness or use interferometric and total internal reflection techniques to directly measure and calibrate the cell–sample distance under both conditions [6–8].

5.3.1.2 Imaging in Air: Wrinkled CFD Cells

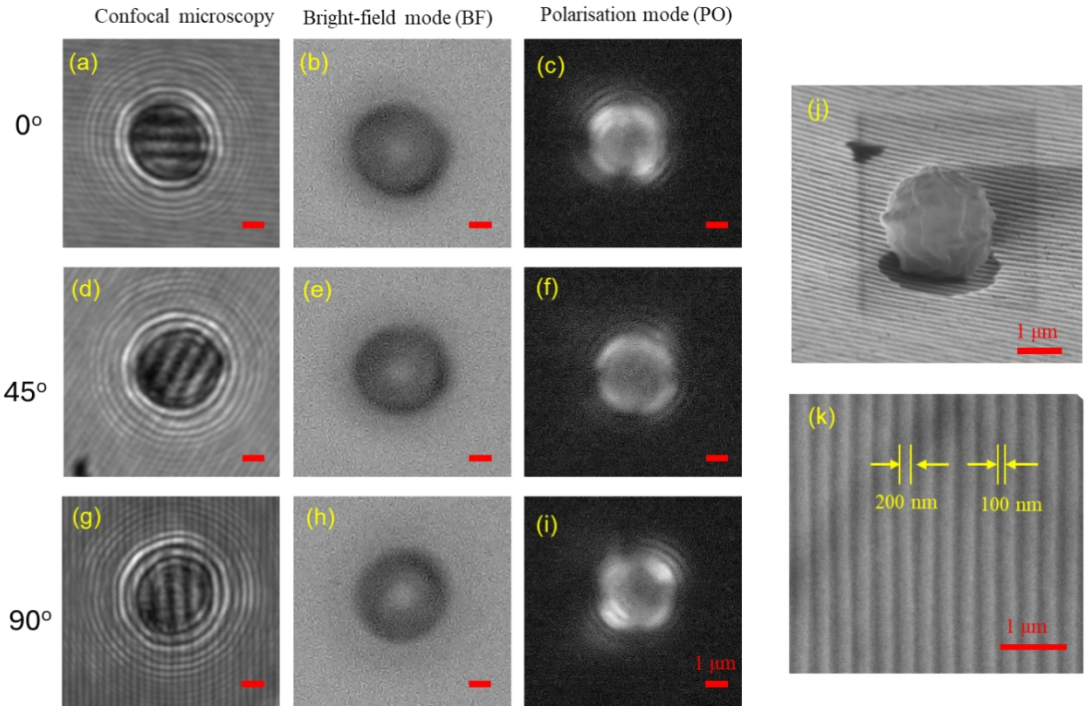

Figure 5.4 (a–i) Sequential confocal (left), BF (middle), and PO (right) images of a wrinkled CFD cell in air with polariser orientations of 0°, 45°, and 90°. (j) SEM image of the cell with 15 nm gold-coating; (k) SEM of Blu-ray disc grooves. The magnification is approximately 2.4x.

When imaged in air, CFD cells exhibited distinct optical behaviour, as shown in Fig. 5.4 (a-i), multimodal imaging was performed on a representative wrinkled CFD cells in air using

confocal, BF and PO modes of wide-field microscopy under polariser orientations of 0°, 45°, and 90°. The introduction of varying polariser orientations is because previous research [9] suggested that Blu-ray discs are polarisation-sensitive. In particular, when imaging the Blu-ray disc through a microsphere, the best image contrast can be achieved when the polariser is oriented at 45° relative to the direction of the disc's grooves.

In this case, after fixation, most CFD cells were unable to resolve the Blu-ray disc patterns under wide-field microscopy. Only confocal microscopy succeeded in resolving the patterns, owing to its shorter illumination wavelength (405 nm vs ~450 nm in white-light imaging), as well as its confocal imaging mode. In the confocal configuration, the pinhole strongly improves optical sectioning by rejecting out-of-focus light, suppressing background scattering and stray illumination, and thereby enhancing image contrast and effective resolution.

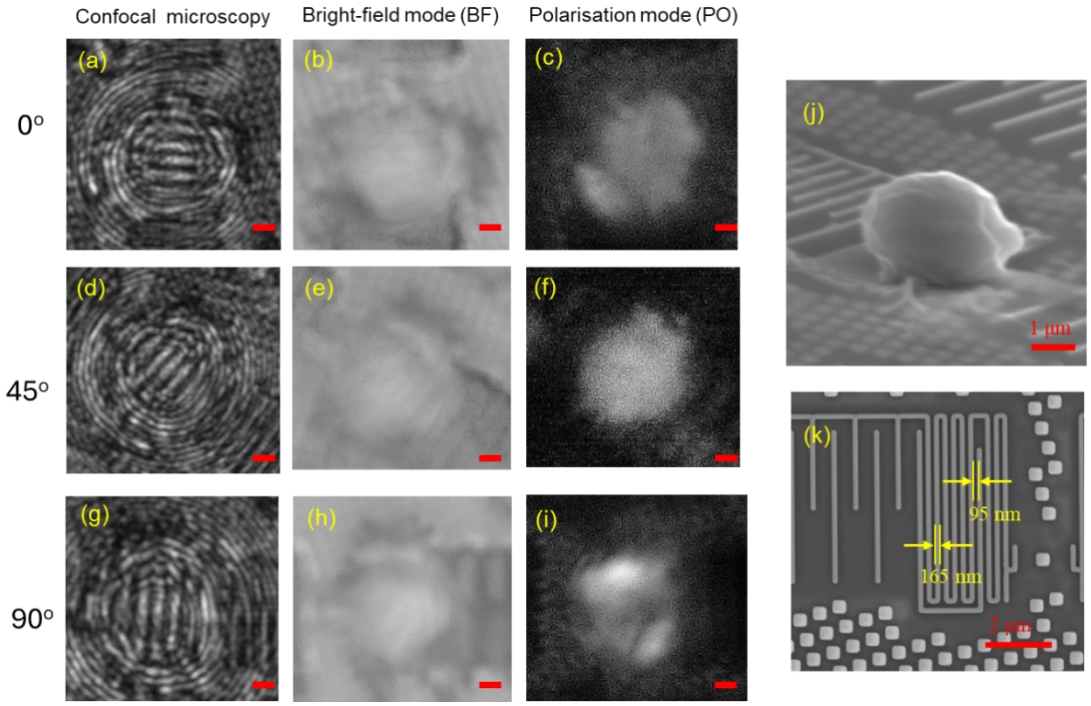

Figure 5.5 (a–i) Sequential confocal (left), BF (middle), and PO (right) images of a wrinkled CFD cell in air with 0°, 45°, 90° polarisations. (j) SEM image of wrinkled CFD cell; (k) SEM image of nanostructured Si chip. The magnification is approximately 2.4x.

Similar experiments on Si chips (Fig. 5.5) yielded comparable results: no subwavelength patterns were resolved under wide-field imaging at all polariser orientations, but confocal microscopy produced weakly resolved features (Fig. 5.5 a, d, g).

The limited performance can be attributed to dehydration-induced surface wrinkling and cell

wall shrinkage, in Fig. 5.4 (j), 5.5 (j), which scatter light and distort the focusing field despite the cells maintaining near-unity height-to-width ratios.

5.3.1.3 Imaging in Air: Smooth CFD Cells

To isolate the effect of surface quality, Smoother CFD cells were re-examined. On Blu-ray disc, confocal microscopy resolved Blu-ray subwavelength 100 nm grooves with high clarity. Under wide-field conditions, no patterns were visible in BF mode at any angle, nor in PO mode at 0° or 90°, however, limited groove patterns became resolvable at 45°. The intensity profiles, taken along the red dashed lines indicated in Fig. 5.6 (c, f, i) and plotted in Fig. 5.6(k), confirmed this observation. At 45°, the profile shows distinct intensity variations corresponding to the ~100 nm-wide Blu-ray grooves.

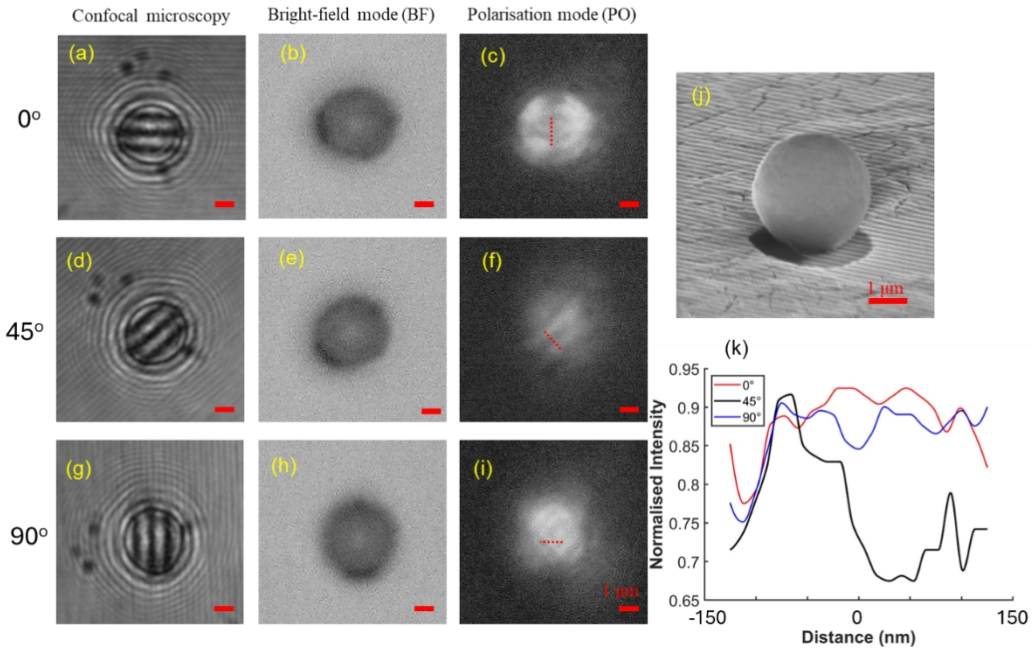

Figure 5.6 (a–i) Sequential confocal (left), BF (middle), and PO (right) images of a smooth CFD cell in air under 0°, 45°, 90° polariser orientations. (j) SEM image of the cell with 15 nm gold-coating; (k) intensity profiles along red dashed lines in (c), (f), (i). The magnification is approximately 2.4x.

Further experiments on Si chip (Fig. 5.7) confirmed this trend. Smooth CFD cells achieved significantly improved imaging contrast compared with wrinkled ones. Under wide-field imaging in BF mode, the 95 nm gaps on the Si surface could be resolved at all three polariser orientations. However, the corresponding intensity profiles (Fig. 5.7 k) revealed that the image contrast at 0° and 90° was considerably lower than that at 45°. In particular, at 0°, only a single groove was weakly resolved with limited contrast, while the intensity profile at the position corresponding to the second groove exhibited random fluctuations. For PO images, however, failed to reveal distinct features at any angle, suggesting that the enhancement

originates mainly from near-field focusing rather than polarisation filtering.

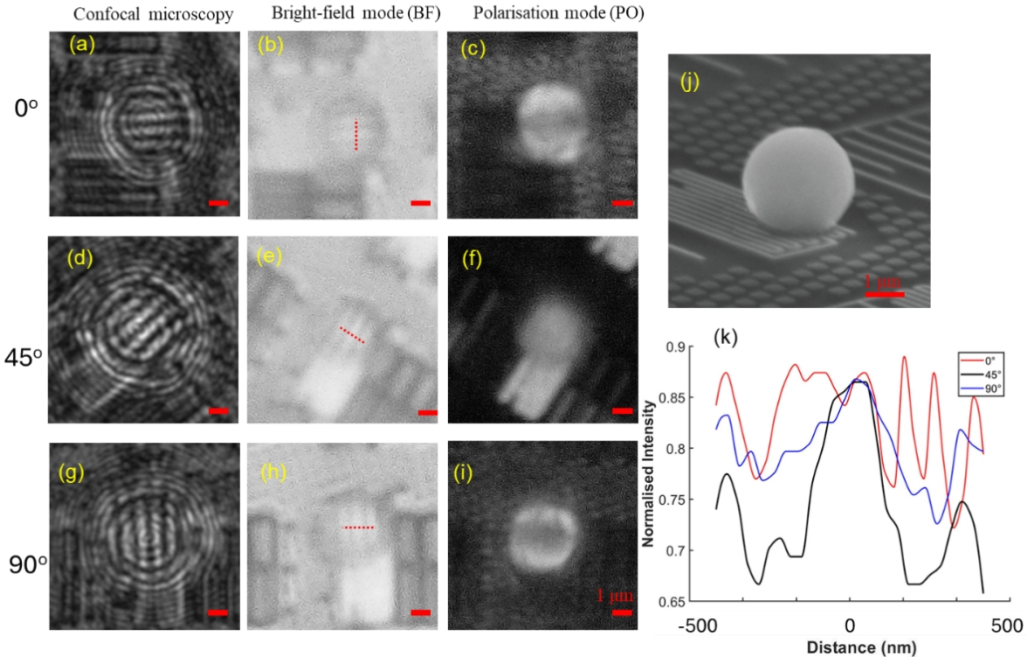

Figure 5.7 (a–i) Sequential confocal (left), BF (middle), and PO (right) images of a CFD cell in air with polariser orientations of 0°, 45°, and 90° (rows 1–3). (j) SEM image of CFD cell. (k) Intensity profiles along red dashed lines in images (b), (e) and (h), respectively. The magnification is approximately 2.4x.

5.3.1.4 Summary of Full-Spherical Cell Imaging

The key results of full-spherical cells are summarised as follows:

1. HS cells (in water): No super-resolution observed; unstable immersion prevents consistent near-field coupling.

2. Wrinkled CFD cells (in air): Limited enhancement; surface wrinkles cause scattering and focus distortion.

3. Smooth CFD cells (in air): Clear sub-diffraction imaging, strongest at 45° polarisation; act as functional dielectric microspheres.

5.3.2 Super-hemispherical Yeast Cells

5.3.2.1 Imaging on Blu-ray Disc: ADSH cells

Unlike the full-spherical yeast cells, the ADSH cells exhibit significantly improved morphological uniformity. Almost all cells preserve a complete, well-defined super-hemispherical shape, and their cell walls remain smooth rather than wrinkled caused by multi-step dehydration during chemical fixation. As a result, the transmitted and focused light

fields become more stable and coherent, leading to clearer and higher-contrast imaging performance.

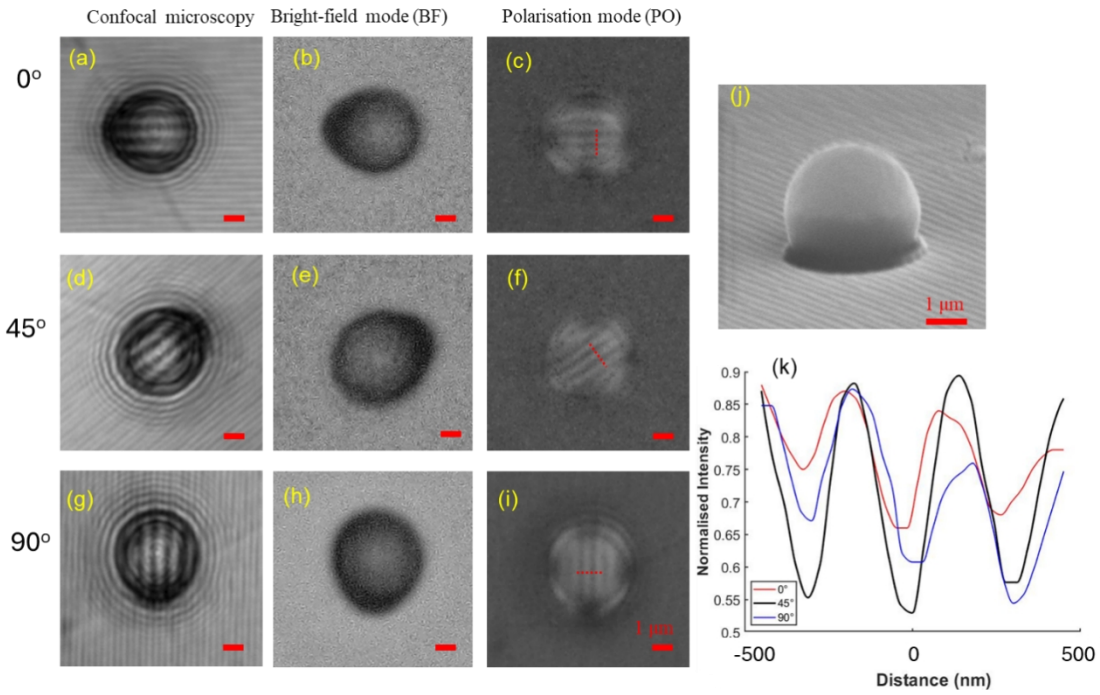

Figure 5.8 (a–i) Sequential confocal (left), BF (middle), and PO (right) images of an ADSH cell in air under polariser orientations of 0°, 45°, and 90° (rows 1–3). (j) SEM image of the cell with 15 nm gold-coating. (k) Intensity profiles along the red dashed lines in images (c), (f), and (i), respectively. The magnification is approximately 2.0x.

The imaging results of an ADSH cell (Fig. 5.8 j) placed on a Blu-ray disc are presented in Fig. 5.8 (a–i). Under BF mode with unpolarised illumination (Fig. 5.8 b, e, h), the subwavelength groove patterns were not resolved, which was consistent with the behaviour observed for spherical cells. However, once the imaging mode was switched to PO mode, a remarkable improvement was observed. In contrast to a few of smooth CFD cells, which could only partially resolve the Blu-ray grooves at polariser orientations of 45°, the ADSH cell successfully revealed the subwavelength structures all three tested polariser orientations. The normalised intensity profile shown in Fig. 5.8 (k) indicates that the highest contrast occurs at 45°, which in agreement with previous findings [9]. Moreover, although the grooves patterns remain resolvable at 0° and 90°, their contrasts are noticeably lower—specifically, the lowest at 0°, followed by 90°. This clear polarisation dependence indicates that the super-hemispherical geometry provides strong and stable near-field coupling across different orientations.

5.3.2.2 Imaging on Si Chip: ADSH cells

Further measurements were conducted using ADSH cells placed on a nanostructured Si chip, as shown in Figure 5.9. Under confocal microscopy, the subwavelength pattern was clearly resolved. More importantly, under BF mode, ADSH cell successfully revealed the subwavelength structures all three tested polariser orientations, with highest and sharpest contrast occurring at 45°, as evidenced by the intensity profile in Fig. 5.9 (k).

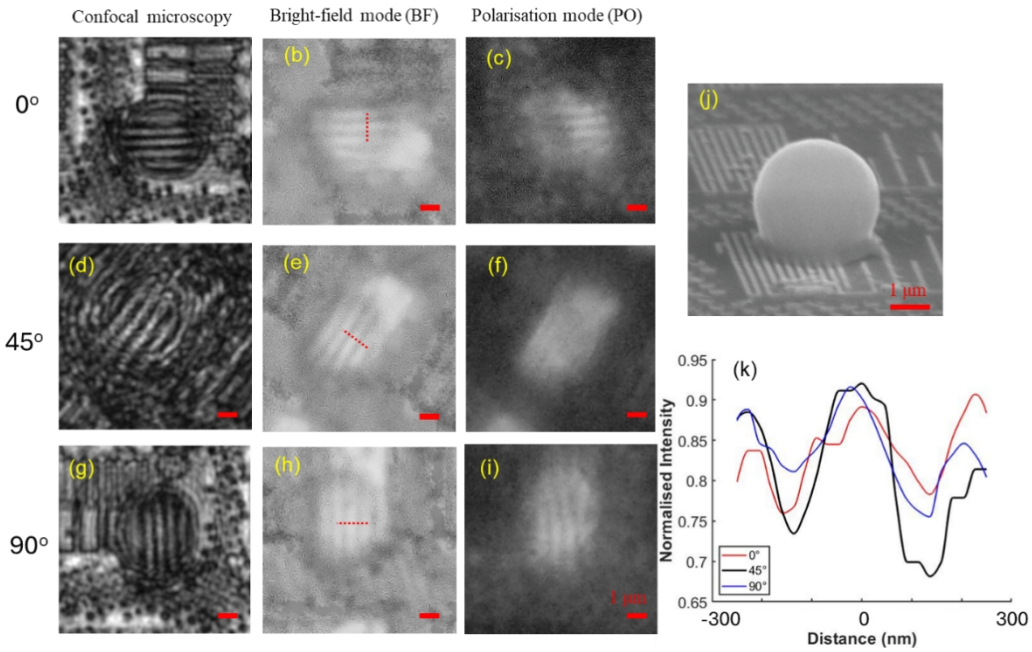

Figure 5.9 (a–i) Sequential confocal (left), BF (middle), and PO (right) images of an ADSH cell in air with polariser orientations of 0°, 45°, and 90° (rows 1–3). (j) SEM image of the cell. (k) Intensity profiles along red dashed lines in images (b), (e) and (h), respectively. The magnification is approximately 2.0x.

In contrast, under PO mode, the pattern could only be resolved at 0° and 90°. At 45°, strip-like features were observed, but they were insufficient to fully reveal the subwavelength pattern. This reversal in polarisation response compared with Blu-ray disc surfaces likely arises from the difference in surface material and refractive-index contrast, which modifies local field distributions at the cell–substrate interface.

5.3.2.3 Summary of ADSH Cell Imaging

The key results are summarised as follows:

1. Blu-ray disc imaging: Clear subwavelength resolution achieved in PO mode at all polariser orientations; strongest contrast at 45° polarisation.

2. Si chip imaging: Stable, reproducible sub-100 nm resolution under BF mode at all orientations, particularly under 45° polarisation; polarisation-dependent contrast variations

linked to substrate effects.

Overall, the ADSH geometry provides the most stable and consistent super-resolution imaging performance among all cell configurations studied. The natural drying process produces an optimised geometry for near-field coupling, offering a simple, low-cost, and reproducible route to biological superlenses suitable for practical imaging applications.

5.4 Simulation Analysis and Discussion

To further investigate the experimental differences in imaging performance under various polariser orientations, numerical simulations were conducted using CST Studio (High Frequency module, Time Domain Solver). The analysis focused on the three-dimensional super-hemispherical configuration (ADSH cells), which demonstrated the most consistent and reproducible imaging performance among the three cell types. In contrast, since the CFD cells did not achieve an ideal fixation, it was difficult to obtain spherical geometries comparable to those of dielectric microspheres. Moreover, their imaging performance was inferior to that of the ADSH cells.

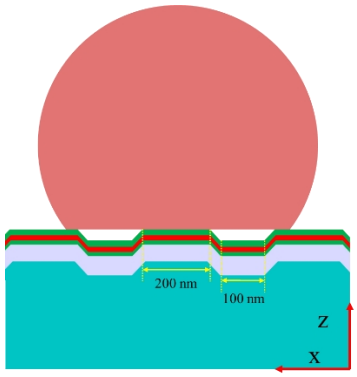

Figure 5.10 Schematic illustration of the super-hemispherical yeast (ADSH) cell placed on the Blu-ray disc substrate, where different colours represent the multilayer structure. For the Si chip model, each layer was simplified and defined as pure Si to maintain the same morphology as the Blu-ray model.

As illustrated in Fig. 5.10, a simplified 3D super-hemispherical configuration was constructed to represent ADSH cells. Specifically, it has a height-width ratio of 0.8 and was placed directly above a nanostructured substrate. Two types of substrates considered: a multilayer Blu-ray disc and a homogenous and single-layer Si chip. The Blu-ray disc consisted of a substrate layer, an Ag-alloy reflective layer, a ZnS–SiO_2 dielectric layer, an inorganic recording layer, and a top ZnS–SiO_2 dielectric layer [10]. The thicknesses of each layer were set to infinite (substrate), 100 nm, 10 nm, 12 nm, and 25 nm. The structural dimensions (200

nm strip width and 100 nm groove width) and material optical constants were defined to closely correspond to the actual samples. The Si chip model was derived directly from the Blu-ray disc structure to ensure morphological consistency for comparison. Therefore, instead of using the actual structural parameters of the Si chip, all layers were defined as pure silicon based on the Blu-ray disc 3D model. This simplification was intended to isolate the simulation variables, particularly the influence of varying structural geometry on the optical response.

Figure 5.11 presents the actual 3D models implemented in CST Studio, in which the groove orientation on the substrate was set at a 0°, 45° and 90° angle relative to the analyser polariser orientation. A linearly polarised plane wave with wavelength of 455 nm (100% y-polarised) was set propagating along the −z direction, illuminating the cell–substrate model. The electromagnetic field distributions were calculated in the time domain, and the electric field intensity of scattered light was extracted at the upper boundary of the cell, representing the light captured by the far-field receiver or microscope objective. To quantify the polarisation angle-dependent scattering efficiency, the electric field components were integrated along both the x and y directions. The conversion ratio was then defined as the integral of the x-polarised field intensity divided by that of the y-polarised component. This ratio provides a quantitative measure of cross-polarisation coupling induced by the cell–substrate interaction.

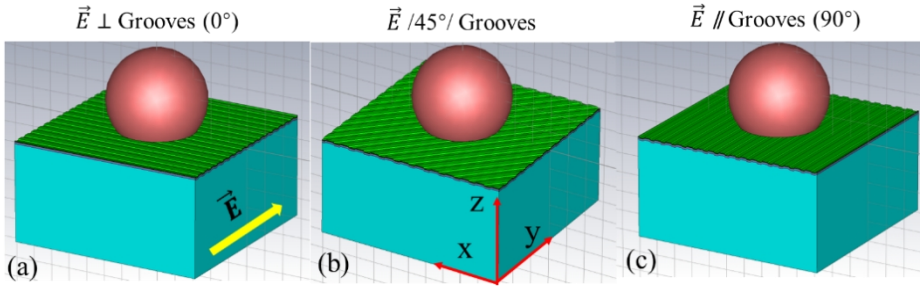

Figure 5.11 Three-dimensional CST models of ADSH cells on nanostructured substrates constructed in CST Studio under polariser orientations of (a) 0°, (b) 45°, and (c) 90°, respectively.

The simulated conversion efficiencies are summarised in Table 5.1 and visualised in Fig 5.12. It can be observed that only a small fraction of the scattered light was converted into the x-polarised component. However, the conversion efficiency reached its maximum when the polariser orientation was 45°, followed by 90°, and was the lowest at 0°. This trend is consistent with the experimental imaging results presented in Section 5.3.2, where the best image contrast was also obtained at 45°. The enhanced x-polarisation conversion at this orientation indicates stronger coupling between the incident electric field and the

subwavelength grooves. In contrast, at 0° and 90°, the lower converting efficiency between the polarisation direction and groove orientation reduces coupling efficiency, leading to weaker field confinement and lower contrast in the far-field image.

Table 5.1 Percentage of the y-polarised incident light converted into x-polarised components in the far field for Blu-ray and Si samples under different polariser orientations (0°, 45°, and 90°).

Polariser orientation	Blu-ray disc	Si Chip
E /45°/ Line	**3.89%**	**4.14%**
E// Line (90°)	**3.10%**	**2.95%**
E ⊥ Line (0°)	**2.15%**	**2.10%**

In summary, these simulation results provide clear physical evidence that the superior imaging performance of ADSH cells originates from the interplay between cell morphology and polarisation-dependent near-field coupling. The smooth super-hemispherical geometry enables efficient confinement and directional scattering of the incident light, while the 45° polarisation aligns the electric field with the optimal coupling direction of the subwavelength grooves. This combined effect explains the experimentally observed maximum contrast and consistent sub-diffraction resolution obtained under this condition.

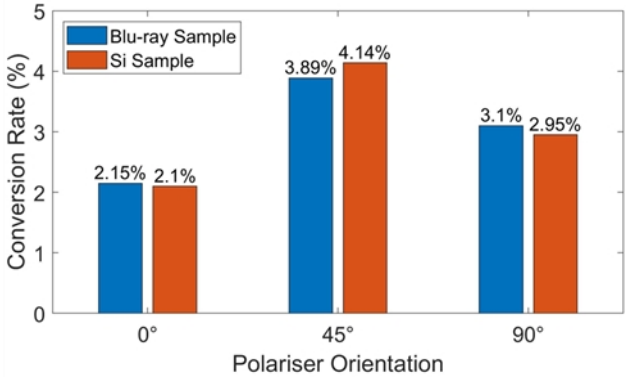

Figure 5.12 Bar plot showing the percentage of y-polarised incident light converted into x-polarised components in the far field for Blu-ray and Si samples under polariser orientations of 0°, 45°, and 90°. These values are based on the conversion efficiencies reported in Table 5.1.

5.5 Summary

In this chapter, three morphological variants of yeast cells (HS, CFD and ADSH), were systematically characterised and evaluated as bio-superlenses. SEM analysis revealed that chemical fixation preserved the global cell shape, however, surface wrinkles were observed in most of CFD cells, which degraded optical performance. In contrast, the ADSH cells exhibited smoother surfaces and superior morphological uniformity, providing more stable

light focusing and higher imaging contrast.

Optical imaging experiments demonstrated that only the super hemispherical yeast cells achieved consistent subwavelength resolution on both Blu-ray disc and Si chip substrates. The imaging contrast was strongly dependent on the polariser orientation, reaching its maximum at 45°, which corresponds to optimal coupling between the incident field and the groove direction.

Numerical simulations further indicate this polarisation dependent behaviour and confirmed that enhanced conversion efficiency from y- polarised to x- polarised components occurs at 45°, leading to an improved near field confinement and far field image contrast.

Overall, the combined experimental and simulation results highlight the critical role of cellular morphology and polariser orientation in determining the optical response of bio-derived superlenses. These findings provide mechanistic insight and design guidance for developing stable, cost-effective biological superlenses for future near-field imaging applications.

5.6 References

[1] J. N. Monks, B. Yan, N. Hawkins, F. Vollrath, Z. Wang, “Spider Silk: Mother Nature’s Bio-Superlens,” Nano Lett. 2016, 16, 9, 5842–5845.

[2] Y. Li, X. Liu, B. Li, “Single-cell biomagnifier for optical nanoscopes and nanotweezers,” Light Sci Appl. 2019, 8, 61.

[3] C. Jiang, Y. Yue, B. Yan, T. Dong, X. Cui, P. Chen, Z. Wang, “Label-free non-invasive subwavelength-resolution imaging using yeast cells as biological lenses,” Biomed. Opt. Express. 2021, 12, 11, 7113–7121.

[4] X. Liao, H. Yu, Z. Ge, T. Zhang, Y. Zhong, B. Liu, L. Liu, “Assembly method of biological lens array based on maskless lithography,” Sci Sin Tech. 2023, 53, 4, 536–546.

[5] N. Schuergers, T. Lenn, R. Kampmann, M. V. Meissner, T. Esteves, M. Temerinac-Ott, J. G. Korvink, A. R. Lowe, C. W. Mullineaux, A. Wilde, “Cyanobacteria use micro-optics to sense light direction,” eLife. 2016, 5, e12620.

[6] K. D. Hammond, J. B. Freund, and M. L. Perl, “Control of cell–substrate separation using microfluidic confinement,” Lab Chip. 2014, 14, 12, 2295–2302.

[7] L. Rovati, L. D. Cecilia and S. Cattini, “On the Feasibility of Absolute Distance Measurement by Using Optical Feedback Into a Superluminescent Diode Cavity,” IEEE Trans. Instrum. Meas. 2020, 69, 5, 2495–2506.

[8] G. A. Truskey, J. S. Burmeister, E. Grapa, and W. M. Reichert, “Total internal reflection fluorescence microscopy (TIRFM): II. Topographical mapping of relative cell/substratum separation distances,” J. Cell Sci. 1992, 103, 2, 491–499.

[9] R. Ye, X. Zhang, L. Zhi, Y. Cao, S. Melinte, Z. Wang, S. Yang, “Microsphere-assisted super-resolution polarized light microscopy for polarization-sensitive materials,” Opt. Lett. 2025, 50, 3, 908–911.

[10] Y. Hosoda, T. Izumi, A. Mitsumori, F. Yokogawa, S. Jinno, H. Kudo, “Inorganic recordable disk with more eco-friendly material for blue,” Jpn. J. Appl. Phys. 2003, 42, 1040–1041.

Chapter 6 Wide-angle Metamaterial Edge Filter

6.1 Introduction

As reviewed in Chapter 2, conventional thin-film interference filters exhibit strong angular sensitivity. Increasing the AOI alters the effective optical path length and phase thickness in the multilayer stack, resulting in a pronounced spectral blue-shift and degraded transmission or blocking characteristics.

Several advanced structural strategies have been proposed to address this issue. While 1D, 2D, and 3D PhCs can achieve certain degrees of angular tolerance through periodic structural design, their spectral stability and tunability are often constrained by intrinsic interference effects, and their fabrication, especially for 2D and 3D structures, is usually complex and costly [1–3]. Hyperbolic metamaterials enable angle-invariant propagation for TM polarisation, yet high metallic absorption limits their transmission efficiency, and their anisotropic design poses broadband challenges [4].

Among recent developments, Lotti et al. demonstrated a “small-shift” metamaterial long-pass edge filter using a single meta-film layer (MFL) of SiNS array [5]. While this approach showed reduced spectral shift compared to conventional thin films, it lacked substrate and ARC integration, resulting in insufficient blocking below 400 nm and limited transmission above 900 nm.

In this work, we introduce a multi-layer SiNS design that significantly increases the blocking performance in the short-wavelength stop band, together with an optimised MgF_2 ARC to substantially boost transmission in the long-wavelength pass band. The proposed configuration achieves an optical density of OD = 2.55 at AOI = 60° (TE polarisation)—corresponding to only 0.28% residual transmission—while maintaining a stable pass-band with minimal spectral shift across a wide angular range from 0° to 60°. Compared to all other reported metamaterial edge filters, this design delivers superior angular robustness, higher blocking efficiency, and improved pass-band throughput. Such performance is particularly critical for applications such as wide-angle imaging, hyperspectral sensing, laser protection, and aerospace optics, where consistent spectral response is required under varying incidence angles. Furthermore, a design protocol which combines both numerical simulations based on FIT, and analytical optimisation based on TMM was proposed and successfully applied in

designing above filters presenting a new design paradigm for optimising such similar filters.

6.2 Optical Response of a Single Nanosphere

To aid the understanding of the underlying nanoparticle behaviour, we first examined the extinction and transmission characteristics of a SiNS (R_{SiNS} = 70 nm), without and with a gold shell (T_{shell} = 20 nm), embedded in various dielectric environments. These results are summarised in Fig. 6.1. Sub-image (a) reveal that single SiNS exhibits strong extinction in short wavelength regime. According to ref. [6], when the size of SiNS is small compared to the operating wavelength, this strong extinction is attributed to electric and magnetic dipole resonances, as seen the black solid line in Fig. 6.1 (a), respectively. As a result, a stop-band is generated approximately from 350–600 nm in image (b). However, for the pass-band out of resonances wavelength, the optical response of SiNS as well as host medium can be described by the average refractive index of dielectric material and silicon. Therefore, incident light can pass through the MFL with very few extinctions.

Furthermore, the host refractive index significantly influences both resonance strength and spectral position. This analysis supports the selection of SiNS core and motivates the parameter space used in our design optimisation. Although such single-particle models cannot fully capture the complex interactions in periodic arrays, they offer essential physical insights for guiding multilayer configuration choices. These single-particle observations inform the design of periodic structures with enhanced spectral control.

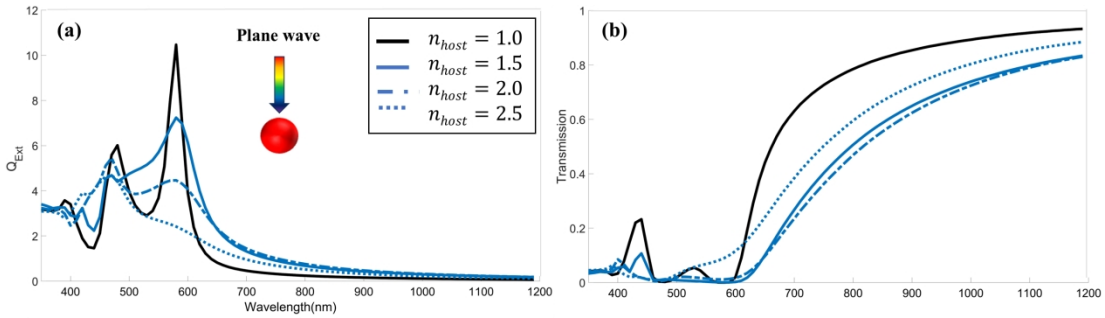

Figure 6.1 (a) Extinction coefficients and (b) approximated transmittance spectra as a function of incident wavelength for a single silicon nanosphere (SiNS, R_{SiNS} = 70 nm) under varying refractive indices of the host medium.

6.3 Wide-angle edge filter design

In this work, we introduce a multi-layer design that can significantly increase the blocking performance in the stop-band, as well as the application of an ARC design to substantially

boost the transmission performance in the long-wavelength pass-band. This innovation yields an edge filter that surpasses all other reported metamaterial filters in the literature, delivering a high optical density (OD = 2.55, 0.28%) with minimal spectral shift across an extensive angular range (0°–60°). Such a performance is crucial for a multitude of applications that demand consistent results over various angles of incidence.

6.3.1 Conventional Edge Filter

A conventional thin-film edge filter (LP0) was presented to illustrate the typical blue-shift behaviour under oblique incidence. LP0 is an example conventional edge filter, which uses SiN and MgF_2 as high- and low-index materials with a refractive index from reference [7, 8], respectively. Fig. 6.2 depicts the transmission spectra of a conventional edge filter (LP0 design) based on classical thin-film technology. LP0 consists of 49 layers of high and low refractive index materials, and its configuration is shown in Table 6.1, in which the quarter-wavelength thicknesses of the high (SiN) and low index (MgF_2) material (with 445 nm as a reference wavelength) are represented as H and L, respectively. The constant 0.8 allows the edge wavelength to be tuned to approximately 500 nm at normal incidence.

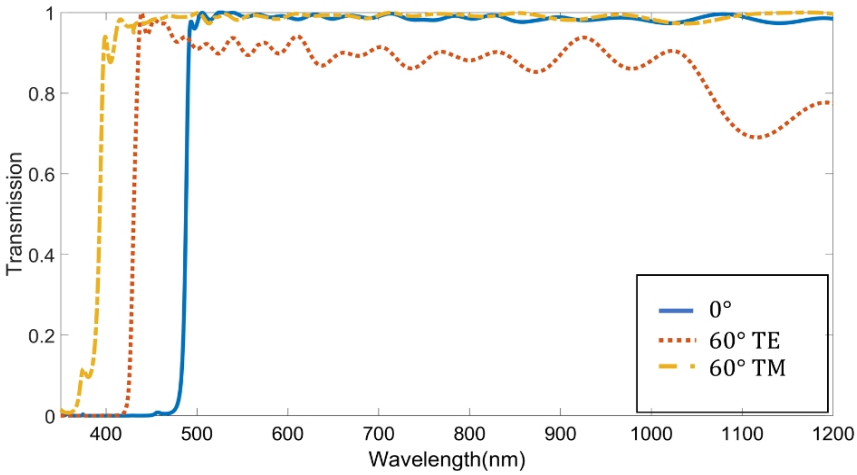

Figure 6.2 A classical edge filter exhibiting blue-shift phenomena.

The blue shift of the spectrum is approximately 80 nm when the incident angle is increased from 0° to 60° for the TE waves and 100 nm for the TM waves. The blue shift in the thin-film filters at increased angles of incidence results from changes in phase thickness and the variation of effective admittance, influenced by the Brewster angle, which separates the band edges at higher angles [9]. This shift does not satisfy the requirements for numerous applications. Ideally, the wavelength shift should be less than 10 nm for it to be suitable for practical applications.

6.3.2 Metamaterial Based Edge Filter Configurations

Fig. 6.3 presents the designs used in this study, focusing on the integration of SiNSs within various configurations, as follows:

(a) The foundational design features a single SiNS within a host medium.

(b) The single-layered unit cell arrays SiNSs homogeneously, exploring basic optical manipulations.

(c, d) Multi-layered variants stack such units to refine the edge characteristics.

(e) The final design adds MgF_2 as the ARC, with the thickness determined by ESM, to the multi-layer structure, optimising transmission.

We chose MgF_2 as the material for the ARC due to its low refractive index (~1.38), which falls between the refractive index of the air and MFLs. Additionally, it offers high transparency across a broad wavelength range from UV to IR bands and stable mechanical properties [10].

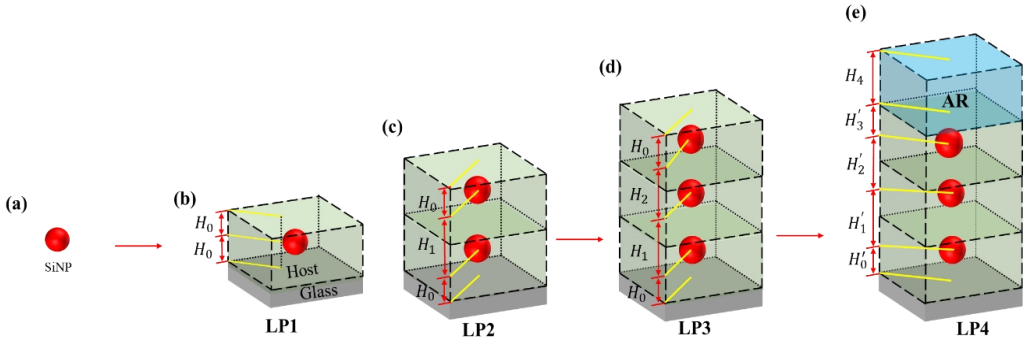

Figure 6.3 Design schematics for edge filters: (a) A SiNS that should be embedded in the host medium. (b) Single-layered unit cell. (c) Two-layered unit cell. (d) Three-layered unit cell. (e) Three-layered unit cell with ARC.

We categorize the designs as follows:

LP1–LP4 are all composed of infinite unit cells in a primitive cubic lattice configuration with a fixed period of D = 145 nm. In each MFL, one unit cell consists of a SiNS with a radius of R = 60 nm and a refractive index from reference [11] embedded in the dielectric SiN host medium and a glass substrate [12]. The dispersion of all used materials was considered, and the corresponding wavelength-dependent refractive indexes are depicted in *Appendix B*. The numerical simulations conducted using CST employed a mesh accuracy of λ/10 for the host

material and $R/5$ for the SiNSs, with a wavelength ranging from 350 nm to 1200 nm. The distance of the incident port is three times the length of the longest wavelength (1200 nm), totalling 3600 nm. The output port is directly connected to the bottom surface of the substrate to emulate a thick substrate of more than 100 μm thick.

Table 6.1 The configuration of 5 long-pass (LP) edge filters used in this paper. LP1-LP4 are metamaterial-based edge filters, and their corresponding unit cell figures are listed in the brackets.

Design ID	Long-Pass (LP) Edge Filter (H: High-index material layer with quarter-wavelength thickness, L: Low-index material layer with quarter-wavelength thickness, and the reference wavelength is 445 nm) (M: meta-layer, ARC: MgF_2 used as anti-reflection coating)
LP0	$Air\|0.8(0.5H\ L\ 0.5H)^{12}\|Glass$
LP1	$Air\|M\|Glass$ (Fig 5.3 b)
LP2	$Air\|(M)^2\|Glass$ (Fig 5.3 c)
LP3	$Air\|(M)^3\|Glass$ (Fig 5.3 d)
LP4	$Air\|ARC\|(M)^3\|Glass$ (Fig 5.3 e)

The ACR design process leverages the ESM software's needle synthesis function, which differs from the simple quarter-wave design at one wavelength. Specifically, ESM incorporates the effective index of the MFL and employs needle synthesis for calculating the anti-reflective coating, with the capability of targeting multiple transmission peaks across various wavelengths, rather than optimising for a single wavelength.

6.3.3 Design and Optimisation Processes

In this work, the term 'stop-band' (350 nm–480 nm) denotes the band where the optical density (OD =-logT) exceeds 1, while the cut-on wavelength ($\lambda_{cut\text{-}on}$) is defined as the wavelength where T equals $0.5T_{peak}$. The pass-band extends from the edge wavelength to 1200 nm.

Fig. 6.4 presents the key results on the transmission spectra contour plot for the four edge filter designs, LP1, LP2, LP3, and LP4 (λ_{edge}~500 nm), based on SiNSs metamaterials under various AOI, as calculated by the CST. This result incorporates physics such as single particle resonance modes (dipole or high-order modes), near-field interactions of neighbouring particles, and periodic effects resulting from the unit cell designs [5, 6]. Both TE and TM incident polarisations are considered. The designated edge wavelength of 500 nm can be adjusted by modifying the particle size and the host material, as detailed in section 6.3.5 below.

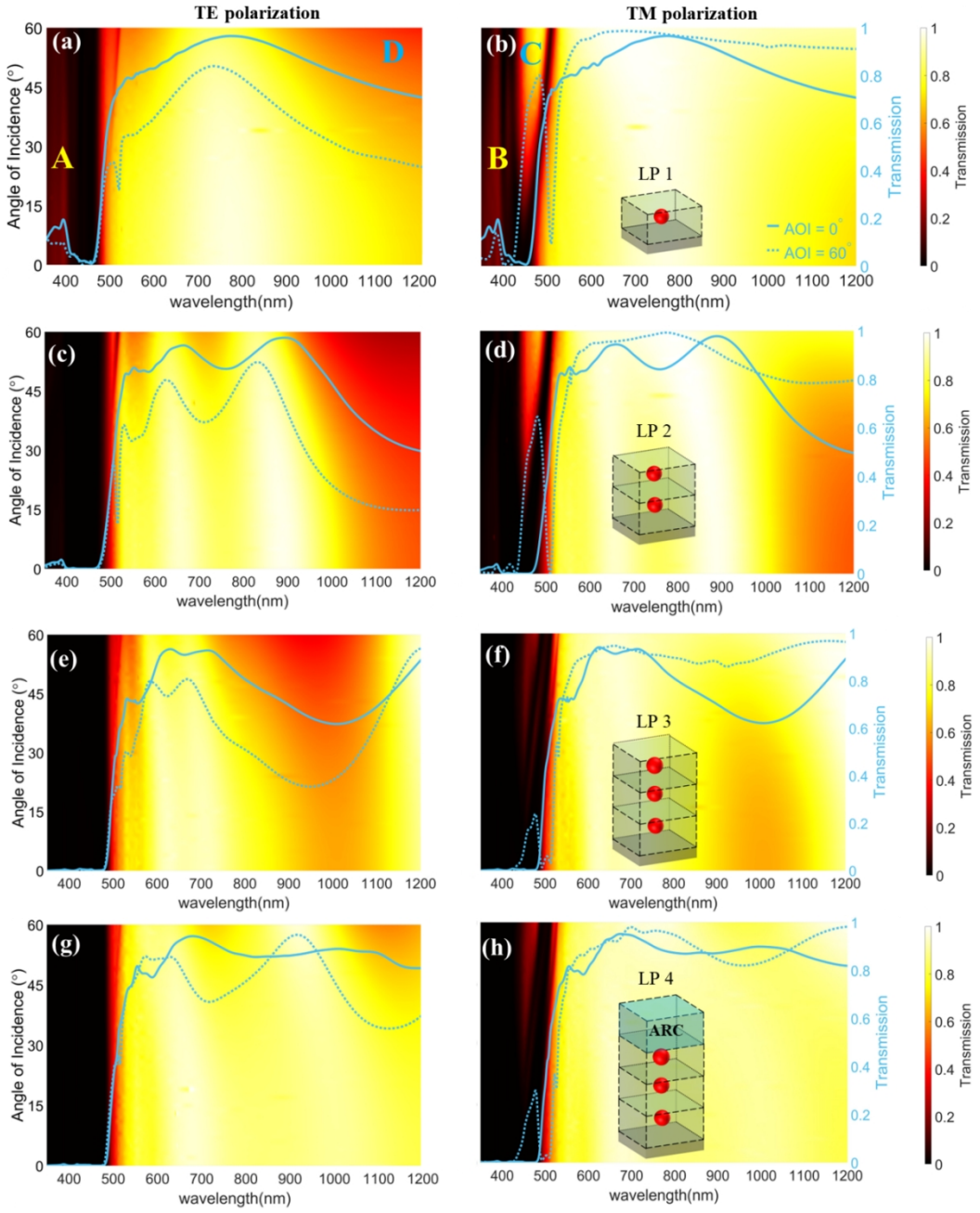

Figure 6.4 Transmission spectra contour plot for LP1 (a, b), LP2 (c, d), LP3 (e, f), and LP4 (g, h)

designs and with TE (left column) and TM (right column) polarisations. The solid and dashed lines denote transmissions at 0° and 60° incident angles, respectively. Zones A, B, C, and D in (a, b) highlight targeted undesired peaks for elimination in subsequent designs.

LP1 design Fig. 6.4 (a, b): This single-layer design, which is akin to the study by Lotti et al. [5], incorporates a new glass substrate for practical considerations. Consequently, although the results slightly differ from those in reference [5], all of the key features remain consistent, as follows: there is a clear demonstration of edge filter behaviours and wide-angle performance, alongside poor performances in both the stop band and the pass band. In the stop band (wavelength <480 nm), weak blocking performance occurs below 400 nm for all of the AOIs, denoted by undesired peaks in Zones A, B, and C in Fig. 6.4 (a, b), respectively. Meanwhile, in the pass-band, the overall transmission in the NIR regime significantly attenuates as the TE-polarised AOI increases, as marked by Zone D in Fig. 6.4 (a). Overcoming these challenges proves daunting, due to the single-layer design's restricted parameter adjustability. However, the integration of the multi-layer and ARC designs furnishes additional design flexibility, effectively mitigating these issues in LP1.

LP2 design Fig. 6.4 (c, d): The implementation of the second layer (H_1 = 255 nm) can instantly improve the blocking performance in Zones A and B, due to the greater absorption offered by an extra layer of SiNSs. The H_1 = 255 nm was determined by the parametric scanning of the CST STUDIO to extend the high transmission band in the NIR wavelength regime while maintaining a sharp edge, as shown in Fig. 6.5. In addition, Fig. 6.4 (d) indicates that the peak in Zone C can slightly suppress but is still unacceptable. We also observed a decrease in the transmitting performance in the longer wavelength (>900 nm), which can be attributed to the increased optical thickness of the host medium. This causes a mismatch between the admittance of the host medium layer and that of the air. However, we demonstrate that such undesired effects can be mitigated by incorporating an ARC, as illustrated in the final optimised LP4 design.

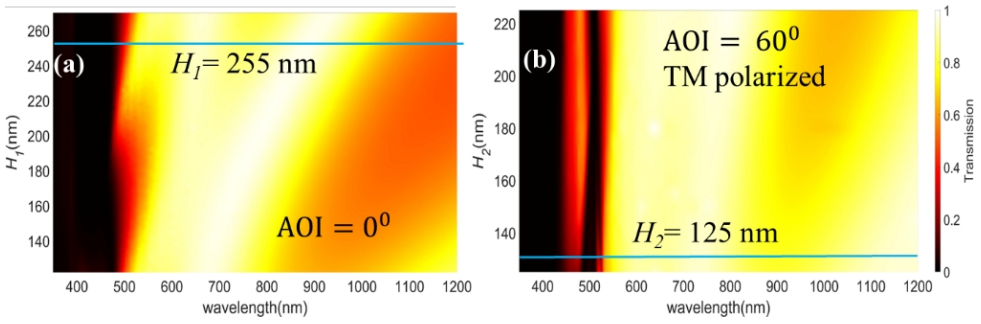

Figure 6.5 The transmission spectra dependence of edge filter on (a) and (b), longitudinal distances,

H_1 and H_2, between two adjacent SiNSs MFLs.

LP3 design Fig. 6.4 (e, f): We implemented a three-layered design to enhance stop band blocking performance. This configuration (H_2 = 125 nm, as depicted in Fig. 6.4 (d)) demonstrated significantly improved stop band blocking performance for both polarisations. The determination of H_2 = 125 nm is shown in the in Fig. 6.5, which shows the narrower bandwidth of the peak in Zone C. For TE polarisation, the stop band achieves near-perfect blocking, as seen in Fig. 6.4 (e), with all wavelengths being completely blocked within the stop-band under all of the AOIs, resulting in an average OD of up to 2.55. This effectively resolves the issue observed in Zone A of the LP1 design. In the case of TM polarisation, the unwanted peaks in Zone B are entirely removed; moreover, while the peaks in Zone C are not fully eliminated, they still show a significant improvement compared to that of the LP1 design. The attenuation of transmission in the longer wavelength (900–1100 nm) is still observed, due to the absence of an ARC.

LP4 design Fig. 6.4 (g, h): Building upon LP3, the LP4 design achieves further enhancement with the addition of an ARC layer. The systematic optimisation of the design parameters, conducted by ESM and validated by CST, yields specific dimensions for LP3 with optimal performance (H_0' = 133.61 nm, H_1' = 256.46 nm, H_2' = 124.77 nm, H_3' = 96.27 nm, and H_4 = 150.45 nm).

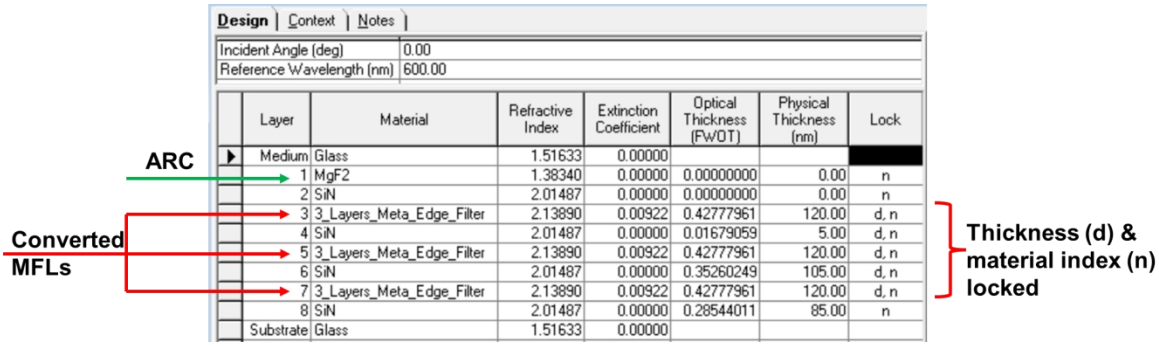

Design | Context | Notes

Incident Angle (deg)	0.00
Reference Wavelength (nm)	600.00

	Layer	Material	Refractive Index	Extinction Coefficient	Optical Thickness (FWOT)	Physical Thickness (nm)	Lock
▶	Medium	Glass	1.51633	0.00000			
	1	MgF2	1.38340	0.00000	0.00000000	0.00	n
	2	SiN	2.01487	0.00000	0.00000000	0.00	n
	3	3_Layers_Meta_Edge_Filter	2.13890	0.00922	0.42777961	120.00	d, n
	4	SiN	2.01487	0.00000	0.01679059	5.00	d, n
	5	3_Layers_Meta_Edge_Filter	2.13890	0.00922	0.42777961	120.00	d, n
	6	SiN	2.01487	0.00000	0.35260249	105.00	d, n
	7	3_Layers_Meta_Edge_Filter	2.13890	0.00922	0.42777961	120.00	d, n
	8	SiN	2.01487	0.00000	0.28544011	85.00	n
	Substrate	Glass	1.51633	0.00000			

Figure 6.6 The interface of the ESM with LP3 converted and modelled accordingly. MgF_2 was selected as the top anti-reflection coating (ARC), while two additional SiN layers were inserted between the MgF_2–MFL and MFL–glass interfaces. The "Lock" panel was used to fix specific parameters in order to maintain consistency during the optimisation process.

The determination of thickness group used above were obtained by a series of optimisation processes. First, converting inhomogeneous LP3 to a homogeneous MFL with an effective refractive index obtained by applying extraction method described in methodology section, as seen in Fig. 6.6. MgF_2 was selected as top ARC, while two additional SiN layers were

inserted between MgF_2-MFL and MFL-Glass interfaces enabling greater flexibility for ESM in determining the optimal thickness combination for the whole thin-film group. The thickness and material indices of MFLs' components were locked manually to ensure consistency with all the parameters used in LP3. Second, the optimisation target was defined as achieving zero reflectance (R = 0) across the wavelength range of 550–1200 nm, for both TE and TM polarisations, over incidence angles from 0° to 60° in 20° step width. The spectral resolution for the optimisation was set to a 25 nm wavelength step. Finally, the simplex refinement algorithm was employed to optimise the design. This method focuses solely on adjusting the thicknesses of existing layers without generating new layers, thereby significantly reducing computational time and resource consumption. Its efficiency and simplicity make it particularly well-suited for scenarios where the layer structure is fixed and only fine-tuning is required to meet the optical performance targets.

LP4 demonstrates a superior overall performance, with the unwanted peaks in Zones A, B, and C being significantly reduced or eliminated, resulting in significant improvements in stop band characteristics with a max average OD = 2.55. Meanwhile, the transmission in the pass band, particularly at wavelengths of >900 nm, experiences substantial enhancement, with the average transmission exceeding 80% across the AOIs ranging from 0° to 60° for both polarisations.

6.3.4 Key Performance Comparisons

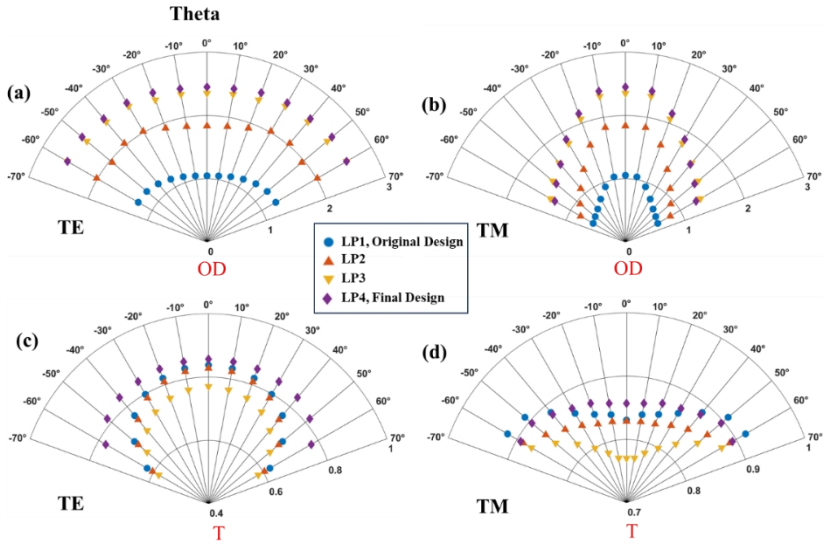

Figure 6.7 (a, b) The average OD for stop band (350 nm–480 nm) and (c, d) average transmission for pass band (500 nm–1200 nm) of 4 edge filters under different AOIs (represented as Theta) and with both TE (left) and TM (right) polarised incidence.

OD performance of stop band: Fig. 6.7 illustrates a comparison of the average transmission rates for designs LP1–L4 for the stop-band (350 nm–480 nm). As the number of MFLs increases, the blocking performance (OD) shows a significant improvement for both TE- and TM-polarized modes, as follows: the OD of the LP3 design increases by 1.31 compared to LP1; and by 0.52 compared to LP2 for TE polarisation. In terms of TM polarisation, the results exhibit less improvement, with the average OD of the LP1 design sharply decaying at high AOI, due to the presence of unwanted peaks. The OD of the LP3 design is approximately 0.71 higher than that of LP1.

The introduction of the ARC layer slightly improves the blocking performance for TE-polarised light across almost all of the AOIs, and the variation of OD for TM-polarised incidence is less than ±0.15. Importantly, our optimised design, LP4, achieves the highest reported optical density for metamaterial-based edge filters to date, as follows: OD = 2.45 (AOI = 0°), OD = 2.55 (AOI = 60°, TE), and OD = 1.29 (AOI = 60°, TM), compared to the previous single-layer LP1 design with OD = 1.05 (AOI = 0°), OD = 1.25 (AOI = 60°, TE), and OD = 0.59 (AOI = 60°, TM).

We also calculated the OD at an AOI of 0° for an increased number of layers. We found that the OD (AOI = 0°) approaches a maximum value that can be approximated by the following formula:

$$OD \approx \frac{12}{4.6 + \exp\left[-1.54 * (x - 2.33)\right]} \tag{6.3.1}$$

Here, the optical density (OD) exhibits an increasing trend with the number of layers but begins to plateau at around six layers, reaching a maximum OD of approximately 2.60. This occurs because the threshold defining the stop band is set at 10% (OD = 1) in this paper, thereby limiting the upper limit of the average OD. However, if the threshold for the stop-band is reduced to 1% (OD = 1), a much higher average OD can be achieved.

As the number of MFLs grows, the average transmission of each filter with the absence of an ARC decreases for both TE- and the TM-polarised incident lights at all AOIs. This is because the total optical admittance of the MFLs and substrates mismatches the admittance of the air. The design incorporating an optimised ARC layer provides an enhancement for transmitting performance, particularly at higher AOIs, in comparison to the other three designs lacking an ARC layer. While the improvement remains relatively modest during normal incidence and low AOI, which is attributable to less reflection at a lower AOI, the improvement in transmitting performance becomes apparent as the AOI increases. The disparity in

transmission between the final design and the single-layer design reaches a notable increase from 62% to 77%, at 0.15. For the TM model, the single-layer design exhibits a consistently high average transmission for all of the AOIs above 84%. Moreover, the transmission does not experience a substantial decline, as observed in the TE incidence, when the number of MFLs is increased.

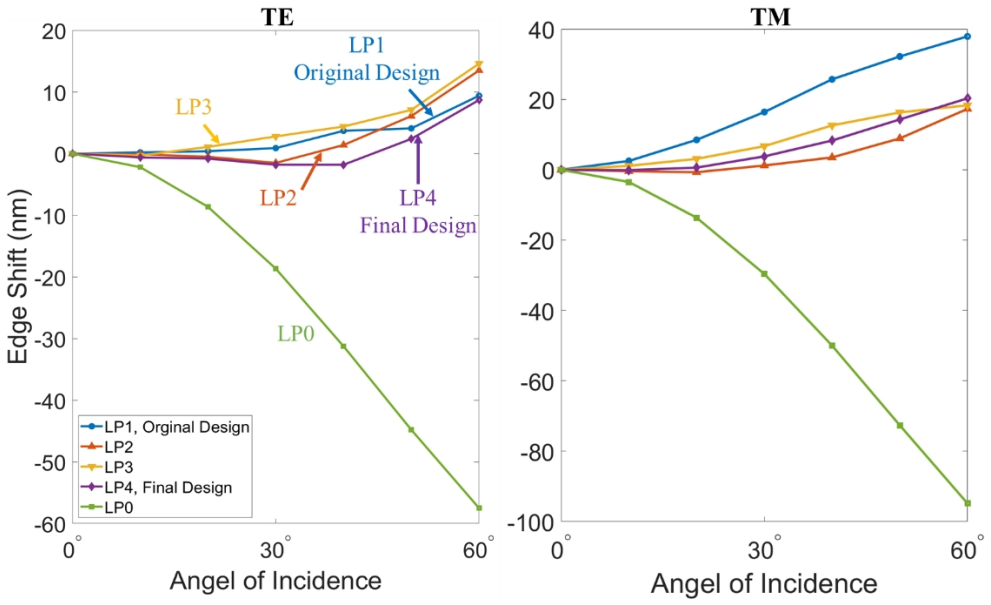

(a) (b)

Figure 6.8 The shift of edge wavelength of LP0–4 with TE- (a) and TM- (b) polarised AOI.

Edge shift performance: The edge shifts of all of the above designs are shown in Fig 6.8, showcasing the remarkable angular intolerance performance of SiNSs-based edge filters at a high TE-polarised AOI. The maximum blue shifts (AOI = 60°) of the conventional edge filter are approximately 55 nm and 95 nm with TE- and TM-polarised incidences, respectively. However, the maximum edge shift of the LP1 single-layer design reaches to 9.42 nm at 60°. This low angular sensitivity is inherent in all multi-layered edge filters, with the final design incorporating an ARC exhibiting an even greater insensitivity across all of the AOIs. For the TM-polarised incidence, the edge shifts are much more severe than those of the TE incidence. Specifically, the red shift of the edge for the single-metalayer filter rapidly raises to 37.92 nm and the edge shift is significantly reduced by at least 50% for all of the AOIs after the introduction of multilayers of SiNSs array and the ARC layer.

6.3.5 Tunability of Edge Filter

While our design has a fixed edge wavelength of 500 nm, it is feasible to adjust the edge

wavelength by modifying the nanoparticle size and the material to suit various application requirements. Fig. 6.9 illustrates the particle size and the material variations that can be employed to tune the design wavelength across the entire visible spectrum. To make the results more generalisable and widely applicable, the model used for simulation is a simplified three-metalayer configuration consisting of a glass substrate and three stacked MFLs directly derived from LP1 instead of being deeply optimised, like LP3, with optimised longitudinal centre-to-centre distance. Crystal silicon nanoparticles enable wavelength tuning between the range of 380 and 520 nm, whereas amorphous silicon allows tuning within the 450–650 nm range.

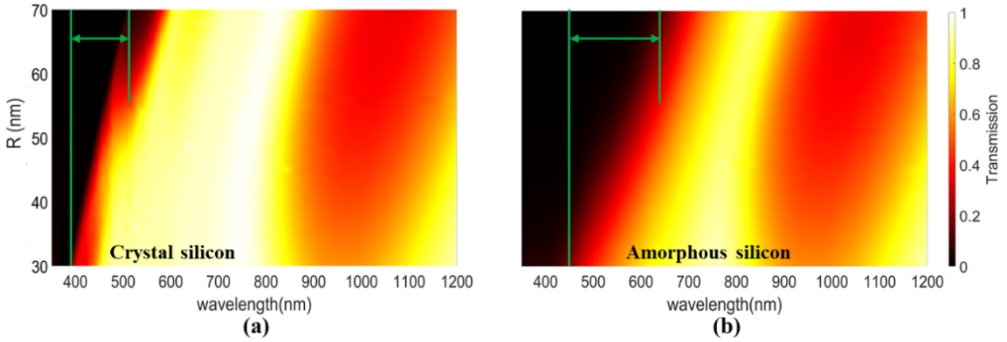

Figure 6.9 Tunability of edge wavelength range (highlighted by green arrows) in the three-metalayer configuration based on three stacked MFLs from LP1 by varying silicon nanoparticle size and applying (a) crystal and (b) amorphous silicon.

6.4 Conclusion

In summary, utilising a combined design and optimisation approach involving full-wave simulation and classical thin-film design methods, we have optimised wide-angle metamaterial long-pass edge filters incorporating SiNSs and an ARC. Through systematic adjustments and rigorous validation, our three-MFL design achieved a significantly higher OD compared to the original design, with enhanced transmission in TE polarisation (62–77%) and higher ODs of 2.55 (AOI = 60°, TE) and 1.36 (AOI = 60°, TM). This exceptional performance renders it suitable for applications demanding consistent results across diverse angles of incidence. Moreover, the tunability of edge wavelengths enhances its adaptability to specific application requirements. Our study significantly advances the field of high-efficiency metamaterial optical components, offering an enhanced performance and versatility in various optical systems.

6.5 References

[1] X. F. Xu, J. Y. Ding, “A wide band-pass filter of broad angle incidence based on one-dimensional metallo-dielectric ternary photonic crystal,” Opt. Quant. Electron. 2009, 41, 1027–1032.

[2] Yoshiaki Kanamori, Toshikazu Ozaki, and Kazuhiro Hane, "Reflection color filters of the three primary colors with wide viewing angles using common-thickness silicon subwavelength gratings,” Opt. Express. 2014, 22, 21, 25663–25672.

[3] H. J. Choi, S. Choi, Y. E. Yoo, E. Jeon, Y. Yi, S. Park, D. S. Choi, H. Kim, “Transmission-type photonic crystal structures for color filters,” Opt. Express. 2013, 21, 15, 18317–18324.

[4] F. Wu, G. Lu, C. Xue, H. Jiang, Z. Guo, M. Zheng, C. Chen, G. Du, H. Chen, “Experimental demonstration of angle-independent gaps in one-dimensional photonic crystals containing layered hyperbolic metamaterials and dielectrics at visible wavelengths,” Appl. Phys. Lett. 2018, 112, 4, 041902

[5] F. Lotti, A. Mirzaei, P. Wang, A.E. Miroshnichenko, A.V. Zayats, “Nanoparticle-based metasurfaces for angular-independent spectral filtering applications,” J. Appl. Phys. 2019, 126, 213101.

[6] D. A. Shilkin, E. V. Lyubin, M. R. Shcherbakov, M. Lapine, A. A. Fedyanin, “Directional optical sorting of silicon nanoparticles,” ACS Photonics. 2017, 4, 2312–2319.

[7] K. Luke, Y. Okawachi, M. R. Lamont, A. L. Gaeta, M. Lipson, “Broadband mid-infrared frequency comb generation in a Si_3N_4 microresonator,” Opt. Lett. 2015, 20, 4823–4826.

[8] M. J. Dodge, “Refractive properties of magnesium fluoride,” Appl. Opt. 1984, 23, 1980–1985.

[9] J. N. Monks, J. Williams, A. Hurst, Z. Wang, “Shift-free fixed-line laser protection filter technology,” in Technologies for Optical Countermeasures XVII; and High-Power Lasers: Technology and Systems, Platforms, Effects IV, Online, 2020, 1153908.

[10] M. F. Silva, S. Pimenta, J. A. Rodrigues, J. R. Freitas, M. Ghaderi, L. M. Goncalves, G. de Graaf, R. F. Wolffenbuttel, J. H. Correia, “Magnesium fluoride as low-refractive index material for near-ultraviolet filters applied to optical sensors,” Vacuum. 2020, 181, 109673.

[11] C. Schinke, P. C. Peest, J. Schmidt, R. Brendel, K. Bothe, M. R. Vogt, I. Kröger, S. Winter, A. Schirmacher, S. Lim, et al., “Uncertainty analysis for the coefficient of band-to-band absorption of crystalline silicon,” AIP Adv. 2015, 5, 067168.

[12] M. R. Vogt, H. Hahn, H. Holst, M. Winter, C. Schinke, M. Köntges, R. Brendel, P. P. Altermatt, “Measurement of the optical constants of soda-lime glasses in dependence of iron content, and modeling of iron-related power losses in crystalline Si solar cell modules,” IEEE J. Photovolt. 2016, 6, 111–118.

Chapter 7 Wide-angle Metamaterial Bandpass Filter

7.1 Introduction

Bandpass filters demand not only high blocking on both sides of the pass-band but also stable transmission over a wide range of incidence angles. As summarised in Chapter 2, existing strategies, particularly metal–dielectric–metal (MDM) configurations, have been widely investigated for blue-shift mitigation [1–3]. MDM designs provide improved angular robustness but suffer from Ohmic losses that restrict peak transmission, often to below 50%. In addition, their transmission still decreases significantly at large AOI due to reduced coupling efficiency and enhanced reflectivity of the metallic layers.

In addition, the literature reports other mitigation strategies such as one-dimensional photonic crystals (1D PhCs) and hyperbolic metamaterials (HMMs) [4–6]. 1D PhCs are limited by polarisation sensitivity, where under TM incidence the Brewster angle effect can cause reflection dips and spectral distortion, leading to inconsistent angular transmission. HMMs, in contrast, provide angular invariance primarily for TM polarisation but generally suffer from intrinsically low transmission due to metallic absorption. These limitations have already been reviewed in Chapter 2.

In 2019, Lotti et al. proposed a bandpass design using silicon nanospheres (SiNS) and gold (Au) to form Si–Au core–shell structures, which demonstrated moderate AOI-insensitive behaviour [7]. However, their single-meta-layer configuration lacked proper anti-reflection coatings and suffered from performance limitations, including insufficient optical density (OD) above 1050 nm and pass-band distortion under TE polarisation at high AOI.

Building upon the metamaterial edge filter developed in Chapter 6, we further explored the design of a wide-angle tolerant bandpass filter. Here, the hybrid numerical–analytical design protocol successfully applied in Chapter 6 is extended to bandpass filtering, ensuring a consistent and efficient optimisation framework. This chapter presents a hybrid bandpass design composed of multiple stacked metasurfaces of gold-coated SiNS (SiNS–Au), integrated with a one-dimensional photonic crystal (1D PhC) edge filter.

The choice of a 1D configuration is motivated not only by its intrinsic photonic bandgap physics that have been reviewed in Chapter 2, but also by its practical advantages in our

optimisation framework. Its simple layered architecture allows seamless integration into the effective-medium (ESM) design protocol, enabling rapid thickness optimisation and thus enhancing the efficiency of the hybrid design strategy.

In this configuration, the 1D PhC serves as an angularly robust edge filter that complements the LSPR-driven spectral shaping of the SiNS@Au multilayers, effectively suppressing side-lobes near the pass-band edge (especially in the 600–700 nm range). The final filter achieves a narrow transmission peak of ≈80%, with an average optical density of OD ≥ 2.31 in both stop bands, and exhibits minimal spectral shift up to AOI = 60° under TE polarisation. Such performance highlights a substantial improvement over previous single-layer core–shell designs and proves the design strategy of combining meta-film layers (MFLs) with 1D photonic structures.

7.2 Optical Response of a Single Nanosphere

The underlying working mechanism of the bandpass filter originates from the SiNS-based design, where the short-wavelength regime exhibits strong blocking performance due to the high extinction of silicon. To further tailor the spectral response and introduce an additional stop band in the near-infrared (NIR) region, a thin gold shell can be incorporated around the SiNS core. The presence of the metallic shell not only excites localized surface plasmon resonances (LSPRs) but also modifies the spectral position of the intrinsic Mie modes of the silicon nanoparticles. These plasmonic resonances enhance the overall extinction in the longer wavelength region and lead to the emergence of a new stop band, which in turn defines a well-resolved pass-band between the visible and NIR spectral ranges. Specifically, the gold shell produces a dominant plasmonic response beyond 1000 nm, resulting in considerable extinction and effective suppression of transmission, as illustrated in Fig. 7.1.

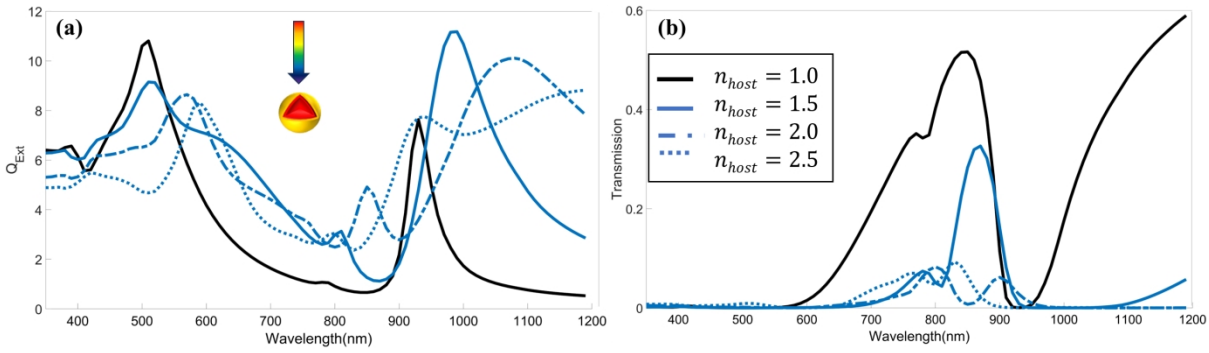

Figure 7.1 (a) Extinction coefficients and (b) approximated transmittance spectra as a function of incident wavelength for a single silicon nanosphere (SiNS, R_{SiNS} = 70 nm) with a gold shell (T_{shell} = 20 nm) under varying refractive indices of the host medium.

7.3 Wide-angle Edge Filter Design

7.3.1 Conventional Bandpass Filter

We begin by demonstrating the classical *blue-shift* phenomenon commonly observed in traditional thin-film bandpass filters currently available on the market. The ordinary thin-film bandpass design in Fig 7.2 (a) consists of three distinct thin-film groups, each repeatedly stacked to enhance the out-of-band blocking. This design comprises 60 alternating layers of high-index titanium dioxide (H~TiO_2) and low-index silicon dioxide (L~SiO_2), without the use of nanospheres [8, 9]. Two constants, 1.75 and 0.75, are introduced to the first and third groups, respectively, to broaden the pass-band through varying effective refractive index by changing reference wavelength. These three primary thin-film groups can be subdivided into multiple sub-groups with gradually varied scaling constants, as BP0 in Fig. 7.2 (b) showing. This subdivision creates a smoother refractive index profile transition, which reduces impedance mismatch across the stack and improves blocking and transmitting performance at high AOI, especially for TM polarisation, as seen in Fig. 7.2 (d).

As a result, the optimised conventional thin-film bandpass filter shown in Fig. 7.2 (b, d) was used for further comparison, designated as BP0 in Table 7.1, Both the number of layers and their thicknesses are carefully optimised to achieve high bandpass performance. Any reduction in layer count or deviation from the optimised configuration leads to a notable decline in filtering efficiency.

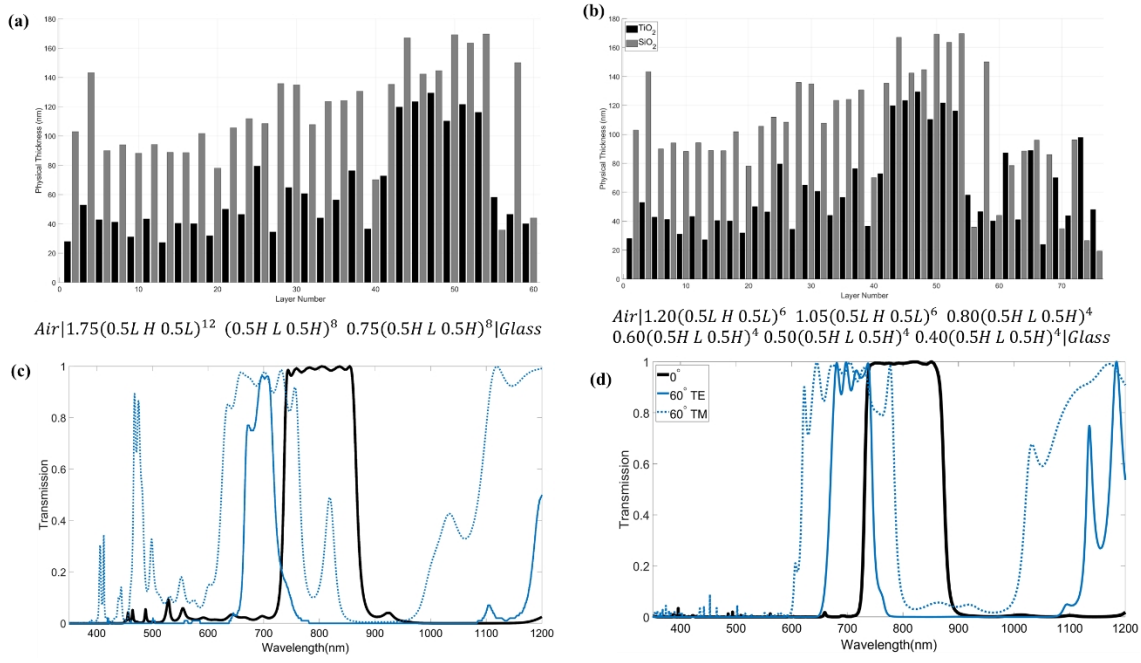

Figure 7.2 The thickness information of (a) optimised and (b) unoptimised conventional thin-film bandpass filters. (c, d) The transmittance comparison between two thin-film bandpass

filters.

Simulation results reveal a significant degradation in performance at oblique angles of incidence. As illustrated by both bule solid and dashed lines in Fig. 7.2 (b), the filter exhibits a pronounced blue shift of the central wavelength, narrowing of the pass-band under TE polarisation, and diminished stop-band blocking under TM polarisation. This angular sensitivity is primarily attributed to phase delay variations and the Brewster angle effect [10]. As the incidence angle increases, the effective optical path length within the multilayer stack becomes longer, necessitating a shorter wavelength to satisfy the constructive interference condition. The shifted wavelength can be approximated by the following expression [10]:

$$\lambda_\theta \approx \frac{\lambda_0}{2}\left(\frac{n_{H,\theta}}{n_H} + \frac{n_{L,\theta}}{n_L}\right) \tag{7.3.1}$$

where n_H and n_L denote the refractive indices of high- and low- indices material, respectively. $n_{H,\theta}$ and $n_{L,\theta}$ represent the effective indices of materials at AOI of θ. They can be expressed as $n_{H,\theta} = n_H cos\theta$ and $n_{L,\theta} = n_L cos\theta$ for TE polarisation, and $n_{H,\theta} = n_H sec\theta$ and $n_{L,\theta} = n_L sec\theta$ for TM polarisation.

7.3.2 Metamaterial Bandpass Filter Configurations

We present a series of metamaterial-based bandpass filter designs to illustrate the designing process, building upon previous single-MFL design to achieve improved blocking performance and angle insensitivity. The unit cell structures are schematically illustrated in Fig. 7.3, with their corresponding layer configurations detailed in Table 7.2.

The designs include:

Fundamental Unit Cell: A silicon nanosphere (SiNS) coated with a gold shell, with a total diameter of $2(R_{SiNS} + T_{Shell})$.

(a) BP1 – Single-Meta-Layer Bandpass Filter (Lotti's Design): A single-MFL configuration embedding gold-coated SiNS in a host medium, serving as the baseline reference.

(b) BP2 – Multi-Meta-Layer Bandpass Filter: A two-MFLs structure, introduced to enhance blocking performance while maintaining AOI insensitivity, addressing the limitations of BP1.

(c) BP3 – Optimised Bandpass Filter with 1D Photonic Crystal Edge Filter: A further optimised design, incorporating a 1D-PhC-based edge filter, significantly improving pass-band transmission at TE polarisation while maintaining strong blocking performance.

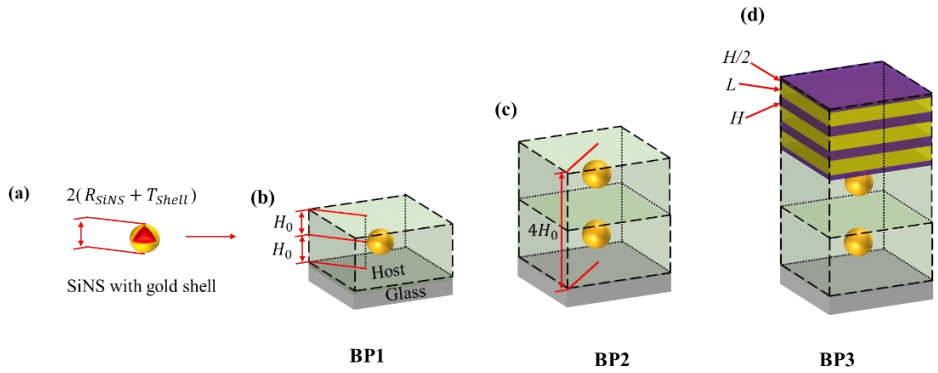

Figure 7.3 The schematic illustration of (b) single-MFL, (c) two-MFLs and (d) hybrid design with the fundamental gold coated SiNS as shown in (a).

Table 7.1 The configuration of 4 band-pass (BP) edge filters used in this paper. BP1-LP3 are metamaterial-based bandpass filters, and their corresponding unit cell figures are listed in the brackets.

Design ID	**Configurations** **H:** High-index layer (quarter-wavelength) **L:** Low-index layer (quarter-wavelength) **M:** Meta-layer
BP0	$Air\|1.20(0.5L\ H\ 0.5L)^6\ \ 1.05(0.5L\ H\ 0.5L)^6\ \ 0.80(0.5H\ L\ 0.5H)^4$ $0.60(0.5H\ L\ 0.5H)^4\ 0.50(0.5H\ L\ 0.5H)^4\ 0.40(0.5H\ L\ 0.5H)^4\|Glass$ (Fig. 5.11(b), *H:* TiO_2, *L:* SiO_2, $\lambda_{Ref} = 750\ nm$.)
BP1	$Air\|M\|Glass$ (Fig. 7.3 b)
BP2	$Air\|(M)^2\|Glass$ (Fig. 7.3 c)
BP3	$Air\|(0.5H\ L\ 0.5H)^3\|(M)^2\|Glass$ (Fig. 7.3 d, *H:* α-*Si*, *L:* *SiN*, $\lambda_{Ref} = 600\ nm$.)

Our metamaterial-based bandpass filter designs (BP1, BP2, BP3) exhibit significantly improved angular performance over conventional filter design (BP0). Fig. 7.4 presents the contour plots of transmission (T) as a function of wavelength (x-axis) and angle of incidence (y-axis) for TE polarisation (left column: a, c, e, g) and TM polarisation (right column: b, d, f, h). The edge wavelength (λ_{Edge}) is defined as the wavelength where transmission (T) equals $0.5T_{Peak}$, establishing two boundary wavelengths for the pass-band: $\lambda_{Left\text{-}Edge}$ and $\lambda_{Right\text{-}Edge}$. The central wavelength (λ_c) is then determined as: $\lambda_c = (\lambda_{Left\text{-}Edge} + \lambda_{Right\text{-}Edge})/2$. In this work, the pass-band extends from 750 to 850 nm, ensuring high transmission, while the stop-bands (350–680 nm and 850–1200 nm) maintain low transmission (OD ≥ 1, where OD = -log T).

7.3.3 Design and Optimisation

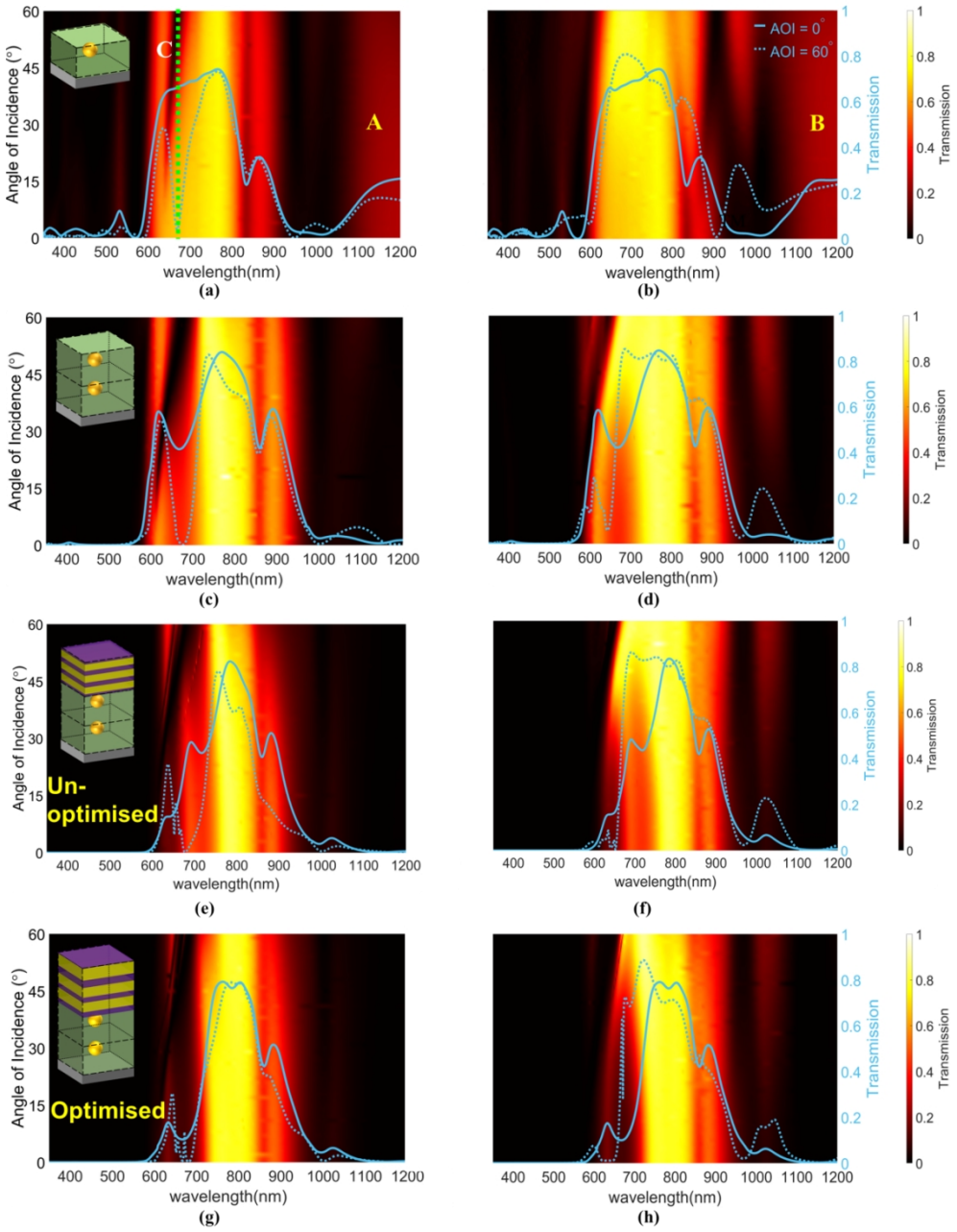

Figure 7.4 Contour plots of transmission spectra for BP1 (a, b), BP2 (c, d), unoptimised BP3 (e, f) and optimised BP3 (g, h) designs under TE (left column) and TM (right column) polarisations. Solid and dashed lines represent transmission at 0° and 60° incidence angles, respectively. Zones A, B, and C in (a, b) indicate critical regions targeted for further optimisation.

The BP1 design (Fig. 7.4 a, b) replicates Lotti's work in Ref. [7] with a single-MFL structure, where H_0 = 150 nm, R_{SiNS} = 70 nm, and T_{Shell} = 20 nm. This design exhibits reasonable angle insensitivity in its pass-band, with a relatively stable central wavelength under varying AOI. However, it suffers from several performance limitations, particularly in the stop-band. Notably, the design demonstrates poor blocking performance in the stop-bands, especially for the longer wavelength region (≥1050 nm), where transmission remains high (T > 0.25), as

highlighted by regions A and B in Fig. 7.4 (a, b), respectively. Additionally, an undesired transmission attenuation band appears between 15° and 60° AOI, as indicated by the green dashed line and zone C in Fig. 7.4 (a). Due to the limited tunability of single-MFL structures, resolving these issues through parameter adjustments alone is challenging. To overcome these limitations, the introduction of multi-MFLs designs and hybrid filtering strategies is crucial, as they provide greater flexibility in tuning optical properties and effectively mitigate performance degradation.

The BP2 design (Fig 7.4 c, d) was developed to enhance stop-band blocking performance in zones A, B and C by employing a two-MFLs structure while keeping all parameters fixed except for a thinner gold shell ($T_{Shell'}$ = 15 nm), reduced from the original 20 nm. The optimal shell thickness was determined through CST parametric sweeping, evaluating the transmission response of the two-MFLs design under varying gold shell thicknesses at 0° AOI to ensure adequate pass-band transmission while maintaining reasonable stop-band blocking performance. However, this modification resulted in an expansion of the pass-band width, which is undesirable and is addressed in BP3 design.

BP3 Design: To address the pass-band broadening in BP2, a 1D ternary photonic crystal-based edge filter $(0.5H\ L\ 0.5H)^3$, where H and L represent quarter-wavelength thickness layers of high-index (α-Si) and low-index (TiO_2) materials with a reference wavelength of 600 nm, was placed on top of BP2 [11]. The objective was to suppress the peaks (Zone C) on the left edge of the pass-band, thereby a narrowed pass-band with sharper spectral edges. As shown in Fig. 7.4 (e), the peak in Zone C was effectively suppressed, even though the thickness of the 1D PhC edge filter was not fully optimised. This result highlights the inherent effectiveness of the 1D PhC structure.

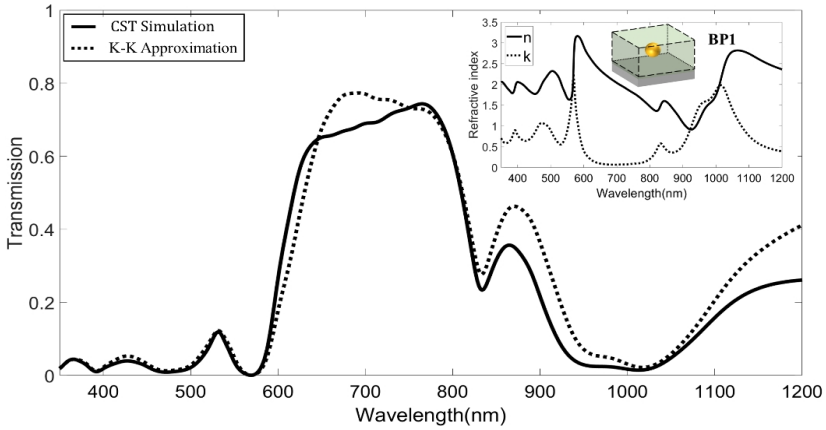

Figure 7.5 Comparison of the transmission spectrums obtained via CST full-wavelength simulation and the K-K approximation. The inset shows the refractive index of the single-metalayer composing of the infinite unit cells.

To further enhance the performance of this hybrid filter, it is essential to maximise the edge blocking functionality of the 1D PhC and improve transmission by matching the admittance of the 1D PhC to that of air, thereby minimising reflection losses at the interface. This process requires efficient TMM optimisation algorism in ESM. With the extracted n_{eff} (plotted in Fig. 7.5), as seen in Fig. 7.6, two MFLs were modelled in ESM, followed by the addition of a photonic crystal-based edge filter. The refinement target was set to zero reflection in the pass-band (750–850 nm) at 0°, 30°, and 60° AOI (TE polarisation) to ensure angle insensitivity. Since blocking performance depends on the SiNS and gold shell, no additional stop-band constraints were imposed.

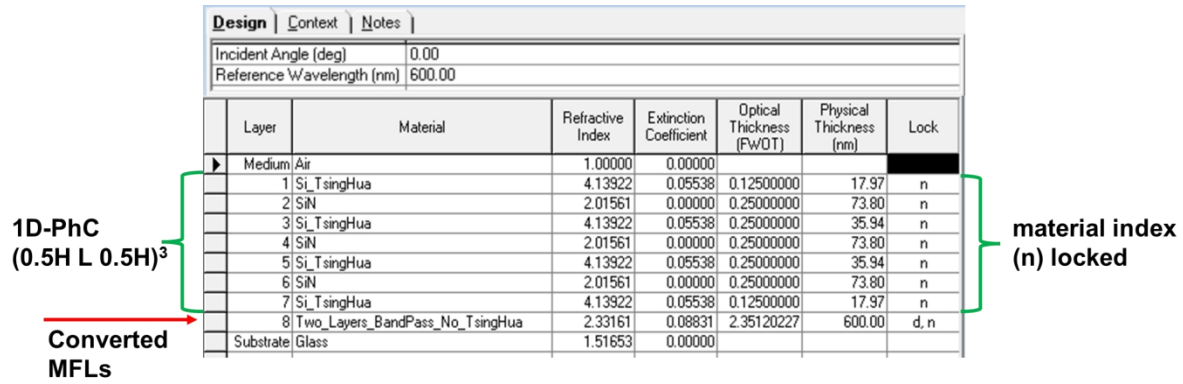

Figure 7.6 The interface of the ESM with BP3 converted and modelled accordingly. The 1D PhC with (0.5H L 0.5H)^3 was placed on the top of BP2. The "Lock" panel was used to fix specific parameters in order to maintain consistency during the optimisation process.

Table 7.2 Thickness information of unoptimised/optimsed BP3

Design ID	**Configurations** **H:** High-index layer (quarter-wavelength) **L:** Low-index layer (quarter-wavelength) **M:** Meta-layer
BP3 (Unoptimised)	$Air\|(0.5H\ L\ 0.5H)^3\|(M)^2\|Glass$ (H:34.52 nm L: 71.86 nm, $\lambda_{Ref} = 600\ nm$.)
BP3 (Optimised)	$Air\|10.05\ nm\|17.92\ nm\|87.08\ nm\|18.36\ nm\|82.08\ nm\|62.13\ nm\|103.60\ nm\|$ $\|(M)^2\|Glass$

For efficiency, Simplex refinement was used, manually removing excessively thick layers (>2× quarter-wavelength optical thickness) and thin layers (<10 nm) while keeping other parameters at default settings. The detailed thicknesses for unoptimised and optimised designs are provided in Table 7.2.

The optimised BP3 exhibits further suppression of Zone C within the 600–700 nm range under TE-polarised incidence (Fig. 7.4 g), ensuring a well-defined pass-band with minimal spectral distortion. Under TM-polarised incidence (Fig. 7.4 h), the pass-band slightly shifts toward shorter wavelengths due to the Brewster angle effect of 1D PhC. However, the overall performance remains substantially improved compared to BP2 and unoptimised BP3, demonstrating the effectiveness of this hybrid approach. The combination of a 1D PhC edge filter with a core-shell nanoparticle-based metamaterial thus presents an effective strategy for addressing optical filtering challenges.

7.3.4 Key Performance Comparisons

We now compare the performance of the three filters (BP1, BP2, optimised BP3) in terms of stop-band optical density (OD) and pass-band transmission (T) as a function of AOI, as shown in Fig. 7.7.

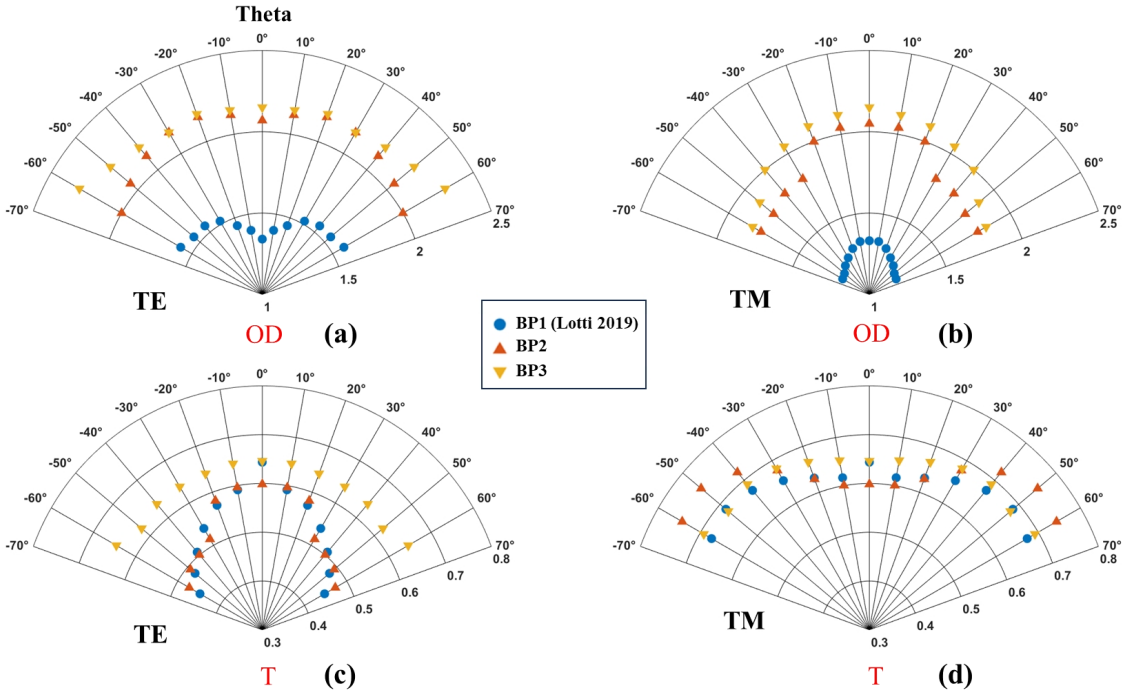

Figure 7.7 (a, b) Average OD for the stop-band and (c, d) average transmission for the pass-band of three bandpass filters (BP1, BP2, BP3) under varying angles of incidence (AOI, represented as Theta) for both TE (left) and TM (right) polarised light. The BP1 design (Lotti et al., 2019) is reproduced from Ref. [7].

Stop-band: The blocking performance improves significantly as additional meta-layers and the edge filter are introduced. The average OD increases from approximately 1.50 to over 2.00, and finally 2.25+ for all AOI, demonstrating the effectiveness of these modifications. For TM polarisation, the average OD improvement achieved by the two-MFLs design and the BP3 design with an additional edge filter is 0.60 ± 0.10 and 0.80 ± 0.10, respectively. These results confirm that increasing the number of MFLs enhances blocking performance, while integrating an edge filter further improves OD in the shorter wavelength region. This effect is particularly pronounced for TE-polarised light at high AOI, as evidenced by a more substantial OD increase in these conditions.

Pass-band: For TM-polarised incidence, the transmission performance of all three designs remains stable, with no significant variation observed. However, the final optimised BP3 design exhibits a more pronounced improvement in TE-polarised transmission at high AOI, as the edge filter leads to a more continuous pass-band under these conditions. The introduction of a second MFL alone does not enhance transmission, as the optical admittance is not optimised to match that of air. This highlights the crucial role of further optimization using ESM, which ensures a well-matched optical interface and significantly improves transmission characteristics.

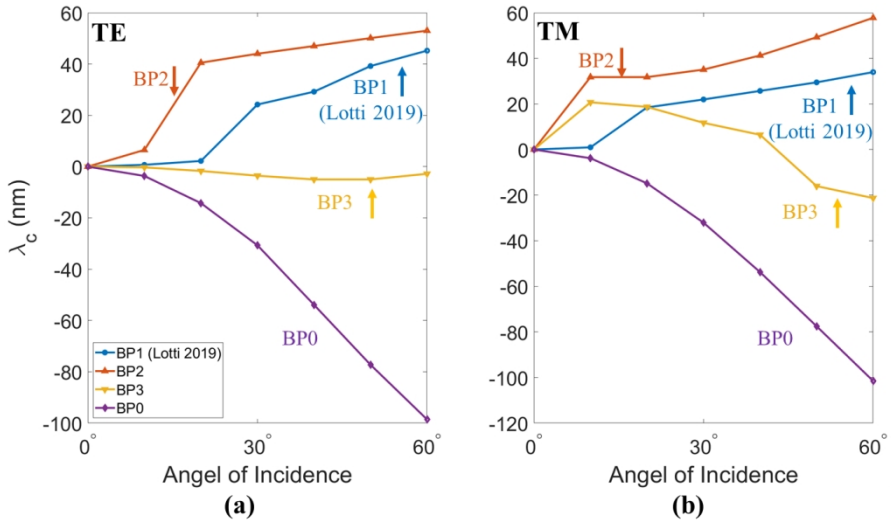

Figure 7.8 Comparison of pass-band central wavelength shift for BP0, BP1, BP2, and BP3 under TE (a) and TM (b) polarisation as a function of AOI.

Next, we compare the central wavelength shift of the pass-band as a function of the incident angle, as presented in Fig. 7.8. Firstly, all metamaterial-based designs (BP1–BP3) exhibit significantly improved angular stability compared to the classical thin-film design (BP0), where a flat line indicates minimal wavelength shift.

For TE polarisation, the final optimised BP3 design demonstrates near shift-free performance, as evident from the flat horizontal line in Figure 7.8 (a). However, for TM polarisation (Fig. 7.8 b), the angular stability of BP3 degrades, becoming comparable to BP1, indicating a weaker performance improvement under TM incidence.

7.3.5 Tunability of Bandpass Filter

Finally, the tunability of the designed filter is illustrated in Fig. 7.9. While the full simulation results are presented in the figure, the observed trends are relatively complex. Here, we highlight the most representative effects for clarity. As shown in Fig 7.9 (a), increasing the radius of SiNSs with a fixed gold shell thickness (T_{shell} = 15 nm) leads to a red-shift and broadening of the pass-band, accompanied by enhanced transmission. In contrast, in Fig 7.9 (b), shows that when the SiNS radius (R_{SiNS} = 70 nm) is held constantly, reducing the gold shell thickness weakens the plasmonic resonance, resulting in diminished blocking in the longer wavelength region. As the shell thickness increases, the original pass-band narrows and eventually vanishes, while a new pass-band emerges in the NIR range.

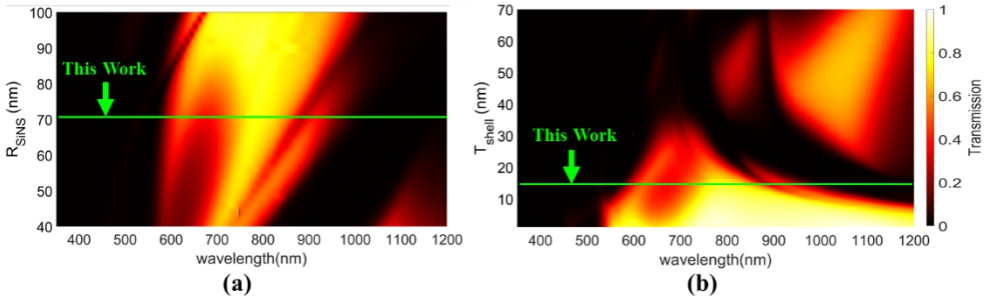

Figure 7.9 Tunability of the transmission spectra for the two-MFLs (BP2) bandpass filter. (a) Effect of varying SiNS radius with a fixed gold shell thickness (T'_{Shell} = 15 nm). (b) Effect of varying shell thickness with a fixed SiNS radius (R_{SiNS} = 70 nm).

7.4 Conclusion

Building upon the success of the edge filter design, we further extended the approach to realise a wide-angle bandpass filter with similarly robust angular performance and enhanced spectral control. we successfully optimized a wide-angle bandpass filter, addressing challenges in blocking efficiency and transmission stability at varying AOI. The optimisation process, incorporating a multi-MFLs design, a photonic crystal-based edge filter, and a hybrid design protocol, significantly enhances performance. The final design achieves higher blocking efficiency, with optical densities up to 2.31 (AOI = 60°, TE) and 1.83 (AOI = 60°, TM), while maintaining near shift-free angular performance and improved average transmission (44 %–65 % and T_{peak} of 80%) under TE polarisation. These enhanced optical properties make the filter well-suited for applications requiring consistent performance across a wide range of AOI. This work contributes to the advancement of high-efficiency metamaterial optical components, offering greater performance, stability, and adaptability for diverse

optical filtering applications.

7.5 References

[1] K. Mao, W. Shen, C. Yang, X. Fang, W. Yuan, Y. Zhang, X. Liu, “Angle Insensitive Color Filters in Transmission Covering the Visible Region,” Sci Rep. 2016, 6, 19289.

[2] K. T. Lee, S. Seo, L. J. Guo, “High-Color-Purity Subtractive Color Filters with a Wide Viewing Angle Based on Plasmonic Perfect Absorbers,” Adv. Opt. Mater. 2015, 3, 3, 347–352.

[3] D. Kim, H. Kim, I. Jung, T. Y. Kim, H. Kwak, J. H. Jung, C. K. Hwangbo, H. J. Park, K. T. Lee, “Manipulation of resonance orders and absorbing materials for structural colors in transmission with improved color purity,” Opt. Express. 2022 30, 7, 11740–11753.

[4] C. H. Chen, K. Tetz, W. Nakagawa, Y. Fainman, “Wide-field-of-view GaAs/AlxOy one-dimensional photonic crystal filter,” Appl. Opt. 2005, 44, 8, 1503–1511.

[5] C. Xue, Y. Ding, H. Jiang, Y. Li, Z. Wang, Y. Zhang, H. Chen, “Dispersionless gaps and cavity modes in photonic crystals containing hyperbolic metamaterials,” Phys. Rev. B 2016, 93, 125310.

[6] B. M. Wells, F. Lotti, M. E. Nasir, A. V. Zayats, V. A. Podolskiy, “Angle-insensitive plasmonic nanorod metamaterial-based band-pass optical filters,” Opt. Express. 2021, 29, 8, 11562–11569.

[7] F. Lotti, A. Mirzaei, P. Wang, A.E. Miroshnichenko, A.V. Zayats, “Nanoparticle-based metasurfaces for angular-independent spectral filtering applications,” J. Appl. Phys. 2019, 126, 213101.

[8] S. V. Zhukovsky, A. Andryieuski1, O. Takayama, E. Shkondin, R. Malureanu, F. Jensen, A. V. Lavrinenko, “Experimental demonstration of effective medium approximation breakdown in deeply subwavelength all-dielectric multilayers,” Phys. Rev. Lett. 2015, 115, 177402.

[9] L. V. Rodríguez-de Marcos, J. I. Larruquert, J. A. Méndez, J. A. Aznárez, "Self-consistent optical constants of SiO_2 and Ta_2O_5 films," Opt. Mater. Express, 2016, 11, 2016,3622–3637.

[10] R. Benz, M. Nazari, T. Amochkina, M. Trubetskov, “Optimizing thin-film material combinations for immersed narrow-bandpass filters in the VIS and NIR range,” Adv. Opt. Thin Films. 2024, 1302006, III.

[11] C. Ji, C. Yang, W. Shen, K. Lee, Y. Zhang, X. Liu, L. J. Guo, “Decorative near-infrared transmission filters featuring high-efficiency and angular-insensitivity employing 1D photonic crystals. Nano Res. 2019, 12, 543–548.

[12] M. R. Vogt, H. Hahn, H. Holst, M. Winter, C. Schinke, M. Köntges, R. Brendel, P. P. Altermatt, “Measurement of the optical constants of soda-lime glasses in dependence of iron content, and modeling of iron-related power losses in crystalline Si solar cell modules,” IEEE J. Photovolt. 2016, 6, 111–118.

Chapter 8 Conclusions and Future Works

8.1 Conclusions

This thesis set out to understand how spherical micro- and nanostructures govern the behaviour of light, and how these interactions can be harnessed to push optical performance beyond classical limits. By examining solid-immersion lenses, biological cells and nanosphere-based resonators within a unified physical framework, the research reveals consistent principles linking imaging and filtering across different length scales.

The study of TiO_2 metamaterial solid-immersion lenses (mSILs) demonstrated that their imaging performance is fundamentally dictated by geometry. When full-spherical, hemispherical and super-hemispherical lenses were produced under identical fabrication conditions, the super-hemispherical design consistently delivered the strongest super-resolution capability, resolving 60 nm gaps on semiconductor chips in air. It also maintained better image contrast and a wider field-of-view than the other geometries. SEM characterisation confirmed that lenses showing greater nanoparticle penetration at the base interface produced clearer images, indicating that strong near-field coupling at the lens–sample boundary is essential. Numerical simulations supported these results by showing that super-hemispherical lenses create more confined photonic nanojets that sustain evanescent-to-propagating wave conversion.

A data-driven modelling approach was also explored to support these findings. A deep-learning image-translation model was trained to approximate the contrast improvements produced by mSIL imaging and reproduced several geometry-dependent trends observed experimentally. Although preliminary, this digital-twin approach demonstrates the potential of machine learning to assist interpretation and prediction of mSIL performance, complementing physical experiments and simulations.

The study of biological yeast-cell lenses showed a clear dependence on cell geometry. Fresh or chemically fixed spherical cells did not produce sub-diffraction images in either water or air. In contrast, naturally collapsed cells with a flattened base and modified curvature consistently resolved ~100 nm Blu-ray features in air with stable and repeatable performance. These results suggest that the mechanical shape of the cell is far more important than its

biological composition. A collapsed geometry provides the near-field confinement and effective substrate contact needed for superlensing under ambient conditions.

The studies on nanosphere-based metamaterial filters reaffirmed the importance of spherical symmetry for robust optical responses. Using a hybrid design method that combined Mie-resonance simulations, effective-index extraction and thin-film optimisation, long-pass edge filters were produced with substantially improved angular stability. The optimised Si nanosphere design reduced angular spectral shifts from around 80 nm in a classical thin-film filter to less than 10 nm up to ±60° incidence, while maintaining strong blocking with optical density values above 2.55 (TE). The SiNS@Au-based bandpass filters showed similarly robust behaviour, sustaining high optical density across their stop-bands and exhibiting minimal pass-band drift compared to conventional design and previous metamaterial designs for both TE and TM polarisations.

Taken together, these findings present a unified picture: spherical micro- and nanostructures enable precise, stable and predictable light manipulation when their geometry and interface conditions are carefully engineered. This work demonstrates that super-resolution imaging down to 60 nm in air, and wide-angle filtering with spectral shifts below 10 nm, can be achieved through relatively simple but well-designed spherical architectures. The additional machine-learning component, used in a supporting role, highlights how data-driven tools may further enhance the analysis and optimisation of such systems. Overall, the thesis establishes spherical structures as a versatile foundation for compact optical technologies that overcome the classical constraints of diffraction and angle sensitivity.

8.2 Future Work

The findings in this thesis suggest several directions for further development. Although the mSIL studies clarified the geometric conditions required for strong super-resolution performance, there is room to optimise both the material systems and the operating environment. One extension is to investigate high-index materials beyond TiO_2, including chalcogenide glasses, GaP or tailored composites, which may provide stronger photonic nanojets or deeper near-field penetration. In parallel, controlled adjustment of the lens–sample interface, such as using ultrathin lubricating layers, adaptive spacers or engineered surface textures, could stabilise the coupling process and improve repeatability in practical imaging applications.

Another direction involves integrating mSILs into dynamic or scanning platforms. In this thesis, the lenses operate in a static, contact-based mode. Mounting optimised mSILs onto MEMS actuators, micro-robotic translation stages or tip-based scanning systems could enable large-area imaging, automated positioning and hybrid optical–mechanical mapping. Such implementations would be especially valuable for industrial inspection tasks where throughput and robustness are essential.

The biological superlensing results also highlight open questions regarding the mechanical and optical roles of cell deformation. Although collapsed yeast cells consistently produced sub-diffraction imaging, the factors driving collapse, including membrane elasticity, water loss and cell–substrate interactions, require further study. Integrating optical characterisation with methods such as atomic force microscopy or interferometric profilometry could help quantify the deformation states that enable effective lensing. In addition, exploring other biological systems such as algae, bacteria or synthetic microcapsules with controlled refractive index and geometry may lead to more stable and reproducible biological lens platforms with improved imaging performance.

The metamaterial-filter results highlight a pathway for scalable, wide-angle optical components, but bringing these designs into practical devices will require advances in fabrication. Future work should investigate large-area assembly techniques for nanospheres, particularly the block copolymers (BCPs). For instance, polystyrene-b-poly (ethylene oxide) (PS-b-PEO) have demonstrated strong potential for forming highly ordered porous nanostructures with interstitial spacings as small as 30 nm via annealing-driven self-assembly. Extending the design methodology to include multi-band or tuneable filters, for instance through phase-change materials, liquid-crystal layers or strain-engineered substrates, would considerably broaden the range of achievable functionalities.

From a modelling perspective, the hybrid design approach demonstrated here could be further developed into a general optimisation framework. Incorporating fast surrogate models, reduced-order methods or lightweight machine-learning predictors would allow rapid exploration of design parameters while accounting for fabrication tolerances and environmental variations. The imaging digital-twin model explored in this thesis represents an early example of such data-driven support. In future, more targeted models that integrate physical constraints or incorporate a larger training corpus could provide predictive tools for

both imaging and filtering, assisting in design validation, inverse optimisation and experiment planning.

Finally, both the imaging and filtering technologies developed in this work possess strong potential for real-world applications. High-resolution mSIL systems may be integrated into semiconductor inspection tools, biological microscopy platforms or portable diagnostic devices. Angle-robust metamaterial filters could improve hyperspectral cameras, laser-blocking eyewear, compact spectrometers or outdoor imaging systems where variable illumination angles are unavoidable. Translating these research outcomes into practical systems will require collaboration across optical design, materials processing and device engineering, but the foundational principles demonstrated here provide a clear route forward.

In summary, the thesis opens several avenues for developing next-generation optical components based on spherical micro- and nanostructures. Future research that combines improved materials, advanced fabrication, refined modelling and application-driven integration will continue to expand the capabilities of these versatile photonic systems.

Author Contribution Statement

This thesis is based on original research conducted by the author under the academic supervision of the project supervisors. Except for the explicitly noted collaborative elements. All chapters including their experimental work, numerical simulations, theoretical developments, data analysis, and written content were primarily designed, executed, and completed by the author.

All experimental datasets used throughout this thesis, including SEM and optical imaging datasets for super-resolution studies and for machine-learning training, were fully generated, curated, and prepared by the author.

Deep-learning contribution (Chapter 4)

The deep-learning component in Chapter 4, *"Shape-Dependent TiO_2 mSIL Super-Resolution Imaging"*, Section 4.3 *"Deep Learning–Enabled SEM–Optical Translation"*, represents a collaborative element of the project. Specifically:

- The author generated, processed, and curated all SEM and optical training datasets.
- The author conducted the scientific interpretation and integrated the machine-learning outputs into the imaging analysis and digital-twin framework.
- Ms Fiza Khan, a collaborating PhD student, implemented and optimised the SinCUT model and developed the associated training pipeline.

Wide-Angle Metamaterial Edge Filter (Chapter 6)

Chapter 6, *"Wide-Angle Metamaterial Edge Filter"*, benefited from technical discussions and advisory suggestions from Dr James Monks and industry collaborators. These contributions helped refine certain design considerations and contextual understanding, but all modelling, simulations, analysis, and writing in this chapter were carried out by the author.

All other remaining experimental designs, imaging studies, simulation workflows, theoretical developments, data interpretation, and the writing of all chapters are the sole work of the author These works are undertaken within the normal expectations of doctoral supervision.

Appendix A: Mie Theory Fundamentals

In Mie theory, the optical responses are primarily determined by following parameters: the particle size (a), refractive index (n_p), incident light wavelength (λ) and refractive index of medium (n_m).

In free space, the electric and magnetic fields inside and outside a sphere illuminated by a plane wave satisfy the vector Helmholtz equation:

$$\nabla^2 E + k^2 E = 0,\ \nabla^2 H + k^2 H = 0 \tag{A.1}$$

where $k = \frac{\omega}{c}\sqrt{\varepsilon}$ is wave vector derived angular frequency ω, speed of light c and permittivity ε; ∇ is the Laplacian.

We consider an incident plane wave propagating along z-axis and the electric and magnetic vector are directed along x- and y-axis, respectively. The electric field and magnetic field of scattered (indicated by index "s") and internal (indicated by index "a") waves can be expressed in a spherical coordinate system by {r, θ, φ}:

$$E_r^{(s)} = \frac{\cos\varphi}{(k_m r)^2}\sum_{\ell=1}^{\infty} \mathrm{i}^{\ell+1}(2\ell+1)a_\ell \zeta_\ell(k_m r)P_\ell^{(1)}(cos\theta) \tag{A.2.a}$$

$$E_\theta^{(s)} = -\frac{\cos\varphi}{k_m r}\sum_{\ell=1}^{\infty} \mathrm{i}^{\ell+1}\frac{2\ell+1}{\ell(\ell+1)}\left[a_\ell \zeta_\ell'(k_m r)P_\ell^{(1)'}(cos\theta)sin\theta - ib_\ell \zeta_\ell(k_m r)\frac{P_\ell^{(1)}cos\theta}{sin\theta}\right] \tag{A.2.b}$$

$$E_\varphi^{(s)} = -\frac{\sin\varphi}{k_m r}\sum_{\ell=1}^{\infty} \mathrm{i}^{\ell+1}\frac{2\ell+1}{\ell(\ell+1)}\left[a_\ell \zeta_\ell'(k_m r)\frac{P_\ell^{(1)'}(cos\theta)}{sin\theta} - ib_\ell \zeta_\ell(k_m r)P_\ell^{(1)'}cos\theta sin\theta\right] \tag{A.2.c}$$

$$H_r^{(s)} = -\frac{\sqrt{\varepsilon_m}\sin\varphi}{k_m r}\sum_{\ell=1}^{\infty} \mathrm{i}^{\ell+1}(2\ell+1)b_\ell \zeta_\ell(k_m r)P_\ell^{(1)}cos\theta \tag{A.2.d}$$

$$H_\theta^{(s)} = -i\sqrt{\varepsilon_m}\frac{\sin\varphi}{k_0 r}\sum_{\ell=1}^{\infty} \mathrm{i}^{\ell+1}\frac{2\ell+1}{\ell(\ell+1)}\left[a_\ell \zeta_\ell(k_m r)\frac{P_\ell^{(1)}cos\theta}{sin\theta} + ib_\ell \zeta_\ell'(k_m r)P_\ell^{(1)'}cos\theta sin\theta\right] \tag{A.2.e}$$

$$H_\varphi^{(s)} = -i\sqrt{\varepsilon_m}\frac{\cos\varphi}{k_0 r}\sum_{\ell=1}^{\infty} \mathrm{i}^{\ell+1}\frac{2\ell+1}{\ell(\ell+1)}\left[a_\ell \zeta_\ell'(k_m r)P_\ell^{(1)'}(cos\theta)sin\theta + ib_\ell \zeta_\ell(k_m r)\frac{P_\ell^{(1)}cos\theta}{sin\theta}\right] \tag{A.2.f}$$

$$E_r^{(a)} = \frac{\cos\varphi}{(k_p r)^2}\sum_{\ell=1}^{\infty} \mathrm{i}^{\ell+1}(2\ell+1)c_\ell\psi_\ell(k_p r)P_\ell^{(1)}(cos\theta) \quad \text{(A. 3. a)}$$

$$E_\theta^{(a)} = -\frac{\cos\varphi}{k_p r}\sum_{\ell=1}^{\infty} \mathrm{i}^{\ell+1}\frac{2\ell+1}{\ell(\ell+1)}\left[c_\ell\psi_\ell^{'}(k_p r)P_\ell^{(1)^{'}}(cos\theta)sin\theta - id_\ell\psi_\ell(k_p r)\frac{P_\ell^{(1)}cos\theta}{sin\theta}\right] \quad \text{(A. 3. b)}$$

$$E_\varphi^{(a)} = -\frac{\sin\varphi}{k_p r}\sum_{\ell=1}^{\infty} \mathrm{i}^{\ell+1}\frac{2\ell+1}{\ell(\ell+1)}\left[c_\ell\psi_\ell^{'}(k_p r)\frac{P_\ell^{(1)^{'}}(cos\theta)}{sin\theta} - id_\ell\psi_\ell(k_p r)P_\ell^{(1)^{'}}cos\theta sin\theta\right] \quad \text{(A. 3. c)}$$

$$H_r^{(a)} = -\frac{\sqrt{\varepsilon_m}\sin\varphi}{k_p r}\sum_{\ell=1}^{\infty} \mathrm{i}^{\ell+1}(2\ell+1)d_\ell\psi_\ell(k_p r)P_\ell^{(1)}cos\theta \quad \text{(A. 3. d)}$$

$$H_\theta^{(a)} = -i\sqrt{\varepsilon_m}\frac{\sin\varphi}{k_0 r}\sum_{\ell=1}^{\infty} \mathrm{i}^{\ell+1}\frac{2\ell+1}{\ell(\ell+1)}\left[c_\ell\psi_\ell(k_p r)\frac{P_\ell^{(1)}cos\theta}{sin\theta} + id_\ell\psi_\ell^{'}(k_p r)P_\ell^{(1)^{'}}cos\theta sin\theta\right] \quad \text{(A. 3. e)}$$

$$H_\varphi^{(a)} = -i\sqrt{\varepsilon_m}\frac{\cos\varphi}{k_0 r}\sum_{\ell=1}^{\infty} \mathrm{i}^{\ell+1}\frac{2\ell+1}{\ell(\ell+1)}\left[c_\ell\psi_\ell^{'}(k_m r)P_\ell^{(1)^{'}}(cos\theta)sin\theta + id_\ell\psi(k_m r)\frac{P_\ell^{(1)}cos\theta}{sin\theta}\right] \quad \text{(A. 3. f)}$$

where P_ℓ^m are associated Legendre functions while ζ_ℓ and φ_ℓ are spherical Bessel functions. a_ℓ and b_ℓ are scattering wave coefficients while c_ℓ and d_ℓ internal wave coefficients. k_m and k_0 denote the wave numbers in vacuum and host medium, respectively.

Scattering wave coefficients (a_ℓ, b_ℓ) and internal wave coefficients (c_ℓ and d_ℓ) fundamentally determining the near-field profiles are defined as follows:

$$a_\ell = \frac{q_p\psi_\ell^{'}(q_m)\psi_\ell(q_p) - q_m\psi_\ell(q_m)\psi_\ell^{'}(q_p)}{q_p\zeta_\ell^{'}(q_m)\psi_\ell(q_p) - q_m\psi_\ell^{'}(q_m)\zeta_\ell(q_p)} \quad \text{(A. 4. a)}$$

$$b_\ell = \frac{q_p\psi_\ell^{'}(q_p)\psi_\ell(q_m) - q_m\psi_\ell(q_p)\psi_\ell^{'}(q_m)}{q_p\zeta_\ell^{'}(q_p)\psi_\ell(q_m) - q_m\psi_\ell^{'}(q_p)\zeta_\ell(q_m)} \quad \text{(A. 4. b)}$$

$$c_\ell = \frac{q_p\zeta_\ell(q_m)\psi_\ell^{'}(q_m) - q_p\zeta_\ell^{'}(q_m)\psi_\ell(q_m)}{q_p\zeta_\ell^{'}(q_m)\psi_\ell(q_p) - q_m\psi_\ell^{'}(q_p)\zeta_\ell(q_m)} \quad \text{(A. 4. c)}$$

$$d_\ell = \frac{q_p\zeta_\ell^{'}(q_m)\psi_\ell(q_m) - q_p\zeta_\ell(q_m)\psi_\ell^{'}(q_m)}{q_p\psi_\ell^{'}(q_p)\zeta_\ell(q_m) - q_m\psi_\ell(q_p)\zeta_\ell^{'}(q_m)} \quad \text{(A. 4. d)}$$

where q_0, q_p and q_m are crucial size parameters for non-magnetic material determined by four general input parameters including wavelength of incidence light (λ), medium refractive index (n_m), particle radius (a) and particle refractive index (n_p), respectively.

The size parameters can be expressed as follows:

$$\text{Size parameter: } q_0 = \frac{2\pi a}{\lambda} \tag{A. 5. a}$$

$$\text{Particle size parameter: } q_p = q_0 n_p = \frac{2\pi a}{\lambda} n_p \tag{A. 5. b}$$

$$\text{Medium size parameter: } q_m = q_0 n_m = \frac{2\pi a}{\lambda} n_m \tag{A. 5. c}$$

Appendix B: Simulation Data

The refractive indices of the materials utilised in this study are depicted in Fig. B1 [1–7].

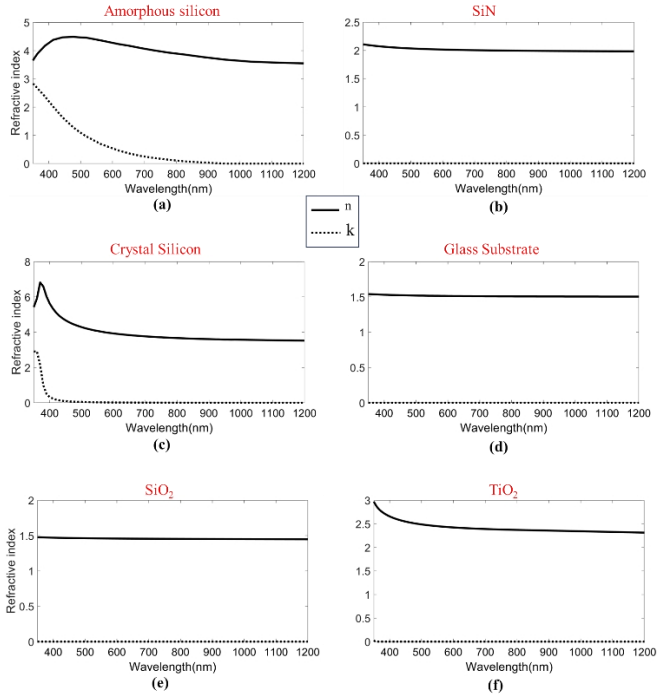

Figure B1 The refractive indices of the materials utilised in this study.

The far-field spectra of the simplified models of (a) sub-mSIL, (d) super-mSIL and (g) full-mSIL lenses under the illumination of an electric dipole parallel to simulation plane are shown in Fig. B2.

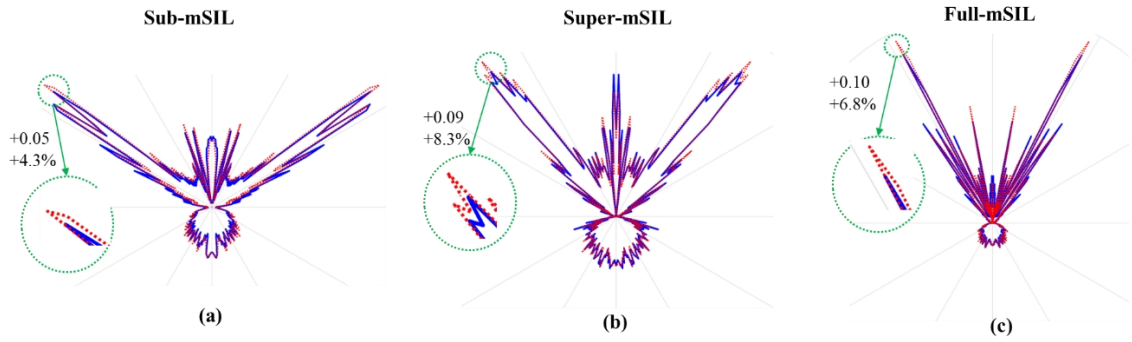

Figure B2 Far-field spectra of the simplified models of (a) sub-mSIL, (d) super-mSIL and (g) full-mSIL lenses under the illumination of an electric dipole with polarisation that is parallel to simulation plane. All other simulation setting were kept unchanged compared to Fig. 4.6.

References:

[1] C. Ji, C. Yang, W. Shen, K. Lee, Y. Zhang, X. Liu, L. J. Guo, "Decorative near-infrared transmission filters featuring high-efficiency and angular-insensitivity employing 1D photonic crystals. Nano Res. 2019, 12, 543–548.

[2] C. Schinke, P. C. Peest, J. Schmidt, R. Brendel, K. Bothe, M. R. Vogt, I. Kröger, S. Winter, A. Schirmacher, S. Lim, et al., "Uncertainty analysis for the coefficient of band-to-band absorption of crystalline silicon," AIP Adv. 2015, 5, 067168.

[3] M. R. Vogt, H. Hahn, H. Holst, M. Winter, C. Schinke, M. Köntges, R. Brendel, P. P. Altermatt, "Measurement of the optical constants of soda-lime glasses in dependence of iron content, and modeling of iron-related power losses in crystalline Si solar cell modules," IEEE J. Photovolt. 2016, 6, 111–118.

[4] L. V. Rodríguez-de Marcos, J. I. Larruquert, J. A. Méndez, J. A. Aznárez, "Self-consistent optical constants of SiO_2 and Ta_2O_5 films," Opt. Mater. Express, 2016, 11, 2016,3622–3637.

[5] S. V. Zhukovsky, A. Andryieuski1, O. Takayama, E. Shkondin, R. Malureanu, F. Jensen, A. V. Lavrinenko, " Experimental demonstration of effective medium approximation breakdown in deeply subwavelength all-dielectric multilayers," Phys. Rev. Lett. 2015, 115, 177402.

[6] L. Y. Beliaev, E. Shkondin, A. V. Lavrinenko, O. Takayama " Optical, structural and composition properties of silicon nitride films deposited by reactive radio-frequency sputtering, low pressure and plasma-enhanced chemical vapor deposition," Thin Solid Films, 2022, 763, 139568.

[7] M.N. Polyanskiy, "Refractiveindex.info database of optical constants," Sci. Data, 2024, 11, 1, 94.